STATE OF CALIFORNIA • DEPARTMENT OF TRANSPORTATION

TECHNICAL REPORT DOCUMENTATION PAGE

TR0003 (REV 10/98)

ADA Notice

For individuals with sensory disabilities, this document is available in alternate formats. For information, call (916) 445-1233, TTY 711, or write to Records and Forms Management, 1120 N Street, MS-89, Sacramento, CA 95814.

1. REPORT NUMBER
CA12-1999

2. GOVERNMENT ASSOCIATION NUMBER

3. RECIPIENT'S CATALOG NUMBER

4. TITLE AND SUBTITLE
Seismic Response of Precast Columns with Energy Dissipating Joints

5. REPORT DATE
May 25, 2011

6. PERFORMING ORGANIZATION CODE

7. AUTHOR
Sarira Motaref, M. Saiid Saiidi, David H. Sanders

8. PERFORMING ORGANIZATION REPORT NO.
CCEER-11-01

9. PERFORMING ORGANIZATION NAME AND ADDRESS
Center for Civil Engineering Earthquake Research
Department of Civil Engineering/258
University of Nevada
Reno, NV 89557

10. WORK UNIT NUMBER

11. CONTRACT OR GRANT NUMBER
59A0591

12. SPONSORING AGENCY AND ADDRESS
California Department of Transportation
Division of Research, Innovation and System Information (MS-83)
1227 O Street
Sacramento, CA 95814

13. TYPE OF REPORT AND PERIOD COVERED

14. SPONSORING AGENCY CODE

15. SUPPLEMENTARY NOTES
Prepared in cooperation with the State of California Department of Transportation

16. ABSTRACT

Accelerated bridge construction (ABC) in seismic areas requires particular attention to connections because of the need to dissipate energy. Five one-third scale segmental bridge columns and one 0.3-scale two-column bent with plastic hinges incorporating different advanced materials were designed and tested on one of the shake tables at the University of Nevada, Reno. The models were subjected to the Sylmar earthquake (Northridge 1994) record with increasing amplitudes until failure. All segmental models were cantilever with longitudinal steel dowels connecting the base segment to the footing. Unbonded post-tensioning (PT) was used to connect the segments and to minimize the residual displacements. Energy dissipation took place mostly through the yielding of the longitudinal bars in the base segment. Conventional reinforced concrete was used in the plastic hinge of a reference column. In one of the models, a built-in elastomeric pad integrated with the footing and a concrete segment constituted the plastic hinge. The other two columns incorporated ECC(engineered cementitious composite) and FRP (fiber reinforced polymer) wrapping at the lower two segments. The effectiveness of repair with FRP wraps was also studied by repairing and retesting of the reference column. A two-column pier with precast columns, precast footing and precast cap beam was also built. One column in a two-column pier with precast columns, precast footing and precast cap beam was also built. One column in the bent consisted of a conventional concrete material except for the plastic hinge in which ECC was used. The other was a GFRP tube reinforced concrete column. The column-pier cap connection waws a telescopic steel pipe-pin to facilitate construction and to provide a moment free connection, the test results showed that the proposed models are suitable for accelerated bridge construction in high seismic zones because of their superior

17. KEY WORDS
Seismic Performance, Precast, Segmental, Column, Shake Table, Unbonded Post-tensioning, Built-in Rubber Pad, ECC, FRP, GFRP Tube, Pipe-Pin

18. DISTRIBUTION STATEMENT
No restrictions. This document is available to the public through the National Technical Information Service, Springfield, VA 22161

19. SECURITY CLASSIFICATION *(of this report)*
Unclassified

20. NUMBER OF PAGES
762

21. COST OF REPORT CHARGED

Reproduction of completed page authorized.

DISCLAIMER STATEMENT

Report Number CCEER-11-01

Seismic Response of Precast Bridge Columns with Energy Dissipating Joints

Sarira Motaref
M. Saiid Saiidi
David H. Sanders

Center for Civil Engineering Earthquake Research
Department of Civil Engineering/258
University of Nevada
Reno, NV 89557

May 2011

Abstract

Accelerated bridge construction (ABC) is attractive in congested urban areas and environmentally sensitive regions because it minimizes traffic delays and construction site safety risk. Precast bridge components are an essential for ABC to succeed. However, knowledge of the behavior and performance of precast bridge columns and their connections during earthquakes is lacking, and consequently their widespread use in high seismic hazard regions is yet to be realized. ABC in seismic areas requires particular attention to connections because of the need to dissipate energy.

The purpose of this study was to develop precast column details that are able to dissipate energy under seismic loads. Several innovative precast concrete columns were designed, and studied experimentally on a shake table and analyzed. Two types of precast bridge columns were studied, including segmental columns and monolithic columns.

The first part of the project included studying four segmental concrete cantilever column models with plastic hinges incorporating different advanced materials to reduce damage under earthquake loads. All the models were of one-third scale with longitudinal steel dowels connecting the base segment to the footing. Unbonded post-tensioning was used to connect the segments and to minimize residual displacements. Energy dissipation took place mostly through the yielding of the longitudinal bars in the base segment. The columns were tested on one of the shake tables at the University of Nevada, Reno and were subjected to the Sylmar hospital ground motion (Northridge, California earthquake of 1994) with increasing amplitudes until failure.

One of the four column models constituted the benchmark case (SC-2). In this column conventional reinforced concrete detail was used in the base segment. The performance of other specimens having innovative materials in plastic hinges was compared with SC-2 to evaluate their merit relative to SC-2. The second specimen was a segmental concrete column incorporating an elastomeric bearing pad in the plastic hinge (SBR-1). The other two columns incorporated ECC (engineered cementitious composite) and unidirectional CFRP (carbon fiber reinforced polymer) fabrics in the lower two segments (SE-2 and SF-2), respectively. The purpose of using the elastomeric pad was to minimize damage while dissipating energy through yielding of the longitudinal bars and deformation of the rubber. Ductile behavior of the ECC resulted in less damage at the interface of the base and second segments in SE-2, and the column was able to sustain its lateral capacity under large drifts. The FRP wrapping provided confinement for the concrete and increased the displacement ductility capacity. The concrete damage in SF-2 was minimal and yielding of the longitudinal bars in the plastic hinge was more extensive. Compared to standard precast concrete segmental columns (those with no monolithic connection between the base segment and the footing), all specimens showed superior performance with minimal residual displacement and larger energy dissipation. The effectiveness of repair with CFRP wraps was also studied by repairing and retesting SC-2. The results showed that the strength and ductility capacity of the repaired model were improved compared to the original column, although the initial stiffness was lower. The relatively simple and effective repair procedure demonstrated that it is possible to quickly repair and restore the bridge.

The second part of the project was testing and analysis of a 0.3-scale two-column bent incorporating two precast columns, precast footing, and a precast cap beam. Two openings were formed in the footing during the construction to allow for placement of precast columns. The embedment length was designed in such a way as to transfer the full plastic moment of the column to the footing. One column was built with conventional reinforced concrete, but incorporated ECC in the plastic hinge zone instead of concrete (RC-ECC column). The other column consisted of a GFRP (glass fiber reinforced polymer) tube with +/- 55-degree fibers filled with concrete (FRP column). The column-pier cap connection was a telescopic steel pipe-pin to facilitate construction. The bent was tested to failure, which was due to fracture of longitudinal bars in the RC-ECC column, and rupture of GFRP fibers in the FRP column. Test results showed that the embedment length was sufficient to develop the plastic moment completely in both columns. It was further found that the seismic performance of both columns was satisfactory and that the pipe-pin connections performed well in that they remained damage free, as intended.

Comprehensive analytical models were developed using program OpenSees for all the test models and acceptable correlation was achieved between the measured and calculated data. This program is used for nonlinear dynamic analysis of structures using a variety of element models. The test results showed that the proposed models are suitable for accelerated bridge construction in high seismic zones (where large drifts are expected during earthquakes) because of their superior performance, such as fast construction, large energy dissipation, minimal damage in the plastic hinge zone and minimal residual displacement. Extensive parametric studies were performed to develop design methods for precast columns and to understand the influence of important factors on the capacity and performance of specimens. Seismic design methods for segmental columns and precast bent based on the test observations, measured data, and parametric studies were developed.

Executive Summary

1. Introduction

Accelerated bridge construction (ABC) is attractive because it minimizes traffic delays and construction site safety risk. Precast bridge components are essential for ABC to succeed. However, knowledge of the behavior and performance of precast bridge columns and their connections during earthquakes is lacking, and consequently their widespread use in high seismic hazard regions is yet to be realized. ABC in seismic areas requires particular attention to connections and plastic hinges because of the need to dissipate energy. In standard segmental column construction the end segments are not fixed to the footing or the cap beam. Studies have shown that, under seismic loading, standard segmental columns offers minimal energy dissipation because of the discontinuity of longitudinal reinforcement. Connecting the end segment to the footing or the cap beam via reinforcing bars (monolithic connection) provides energy dissipation capability under seismic loading through yielding of the bars (Fig. 1). The end segments may be made of reinforced concrete that are similar to the other segments. However, ABC provides an opportunity to further improve the seismic performance of bridge columns by utilizing materials such as elastomeric bearing pad, FRP (fiber reinforced polymer), and ECC (engineered cementitious composite) in plastic hinge zones of the end segments and increase energy dissipation while minimizing damage.

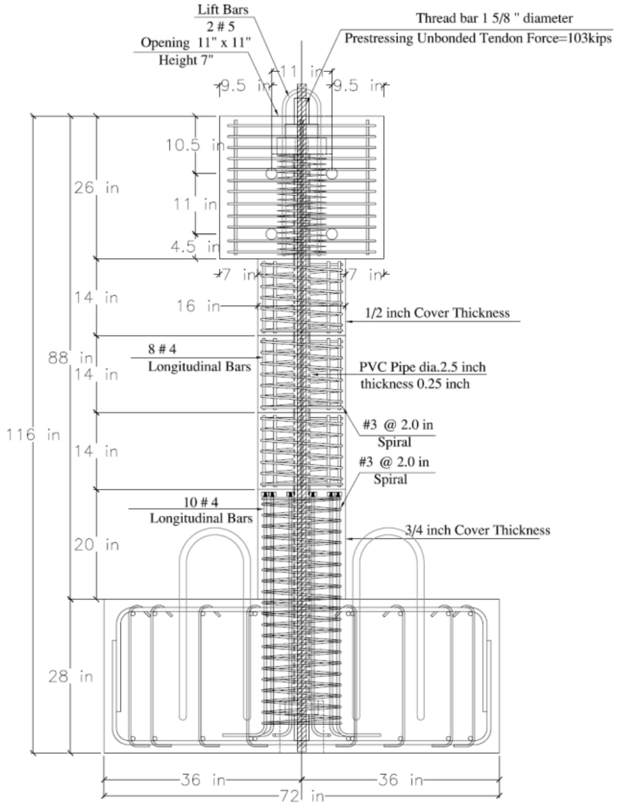

Fig. 1- Segmental Columns with the Base segment Connected to the Footing

An alternative to segmental columns for ABC is a single-segment precast column (Fig. 2). The precast column may be made with conventional reinforced concrete (RC) or FRP tubes filled with concrete. An opening with sufficient depth in the footing allows for embedment of the column and development of its plastic moment at the top of the footing. In some concrete bridges columns, one end may be detailed to act as a pin to eliminate moments while transferring shear and axial loads to the connecting element. Pipe-pin hinges could be effectively used in precast bridge construction because of their ease of construction. Pipe-pin hinges provide a moment free connection between the columns and the cap beams.

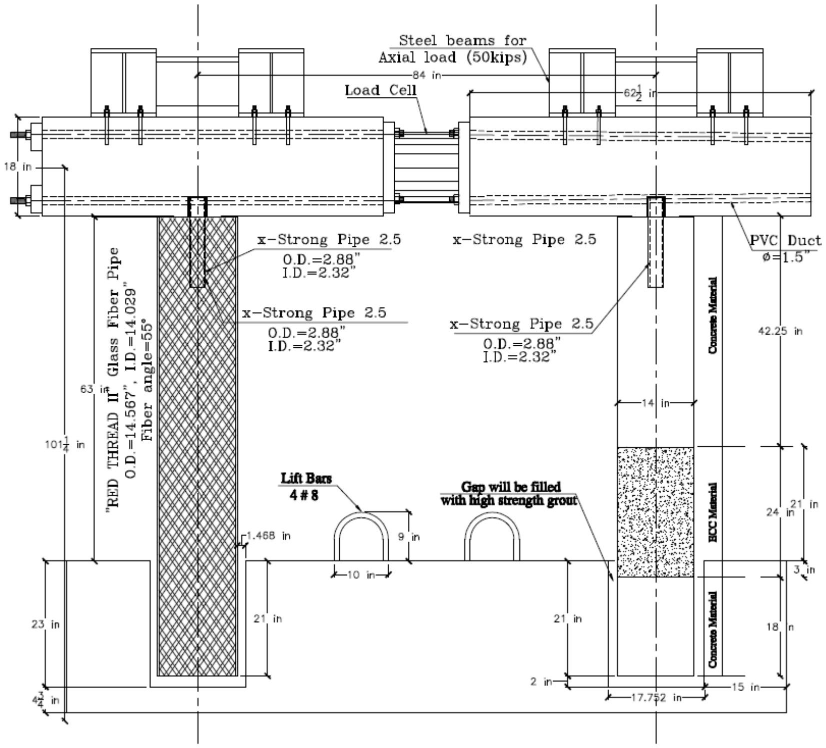

Fig. 2- Precast Monolithic Columns

2. Research Objective

The purpose of this study was to develop precast column details that are able to dissipate energy under seismic loads while minimizing damage. This research involved analytical and experimental investigation of the performance of precast bridge columns under lateral seismic loading. The main goal of the study was to investigate different details of precast columns and identify their seismic performance characteristics and their relative merit with respect to ductility, energy dissipation, and damage. Two types of precast bridge columns were studied: segmental columns and single-segment precast columns.

The segmental columns were cantilever members in which the base segment details were the primary variable. The base segment height, base segment longitudinal steel reinforcement, post-tensioning force, application of advanced materials such as elastomeric bearing pad, FRP jacket, and ECC were of prime interest in segmental column studies. Five large-scale column models were constructed and tested in the experimental study of segmental columns.

Design of embedment length, application of pipe-pin hinges in precast construction, use of advanced materials such as FRP tube and ECC in the single-segment precast columns were studied in shake table testing of a large-scale two-column bent model.

To help understand the behavior of different models and evaluate the adequacy of analytical techniques, computer program OpenSees was used in the study of the test models and the subsequent parametric studies.

3. Experimental Studies

A series of experiments was designed and performed at the Large Scale Structure Laboratory at the University of Nevada, Reno (UNR) to study and develop new systems for precast columns that are able to dissipate energy under seismic loads while reducing damage. The specimens were tested on the UNR shake table system and were subjected to different records obtained in Sylmar during the Northridge, California earthquake of 1994. The amplitude of shake table motions was increased in subsequent runs until failure. The specimens included five segmental concrete columns, four of which were detailed with different low-damage plastic hinges and a precast two-column pier.

3.1. Segmental Columns

Segmental specimens were one-third scaled cantilever column models with base segments that were connected to the footing via reinforcing bars to increase energy dissipation under seismic loading. An unbonded post tensioning (PT) rod was used to connect the segments and to minimize residual displacements. In the benchmark column, SC-2 (segmental with concrete), a conventional reinforced concrete detail was used. The performance of other specimens consisting of advanced materials in the plastic hinge region was compared with that of SC-2. The second specimen, referred to as SBR-1 (segmental with built-in rubber pad), was a segmental concrete column incorporating an elastomeric bearing pad in the plastic hinge. The third and forth columns were designated SE-2 (segmental with ECC) and SF-2 (segmental with FRP). SE-2 utilized ECC in the lower two segments. FRP wrap was used in the lower two segments of SF-2 to confine the concrete and minimize damage at interface between the base and second segments. The study included a limited investigation of the effect of repair on segmental columns by repairing SC-2 with FRP fabrics and retesting the column.

The diameter of the columns was 16 in. (406 mm) and their height was 72 in. (1829 mm), leading to an aspect ratio of 4.5. The column height was taken as the distance from the top of the footing to the centerline of the column loading head where the inertial load was applied. The clear column height was 62 in. (1580 mm) (Fig. 1). The total base segment depth was 20 in. (508 mm). The base segment height in the SBR-1 included 8 in. (203 mm) rubber pad and 12 in. (305 mm) reinforced concrete. Details of the bearing are shown in Fig. 3. The base and second segments of SF-2 and SC-2R were wrapped with two 0.04-in. (1-mm) thick layers of FRP. The two lower segments of SE-2 were made out of ECC. The longitudinal steel ratio was 1% in the base segment of SC-2, SF-2, and SE-2, and 1.20% in the base segment of SBR-1. The depth of the segment two, three and four was 14 in. (356 mm) in all segmental column models. Due to the discontinuity between segment two and higher, the longitudinal reinforcement was not expected to yield, and hence only a small amount of longitudinal steel was provided. The total axial load on the columns was comprised of 80 kips (355.8 kN) gravity load and 100 kips (444.8 kN) post-tensioning force. The total axial load corresponded to an axial load index (ALI) of 0.20. ALI is defined as the ratio of the axial load to the product of the gross section area and the concrete compressive strength. A 1-5/8 in. (40 mm) diameter PT unbonded high strength bar was used in the column central core. The rod was anchored in the foundation below the column and in the head at top of the column.

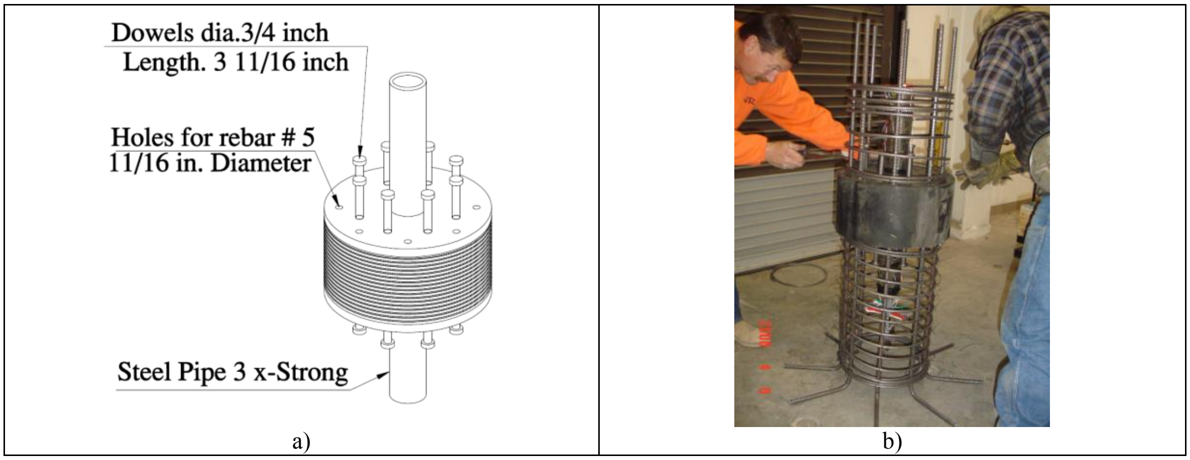

a) b)

Fig. 3- a) Elastomeric Bearing Pad in SBR-1 b) Base Segment Configuration

Construction stages column included building the steel cages (Fig. 4 (a)), casting the footing, casting the segments using match cast method, and assembling the columns. Column segments were assembled on the shake table in approximately three hours (Fig. 4 (b)). A small amount of epoxy was applied on top of each surface before placing the next segment to stabilize the segments during construction. The segmental columns were subjected to a series of Sylmar ground motions with the acceleration amplitude scaled by 0.1, 0.25, 0.5, 0.75, 1, 1.25, and 1.5 in subsequent runs. The full Sylmar motion had the maximum acceleration of 0.61g.

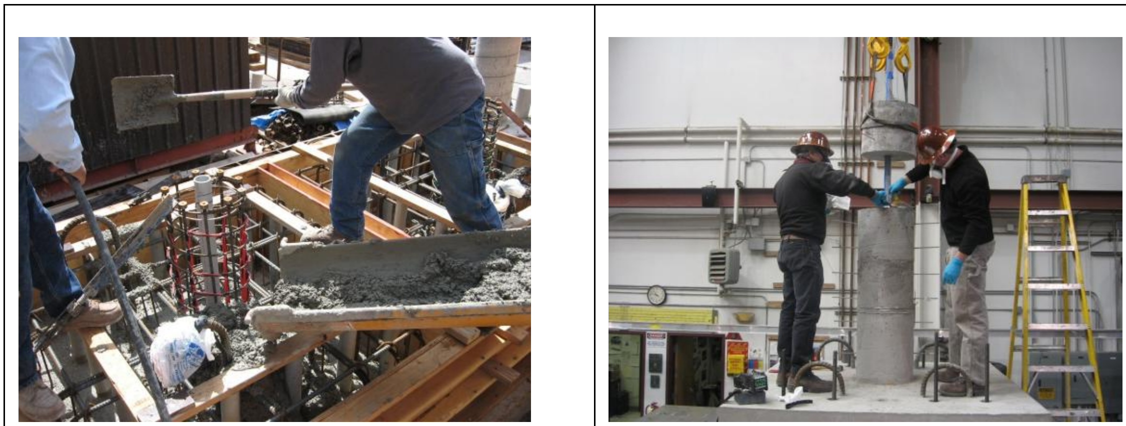

a) b)

Fig. 4- Footing and the Base Segment steel Cages, b) Assembling Process in Segmental Columns

The main failure mode in segmental columns was concrete spalling at the interface between the base and second segments. Failure of concrete was attributed to the large cyclic compressive strains from opening and closing action at the interface and the fact that the surface concrete and the concrete at the interface of the segments were not confined. The extension of damage was different in different segmental columns depending on the material in the first two segments. Segmental columns after experiencing 10% drift are shown in Fig. 5. The most extensive cover spalling was observed in SC-2 (Fig. 5 (a)). SBR-1 also experienced concrete spalling at the interface between the base and second segments, but the damage was not as extensive as that in SC-2. The lower part of the base segment in SBR-1 was free from damage due to the incorporation of the elastomeric bearing pad (Fig. 5(b)). The FRP jacket ruptured in SF-2 and SC-2R but the concrete spalling was minor compared to that of SC-2 (Figs. 5 (c) and (e)). The minimal damage observed in SF-2 and SC-2R revealed that using FRP jacket can reduce the concrete spalling substantially. FRP rupture in SC-2R was more severe than the rupture in SF-2. The weak bond between the repair grout and concrete in SC-2R is believed to have caused the damage. The cover spalling in SE-2 was minimal and limited to two sides of the interface. Minimal ECC spalling was observed due to the ductile behavior of ECC material (Fig. 5 (d)).

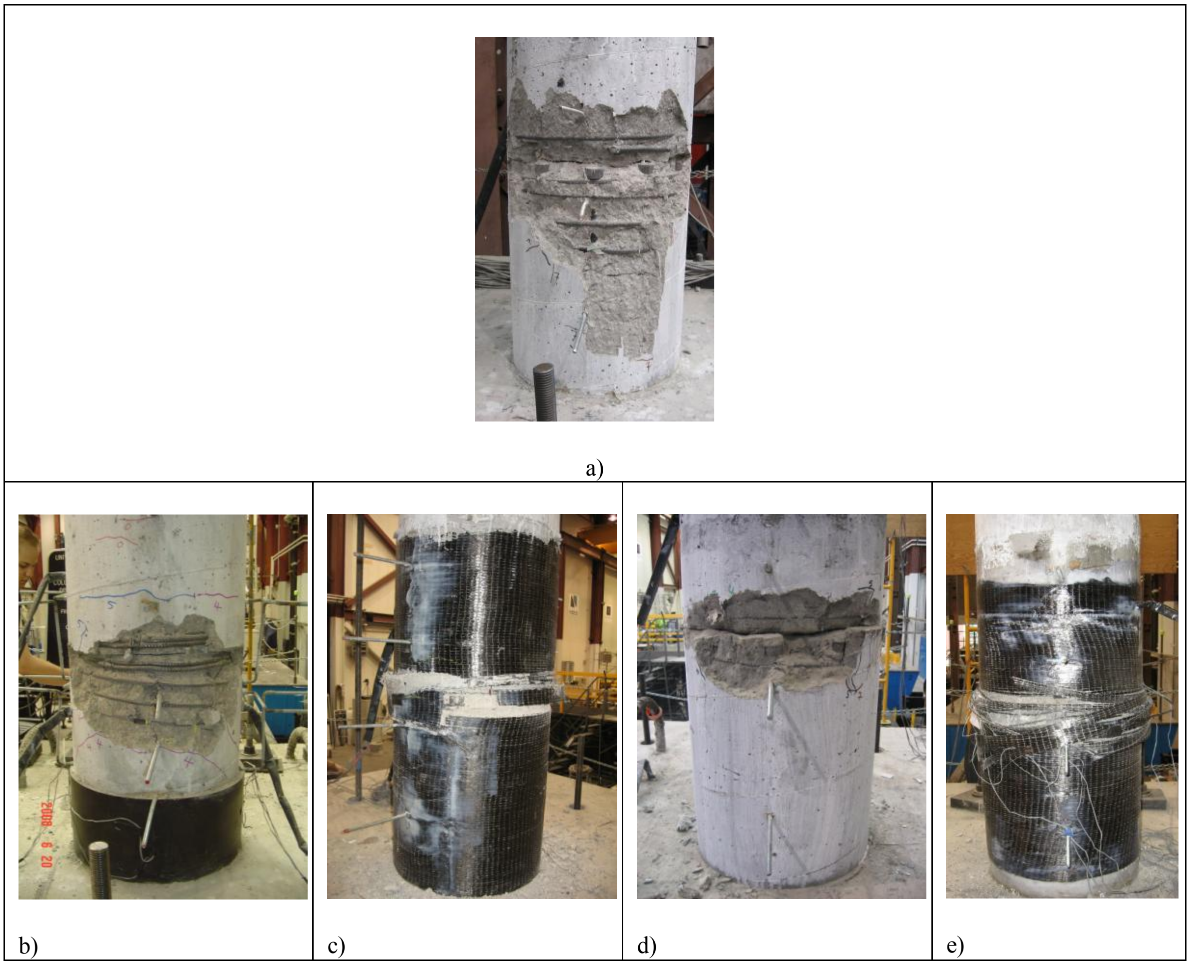
a)

b)

c)

d)

e)

Fig. 5- Apparent Damage at 10% Drift for a) SC-2, b) SBR-1, c) SF-2, d) SE-2, e) SC-2R

The lateral load capacities in segmental columns with innovative detail are compared with that of the reference column (SC-2) in Fig. 6. The average response envelope in the positive and negative displacement directions was used to compare the lateral load response of the columns. Segmental columns showed various lateral load capacities under the dynamic motion. This difference in the capacity was because of different details and various extension of damage in columns.

Figure 6 (a) shows the normalized lateral load response in SBR-1 and SC-2. Since the longitudinal steel ratios were different in SC-2 and SBR-1, the normalized load-deflection envelopes were used to compare their performances. Normalizing was conducted by dividing the loads by the lateral load capacity at 5% drift ratio. The force at 5% drift was chosen for normalizing, since 5% drift is considered to be a large drift ratio that might be expected under strong earthquakes. It can be seen that the initial stiffness of SBR-1 was smaller than the SC-2 stiffness. This is because of the lower compressive modulus of elasticity of the rubber compared to that of concrete. The normalized peak lateral force in SC-2 was 1.01 at a drift ratio of 4.2%, and the strength deteriorated after this displacement. In contrast, SBR-1 was able to maintain its capacity even at a drift ratio of 14%. The maximum normalized lateral force in SBR-1 was 1.16 that was 15% larger than the SC-2 capacity. The maximum lateral load capacity of SF-2 and SC-2 were 30.3 kips (134.6 kN) and 22.1 kips (98.5 kN), respectively (Fig. 6(b)). The lateral load capacity of SF-2 was 32% larger than that of the SC-2. The larger capacity of SF-2 was attributed to the confinement provided by the CFRP jacket, which delayed failure of concrete at the interface of its bottom two segments. The maximum measured drift capacity of SF-2 was 15%, which was 36% larger than the SC-2 drift capacity. Unlike SC-2, no degradation in the capacity of SE-2 was observed due to the ductile behavior of ECC, which resulted in minimal spalling and minor section loss at the interface of two lower segments (Fig. 6 (c)). The maximum lateral load capacity and ultimate drift ratio of SC-2 were slightly larger than that of SE-2. The maximum lateral load capacity in SE-2 was 22-kips (97.8-kN). The maximum lateral force in SC-2R was 32 kips (142.3kN), which was 45% larger than that of SC-2, and it did not deteriorate (Fig. 6 (d)). However, the initial stiffness of SC-2 was not restored by the repair due to material degradation during the original column tests. The larger capacity of SC-2R was attributed to the confinement provided by the CFRP jacket, which delayed failure of concrete at the interface of its bottom two segments. The ultimate drift in SC-2R was 14.8%, which was 35% larger than drift in SC-2. The successful performance of SC-2R demonstrated that the repair of column SC-2 was effective in restoring its strength and drift capacity.

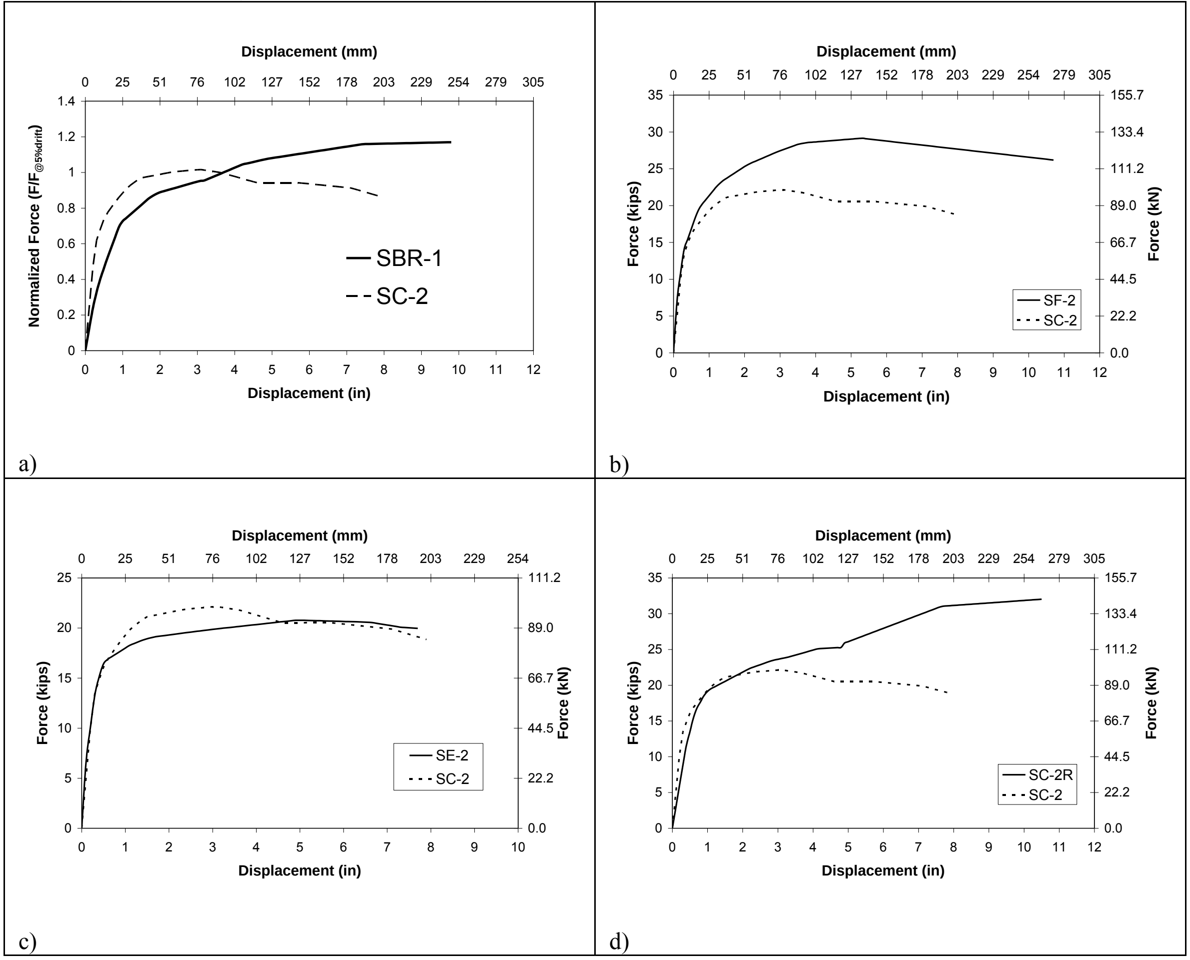

Fig. 6- Comparison of Backbone Curves in SC-2 versus a) SBR-1, b) SF-2, c) SE-2,d) SC-2R

In general residual displacements were minimal in all segmental columns due to unbonded post tensioning system. The post-tensioning rod was designed such that the maximum estimated force in the rod would not exceed 70% of the yield strength. Therefore, the force in the rod was always in elastic region, and after unloading the elongation was fully recovered.

The dissipated energy was calculated by integrating the area enclosed by the force displacement hysteretic curves. A conventional precast concrete segmental column, similar to SC-2, but with no dowels connecting the base segment to the footing was analyzed using OpenSees [OpenSees Manual, 2005] to quantify the effect of fixed base connections of the test models on energy dissipation. The dissipated energy was plotted against the maximum displacement for each run in Fig. 7. Comparison of graphs at drift ratios of 4% and 8% showed that the dissipated energy in segmental columns with the base segment connected to the footing was 2 to 4 times larger than that of a column with no dowels connecting the base segment and the footing. At the ultimate displacement of 10.5 in. (267 mm) (14.5 % drift), SC-2R, SBR-1 and SF-2 dissipated higher energy than other columns.

Using FRP jacket in SF-2 and SC-2R delayed concrete failure and increased the energy dissipation due to increased yielding of the bars. Flexural deformation of elastomeric pad in the plastic hinge of SBR-1 increased dissipated energy and eliminated the damage in that area.

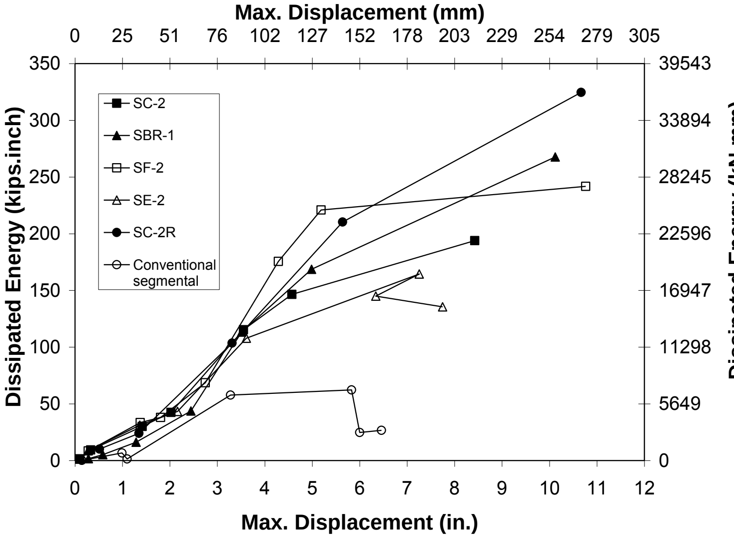

Fig. 7- Comparison of Dissipated Energy in Segmental Columns

3.2. Precast Two-Column Pier

A precast two-column pier PFEB (precast FRP-ECC bent) was also tested and analyzed to investigate the feasibility and seismic performance of single-segment precast columns. Two innovative details were used in the columns of the pier: one column was a conventional concrete column incorporating ECC in the plastic hinge zone, and the other was a FRP tube filled with concrete. Pipe-pin hinges were used at column-cap beam connections. The diameters of RC-ECC column and FRP columns were 14 in. (355 mm) and 14.567 in (370 mm), respectively. The column height was 63 in. (1600 mm) leading to an aspect ratio of 4.5. The column height was taken as the distance from the top of the footing to the bottom of the cap beam where the pipe hinge was located. The total column height including the part embedded in the footing was 86 in. (2184 mm). The FRP tube was Red Thread® II pipe with the wall thickness of 0.269 in (6.83 mm). The fibers were at +/-55° providing strength in the longitudinal and hoop directions. The longitudinal steel ratios in RC-ECC column and FRP column were 1.60% and 0.46%, respectively. A 2-1/2 x-Strong steel pipe was used as the pipe-pin for both of the columns. Two openings were designed in the footing to provided space for anchoring the columns (Fig. 8). The depth of the opening was 23 in. (584 mm) and was equal 1.50 times the column diameter plus 2 in. (50 mm) gap underneath of column.

Construction of PEFB included building the steel cages, casting of concrete in the footing and columns, and assembling the bent. Assembling the bent included inserting the columns in to the footing holes, placing the cap beam, and filling the gap with a low-shrinkage grout. Figures 8 (a) and (b) show inserting RC-ECC column in to the footing and the bent after assembly, respectively.


a)
b)

Fig. 8- a) Inserting the Columns in to the Footing, b) PEFB after Assembly

The bent was subjected to a series of six gradually increasing excitations simulating the 1994 Northridge Sylmar station acceleration record with a PGA of 0.91g. The scaling factors were 0.1, 0.4, 0.7, 1.0, 1.3, and 1.65 with the corresponding PGA values of 0.091 g, 0.364 g, 0.637 g, 0.91 g, 1.183 g, 1.44 g, respectively.

Figure 9 shows the plastic hinges after the last test when the column bases failed. Due to ductile behavior of ECC, spalling was minor, and it was limited to 5 in. (127 mm) height of RC-ECC column from top of the footing (Fig. 9 (a)). Three steel longitudinal bars ruptured in the RC-ECC column. Two of the bars were in the south side, and one was in the north side of the column.

Extensive FRP rupture occurred on the south face of FRP column at failure (Fig. 9(b)). To investigate the condition of longitudinal bars in the FRP column, the FRP tube was removed, and two buckled bars were observed on the south side of the FRP column (Fig. 9(b)).

a)

b)

Fig. 9- Apparent Damage at Failure Point in a) RC-ECC Column, b) FRP Column

The average response envelope of columns in the positive and negative displacement directions is compared in Fig. 10 (a). The maximum lateral load capacity of FRP column was 33.7 kips (149.9 kN) that was 30% larger than that of the RC-ECC column. The maximum lateral load capacity of RC-ECC column was 24.7 kips (109.8 kN). There was a large drop in the lateral load capacity of both column that was due to the rupture of FRP tube in FRP column and rupture of longitudinal bars in the RC-ECC column.

The initial stiffness of the columns was the same, but the hardening after yielding was substantially more significant in the FRP column because the FRP tube remained elastic. The ductility capacity of RC-ECC column was 7.77 compared to the FRP column ductility capacity, which was 5.77. The larger ductility of RC-ECC column was due to the larger effective yield displacement of the FRP column.

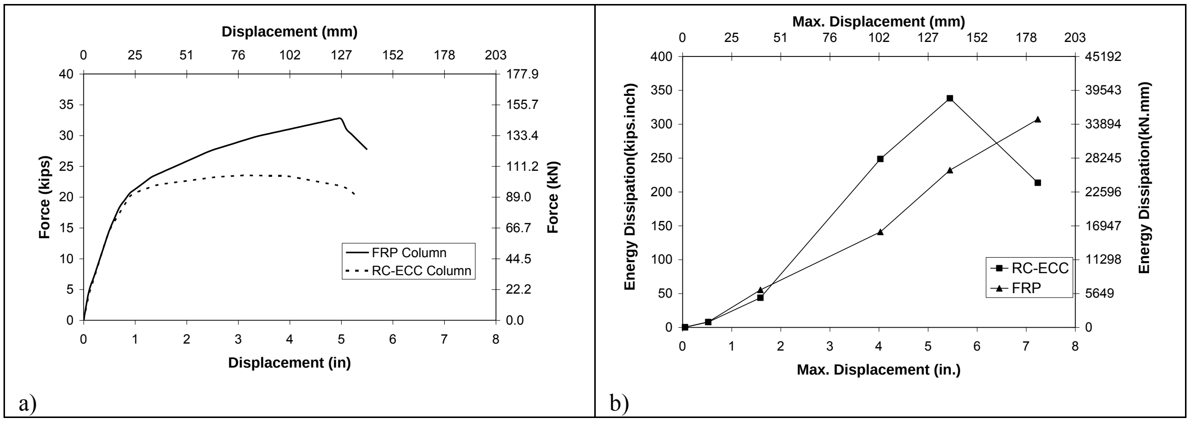

Fig. 10- Comparison of a) Back Bone Curves and b) Dissipated Energy in PEFB Columns

The dissipated energy versus the maximum displacement during each run is plotted in Fig. 10 (b). The energy dissipation was larger in RC-ECC column in all the runs except the last run when the bars ruptured during Run 6. The cumulative dissipated energy in RC-ECC column was 13% larger than that of the FRP column, although its lateral load capacity was 30% less than that of the FRP column. The steel ratio in RC-ECC column was 1.6 % compared to the steel ratio of 0.46% that was used in FRP column. The larger energy dissipation in RC-ECC column was attributed to the higher steel ratio and usage of ECC in its plastic hinge.

4. Analytical Studies

Comprehensive analytical models were developed using program OpenSees for all the test models. This program is used for nonlinear dynamic analysis of structures using a variety of element models. The analytical models were utilized to model the specimens for the design phase prior to the tests and to evaluate their adequacy in duplicating the measured response.

The column sections were defined using a fiber model with the measured material properties of the test columns. The analytical model was used to determine forces, displacements, post-tensioning forces, segment separation, and material strains. The analytical model for the segmental columns used in the OpenSees analyses is shown in Fig. 11. Post-tensioning rod elements were defined at the same height of those of the column. Using equalDOF command in OpenSees, horizontal deformation and rotation of PT nodes became similar to that of the column nodes.

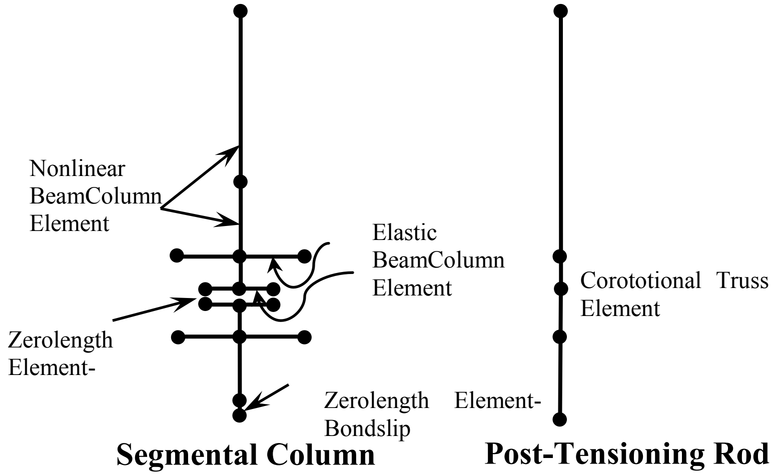

Fig. 11- Schematic Analytical Model for Segmental Columns

The measured and calculated cumulative force-displacement hysteresis curves for the segmental columns are plotted in Fig. 12. Generally, close agreement was seen between the calculated and measured force-displacement response of all segmental columns. The maximum lateral load capacity of all columns was slightly overestimated in the negative direction of motion.

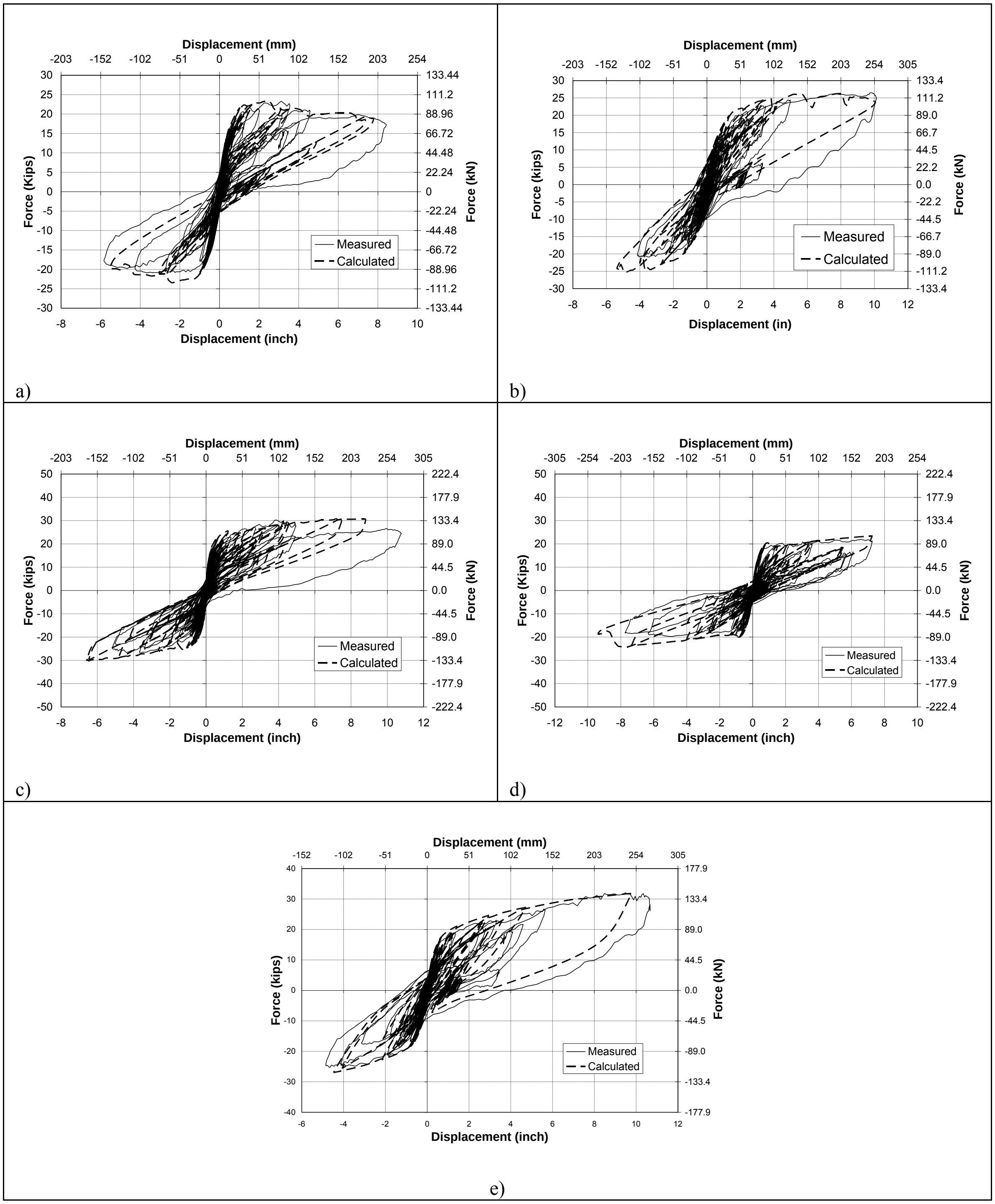

a)

b)

c)

d)

e)

Fig. 12- Accumulated Force-Displacement Hysteresis Curves for a) SC-2, b) SBR-1, c) SF-2, d) SE-2, e) SC-2R

The OpenSees model for the two-column bent is shown in Fig. 13. Two different sections were defined for RC-ECC column including the ECC and concrete. The FRP column section included the FRP tube material in the cover and confined concrete in the core. The columns were modeled by assigning the "nonlinearBeamColumn"elements. Since the pipe-pin detail was originally designed for larger demands and their capacity was larger than what was required in PEFB, it was assumed that the pipe-pins remained elastic in the analytical model.

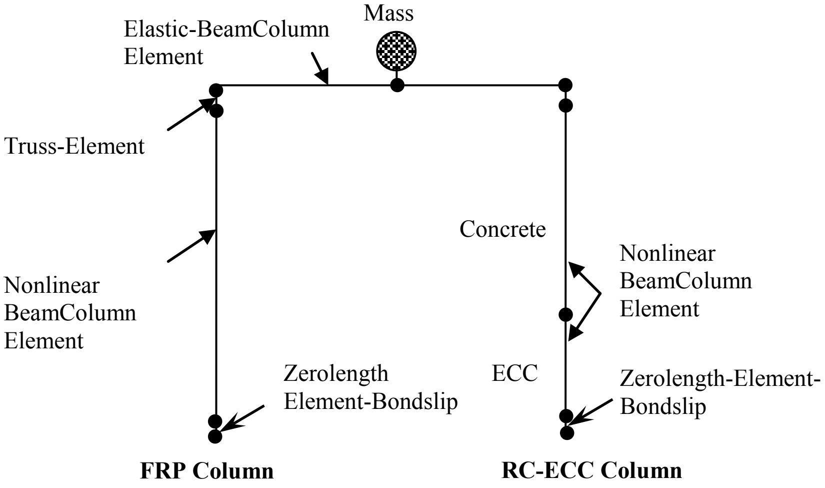

Fig. 13- Schematic Analytical Model of PEFB

The measured and calculated force-displacement curves of the bent are shown in Fig. 14. Good match was achieved between the measured and calculated force-displacement of bent before the last run. The maximum calculated lateral load capacity of the bent was only 0.4% larger than the maximum measured capacity. There was a large drop in the lateral load capacity due to rupture of FRP tube and rupture of longitudinal bars in RC-ECC column. These effects were not captured by the analytical model. The calculated and measured maximum displacements were nearly the same in the positive direction but not in the negative direction.

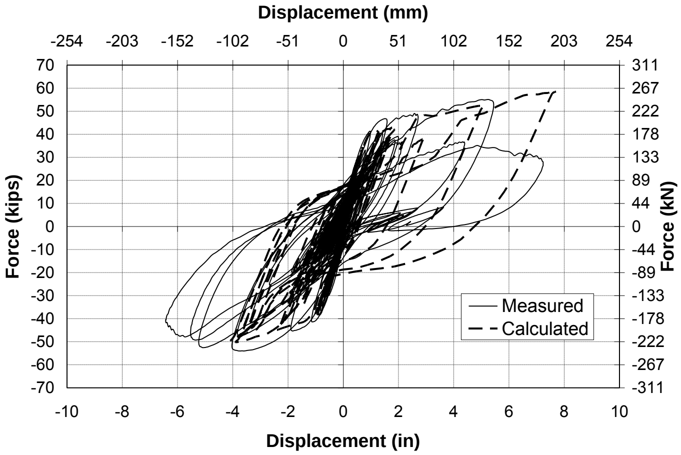

Fig. 14- Accumulated Force-Displacement Hysteresis Curves for the Bent

5. Parametric Studies

The analytical models were found to be reliable because they generally led to acceptable correlation with the experimental data. To determine the effect of variables that were not included in the experimental studies, the analytical models were used to determine the sensitivity of the response to changes in different variable. The parametric studies were conducted for SC-2, SBR-1, and concrete-filled FRP tube. It was assumed that the columns are cantilever. The effect of parameters such as base segment height, longitudinal steel reinforcement ratio, concrete strength, and initial post-tensioning force was studied in SC-2. In SBR-1, the rubber pad thickness and shape factor were varied. The performance of SC-2 was also compared with a conventional segmental column with no dowels connecting the base segment to the footing. The effects of FRP tube thickness, FRP tube fiber orientation, and longitudinal steel reinforcement ratio were studied in the concrete-filled FRP column. Each column was analyzed under two half cycle loadings with maximum drift ratios of 5% and 10%. The force-displacement response of columns under 5% drift ratio is discussed in the executive summary. The basic model in the SC-2 and SBR-1 studies was a segmental column with the base segment monolithically connected to the footing.

The force-displacement response of SC-2 with different base segment heights is shown in Fig. 15 (a). No drop in the lateral load capacity was observed in the columns with base segment heights of 32 in. (813 mm) and 40 in. (1016 mm) (0.44 and $0.55\times$column height, respectively), the full moment capacity was developed, no opening occurred between the base and second segments, and the behavior was similar to that of monolithic concrete columns. The opening between the end and adjacent segments occurs when the interface cracks. The tensile stress at extreme fiber occurs when the moment is equivalent to the "cracking moment" of the interface. When the base segment is sufficiently tall, the cracking moment occurs within the base segment and joint does not open.

Figure 15 (b) shows the force-displacement response of SC-2 with different steel ratios in the base segment. The full moment capacity in the column incorporating 0.5% longitudinal steel ratio was developed and no joint opening was seen in this model. When small amount of longitudinal steel ratio is placed in the base segment, the difference between the cracking moment and the full moment capacity of the section is small; therefore, the cracking moment occurs within the base segment and the full moment capacity is developed.

Figure 15 (c) shows that using high strength concrete increased the maximum lateral load capacity and decreased the residual displacement. The improvement in response was attributed to delay in failure of concrete at the interface between the lower two segments.

The force-displacement response of SC-2 with variable initial PT force is shown in Fig. 15 (d). This figure shows that a very low PT force results in steep strain hardening in the pushover curve while using a relatively high initial PT force results in lower overall ductility and degrading strength. The separation between the segments was delayed in the columns with larger initial PT force; therefore, a larger moment capacity was developed at the base segment that led to a larger lateral load capacity. After separation between the lower segments, all columns with different initial PT force showed similar capacities.

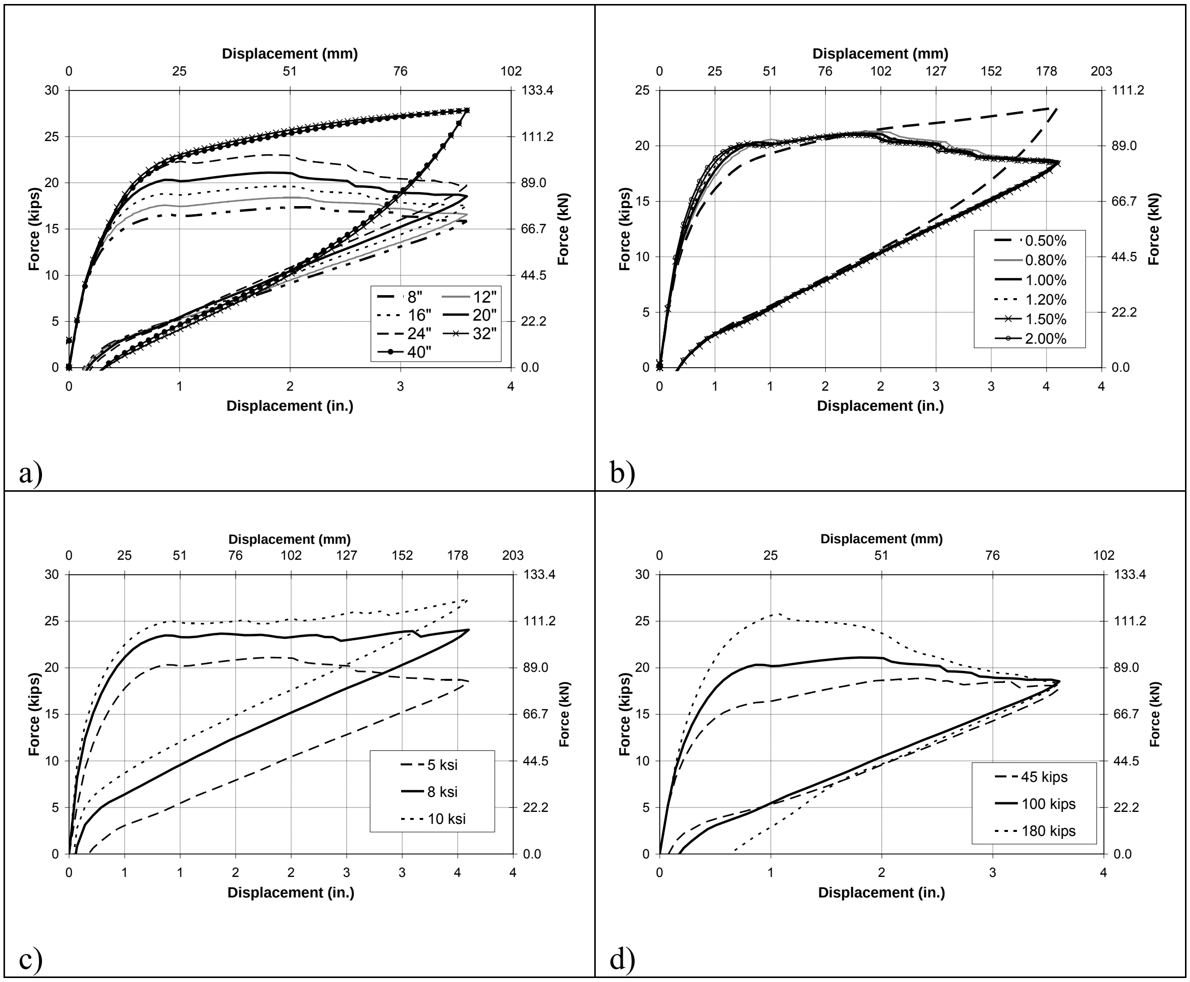

Fig. 15- Force-Displacement Cyclic Curve for SC-2 with Different a) Base Segment Heights, b) Steel Ratios, c) Concrete Strengths, d) PT Force Levels

The force-displacement curve for SBR-1 with variable bearing thicknesses and shape factors are shown in Figs. 16 (a) and (b).

Figure 16 (a) shows that the initial stiffness of the column with thicker elastomeric bearing was lower than that of the column incorporating a shorter bearing pad, as expected. The maximum lateral load capacities of the columns were approximately the same. The Shape factor for a bearing is defined as the ratio of the loaded area to the total force-free area. The columns with lower shape factors exhibited lower initial stiffness. The lateral load capacity in the column with low shape factor rubber pad of 5 was 5% larger than that of the basic model when the column was loaded to 10% drift ratio. The difference was due to more extensive yielding and strain hardening of the longitudinal steel. The residual displacement in column with a shape factor of 5 was 40% larger than those of other columns for loading to 5% drift ratio due to more extensive yielding of the longitudinal bars and the resulting permanent strains.

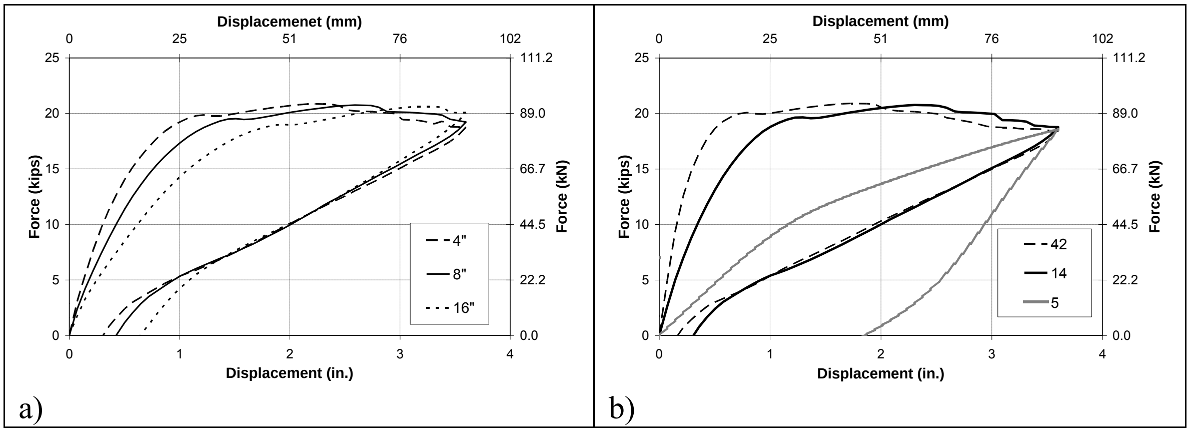

Fig. 16- Force-Displacement Cyclic Curve for SR-1 with Different a) Bearing Pad Heights, b) Shape Factors

To compare the effect of using a base segment that is fixed to the footing, a conventional segmental column was analyzed using OpenSees. In a conventional segmental column the base segment is not connected to the footing by dowels and the only connection is through the post-tensioning rod. Figure 17 shows that the lateral load capacity of SC-2 was 26% larger than that of conventional segmental column because of the moment connection at the base.

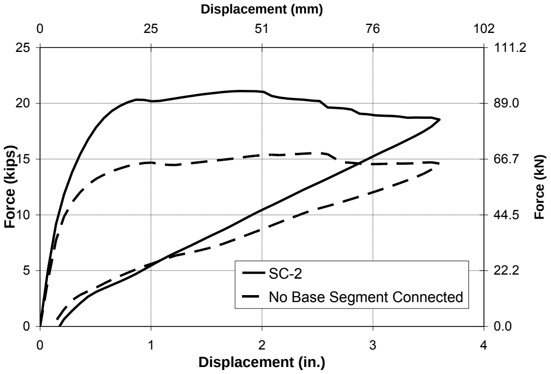

Fig. 17- Comparison between the Force-Displacement Cyclic Curves of SC-2 and Conventional Segmental Column

Figure 18(a) shows the force-displacement response of FRP columns with different FRP tube thicknesses. The initial stiffness in all cases was the same, but the maximum lateral load capacities increased for thicker tubes. The thicker tubes provide more confinement to the concrete and increased its strength and ductility.

The force-displacement response of FRP column with different fiber orientations is shown in Fig. 18 (b). The lateral load capacity was the highest when the fiber orientation of $\pm 35^\circ$ was used. Higher lateral load capacity in the cases with smaller fiber angles was attributed to their larger longitudinal component of fiber stress.

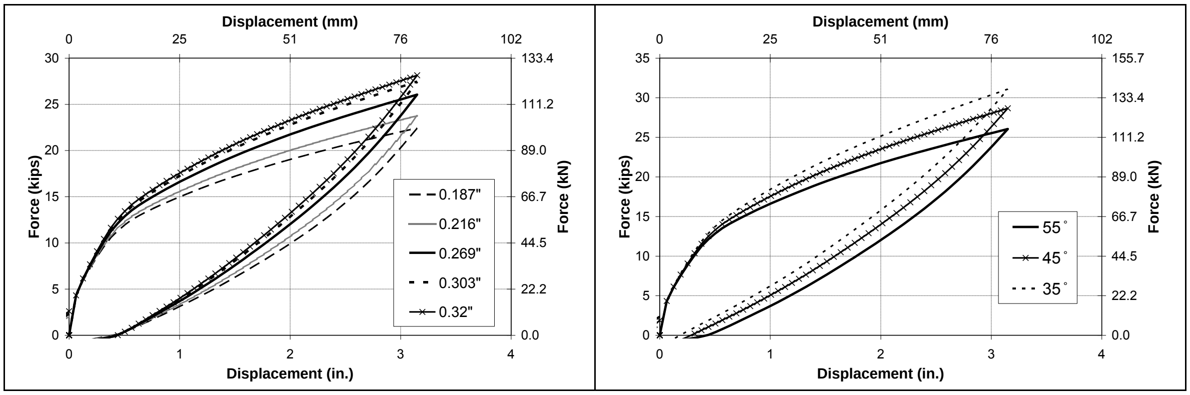

Fig. 18- Force-Displacement Cyclic Curve for FRP Column with Different a) Tube Thickness, b) Fiber Orientations

6. Design Method

Seismic design methods for segmental columns and precast bent were developed based on the test observations, measured data, and parametric studies.
Design methods for end segment height, post-tensioning force, and elastomeric bearing pad are discussed for segmental columns. Recommendations for embedded length and flexural design of precast FRP column were also developed, but are presented in the main body of the report.

6.1. Selection of End Segment Height

The "end segment" refers the base segment in cantilever columns or the top and bottom segments in columns with fixed top and bottom connections. To eliminate joint opening at segment interfaces, the end segment height should be at least as tall as the distance between the point of ultimate moment and cracking moment (M_{crack}). When small amount of longitudinal steel ratio is placed in the end segment, the difference between the cracking and the moment capacity of the section is relatively small; therefore, a short end segment is required to develop the full moment capacity of the section without opening between the end segment and adjacent segment. In columns with relatively high longitudinal steel reinforcement in the end segment, the ultimate moment is relatively large and the difference between the ultimate and cracking moment is large. Therefore, a taller end segment is required if opening between segments is to be avoided. The expected increase in the PT force under lateral displacement should be included in analysis of the moment capacity and the cracking moment. It is recommended to increase the initial PT force by 30% when calculating the ultimate moment capacity of the column section. The following modified equation of f_r is recommended to calculate M_{crack} in segmental columns.

$$f_r = 17.5\sqrt{f'_c} \ (psi) \qquad \text{Eq. 1}$$

$$f_r = 1.45\sqrt{f'_c} \ (MPa) \qquad \text{Eq. 2}$$

The coefficient in these equations was based on the measured test data in this study. The larger f_r compared to those recommended by ACI and AASHTO is attributed to the application of epoxy between the segments to keep the segments aligned during assembly. The end segment height is calculated based on similar triangle relationships (Fig. 19).

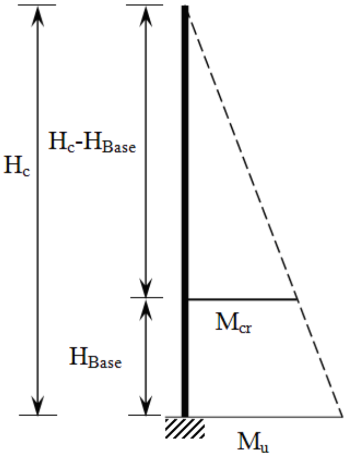

Fig. 19- The Ultimate and Cracking Moments along the Column Height

6.2. Post-Tensioning Design

To minimize residual displacement, the tendons should be designed to remain elastic at ultimate lateral loads, thus retaining their recentering ability (Eq. 3).

$$F_{i(PT)} + \Delta P < F_{y(PT)} \qquad \text{Eq. 3}$$

Where $F_{i(PT)}$ is the initial PT force and ΔP is the increase in PT force at ultimate displacement. $F_{y(PT)}$ is the yield force of PT tendon(s). The studies on the unbonded post-tensioned segmental columns including the current study showed that the PT force increases by 100% to 150% under large lateral displacements.

$$\Delta P \approx [1 \;\; to \;\; 1.5] \times F_{i(PT)}$$

$$F_{i(PT)} \approx [0.4 \;\; to \;\; 0.5] \times F_{y(PT)} \qquad \text{Eq. 4}$$

It is recommended by Hews and Priestley, (2002) that the maximum axial load ratio during seismic event should be less than or equal to 0.3.

$$\frac{F_{pt} + F_{gravity}}{f_c' A_g} < 0.3$$ Eq. 5

Where:

F_{pt} =Post-tensioning force

$F_{gravity}$ =Gravity load

f_c' =Concrete strength

A_g =Area of column section

Therefore, based on Eq. 4 the initial PT force ($F_{i(PT)}$) may be $0.4 \times F_{y(PT)}$. Combining Eqs. 4 and 5 gives Eq. 6 for the PT rod or tendon area.

$$A_{pt} = \frac{0.3 \times f_c' A_g - F_{gravity}}{0.4 \times f_{y(pt)}}$$ Eq. 6

The increase of PT force under design level drift (ΔU) may be estimated more accurately based on Eqs. 7 and 8 for two modes of segment interface behavior: (1) with opening and (2) without opening, respectively.

If

$$H_{base} < \frac{H_c \times (M_u - M_{crack})}{M_u} \qquad \Delta P = \frac{D \times A_{pt} \times E_{pt} \times \Delta U}{4 \times L_t \times (H_c - H_{base})}$$ Eq. 7

$$H_{base} \geq \frac{H_c \times (M_u - M_{crack})}{M_u} \qquad \Delta P = \frac{A_{pt} \times E_{pt} \times \Delta U^2}{L_t \times \sqrt{H^2 + \Delta U^2}}$$ Eq. 8

Where H_{base} and H_c are the end segment height and column height to the inflection point, respectively. M_u and M_{crack} are ultimate moment and cracking moment described in section 6.1, respectively. Also, L_t is the length of unbonded PT rod, A_{pt} is the PT rod area, and E_{pt} is the modulus of elasticity of PT rod. D is column diameter and H in Eq. 8 can be calculated from Eq. 9.

$$H = H_c - \frac{L_p}{2}$$ Eq. 9

Where:

L_p= Plastic hinge length, calculated from Eqs. 10(a) and 10(b) [Paulay and Priestley, 1992]

$L_p = 0.08 \times H_c + 0.15 \times d_b \times f_y \ (ksi)$ Eq. 10a

$L_p = 0.08 \times H_c + 0.022 \times d_b \times f_y \,(MPa)$ Eq. 10b

Finally it is necessary to check

If $F_{i(PT)} + \Delta P < F_{y(PT)}$ OK Eq. 11a

If $F_{i(PT)} + \Delta P > F_{y(PT)}$ NG Eq. 11b

If Eq. 11 (a) is satisfied, the designer might consider reducing the PT area. Otherwise, the PT area will need to be increased.

6.3. Elastomeric Bearing Pad Design

The elastomeric bearing pad was designed by controlling the failure of the rubber when it was subjected to axial compression and bending moment. The bearing diameter is selected as the column diameter, D. The initial bearing thickness is assumed to be $D/2$, but it needs to be checked if the selected height is sufficient to provide a larger rotational capacity than the demand.

$\theta_c \geq \theta_d$ Eq. 12

θ_c and θ_d are rotational capacity and rotational demand, respectively.

The required rotational stiffness of the section is determined by Eq. 8-34.

$$K_\theta = \frac{M_u}{\theta_u} \qquad \text{Eq. 13}$$

M_u and θ_u are the ultimate moment and rotation of the bearing, respectively. A moment-curvature analysis of the rubber pad section including the steel bars and excluding the shear key area can be used to determine the ultimate moment and rotation. The total axial load including the gravity load and the expected PT force should be included in the analysis. In the moment-curvature analysis, the bearing is modeled using an elastic material with modulus of elasticity of E_c. Derham and Kelley (1982) suggested for S>3

$E_c = 5.6 G S^2$ Eq. 14

Where S is the shape factor and G is the shear modulus of rubber. The parametric study showed that choosing low shape factor results in low initial stiffness of the column. Thus, it is recommended to choose a shape factor larger than 15.

Equation 15 provides the required bearing thickness to satisfy the rotational demand.

$$T_r = \frac{E_b I}{K_\theta} \qquad \text{Eq. 15}$$

Where E_b, I, and T_r are the bending stiffness, moment of inertia, and total thickness of bearing, respectively. E_b is calculated using Eq. 16.

$$E_b = E(1 + \frac{2}{3} S^2) \qquad \text{Eq. 16}$$

The selected thickness should be checked against T_r.

If $H_{bearing} > T_r$ OK Eq. 17a

If $H_{bearing} < T_r$ NG Eq. 17b

The bearing thickness should be increased.

7. Summary Observations and Conclusions

7.1. Observations

7.1.1. Segmental Columns

1. The performance of all segmental columns incorporating advanced materials (rubber pad, FRP jacket, and ECC) was better than the performance of SC-2 (reference column) in terms of lateral load capacity and damage.

2. The primary failure mode in segmental columns was concrete spalling at the interface between the base and second segments due to the large cyclic compressive strains from opening and closing action at the interface and the fact that concrete at the interface is not confined. The most extensive spalling was seen in SC-2 and SBR-1, in which conventional concrete was used in the base segments. The least amount of concrete spalling was seen in SF-2 and SC-2R. Spalling of the ECC was minimal in SE-2 due to the ductile behavior of ECC.

3. The largest lateral load capacity in segmental column was observed in SC-2R followed by SF-2 where the two lower segments were wrapped with FRP jacket.

4. Ductile behavior of ECC resulted in minimal spalling and minor section loss at the interface of two lower segments of SE-2. Therefore, no degradation in the capacity of SE-2 was observed.

5. SC-2R, SBR-1 and SF-2 dissipated higher energy than other columns. Using FRP jacket in SF-2 and SC-2R delayed concrete failure and increased the

energy dissipation due to more extensive yielding of the bars. Flexural deformation of elastomeric pad in the plastic hinge of SBR-1 increased dissipated energy and eliminated damage in that area.

6. The residual drift ratios were minimal and lower than 1% in all columns prior to failure.
7. The comparison between the test results and analytical results of a standard segmental column (a column in which the base segment is not fixed to the footing) showed that the dissipated energy in fixed segmental columns was 2 to 4 times larger than that of a standard segmental column.
8. Reasonable agreement was seen between the measured data and calculated results using OpenSees for all segmental columns.
9. The parametric study on SC-2 with different base segment heights and steel ratios indicated that increasing the base segment height or decreasing the base segment steel ratio are effective in developing the full moment capacity of the column and eliminating the opening at the interface between the base and second segments.

7.1.2. Precast Bent

1. Minimal ECC spalling was observed after even after 10% drift ratio in the precast column incorporating ECC in the plastic hinge. Due to ductile behavior of ECC, spalling was minor.
2. No apparent damage was detected in the plastic hinge zone of FRP column before tensile rupture of the FRP tube. Two buckled bars were observed in the FRP column after removing the FRP tube and loose concrete.
3. The post-yielding hardening was substantially more significant in the concrete-filled FRP column compared to RC-ECC column because the FRP tube remained elastic while the steel reinforcing bars in RC-ECC column yielded.
4. The drift capacities of the RC-ECC and FRP column were the same. However, the displacement ductility capacity of the RC-ECC column was larger than that of the FRP column by 35% because of a higher effective yield displacement of the FRP columns.
5. The energy dissipation was larger in the RC-ECC column compared to that of the FRP column.
6. The embedment length of 1.5 times the column diameter in the footing was sufficient to provide full fixity at the base in both the RC-ECC and FRP columns.
7. The post-test analytical results for PEFB reasonably matched the experimental results.

7.2. Conclusions

1. Monolithic connection between the column base segment and the footing provides energy dissipation capacity under seismic loading through yielding of the bars. Energy dissipation in this type of segmental column is 2 to 4 times larger than that of a column with no monolithic connection between the base segment and the footing.

2. Incorporating a rubber pad in the plastic hinge area is effective in improving energy dissipation while substantially reducing damage.

3. Application of ECC in the plastic hinge area improves ductility capacity and significantly reduces damage.

4. FRP jacketing around column segments is effective in reducing damage at junctions of column segments and improving the strength and ductility capacity of the column.

5. Using an unbonded post-tensioning is an effective approach to provide continuity among the column segments and to reduce residual lateral displacements under earthquake loading.

6. Using the proposed method to calculate the end segment height can eliminate the joint opening and allows for development of full moment capacity of the column section.

7. The satisfactory agreement between the measured and calculated data using OpenSees suggest that existing analytical tools may be used to model the seismic performance of bridges with advanced details of the type used in this study.

8. Pier systems with precast monolithic columns, footings, and cap beams with connections of the type included in this study may be used in accelerated bridge construction in areas of moderate and high seismicity.

9. Concrete-filled FRP tube columns incorporating a minimum amount of longitudinal steel are ductile and appropriate for use in earthquake-resistant bridges.

10. Pipe-pin hinges can be effectively used in accelerated bridge construction because of their ease of construction.

Acknowledgments

The research presented in this report was funded by the California Department of Transportation (Caltrans) Agreement No. 59A0591. However, conclusions and recommendations are made by the authors and do not necessarily present the views of the sponsor. Special thanks are due Dr. Li-Hong Sheng, the Caltrans Research Program Manager, for his support and advice. The authors would like to express their appreciation to Dr. Sarah Billington and Dr. Amir Mirmiran for their helpful comments.

The dedicated support of Dr. Patrick Laplace, Paul Lucas, Chad Lyttle, Todd Lyttle, and Robby Nelson of the Large Scale Structure Laboratory, is highly appreciated. UNR students Arash Zaghi, Amir Reza Shoja-Taheri, Ashkan Vosooghi, Christin Linke, Austin Brown, Carlos Cruz, Fatemeh Kavianipour, Jordan Cushman, and Danielle Smith are thanked for their assistance.

Thanks are also due David Buthod of Fiber Glass Systems for generously donating the FRP tube used in the two-column bent, Mr. Edward R. Little of Surface Systems Incorporation for his assistance regarding the ECC mix design, AVAR-SAS Company for donating the unbonded threaded rods and post-tensioning equipment, ERICO Company for donation of Lenton Terminator, Sika Corporation for providing epoxy, FYFE Company for providing FRP fabrics, and Don Newman for construction of the test models.

This report is based on a PhD dissertation by the first author supervised by the other authors.

TABLE OF CONTENT

LIST OF TABLES

LIST OF FIGURES

1. INTRODUCTION

1.1. Introduction

Conventional bridge construction involves a time consuming process associated with possible traffic delays and risk to public safety. In contrast, prefabricated bridge systems allow for accelerated bridge construction (ABC) with a relatively short construction period thus minimizing interruption to the highway network and construction site safety risk. While precast superstructure components have been extensively used, precast columns are relatively rare. Ease of construction and transportation to the site makes segmental columns a particularly attractive type. In standard segmental column construction the end segments are not fixed to the footing or the cap beam. Studies have shown that, under seismic loading, standard segmental columns offers minimal energy dissipation, which results in considerable damage as a result of the discontinuity of longitudinal reinforcement and rocking of the column [Hews and Priestley, 2002].

Connecting the end segment to the footing or the cap beam via the reinforcing bars (monolithic connection) provides energy dissipation capability under seismic loading through yielding of the bars. The segments are connected by a post-tensioning system to provide continuity and to minimize residual displacements. The end segments may be made of reinforced concrete that are similar to the other segments. However, ABC provides an opportunity to further improve the seismic performance of bridge columns by utilizing materials such as elastomeric bearing pad, FRP (fiber reinforced polymer), and ECC (engineered cementitious composite) in plastic hinge zones (end segments) and increase energy dissipation while minimizing damage.

An alternative to segmental columns for ABC is building precast columns and then assembling them with the footing and cap beam at the construction site. As an alternative to precast RC (reinforced concrete) columns, FRP tubes filled with concrete could be considered. An opening with sufficient depth in the footing allows for embedment of columns and development of the plastic moment of the column. In some concrete bridges columns, one end may be detailed to act as a pin to eliminate moments while transferring shear and axial loads to the connecting element. Pipe-pin hinges could be effectively used in precast bridge construction because of their ease of construction. Pipe-pin hinges provide a moment free connection between the columns and the cap beams.

1.2. Past Relevant Research

1.2.1. Seismic Design of Precast Segmental Columns

Hewes and Priestley, (2002) studied the performance of unbonded post-tensioned precast concrete segmental bridge columns under lateral earthquake loading. Columns with high aspect ratio and low aspect ratio incorporating steel jackets with variable thickness in the plastic hinge region were tested under simulated lateral seismic loading (Fig. 1-1). The specimens with thicker steel jackets performed better than those with thinner jackets in terms of larger drift ratio capacity and minimal capacity degradation. The unbonded post-tensioning (PT) system with different initial PT force was used in the columns. The residual displacement was minimal and observed column damage was relatively small in general consisting primarily of minor spalling at the column base.

A study on monotonic and cyclic load analyses of unbonded precast segmental substructure systems was carried out by Kwan and Billington, (2003 a, b) (Fig. 1-2). The monotonic analyses showed that columns with a high post-tensioning force have lower ultimate displacement capacities due to high compressive stresses that lead to failure of concrete under lower displacements. The cyclic analyses revealed that designs with a high proportion of unbonded post-tensioning have lower energy dissipation and lower residual displacement. Kwan and Billington, (2003 a, b) also evaluated the seismic response characteristics of pier systems by response-history analyses. An equivalent single-degree-of freedom (SDOF) system incorporating the hysteretic behavior derived from the cyclic analyses was developed. From the monotonic and cyclic analyses, the bridge piers were evaluated for functional-level and survival-level seismic performance. A set of criteria for the definition of functional-and survival-level displacement capacities were developed based on residual displacements. The functional-level displacement capacity of the unbonded post-tensioned bridge pier systems was defined as the minimum of 1) Displacement at yielding of unbonded post-tensioning; 2) Displacement leading to 1% residual drift; and 3) 0.7 times survival-level displacement. The criterion proposed for the survival-level displacement was the displacement at which the capacity drops to 90% of the peak load, F_u.

Yamashita and Sanders, (2006) performed shake table tests and analytical studies to investigate the seismic performance of an unbonded prestressed hollow concrete column constructed with precast segments (Fig. 1-3). It was found that using an unbonded prestress system provides excellent drift ratio capacity with limited permanent displacements. The specimen performed very well with essentially no residual displacement and only limited spalling at the base.

Chou and Chen, (2005) tested two unbonded post-tensioned precast concrete-filled steel tube (CFT) segmental bridge columns under lateral cyclic loading. One specimen contained energy-dissipating devices at the base to increase the hysteretic energy (Fig. 1-4). The energy dissipating device consisted of a RSP (reduced steel plate) and stiffeners at both ends. Stiffeners were provided at both ends of the RSP to decrease the un-braced length and prevent the buckling. The test results showed that (1) both specimens could develop the maximum flexural strength at the design drift ratio and achieve 6% drift ratio with small strength degradation and residual displacement, (2) the proposed energy-dissipating device could increase energy dissipation, and (3) the CFT segmental columns rotated not only about the base but also about the segment joints above the bottom segment. All the precast concrete segments were encased in steel tube, minimizing concrete spalling above the bottom segment and spalling at the base at the design drift ratio of 3.5%.

The seismic performance of segmental precast unbonded post-tensioned bridge columns with hollow cross sections was investigated by Ou, et al., (2007). Bonded longitudinal mild steel reinforcement (energy dissipating (ED) bars) crossing the column segment joints was provided to enhance the hysteretic energy dissipation of the columns (Fig. 1-5). It was found that lowering the initial prestressing stress and the use of tendons with longer unbonded length delay tendon yielding. Higher axial force helps prevent the opening of the column segment joints under service loading but tends to decrease the ductility of the columns.

Precast monolithic columns meeting seismic requirements were used in Washington State Department of Transportation bridges for accelerated construction [Khaleghi, 2005]. Reinforcing bars from the top and bottom of the column were extended into the cast-in-place concrete of the cap beam and footing (Fig. 1-6). The precast columns were built off site and were kept in place on a temporary support for casting of foundation. The monolithic connection between precast column and precast girder was designed and detailed to meet the top of the column plastic moment.

A cast-in-place (CIP) emulation pier system and a hybrid pier system incorporating precast concrete columns, precast beam, and cast in place foundation were studied at University of Washington [Hieber, et al., 2005]. Both piers incorporated mild steel reinforcement but vertical unbonded post-tensioning reinforcement was only used in the hybrid system to provide a restoring force that recenters the pier after an earthquake (Fig. 1-7). These piers behave like conventional cast-in-place piers. Both precast piers provided sufficient lateral force resistance for the design earthquake.

1.2.2. Elastomeric Pads

Rubber material is stable under repeated seismic loading with large strains and is known to be durable [Kawashima and Nagai, 2002]. They also have a relatively high damping characteristic [Lindley, 1974]. Because of their relatively low stiffness, elastomeric pads have been used in civil engineering structures as seismic isolators to lengthen structural vibration period and take advantage of reduced seismic forces and higher damping. In 2002 a different application of elastomeric pads was explored by incorporating them in the plastic hinge region of concrete bridge columns [Kawashima and Nagai, 2002]. The concrete in the plastic hinge was replaced by high damping rubber to increase deformation capacity and energy dissipation [Kawashima, et. al, 2006] while reducing concrete damage under an extreme earthquake excitation.

One standard concrete column and one incorporating rubber units ("built-in isolator column") in the plastic hinge area were tested and the results were compared [Kawashima, et. al, 2006]. The longitudinal bars were continuous through the rubber unit. Prestressed tendons were used to provide restoring force and decrease residual displacement (Fig. 1-8). A shear-key was provided at the center of rubber unit to prevent excessive lateral displacement of the column relative to the footing. The longitudinal bars in the rubber unit were subjected to repeated tension and compression with larger strain amplitude under seismic loading. Under a drift ratio exceeding 3% the bars buckled and ruptured (Fig. 1-9). However, concrete damage was limited. It was noted that the rubber provided significant strain hardening compared to conventional reinforced concrete columns. Kawashima and Nagai, (2002) stated that using steel plates in the laminated rubber unit may prevent the local buckling of the longitudinal bars when they are subjected to alternative tension and compression.

1.2.3. A Response of Bridge Columns with ECC

ECC is a fiber-reinforced cement-based composite engineered for high tensile ductility and compressive and tensile strength. ECC contains water, cement, fine sand, fibers, and some common chemical additives. Coarse aggregates are not used in the mix because they adversely affect the unique ductile behavior of the composite. The fibers are typically reinforced with polyvinyl alcohol fibers (PVA) or high modulus polyethylene fibers (PE) (Fig. 1-10). ECC has the ability to reach ultimate tensile strain of approximately 3% to 5% [Li, 1998]. This high strain capacity is nearly 500 times larger than that of conventional concrete and can be attributed to the strain-hardening behavior and unique cracking mechanism of ECC. The stress-strain behavior of ECC in tension and compression is shown in Fig. 1-11. ECC exhibits multiple, fine cracks upon loading in tension as a result of steady-state cracking. ECC displays higher tensile ductility, tensile (strain) hardening behavior and energy dissipation than normal concrete and many fiber-reinforced concrete materials [Li, 1998, Billington and Yoon, 2002, O'Brien, et al., 2009].

Durability of ECC has was found to be excellent in a study by Lepech and Li (2005) who investigated the behavior of ECC under various environmental loads and long term performance. It was determined that the ability of ECC to self-control crack widths under load, resist freeze thaw and hot-cold exposures, withstand fatigue loading, maintain mechanical performance over the long term, and protect steel reinforcement from corrosion can be an effective solution to the problems of poor concrete durability.

Rouse and Billington, (2007) studied shrinkage and creep of ECC. It was found that ECC exhibits higher drying shrinkage and creep strains than an identical cementitious mixture (paste or mortar) without fibers by approximately 30%. Due to the fine cracks on the surface of ECC, permeability is higher and water evaporation is faster. Using extra fine aggregate, high volume of fly ash, and pre-wetted light aggregate can reduce the creep in ECC, significantly.

Billington and Yoon, (2002) applied ECC to precast segmental unbonded post-tensioned bridge columns. ECC was used in the plastic hinge region to increase hysteretic energy dissipation. It was found that all of the specimens with ECC in the plastic hinge region dissipated relatively high energy.

The applicability of PVA-ECC as a repair material was investigated by Wang and Saiidi, (2005). The performance of ECC was found to be satisfactory because it exhibited only limited damage even under large-amplitude motions. Higher force-displacement capacity and ductility were found in the repaired column. ECC was used in combination with SMA (shape memory alloy) longitudinal reinforcement in plastic hinge of a column to minimize the spalling and residual displacements [O'Brien, et al., 2009]. This column experienced lower damage and a higher drift ratio capacity compared to that of a similar conventional concrete column.

1.2.4. Fiber-Reinforced Polymer Composite Jackets

Fiber reinforced polymer (FRP) jackets offer many advantages including: light weight, high strength and stiffness-to-weight ratios, corrosion resistance, and, in particular, ease of installation [Yu, et al., 2006]. These advantages make these materials more suitable for retrofitting bridge columns. Moreover, contrary to other retrofit techniques, FRP jackets do not affect the lateral stiffness of the columns significantly and hence do not alter the bridge dynamic characteristics [Teng, et al., 2002]. Apart from their applications in the retrofit of structures, efforts have been made to explore the use of FRP composites in new construction. One important application of FRP composites is jacket to provide confinement in concrete columns for enhanced strength and ductility. In FRP-confined concrete, the FRP is principally loaded in hoop tension while the concrete is loaded in triaxial compression, so that the strength properties of both materials are used effectively [Teng and Lam, 2004].

Yu, et al., (2006) used FRP in combination of concrete and steel tube. This new type of hybrid member was in the form of a double-skin tube, composed of a steel inner tube and an FRP outer tube with a concrete infill between the two tubes. This hybrid element had a very ductile response because the compressive concrete was confined by the FRP tube and the steel tube provided ductile longitudinal reinforcement.

Within the field of highway structures, several new FRP structural systems have been proposed, designed, and experimentally implemented. These include bridge decks for rehabilitation and new construction, concrete filled FRP shells for drivable piles [Mirmiran, et al., 2000 and Karbhari, et al., 2000]. Johnson, et al., (2005) developed a retrofit method for octagonal single column bents with a pedestal. A glass fiber-reinforced polymer (GFRP) jacket was chosen for strengthening of the column. It was determined that the pedestal retrofit was successful to strengthen the pedestal sufficiently to shift the plastic hinging into the column and keep the pedestal nearly elastic.

1.2.5. Reducing Residual Displacements with Post-Tensioning

An effective approach to reduce residual displacements in columns subjected to earthquake loading is post-tensioning. Tests by Priestley and MacRae (1996), Mander and Chen (1997), Billington and Yoon, 2004, Chou and Chen, (2005), Hewes and Priestley, (2002), Sakai and Mahin, (2004), Yamashita and Sanders, (2006), and Hieber, et al., (2005), revealed that precast concrete elements with unbonded tendons can undergo relatively large lateral drift ratios while exhibiting less residual displacement than conventional cast-in-place (CIP) reinforced concrete (RC) columns. The fact that the post-tensioned tendons were unbonded rather than bonded means that strains in the PT rods were not localized and smaller tendons could be used. Sakai and Mahin, (2004) reported a significant increase in the PT force under large drift ratios. As the column is displaced laterally an axial post-tensioned force tends to return the column to its original position, thus reducing residual displacements. The tests by Sakai and

Mahin, (2004) showed that the columns with unbonded prestressing strands perform very well under strong ground shaking. In another study, Billington and Yoon, (2004) used unbonded post-tensioning to join precast column segments to reduce residual displacements under cyclic loading.

1.2.6. Seismic Design of Pipe-pin Connections in Bridge Columns

Telescopic pipe-pin two-way hinges are used in concrete bridges to eliminate moments while transferring shear and axial loads from bent caps to reinforced concrete columns [Zaghi and Saiidi, (2010)]. The hinges consist of a steel pipe that is anchored in column with a protruded segment that extends into the bent cap. In the study by Zaghi and Saiidi, (2010) it was found that because of their ease of construction pipe-pin hinges could be effectively used in precast bridge construction as well.

1.2.7. Concrete-Filled FRP Tubes

As an alternative to RC columns and concrete filled steel tubes, fiber reinforced polymer (FRP) tubes may be considered. FRP tube can act as a light-weight permanent formwork in new construction of concrete columns in buildings or as piles and pier columns in bridge applications. The tube eliminates the time and cost for traditional formwork and its removal. The tube also acts as a life-long protective jacket for concrete core in hostile environments. Extensive studies in the past decade have shown good performance of CFFT under axial compression, as high tensile strength of FRP is combined with the high compressive strength of confined concrete core [Zhu, 2004].

Zhu and Mirmiran, (2004) studied the feasibility of CFFT columns as either cast-in-place or precast members in conjunction with the reinforced concrete (RC) footing, with emphasis on the system performance of the connection under earthquake loading. Three different types of CFFT to RC footing connections were studied including cast-in-place, grouted precast , and post-tensioned precast. They showed that various CFFT-RC joints performed quite similarly, as long as the FRP tube was properly embedded into the footing.

Shao and Mirmiran, (2003) performed extensive experimental studies consisting of cyclic loading of FRP coupons and lateral cyclic loading of CFFT beam-columns under constant axial load. A cyclic model for FRP-confined concrete in compression and cyclic models for linear and non-linear FRP materials in tension and compression were developed. The study demonstrated the feasibility of using ductile CFFT members for seismic applications. Moderate amount of internal steel reinforcement in the range of 1%-2% was found to improve the cyclic response of CFFT members. The improvement is more significant for under-reinforced FRP tubes. Large amount of longitudinal steel in members with thick FRP tubes was found to be ineffective and lead to premature failure.

1.2.8. Embedded Length for Precast Columns

Precast columns need to be sufficiently anchored into the footing and/or the cap beam to develop their full moment capacity. Pertold, et al (2002) proposed a design model for embedded steel columns based on developing the moment, shear, and axial capacity in the connection using plastic stress distribution analysis (Fig. 1-12). To transfer bending moment, shear and vertical forces, they recommended and embedment length of twice the effective column width.

Zhu et al. (2004) tested three, one-sixth scale CFFT to RC footing connections. The test matrix included a cast-in-place CFFT system with steel starter bars, a precast CFFT system with steel starter bars and grouted joint, and a precast CFFT system with post-tensioned connection. The study showed that the embedment of the CFFT into the footing provides additional benefit for the connection. Zhu et al. (2006) extended this work by testing CFFT column-footing assemblies to investigate construction feasibility and seismic performance of the joints, for both precast and cast-in-place CFFTs, in comparison to conventional RC columns. The FRP tube, when secured properly in the footing, provided both longitudinal reinforcement and hoop confinement to the concrete.

Sadeghian and Fam, (2010) developed an analytical method for a moment connection between circular concrete-filled FRP tubular (CFFT) members and RC footings. The CFFT member was subjected to lateral or lateral and axial loads at its free end. An embedment length equal to 70% of the CFFT column diameter was recommended. This embedment length was the minimum length required to achieve simultaneous material failure of the CFFT outside the footing and bond failure inside the footing. The model was verified using experimental results, and the calculated and measured results agreed well.

1.3. Objectives

This research involved analytical and experimental investigation of the performance of precast bridge columns under lateral seismic loading. The main goal of the study was to investigate different details of precast columns and identify their seismic performance characteristics and their relative merit with respect to ductility, energy dissipation, and damage. Two types of precast bridge columns were studied: segmental columns and precast columns. The segmental columns were cantilever members in which the base segment details were the primary variable. The base segment height, base segment longitudinal steel reinforcement, post-tensioning force, application of advanced materials such as elastomeric bearing pad, FRP jacket, and ECC were of prime interest in segmental column studies. Five large-scale column models were constructed and tested in the experimental study of segmental columns. Design of embedment length, application of pipe-pin hinges in precast construction, use of advanced materials such as FRP tube and ECC in the precast columns were studied in shake table testing of a large-scale two-column bent model. To help understand the behavior of different models and evaluate the adequacy of analytical techniques, computer program OpenSees was used in the study of the test models and the subsequent parametric studies.

1.4. Scope of Study

1.4.1. Experimental Studies

To study and develop new systems for precast columns that are able to dissipate energy under seismic loads while reducing damage, a series of experiments was designed and performed at the Large Scale Structure Laboratory at the University of Nevada, Reno. The specimens were tested on the UNR shake table system and were subjected to the Sylmar hospital ground motion (Northridge earthquake 1994) with increasing amplitudes until failure. The specimens included five segmental concrete columns with different low-damage plastic hinges and a precast two-column pier.

Segmental specimens were one-third scaled cantilever column models with base segments that were connected to the footing via reinforcing bars to increase energy dissipation under seismic loading. An unbonded post tensioning (PT) rod was used to connect the segments and to minimize residual displacements. In the benchmark column, SC-2 (segmental with concrete), a conventional reinforced concrete detail was used. The performance of other specimens consisting of advanced materials in the plastic hinge region was compared with that of SC-2. The second specimen, referred to as SBR-1 (segmental with built-in rubber pad), was a segmental concrete column incorporating an elastomeric bearing pad in the plastic hinge. The third and forth columns were designated SE-2 (segmental with ECC) and SF-2 (segmental with FRP). SE-2 utilized ECC in the lower two segments. FRP wrap was used in the lower two segments of SF-2 to confined the concrete and minimize damage at interface between the base and second segments. The study included a limited investigation of the effect of repair on segmental columns by repairing SC-2 with FRP fabrics and retesting the column.

A precast two-column pier was tested to investigate an alternative for accelerated bridge construction, which is using precast columns that are assembled with the footing and cap beam at construction site. Two innovative details were used in the columns of the pier: one column was a conventional concrete column incorporating ECC material in the plastic hinge area, and the other was a FRP tube filled with concrete. Pipe-pin hinges were used at column-cap beam connections.

In the course of the analytical studies of the specimens it was found necessary to develop a model for confined properties of ECC based on the unconfined ECC strength and transverse reinforcement. Therefore, an experimental study consisting of four groups of cylindrical specimens each with different confinement levels were designed and tested.

1.4.2. Analytical Studies

An extensive analytical study of the test models was performed in this study. OpenSees [Mazzoni, et. al, 2007] software was utilized to model the specimens for the design phase in the pre-test analysis, to develop macro models for precast elements, and to develop a reliable analytical model that used in parametric studies. The parametric studies were conducted only for SC-2, SBR-1, and concrete-filled FRP tube. It was assumed that the columns are cantilever. The effect of parameters such as base segment height, longitudinal steel reinforcement ratio, concrete strength, and initial post-tensioning force was studied in SC-2. In SBR-1, the rubber pad height and shape factor were selected as the parameters. The effects of FRP tube thickness, FRP tube fiber orientation, and longitudinal steel reinforcement ratio were studied in the concrete-filled FRP column. The results of experimental and analytical studies in addition to trends identified in parametric studies were used to develop design methods for various details.

1.5. Document Layout

The first chapter is followed by Chapter 2 explaining the details of the experimental studies, design considerations, specimen drawings, test set up details, material properties, instrumentation, and loading protocols. In Chapter 3, observations and the collected data from the experiments are presented. This chapter includes general observations, force-displacement hysteresis curves, envelopes of the hysteresis curves, measured strains, strain rates, moment-curvatures graphs, PT (post-tensioning) force in segmental columns, residual displacements, energy dissipation, and other measured data.

Chapter 4 is focused on the evaluation of the performance of the test models. Apparent damage, the maximum lateral load capacity, displacement ductility, dissipated energy, and recentering capability were studied and compared for different specimens.

In Chapter 5, a stress-strain model for confined ECC was developed. The test details including sample geometry, material characteristics, confinement reinforcement, instrumentations, test setup, and development of equations for confined ECC are explained in this chapter.

Chapter 6 explains the details of the analytical studies of the test models. The objective was to establish the validity of the modeling assumptions based on the correlation between the analytical and experimental results.

In Chapter 7, the results of the parametric studies on the segmental columns and two-column bent are presented and explained in detail. The parametric study was conducted for different variations of SC-2, SBR-1, and FRP column.

Chapter 8 explains the design method for the different segmental column details. The theoretical concepts that support the design method are presented along with the design procedure.

The content of the document is summarized in Chapter 9. This chapter also presents a list of observations and important conclusions.

Three appendices, A, B, and C are included in the document to present the strain gauge data for all specimen, an example of calculating stress-strain relationship for confined ECC, and OpenSees codes for analytical models of all specimens.

2. TEST MODELS AND EXPERIMENTAL SET-UP

2.1. Introduction

Details of the experimental studies are explained in this chapter. This study included five precast segmental columns with different energy dissipating joints and one precast two-column bent.

For each model the concept and purpose, details of the specimens, design considerations, material characteristics, instrumentation, test setup, and loading protocol are described.

2.2. Selection of Test Specimens

New details for the precast segmental columns were recommended that are suitable for seismic zones. The base segment is connected to the footing via reinforcing bars to provide energy dissipation capacity under seismic loading. To enhance and evaluate the performance of this detail, four precast segmental columns incorporating conventional concrete and advanced materials such as elastomeric bearing pads, ECC (engineered cementitious composite), and FRP (fiber reinforced composite) wrap were built and tested on the UNR shake table system and were subjected to the Sylmar hospital ground motion (Northridge earthquake 1994) with increasing amplitudes until failure. The specimens incorporating conventional concrete was repaired and retested to study the feasibility and the effectiveness of the repair.

An alternative to segmental columns is monolithic precast columns. A two-column pier with precast columns, precast footing and precast cap beam was built. Two innovative details were used in the columns: one column was a conventional concrete column incorporating ECC material in the plastic hinge area, and the other was a FRP tube filled with concrete.

2.3. Precast Segmental Columns

2.3.1. Introduction

Precast segmental specimens were one-third scaled cantilever column models with base segments that were connected to the footing via reinforcing bars to provide energy dissipation capacity under seismic loading. An unbonded post tensioning (PT) rod was used to connect the segments and to minimize residual displacements. No other reinforcement except the post-tensioning connected the segments. It was expected that most of the energy would be dissipated through yielding of the longitudinal bars in the base segments.

In the benchmark column, SC-2 (segmental with concrete), a conventional reinforced concrete detail was used. The performance of other specimens consisting of innovative materials in the plastic hinge region was compared with SC-2. The second specimen, referred to as SBR-1 (segmental with built- in rubber pad), was a segmental concrete column incorporating an elastomeric bearing pad in the plastic hinge. The third and forth columns were designated SE-2 (segmental with ECC) and SF-2 (segmental with FRP). SE-2 utilized ECC in the lower two segments while FRP wrap was used in the lower two segments of SF-2. Column SC-2 was repaired after failure with FRP fabrics and was labeled SC-2R (SC-2 repaired) and tested under the Sylmar ground motion.

2.3.2. General Considerations in Design of Test Specimens

2.3.2.1. Flexural Design

The diameter of the columns was 16 in. (406 mm) and their height was 72 in. (1829 mm), leading to an aspect ratio of 4.5. The column height was taken as the distance from the top of the footing to the centerline of the column head where the inertial load was applied. The clear column height was 62 in. (1580 mm). The total axial load on the columns was comprised of 80 kips (355.8 kN) gravity load and 100 kips (444.8 kN) post-tensioning force. The total axial load corresponded to an axial load index (ALI) of 0.20. ALI is defined as the ratio of the axial load to the product of the gross section area and the concrete compressive strength. The general column properties are listed in Table 2-1.

Each model consisted of five segments. For each column, the lower two segments were unique. The column lateral load capacity was calculated based on the base segment details.

OpenSees software was utilized to study the flexural behavior of the columns and to design the steel ratio at the base segments. The flexural capacity of this detail depends on the dominating failure mode under load application. Two major failure modes were investigated that included yielding of the bars at the base segment and crushing of the material at the interface between the base and second segments due to the gap closing after segments separation. The height of the base segment and amount of steel ratio were two key parameters in determining the failure mode. The height of the base segment was selected to provide sufficient anchorage length for the longitudinal bars to allow for the plastic hinge formation. The total base segment depth in all columns was 20 in. (508 mm). The criteria to select this length were to ensure the development of longitudinal bars and to keep the number of segments at a reasonable level. The amount of steel reinforcement at the base segment was selected such that the longitudinal bars would yield before separation of the segments. The objective was to provide energy dissipation through yielding of the bars.

The OpenSees analysis showed that a steel ratio of less than 1% is necessary at the base segment to allow for yielding of the bars prior to the segments separation. Steel ratio of 1% was chosen for SC-2, SF-2, and SE-2, and steel ratio of 1.20% was selected for SBR-1. The base segment detail for each column is explained in subsequent sections.

The depth of the segment two, three and four was 14 in. (356 mm). Due to the discontinuity between segment 2 and higher, the longitudinal reinforcement was not expected to yield, and hence only a small amount of steel was provided. Therefore, the segments were minimally reinforced with 8-#4 in the longitudinal direction, corresponding to a steel ratio of 0.8%.

2.3.2.2. Shear Design

The shear design of precast segmental columns with unbonded prestressing steel is based on controlling the shear capacity at two locations, within the segment and at interface between the segments.

The shear strength within the segment is composed of contributions from concrete shear resisting mechanism, a truss mechanism, and an axial compression component (Eq. 2-1) [AASHTO, 1999].

$$V_d = V_c + V_s + V_p \qquad \text{Eq. 2-1}$$

Where the

V_d = Total shear capacity

V_c = Concrete shear strength

V_s = Contribution from spiral reinforcement

V_p = Shear strength due to the axial compression

$$V_c = 2K\sqrt{f_c'}b_w d \qquad \text{Eq. 2-2}$$

Where, K = 1.0 for cracked section

f_c' = Compressive strength of concrete, psi

b_w = Thickness of the webs, in.

d = Effective depth, in.

$$V_s = \frac{A_v f_{sy} d}{s} \qquad \text{Eq. 2-3}$$

Where,

A_v = Area of shear reinforcement

f_{sy} = Yield stress of shear reinforcement

d = Effective depth

s = Spacing of shear reinforcement

$$V_p = P_a \frac{(D-c)}{2L} \text{ for } P_a > 0 \qquad \text{Eq. 2-4}$$

$P_a =$ Total axial load

D = Column diameter

c = Compression depth

L = Length of the column between the point of maximum moment and the point of contra-flexure

$$V_p = 0 \text{ for } P_a \leq 0 \qquad \text{Eq. 2-5}$$

$$P_a = F_{si} + \Delta F_s + P \qquad \text{Eq. 2-6}$$

F_{si} = Initial post-tensioning force

ΔF_s = Incremental PT force

P = Applied vertical dead load

The shear capacity at the interface between the segments is mostly due to shear friction which depends on the clamping force provided by the post-tensioning rod and the dead load. The coefficient of friction, (μ) of 0.8 is recommended for two concrete surfaces in ACI 318R-08.

$$V = \mu \, P_a \qquad \text{Eq. 2-7}$$

Transverse reinforcement of # 3 spirals at 2 in. (51 mm) pitch were used in all segments to provide shear capacity along the column as well as confinement for the concrete. The spiral pitch in SF-2 for the segments incorporating FRP wrap was 4 in. (102 mm) due to the extra confinement provided by FRP fibers. Also due to application of high axial load in the column, shear capacity at the interface of the segments was much larger than the shear demand.

2.3.2.3. Design of Footings and Column Heads

In all specimens the footing plan view dimensions were 72 in. (1829 mm) by 72 in. (1829 mm), and were designed to be sufficiently stiff and strong to minimize footing deformation and damage. Details of footings are presented in Figs. 2-1 and 2-2. The footing dimensions and reinforcement were checked for flexure and shear. The height of the footings was 28 in. (711 mm). This thickness was selected so that column would connect properly to the inertial load system. The reinforcement consisted of two top and bottom mats of #6 bars with a clear cover of 1.5 in. (38 mm) at the top and the bottom, and 2.25 in. (57 mm) at the sides. Cross ties (#3) connected the top and bottom mats. Four #10 lift hooks for each specimen lifting were added. In addition, 16 PVC pipes were cast into each footing. These PVC pipes allowed the footing to be securely attached to the shake table. A 8 in. × 8 in. × 9.50 in. (203 × 203 × 241 mm) opening was placed under the footing to provide space for post-tensioning accessories.

One column head was built and reused for all specimens. Details of head block are shown in Fig. 2-3. Since the columns were designed to behave as cantilever members, minimal stresses were expected in the column head region. The column head was 30 in. (762 mm) in length and width. The height of the head was 26 in. (660 mm). Eight #4 bars and twelve #4 stirrups made up the head reinforcements. The clear cover was 1.5 in. (38 mm) on the sides and 0.75 in. (19 mm) on the top and bottom of the head. Four 2.0 in. (51 mm) diameter PVC pipes were cast in each column head. The PVC pipes allow for passage of bolts that connect the inertial mass system to the specimen. An opening with dimensions of 11 in × 11in. × 7.5 in. (280 × 280 × 190 mm) was placed on the top of the loading head for post-tensioning accessories. Figure 2-4 shows the head dimensions and reinforcement details.

2.3.2.4. Post-Tensioning Rod

A 1-5/8 in. (40 mm) diameter PT unbonded high strength bar was used in the column central core. A 2.5 in. (63 mm) diameter PVC pipe was placed at the center of the footing, the segments, and the head block for passage of the unbonded PT rod. The commercial name of PT rod was SAS thread bar and it was provided by the AVAR Company. The rod was anchored in the foundation below the column and in the head at top of the column.

Since the rod was unbonded over the height of the column, strains were not concentrated at crack or interface between segments.

If the initial prestress level is carefully selected, inelastic straining of the prestressing steel does not occur. This is important for several reasons. First, the ability to transfer shear across the component interfaces by shear friction depends on the clamping force provided by the PT rod. Furthermore, the column stiffness also relies on the prestressing force and hence is not reduced drastically if the prestressing is maintained. Finally, the restoring force provided to the column by the prestressing is maintained during and after the earthquake ensuring that the column returns to the original position [Hews and Priestley, 2002].

The OpenSees analysis software was used to estimate the PT force during seismic loading. Other researchers have reported a significant increase in the PT force under large drifts in their experimental studies [Hewes and Priestley, 2002, Sakai and Mahin, 2004]. Analytical parametric studies were conducted to investigate the effects of post-tensioning steel area and initial stress on the force-displacement response of the columns. The key point was keeping the PT force under the yield force in order to guarantee minimum residual displacement at the end of test. The diameter of the rod was selected such that the maximum estimated force in the rod would not exceed 70% of the yield strength. A comprehensive design method of unbonded PT rod used in precast segmental columns is presented in chapter 8.

The initial design force in the PT rod was selected to be 100 kips (444 kN) and was slightly different in each specimens. The force of 110 kips (490 kN) was applied during post-tensioning process considering the losses due to anchorage set and elastic shortening; however, the losses due to friction, creep, shrinkage and relaxation were neglected. It was assumed that the effect of the friction was small because the PT rod was straight. The effect of creep and shrinkage was also expected to be negligible since the concrete ages of the test specimen at post-tensioning was more than 60 days. The reason for neglecting the relaxation was that the period between post-tensioning and shake table testing was less than a week [AASHTO, 2002].

2.3.2.5. Materials

2.3.2.5.1. Concrete

Concrete was ordered with a specified 28-day compressive strength of 5.0 ksi (34.5 MPa). To determine the concrete compressive strength, standard 6 x 12 in (150 x 300 mm) cylindrical samples were taken. The concrete slump was measured before the concrete was cast. A small amount of super plasticizer was added to the batches with low slump to increase workability without reducing the strength. Three cylinders were tested at 7 days, 28 days, and the test day for each casting on a SATEC MKIII-C testing machine. The compressive strength results for different batches are listed in Table 2-2.

It should be noted that SC-2, SF-2 and SE-2 were constructed simultaneously; therefore the concrete compressive strength at 7 and 28 days were the same. The concrete was cast in multi stages due to the match cast construction.

2.3.2.5.2. Steel

Tensile testing was conducted for the lateral spiral #3, the longitudinal #4 and #5 column bars reinforcement. Base segments of SC-2, SF-2 and SE-2 used #4 longitudinal reinforcement. The base segment of SBR-1 incorporated #5 steel longitudinal bars. The spirals in all columns were made of #3 bars. Three samples of #4 and #3 and two samples of #5 bars were tested and subjected to a tensile stress test on a Tinius Olson testing machine. Specimens were designed for a specified yielding stress of 60 ksi (414 MPa). The actual yield stresses of 64 ksi (441 MPa), 74 ksi (510 MPa), and 68 (468 MPa) were measured for #4, # 5, and #3 bars, respectively. Measured stress-strain curves for # 4 bars are shown in Figs. 2-4. The curves displayed a clear plateau after the yield point. The ultimate stress was taken as the maximum stress before bar rupture, and it was 94 ksi (648 MPa). The measured stress-strain curves for two samples of #5 bars and three samples of # 3 bars are displayed in Figs. 2-5 and 2-6. In these graphs the yield point could not be identified; therefore, the yield stress was determined using the 2% offset method. The ultimate stresses of and 97 ksi (648 MPa) and100 ksi (689 MPa) were measured for #5 and #3 bars, respectively.

2.3.2.5.3. Rubber

AASHTO grade 3 natural rubber was used in bearing pad in SBR-1. The rubber mechanical properties were provided by the manufacture, Dynamic Isolation Systems (DIS). The rubber type was shore A, and its durometer (hardness) compression was 58 pts (precision test standard). The ultimate elongation was 664%. The tensile strength was 4508 psi (31 MPa),and the static shear modulus was 115 psi (0.8 MPa).

2.3.2.5.4. FRP

Unidirectional FRP fabric was used in the lower two segments of SF-2 and SC-2R. Three coupons of FRP were made and cured under the same condition as SF-2 condition. The fibers in the samples were in the long direction. The samples were tested under tension using a Tinius Olson testing machine (Fig. 2-7). The coupons were 12 in. (305 mm) long, 1 in. (25 mm) width and consisted of 2 layers of FRP, each layer 0.04 in. (1 mm) thick. Figure 2-8 shows the measured stress-strain curves. The measured modulus of elasticity of the samples was 11000 ksi (75842 MPa) ,and the average ultimate stress was 108 ksi (745 MPa).

2.3.2.5.5. ECC

The base and second segments and the part of footing near the base of the column in SE-2 were built with ECC. ECC was cast in two steps due to the match cast construction.

ECC was ordered with specified 28- day compressive strength of 5.0 ksi (34.5 MPa). To determine the ECC compressive strength, standard 4 x 8 in (100 x 200 mm) cylinders were cast. Three cylinders were tested at 28 days and on the test day for each casting using a SATEC MKIII-C testing machine. The ECC curing process is longer than concrete; therefore, the strength was not measured at 7 days. The compressive strength results are listed in Table 2-3. The ECC strengths on the test day for the base and second segments were 7.1 ksi (49 MPa) and 7.4 ksi (51 MPa), respectively.

2.3.2.5.6. Mortar

A rapid repair mortar with a commercial name of STO was used to repair the SC-2. STO is a low shrinkage, micro silica-modified, and cement-based mortar for structural repair of deteriorated concrete. The specified 3-hour, 1-day, and 7-day compressive strengths of the mortar are 3 ksi (20.7 MPa), 4 ksi (27.6 MPa), and 6.5 ksi (45 MPa), respectively. To determine the mortar compressive strength, three standard 3 x 6 in (75 x 150 mm) cylinders were taken and tested on a SATEC MKIII-C testing machine. The age of cylinders was 6 days when SC-2R was tested. The average measured compressive strength was 7.04 ksi (48 MPa) (Table 2.4).

2.3.2.6. Columns Assembly

The column segments were assembled on the shake table in approximately three hours. Figure 2-9 shows the assembling process. Before assembling, the PT rod was tied at the bottom of the footing by a nut and a steel plate. A small amount of epoxy was applied on the top of each surface before placing the next segment to stabilize the segments during construction (Fig. 2-9 (a)). The epoxy adhesive was Sikadur 31 SBA slow set (70-90 F) and was provided by Sika Corporation. The epoxy adhesive had one hour pot life and eight hours of "open time". The epoxy adhesive was applied to the joint surface within the pot life and the column was post-tensioned within the open time.

Due to application of fresh epoxy on interfaces, the segments were slippery during the post-tensioning process; therefore, 4 pieces of steel members were placed along the column and tightened with straps to keep the column straight (Fig. 2-9 (b)). The last step of column assembly was post-tensioning the PT rod (Fig. 2-9 (c)). A 110-kips (490 kN) force was applied on the PT rod; this force was recorded by the load cell on top of the column head.

2.3.2.7. Instrumentation

To monitor various aspects of the behavior, a large number of strain gauges, Novotechnik displacement transducers, stringpots, load cells, and accelerometers were installed on the specimens. The types of the strain gauges were TML YEFLA-2-3L and YEFLA-5-5L; they were installed on the longitudinal and transverse bars located at the lower one third, particularly near the column and footing interface where plastic hinging was expected.

Four strain gauges were installed on the PT rod in SC-2, SF-2, SE-2 and SC-2R to measure the strain history during the experiment. PT force in the rod was calculated from these gauges and the results were compared with the load cell data.

To measure curvatures and bond-slip rotations, several pairs of displacement transducers were attached to the south and north sides of the columns. Novotechniks at the first level measured the bond slip and base segment rotation, and the rest of the transducers mainly measured the amount of separation between the segments.

Two Unimeasure PA-40 stringpots were attached from the lab wall and a steel frame to the center of column head sides. These instruments served to measure absolute displacements at the top of the column at 72 in. (1828.8 mm) from the top of the footing in orthogonal directions.

A crossbow CXLOZLF1 accelerometer was utilized to record acceleration at the top of columns and was attached to the link assembly. Four additional accelerometers were also placed at the mid height of each column segments to measure the acceleration at different levels.

Two Sensotec Model 41 load cells were placed on the top of the spreader beam to measure axial loads on the columns, and a third load cell was placed on the link assembly to measure lateral forces at the top of the column. Also a load cell was located inside the head opening to measure the post-tensioning rod force.

Instrumentation plans and particular instrumentation on advanced materials are presented for each column in the subsequent sections.

2.3.2.8. Test Setup and Loading Protocol

In preparation for the test, the specimens were centered on the shake table and placed on top of various 1.5 in. (38 mm) thick wooden spacers. A formwork was placed around the footings and grout was cast to a thickness of approximately 2 in. (51 mm). Threaded rods extended through the footing holes and were anchored on top of the footing to securely attach the footing to the shake table and resist overturning moments. The threaded rods were given the force to provide 30 kips (133 kN) clamping force between the footing and the shake table. The mass rig system was connected to the head of the specimen via one rigid link. Threaded rods going through the four PVC pipes in the head held the link and the specimen together. To create an inertial mass of 80 kips (356 kN), three inertial blocks weighing approximately 20 kips (89 kN) each were placed on the mass rig. Including the effective mass of the mass rig frame (20 kips (89 kN)), the total inertial mass of the system was approximately 80 kips (356 kN). To provide the specimens with the axial load they were designed for, a steel spreader beam was bolted to the top of the column head. In addition, two hydraulic jacks connected to an accumulator were placed on top of the spreader beam to apply the axial load. The shake table setup is shown in Figs. 2-10 and 2-11.

The segmental columns were subjected to a series of Sylmar ground motions (Fig. 2-12) with the acceleration amplitude scaled by 0.1, 0.25, 0.5, 0.75, 1, 1.25, and 1.5 in subsequent runs. The time coordinate of the input acceleration was compressed by a factor of $\sqrt{0.33}$ =0.577 to account for the scale of the test model that was 0.33. The testing was continued until failure. To determine the dynamic characteristics of the columns as the level of motions increased, a white noise motion was applied to the specimens after each earthquake motion. The loading protocols are listed in Table 2-5 for all specimens. The loading protocol was slightly different for each specimen. The last motion (1.5 × Sylmar) was repeated for SF-2 and SE-2; since the failure signs were not observed in them after Run 7. Fewer numbers of scaled input motions were applied to SC-2R since this column was repaired and applying numerous motions was not desirable.

2.3.3. SC-2

2.3.3.1. Introduction

SC-2 (segmental with concrete) was a one third scale cantilever precast segmental column. This column was the benchmark for evaluating the advantages or disadvantages of other models incorporating advance materials.

2.3.3.2. Column Details

Figure 2-13 shows the dimensions and geometry of SC-2. SC-2 reinforcement and section details are shown in Figs. 2-14 and 2-15, respectively. Ten #4 headed bars spaced evenly were used in a circular pattern leading to a longitudinal steel ratio of 1.0%. The reason for using the headed bars was to satisfy the anchorage length requirements. These bars were supplied by Erico Company and are labeled Lenton Terminator.

The design of transverse reinforcement in the base segment was controlled by satisfying a displacement ductility demand of 5 for the column, using the Caltrans conventional column design (Caltrans, 2006). The resulting bars, # 3 spirals at 2 in. (51 mm) pitch, were used as the transverse reinforcement in all the segments. The second, third, and fourth segments from the base were identical RC segments. The dimension and reinforcement details of upper segments are presented in section 2.3.2.1.

Details of footing, column head block, and post-tensioning system are presented in sections 2.3.2.3 and 2.3.2.4.

2.3.3.3. Construction

The construction of SC-2 included building the steel cages, casting of concrete in the footing and the segments, and finally assembling the columns. The steel cages were built for the footing and all column segments. Figure 2-16 and 2-17 (b) show the cages for the base segment and typical segments in SC-2, respectively. Strain gauges were installed on the longitudinal and transverse bars of the base and second segment where the maximum strain was expected. Figure 2-17 (a) shows the placement of the base segment steel cage inside the footing. Casting of concrete in SC-2 segments was done in 3 steps. First, the footing and the third segment were built on the construction platform (Fig. 2-17 (c)). The base segment was constructed after the footing was set (Fig. 2-17 (d)). Finally the second and fourth segments were built on top of the base and the third segments using match cast method (Fig. 2-18 (a) and (b)). In the match cast method, a previously constructed segment was used as the form for the next segment. In addition a layer of chemical liquid concrete bond breaker was applied on surface of lower segment to facilitate the removal of the upper segment. Figure 2-19 shows SC-2 after construction and assembly.

2.3.3.4. Instrumentation

To monitor various aspects of the behavior, 121 channels of data were collected during the experiment. The general instrumentation plans are explained in section 2.3.2.8. Figure 2-20 shows the strain gauges plan for SC-2. Strain gauges 1 through 38 measured strains on the longitudinal bars. Strain gauges 39 through 58 measured strains on the spirals, and strain gauges 59 through 62 measured the strain history in the PT rod.

To measure curvature and bond-slip , five pairs of the displacement transducers were attached to the south and north face of the column. Figure 2-21 illustrates the placement and numbering of these transducers.

2.3.4. SBR-1

2.3.4.1. Introduction

SBR-1 (segmental with built-in rubber pad) was a one-third scale cantilever precast segmental column incorporating an elastomeric bearing pad in the plastic hinge. The purpose of using the pad was to minimize damage while dissipating energy through yielding of the longitudinal bars and deformation of the pad.

Kawashima and Watanabe, (2006) used a combination of post-tensioning and high damping rubber in the plastic hinge area of CIP (cast-in place) column models to minimize the damage and increase ductility and energy dissipation ability. The columns failed under moderate lateral drift ratios. The failure mode in the columns was buckling and rupture of longitudinal bars due to unrestrained length in the rubber unit. Unlike the bearing pads used in Japan, the pad in SBR-1 was shimmed and hence buckling of longitudinal bars was prevented.

2.3.4.2. Elastomeric Bearing pad Design

The mechanical properties of elastomeric bearing included shear, bending, and compression stiffness. These stiffnesses are determined using different equations that mostly depend on the shape factor of the elastomeric pad.

The shape factor S was defined by Keys, (1937). Shape factor for a rubber layer is the ratio of the loaded area to the total force-free area (Eq. 2-8). Shape factor is used in most compression stiffness equations of rubber blocks [Aiken, et al., 1989].

$$S = \frac{one\,loaded\ area}{total\,"\,force\ free"\,area} = \frac{Area\,of\ \ pad}{Area\,of\ the\ pad\ circumference} \qquad \text{Eq. 2-8}$$

For example for a round elastomeric bearing, the shape factor is calculated from Eq. 2-9:

$$S = \frac{\frac{\pi D^2}{4}}{\pi D t} = \frac{D}{4t} \qquad \text{Eq. 2-9}$$

Where

D = Diameter

t = Thickness of one rubber layer

The elastomeric bearing pad was designed by controlling the failure of the rubber when it was subjected to axial compression and bending moment. Therefore compressive and rotational stiffness were important in the design of elastomeric pad in SBR-1.

The commonly used equation for the compression stiffness of rubber blocks, derived by

Gent and Lindley (1959), is presented in Eq. 2-10.

$$E_c = E_0(1+2kS^2) \qquad \text{Eq. 2-10}$$

Where,

E_0 = Young‟s modulus

k = Material modifying factors (determined by experiments)

S = Shape factor

In research by Derham (1982) Eq. 2-11 was suggested for S>3

$$E_c = 5.6GS^2 \qquad \text{Eq. 2-11}$$

In which,

G = Shear modulus (obtained from material test)

The bending stiffness of elastomeric bearing can be calculated from Eq. 2-12.

$$K_\theta = \frac{E_b I}{T_r} \qquad \text{Eq. 2-12}$$

$$M = K_\theta \times \theta \qquad \text{Eq. 2-13}$$

In which

$$E_b = E(1+\frac{2}{3}S^2) \qquad \text{Eq. 2-14}$$

T_r = Total thickness of bearing

I = Moment of inertia of bearing stiffness

The OpenSees software was utilized to verify the elastomeric bearing pad design. An elastomeric bearing with an assumed geometry was modeled in the OpenSees as a part of SBR-1. The column was analyzed under dynamic motion and the maximum rotational demand was calculated at the bearing. The rotational capacity of assumed bearing was calculated and compared with the rotational demand.

The assumed bearing pad diameter was equal to the column diameter (16 in. (406 mm)). A thickness of 3/16 in (4 mm) was selected for each rubber layer leading to shape factor of 14. Shear modulus of rubber (G) was 115 psi (0.8 MPa) and compression stiffness of rubber was calculated from Eq. 2-11 and was equal to 126 ksi (868 MPa). The total height of elastomeric pad was considered as plastic hinge length equal to one-half of the column diameter (8 in. (203 mm)) at the first trial and this height was checked against rotational demand of bearing. An elastic material with modulus of elasticity equal to the compression stiffness of the bearing was assigned to a section at the bearing level in OpenSees. Later, this section including the longitudinal bars was assigned to a nonlinear beam column element that had height of bearing (8 in. (203 mm)).

SBR-1 model was analyzed under a specified ground motion and moments and rotations of column at the level of bearing were recorded and required rotational stiffness, K_θ, was calculated from Eq. 2-13. The height of rubber layers (T_r) was calculated from Eq. 2-12 and was added to total thickness of steel shims (1/8 in. (3 mm) thick each. Total thickness of steel shims was calculated assuming that the steel shims were placed between rubber layers.

The total height of bearing was less than the assumed height, indicating that 8 in. (203 mm) bearing thickness was sufficient.

2.3.4.3. Column Details

Figure 2-22 shows the dimensions and geometry of SBR-1. The base segment in SBR-1 included an elastomeric bearing pad in the lower part and reinforced concrete in the upper part and was connected to the footing by steel dowels. Details of the bearing are shown in Fig. 2-23. The total height of the bearing was 8 in. (203 mm) and was composed of 21 layers of rubber and 20 layers of steel shim. Each layer of rubber and steel shim were 3/16 in. (4 mm) and 1/8 in. (3 mm) thick, respectively. The shear deformation in the elastomeric pad was restrained using a central 3-1/2 in. (89 mm) diameter x-strong steel pipe. The steel pipe was welded to the top and bottom plates of bearing but it was free to move in vertical direction, along the bearing height. Eight dowels with ¾ in. (19 mm) diameter and 3-11/16 in. (93 mm) height were welded to the top and bottom steel plates to provide anchorage to concrete. Eight holes with 11/16 in. (17 mm) diameter were drilled through the bearing pad to allow for the passage of the column longitudinal bars. Note that the bearing pad in SBR-1 was designed to act in flexure and not shear. Therefore its function was different than that of base isolator pads that are normally designed to deform in shear.

Figures 2-24 and 2-25 show SBR-1 reinforcement details and the detail of the sections, respectively. The RC portion of the base segment was 12 in. (305 mm) high. Eight #5 bars spaced evenly in a circular pattern were used to reinforce the base segment, leading to a longitudinal steel ratio of 1.2%. This amount of steel at the base segment was selected such that the longitudinal bars would yield before separation of the segments.

The second, third, and fourth segments from the base were identical RC segments. The dimensions and reinforcement details of upper segments are presented in section 2.3.2.1.

The design of transverse reinforcement in the base segment was controlled by satisfying a displacement ductility demand of 5 for the column, using the Caltrans conventional column design [Caltrans, 2006]. The resulting bars, # 3 spirals at 2 in. (51 mm) pitch, were used as the transverse reinforcement in all the segments.

Details of the footing, head block and post-tensioning system are presented in sections 2.3.2.2 and 2.3.2.4.

2.3.4.4. Construction

The construction of SBR-1 included building the steel cages, placing the bearing pad in the base segment, casting of concrete in the footing and the segments, and finally assembling the columns.

The steel cages were built for the footing and all column segments. The elastomeric bearing was supplied by Dynamic Isolation Systems. The longitudinal bars were passed through the bearing holes (Fig. 2-26 (a)). The longitudinal bars, spirals and central steel pipe were instrumented with strain gauges. To satisfy anchorage length at top of the base segment, longitudinal bars were bent with portable rebar bending machine (Fig. 2-26 (b)). The reinforcement cage of the head and other typical segments were built. Figure 2-27 shows typical segments before and after casting of concrete.

Concrete was cast in SBR-1 segments in two steps starting with the footing, base segment, and the third segment (Fig. 2-28). The second and fourth segments and head block were constructed next. Figure 2-29 shows the head block before and after casting of concrete. The second and fourth segments were match cast on the top of the base and third segments. A plastic sheet covered surface of lower segment to break the concrete bond and facilitate the removal of the upper segment. SBR-1 after construction and assembly is shown in Fig. 2-30.

2.3.4.5. Instrumentation

To monitor various aspects of the behavior, 147 channels of data were collected during the experiment. The general instrumentation plans are explained in section 2.3.2.8. Figure 2-31 shows the strain gauge plan for SBR-1. Gauges 1 through 26 measured strains on the longitudinal bars, and gauges 27 through 42 measured strains on the spirals. Four sets of YEFRA-2-5L Rosette strain gauges were attached to the central steel pipe of bearing to measure shear strains. Three pairs of GFLA-3-50 low elastic strain gauges were attached on the rubber at three levels.

To measure curvatures and bond-slip rotations, seven pairs of Novotechnik sensors were attached to the south and north sides of the column. Two pairs of Novotechnik transducers were installed on the east-west faces in horizontal direction to measure the slippage between the base and second segments. Figures 2-32 and 2-33 illustrate the placement and numbering of transducers.

2.3.5. SF-2

2.3.5.1. Introduction

SF-2 (segmental with FRP) was a one-third scale cantilever precast segmental column with the base segment connected to the footing. The first two segments above the footing were wrapped with two layers of unidirectional FRP (fiber reinforced polymer) fabrics with horizontal fibers. The purpose of using the FRP at the lower segments was to confined the concrete and minimize damage at interface between the base and second segments.

2.3.5.2. FRP Confinement Design

According to the guidelines of the California Department of Transportation (Caltrans 1998) for composite column casings, composite jackets for circular lap-spliced columns should be designed for a hoop strain of 0.001 to provide a minimum confinement pressure of 300 psi (2.07 MPa) within the lap splice.

The number of FRP layer in SF-2 was selected to provide a minimum confinement pressure (f_r) of 300 psi (2.07 MPa). The confinement pressure was calculated from Eq. 2-16 [Saiidi et al. 2005].

$$f_r = \frac{2E_j \varepsilon_j t_j}{D} \qquad \text{Eq. 2-16}$$

E_j = Elastic modulus of CFRP

ε_j = 50% of the failure strain of the jacket in direction of fibers

t_j = Thickness of the jacket

D = Column diameter

Assuming column diameter of 16 in. (406 mm), thickness of 0.04 in (1 mm) for each layer of FRP, E_j equal to 11000 ksi (75842 MPa) and ε_j equal to 0.004 based on material properties, 1.4 layers was required to provide confinement pressure of 300 psi (2.07 MPa). Therefore the lower segments were wrapped with 2 layers of FRP.

The concrete properties of the sections wrapped with FRP were determined based on FRP confined concrete properties. Saiidi"s (Saiidi et al. 2005) bilinear stress-strain relationship for FRP-confined concrete was used in this study.

This model is shown in Fig. 2-34. To define the bilinear relationship, the coordinate of the break point and the ultimate point needed to be determined. At the break point the strain was 0.002; therefore,

$\varepsilon_{cy} = 0.002$ Eq. 2-17

and the stress was found as follows

$f'_{co} = f'_c + 0.003\rho_{cf} E_j$ Eq. 2-18

Where

f'_{co} = Concrete stress at start of post yielding branch

f'_c = Unconfined concrete compressive strength

ρ_{cf} = FRP volumetric ratio

For a circular section $\rho_{cf} = \frac{4t_j}{D}$ Eq. 2-19

Where

The ultimate stress was determined using the following equations:

$f'_{cu} = f'_c + 3.5 f_r^{0.7}$ (ksi) Eq. 2-20

$f'_{cu} = f'_c + 6.2 f_r^{0.7}$ (MPa) Eq. 2-21

Where

f'_{cu} = Confined concrete strength

f_r = Confinement pressure (Eq. 2-16)

And ultimate strain was determined from Eq. 2-22.

$\varepsilon_{cu} = \frac{\varepsilon_j}{\nu}$ Eq. 2-22

ε_{cu} = Ultimate strain

ν =Poisson ratio

$\nu = 0.1 - 0.25 \ln \frac{f'_r}{f'_c}$ Eq. 2-23

FRP confined concrete properties were calculated from above equations and used in modeling the SF-2 by OpenSees in the pre-test analyses.

2.3.5.3. Column Details

Figure 2-35 shows the dimensions and geometry of SF-2. SF-2 reinforcement and section details are shown in Figs. 2-36 and 2-37, respectively. The base and second segments in SF-2 were made of 20 in. (508 mm) and 14 in. (356 mm) high concrete segment, respectively, and they were each wrapped with 2 layers of FRP. Ten #4 headed bars spaced evenly were used in a circular pattern leading to steel ratio of 1.0%. The reason for using the headed bars was to satisfy the anchorage length requirements. These bars were supplied by Erico Company and are labeled Lenton Terminator. Figure 2-38 (a) shows the base segment cage detail. The third and fourth segments from the base were identical RC segments. The dimensions and reinforcement details of upper segments are presented in section 2.3.2.1.

The design of transverse reinforcement in the base segment was controlled by satisfying a displacement ductility demand of 5 for the column, using the Caltrans conventional column design [Caltrans, 2006]. Since the FRP was used to provide confinement in the base and second segments, the amount of the transverse reinforcement was lower than that normally used. The resulting bars, # 3 spirals with 4 in. (100 mm) pitch, were used as the transverse reinforcement in first two segments from the base leading to a volumetric spiral steel ratio of 0.7%. The transverse reinforcement in other segments was #3 at 2 in. (51 mm) pitch.

Details of the footing, column head block, and post-tensioning system are presented in sections 2.3.2.3 and 2.3.2.4.

2.3.5.4. Construction

The construction of SF-2 included building the steel cages, casting of concrete in the footing and the segments, wrapping the lower segments with FRP, and finally assembling the columns. The steel cages were built for the footing and all the column segments. The longitudinal and transverse bars at the base and second segments were instrumented with strain gauges. The base segment reinforcement was placed in the footing before casting of concrete (Fig. 2-38 (a)). Casting of concrete in SF-2 segments was done in 3 steps starting with the footing and the third segment (Fig. 2-38 (b)) followed by the casting of the base segment. Finally, the second and fourth segments were match cast on top of the base and the third segments, respectively (Fig. 2-39). A layer of chemical liquid concrete bond breaker was applied on surface of lower segment to facilitate the removal of the upper segment.

Next, the base and second segments were wrapped with FRP. The surface of each segment was ground, cleaned, and covered with epoxy and then FRP fabric was placed on it. The instrumentation including the strain gauges were places on the FRP jacket after column assembly. The process of FRP wrapping is shown in Fig. 2-40. Figure 2-41 shows SF-2 after construction.

2.3.5.5. Instrumentation

To monitor various aspects of the behavior, 127 channels of data were collected during the experiment. The general instrumentation plans are explained in section 2.3.2.8. Figure 2-42 shows the strain gauge plan for SF-2. Strain gauge type of BFLA-5- 3L was installed on FRP. Gauges 1 through 38 measured strains on the longitudinal bars, and Gauges 39 through 58 measured strains on the spirals. Gauges 59 through 62 measured the strains in the PT rod. Strain gauges 63 through 70 were attached on the FRP surface at two levels near the top of the base segment and bottom of the second segment.

To measure curvatures and bond-slip rotations, 5 pairs of Novotechnik sensors were attached to the south and north sides of the column. Figure 2-43 illustrates the placement and numbering of these transducers.

2.3.6. SE-2

2.3.6.1. Introduction

SE-2 (segmental with ECC) was a one-third scale cantilever precast segmental column with the base segment connected to the footing. The first two segments in SE-2 were made of ECC (engineered cementitious composite). The purpose of using ECC in lower segments was to minimize damage due to ductile behavior of ECC while dissipating energy through yielding of the longitudinal bars.

A material with strong potential for seismic applications is ECC. ECC contains water, cement, fine sand, fiber, and some common chemical additives. ECC displays higher tensile ductility, tensile (strain) hardening behavior, and energy dissipation than conventional concrete and many fiber-reinforced concrete materials [Billington and Yoon, 2002].

2.3.6.2. ECC Material Design

ECC was ordered with a specified 28-day compressive strength of 5.0 ksi (34.5 MPa). A local contractor provided the ECC. The mix proportions of the ECC material is given in Table 2-6. The volume fraction of fiber was 2%. ASTM Type I/II Portland cement and FT Bridger fly ash were used. Table 2-7 lists the type of materials used in ECC. The size of sand was # 60 medium. The Kurary PVA KII 8X15 fibers used in the mix. The dried components of ECC including small aggregate, fly ash, and polyvinyl alcohol fibers were combined before transferring to the construction site. Water was added to the batch and mixed by an electric mortar mixer.

The fibers in ECC are expected to provide some confinement. However, in the absence of a confinement model for ECC, the lateral reinforcement was designed to provide full confinement. Following the testing of SE-2 a limited study was conducted to develop a confinement model for ECC. Details of that study are presented in Chapter 5.

2.3.6.3. Column Details

The base and second segments in SE-2 were made of ECC. They were 20 in. (508 mm) and 14 in. (356 mm) high segments, respectively, with reinforcement similar to that used in SC-2 (Fig. 2-44). Detail of reinforcement and column sections of SE-2 are shown in Figs. 2-45 and 2-46, respectively. Ten #4 headed bars spaced evenly were used in a circular pattern leading to a steel ratio of 1.0%. The reason for using headed bars was to satisfy the anchorage length requirements. These bars were supplied by Erico Company and are labeled Lenton Terminator. The design of transverse reinforcement in the base segment was controlled by satisfying a displacement ductility demand of 5 for the column, using the Caltrans conventional column design [Caltrans, 2006]. The resulting bars, # 3 spirals at 2 in. (51 mm) pitch, were used as the transverse reinforcement in all the segments.

The third and fourth segments from the base were identical RC segments. The dimensions and reinforcement details of upper segments are presented in section 2.3.2.1.

Details of footing, column head block, and post-tensioning system are presented in sections 2.3.2.3 and 2.3.2.4, respectively.

2.3.6.4. Construction

The construction of SE-2 included building the steel cages, casting of concrete and ECC, and finally, assembling the columns. The steel cages were built for footing and all column segments. The longitudinal and transverse bars in the base and second segments were instrumented with strain gauges.

The dried components of ECC including small aggregate, fly ash, and polyvinyl alcohol fibers were combined before transferring to the construction site. Water was added to the batch and mixed by an electric mortar mixer.

Casting of concrete and ECC was done in five steps. Concrete was cast in the footing on the construction platform first (Fig. 2-47 (a)). To avoid a weak plane between the bottom of the column and the top of the footing, a $24 \times 24 \times 5$ in. ($610 \times 610 \times 127$ mm) mold was formed in the upper part of the footing around the column and filled with ECC material. ECC was cast in the base segment and part of the footing (Fig. 2-47 (b) and (c)). Next, the second and fourth segments were match cast on top of the base and the third segments. It should be noted that the second segment was made of ECC. In addition, a layer of chemical liquid concrete bond breaker was applied on the surface of the lower segment to facilitate the removal of the upper segment. Figure 2-48 shows SE-2 after construction and assembly.

2.3.6.5. Instrumentation

To evaluate various aspects of the behavior, 119 channels of data were collected during the experiment. The general instrumentation plans are explained in section 2.3.2.8. Figure 2-49 shows the strain gauge plan for SE-2. Gauges 1 through 38 measured strain on the longitudinal bars. Gauges 39 through 58 measured strain on the spirals. Gauges 59 through 62 measured the strain history in PT rod.

To measure curvatures and bond-slip rotations, 5 pairs of Novotechnik sensors were attached to the south and north face of the column. Figure 2-50 illustrates the placement and numbering of these transducers.

2.3.7. SC-2R

2.3.7.1. Introduction

Column SC-2 was repaired after the final test and was labeled SC-2R (segmental with concrete, repaired). SC-2 experienced considerable damage including concrete spalling at the interface between the base and second segments. The longitudinal bars at the base segment of SC-2 yielded but did not rupture. To study the feasibility and the effectiveness of the repair for current segmental detail, it was proposed to repair SC-2 and wrap the lower segments with a CFRP jacket. Among different jacket systems, FRP jacket was selected due to ease of installation and other advantages such as high strength to weight ratio. FRP wrapping provides confinement for the concrete and increases its ductility.

2.3.7.2. Column Details

SC-2 R had the same detail as SC-2 including geometry and reinforcement. The lower part of SC-2R was wrapped with two layers of FRP to provide a minimum confinement pressure (f_r) of 300 psi (2.07 MPa) and ductility for the damaged column. Column details are shown in Fig. 2-51.

2.3.7.3. Repair Process

Repair of column SC-2R included removing the loose concrete, patching the damaged part with non shrinkage high strength mortar, and wrapping the column with FRP fabrics.

At the end of SC-2 shake table experiment, the instrumentations attached to the lower part of the column were removed and loose concrete was detached from the damaged area (Fig. 2-52). A mortar with trade name of “STO Rapid Repair Mortar” was used. STO was a low-shrinkage, micro silica-modified, and cement-based mortar for structural repair of deteriorated concrete. Due to very low workability, the mortar was applied to the spalled area by hand and was consolidated by thumb pressure. After concrete patching, the surface was smoothed by a trowel (Fig. 2-53). A Sonotube segment was placed around the repaired zone for 24 hours to cure the mortar.

A length of 27.5 in. (700 mm) was wrapped with two layers of FRP. Each layer of FRP jacket was 0.04 in. (1 mm) thick and extended from 3 in. (76 mm) above the footing to the middle of the second segment. A thin layer of epoxy was applied on column surface before FRP attachment (Fig. 2-54). The curing time for FRP was 7 days and the column was retested after this time. Figure 2-55 shows SC-2R after repair and before the test.

2.3.7.4. Instrumentation

The instrumentation plan in SC-2R was similar to that of SC-2. No strain gauges were lost after testing SC-2. The strain gauge plan and Novotechnik plan for SC-2R are shown in Figs. 2-56 and 2-57, respectively. FRP jacket was instrumented with eight BFLA-5-3L strain gauges to measure the strain history during the test. These strain gauges were installed at 1 in. (25 mm) above and below the interface of the base and second segments.

2.4. Two- Column Bent Specimen

2.4.1. Introduction

An alternative to segmental columns for accelerated bridge construction is building monolithic precast columns off site and then assemble them with the footing and cap beam at construction site. To study this type of construction, specimen PFEB (precast FRP-ECC bent) was built and tested at UNR. PFEB was a 0.3-scale bent incorporating two monolithic precast columns, a footing, and a cap beam that were built separately. Two innovative details for columns were included in PEFB. Pipe-pin hinges were used at column-cap beam connections. This type of connections has been used in precast construction and has been extensively studied [Zaghi and Saiidi, 2008]. It was found that because of their ease of construction pipe-pin hinges could be effectively used in precast bridge construction as well. Two molds were formed in the footing during the construction to allow for embedment of the columns. The embedded length was designed in such a way to transfer the full plastic moment of the column and provide complete rigidity.

2.4.2. Bent Details

Figure 2-58 displays the bent geometry. One column was a conventional reinforced concrete column incorporating ECC material in the plastic hinge area and the other was a FRP tube filled with concrete. The reinforced concrete column with ECC in the plastic hinge region was labeled RC-ECC column and the concrete filled FRP tube was labeled FRP column. By taking advantage of a load cell in the middle of the cap beam, it became possible to measure the shear in each column. Due to the hinge action of the pipe-pin detail, no moment was transferred between the columns and cap beam; thus, the moment in the beam was minimal and effect of the load cell on the global response was negligible. The diameters of RC-ECC column and FRP columns were 14 in. (355 mm) and 14.567 in (370 mm), respectively. The column height was 63 in. (1600 mm) leading to an aspect ratio of 4.5. The column height was taken as the distance from the top of the footing to the bottom of the cap beam where the pipe hinge was located. The total column height including the part embedded in the footing was 86 in. (2184 mm).

Large scale concrete filled FRP tube referred to as CFFT was first developed and tested by Zhu et al., (2006). The FRP tube was Red Thread® II pipe with outside diameter of 14.567 in (370 mm) and wall thickness of 0.269 in (6.83 mm) chosen from NOV Fiber Glass Systems company production. Red Thread II pipe is a filament wound product using epoxy resins and continuous glass filament with a resin rich interior surface, which was originally developed for piping system in chemical plants. Fibers in this product are aligned at +/-55° providing strength in the longitudinal and hoop directions. To increase the flexural capacity and energy dissipation capacity, 7-#3 longitudinal reinforcement spaced evenly were used in a circular pattern leading to a longitudinal steel ratio of 0.46%. No lateral steel reinforcements were used in this column, except for a few nominal hoops to keep the longitudinal bars in place.

Twenty-four in. (610 mm) of the length located in the plastic hinge zone of RC-ECC column was made of ECC. This length was from 3 in. (76 mm) below the footing top surface to 21 in. (533 mm) above the footing (Fig. 2-58). 8 #5 headed longitudinal bars spaced evenly were used in a circular pattern leading to steel ratio of 1.6 %. The reason for using the headed bars was to satisfy the anchorage length requirements at the bottom of the column. These bars were supplied by Erico Company and are labeled Lenton Terminator. The design of transverse reinforcement in the column was controlled by providing a displacement ductility capacity of 5 for the column, using the Caltrans conventional column design method [Caltrans, 2006]. The resulting bars were # 3 spirals at 2 in. (51 mm) pitch. The reinforcement detail of PEFB is shown in Fig. 2-59. Figure 2-60 shows the section detail including the dimensions and reinforcements.

Pipe-pin hinges were used at top of the columns. Details of pipe-pin are displayed in Fig. 2-61. The pipe specifications are listed in Table 2-9. A 2-1/2 x-Strong steel pipe was used as the pipe-pin for both of the columns. The details and dimensions of pipe-pins in PEFB were similar to those in a previous project on studying the behavior of pipe-pin hinges in a two column bent. The pipe-pin detail was originally designed for larger demands; therefore, their capacity was larger that what was required in PEFB. Outer pipe diameter and thickness were 2.88 in (73.15 mm) and 0.276 in (7 mm), respectively. The embedded length of the pipe-pin was 13 in (330 mm) and the protruded length was 3.5 in (89 mm). The gap thickness between the pipe-pin and the steel can was 0.15 in (3.8 mm), and the horizontal gap (hinge throat thickness) was 0.25 in (6.35 mm). The exterior can thickness was 0.15 in (3.8 mm). Six 3/16 in (4.76 mm), 1 in (25.4 mm) long steel studs welded on the top side of the can to stabilize it . The spiral around the pipe-pin was Wire 2.5 with diameter of 0.178 in. (4 mm) and 0.75 in. (19 mm) pitch.

The footing was $132\times 48\times 28.75$ in. ($3353\times 1220\times 730$ mm) with two openings to allow for embedding of the columns. The embedded length in the footing was 23 in. (584 mm). Details of footing and cap beam are presented in sections 2.4.3.4 and 2.4.3.5.

2.4.3. Specimen Design

2.4.3.1. Flexural Design

The columns had a length of 63 in. (1600 mm). The RC-ECC column diameter was 14 in. (355.6 mm) with longitudinal steel ratio of 1.6%. Pre-test pushover analyses in OpenSees showed that the lateral load capacity of this column was approximately 29 kips (129 kN).

FRP tube had 14.567 in. (370 mm) diameter with wall thickness of 0.269 in. (6.83 mm).

A model for the longitudinal behavior of the FRP column was used to conduct moment-curvature analysis [Zhu, 2004]. The longitudinal steel ratio in the FRP column was 0.46% to provide the same moment capacity as RC-ECC column at approximately 5% drift. The capacity of the FRP column at 12% drift was estimated at 37 kips (164 kN).

The axial load in each column was 50 kips (178 kN), which resulted in an axial load index (ALI) of 0.065 for the 14 in. (355.6 mm) diameter column with specified concrete strength of 5.0 ksi (34.5 MPa). ALI is defined as ratio of the axial load to the product of the compressive strength of concrete and the cross section of the column. Total weight of the mass rig was 100 kips (444.8 kN) corresponding to the total vertical load on the bent.

2.4.3.2. Shear Design

The Caltrans design guideline was followed for shear design of the RC-ECC column [Caltrans, 2006]. The design shear capacity, V_n, is determined using the following method:

$$\varphi V_n \geq V_o \qquad \text{Eq. 2-22}$$

$$V_n = V_c + V_s \qquad \text{Eq. 2-23}$$

$$V_c = 0.8 v_c A_g \qquad \text{Eq. 2-24}$$

$A_g =$ Gross section area in^2 (mm^2)

$v_c =$ Concrete shear capacity by taking into account member target ductility and axial load psi (MPa)

$$v_c = \begin{cases} Factor1 \times Factor2 \times \sqrt{f'_c} \leq 4\sqrt{f'_c} & \text{(psi)} \\ Factor1 \times Factor2 \times \sqrt{f'_c} \leq 0.33\sqrt{f'_c} & \text{(MPa)} \end{cases} \qquad \text{Eq. 2-25}$$

$$Factor1 = \begin{cases} 0.3 \leq \dfrac{\rho_s f_{yh}}{0.15} + 3.67 - \mu_d < 3 & \text{(ksi)} \\ 0.025 \leq \dfrac{\rho_s f_{yh}}{12.5} + 0.305 - 0.083\mu_d < 0.25 & \text{(MPa)} \end{cases} \qquad \text{Eq. 2-26}$$

$$Factor2 = \begin{cases} 1 + \dfrac{P_c}{2000 A_g} < 1.5 & \text{(psi)} \\ 1 + \dfrac{P_c}{13.8 A_g} < 1.5 & \text{(MPa)} \end{cases} \qquad \text{Eq. 2-27}$$

$$V_s = \frac{\pi A_b f_{yh} D'}{2s} \qquad \text{Eq. 2-28}$$

$$\rho_s = \frac{4A_b}{D's} \qquad \text{Eq. 2-29}$$

$\rho_s =$ Transverse steel ratio

$f_{yh} =$ Yield strength of transverse steel ksi (MPa)

$\mu_d =$ Displacement ductility

$P_c =$ Axial load on the column Lb (N)
$A_b =$ Spiral leg area inch^2 (mm^2)
$D' =$ Diameter of central cord of spiral inch (mm)
$s =$ Spiral pitch inch (mm)

No design code is available for designing the FRP column for shear. The same formulation for conventional reinforced concrete was used for the FRP column with the assumption that hoop strength of FRP tube plays the role of steel spiral. To do so, these terms are defined as:

$$V_n = V_c + V_{FRP} \qquad \text{Eq. 2-30}$$

$$V_{FRP} = \frac{\pi\, t_{FRP}\, f_{FRP,h} D_{FRP}}{2} \qquad \text{Eq. 2-31}$$

$$\rho_{FRP} = \frac{4t_{FRP}}{D_{FRP}} \qquad \text{Eq. 2-32}$$

$f_{FRP,h} =$ Tensile strength FRP tube in hoop direction ksi (MPa)
$D_{FRP} =$ Diameter of central cord of FRP tube in (mm)
$t_{FRP} =$ Thickness of FRP tube in (mm)

The concrete shear capacity in the FRP tube column was determined using the same method used for the RC-ECC column.

2.4.3.3. Pipe-Pin Design

A practical procedure to determine the lateral load capacity of the pipe-pin column hinges was developed by Zaghi and Saiidi, (2010). The method may also be used in design through an iterative process. Detailed background information is presented in Zaghi and Saiidi (2010).

In this method, the "reference lateral load capacity", H_o, associated with the cracking mechanism in Fig. 2-62 (a) is first estimated. The "upper limit lateral load capacity", H_{cr}, associated with the cracking mechanism in Fig. 2-62 (b) is then obtained under the maximum effective axial load. Finally, the nominal capacity of the hinge is obtained by interpolating between H_o and H_{cr} using the actual level of axial load. The ultimate lateral capacity at the interface accounts for reduction due to the impact resulting from the slippage at the interface between the column and the superstructure after the friction capacity at the interface is exceeded.

The seismic lateral load demand, V_o, is based on the over strength shear associated with the overstrength moment (SDC, Section 4.3). The lateral capacity of the pipe-pin hinge is conservatively determined based on the nominal material properties.

- **Nominal Lateral Load Capacity of Pipe-Pin Hinges**

$$\varphi H_n > V_o + F_{impact} \qquad \varphi = 0.75 \qquad \text{Eq. 2-33}$$

$$H_n = H_o + (H_{cr} - H_o)\left(\frac{N}{N_u}\right)^{0.7} \qquad \text{Eq. 2-34}$$

$$F_{impact} = 1.9\frac{G \times EI}{L_c^{\ 3}} \qquad \text{Eq. 2-35}$$

- **Reference Lateral Load Capacity**

$$H_o = 1.17\sqrt{M_u D_p f_c'} \le \frac{2A_g f_u}{\pi\sqrt{3}} + \begin{cases} 0.93A_{cp}\sqrt{f_c'} & \text{(ksi)} \\ 2.47A_{cp}\sqrt{f_c'} & \text{(MPa)} \end{cases} \qquad \text{Eq. 2-36}$$

$$M_u = 1.45 f_y \left(r_1^3 - r_2^3\right) \qquad \text{Eq. 2-37}$$

- **Upper Limit Lateral Load Capacity**

$$H_{cr} = \begin{cases} \text{Factor 1} \times \left(0.16A_c\sqrt{f_c'} + \dfrac{A_{sp1} f_{ys} d_1}{s_1}\right) + \dfrac{A_{sp2} f_{ys} d_2}{s_2} + \dfrac{1.45M_u}{D_{bearing} + D_p} \text{(ksi)} \\ \text{Factor 1} \times \left(0.4A_c\sqrt{f_c'} + \dfrac{A_{sp1} f_{ys} d_1}{s_1}\right) + \dfrac{A_{sp2} f_{ys} d_2}{s_2} + \dfrac{1.45M_u}{D_{bearing} + D_p} \text{(MPa)} \end{cases} \qquad \text{Eq. 2-38}$$

$$\text{Factor 1} = 0.45\frac{D_{bearing}}{B} + 0.6 \qquad \text{Eq. 2-39}$$

For circular columns: $A_c = \frac{\pi}{4}\left(B^2 - D_p^{\ 2}\right)$ Eq. 2-40

- **Maximum Effective Axial Load**

$$N_u = \begin{cases} \text{Factor 1} \times A_c & \text{(ksi)} \\ 0.007 \times \text{Factor 1} \times A_c & \text{(MPa)} \end{cases} \qquad \text{Eq. 2-41}$$

Note that the effect of concrete inside the pipe is included in Eq. 2-38 through the factor of 1.45, which was obtained from extensive analytical studies (Zaghi and Saiidi 2010). The mechanism associated with Eq. 2-38 is shown in Fig. 2-62 (b). “Factor 1” in Eq. 2-39 is the ratio of diagonal failure plane area in Fig. 2-62 (b) and the gross cross sectional area of the column.

2.4.3.4. Footing Design

The geometry and reinforcement detail of PEFB footing are displayed in Figs. 2-63 and 2-64, respectively. The footing was designed to be sufficiently stiff and strong to minimize footing deformation and damage. The footing reinforcement was designed for the flexure and the dimensions were checked for shear. The length of the footing was 132 in. (3353 mm) and the width was 48 in. (1220 mm). The thickness of the footings was 28.75 in. (730 mm). This thickness was selected so that the bent could be properly connected to the inertial load system. Two round shape openings were designed in the footing to provided space for embedding the columns. However, hexagonal shape openings were formed in the footing for ease of construction. The depth of the opening was 23 in. (584 mm) and was equal 1.50 times of column diameter plus 2 in. (50 mm) gap underneath of column. The hexagonal whole side dimension was 7.5 in. (190 mm), and it provided sufficient space for a 14 in. (355 mm) diameter column plus 1.5 (38 mm) gap around it. The thickness of the footing under the opening was 4.75 in. (120 mm) and it was sufficient to prevent punching shear. The reinforcement consisted of two top and bottom mats of #6 bars with a clear cover of 1.5 in. Vertical #3 cross ties were used in the footing. Four pairs of #6 bars were placed at 45° on the top reinforcing mat to prevent diagonal cracks around the column. Four #10 lift hooks were installed in the footing. In addition, 32 PVC pipes were cast into the footing. These PVC pipes allowed the footing to be securely attached to the shake table.

2.4.3.5. Bent Cap Design

Bent cap was reused from a previous project on studying the behavior of pipe-pin hinges in a two column bent. PEFB was designed to reuse the cap beam. The cap beam consisted of two parts with a load cell in between. Each part of the bent cap was $18 \times 18 \times 62.5$ in. ($457 \times 457 \times 1587$ mm) (Fig. 2-65). The longitudinal reinforcement included 3#5 bars at top and 4#5 at the bottom. Four high strength 1 in (25 mm) diameter all threaded rods were used to post tension the beam segments to the middle load cell and the link swivel head. The total prestressing force was approximately 200 kips (890 kN). This post tensioning force guarantees that the load cell would not separate.

2.4.3.6. Column Embedment Length Design

The column embedment length in the footing was designed so that the full moment capacity of the column can be developed at the top of the footing. The column footing connection is subjected to axial load, shear, and bending moment (Fig. 2-66). The stress distribution can be simplified using the rigid plastic stress theory (Petrold, et al., 2000 a, b) (Fig. 2-67). The concrete stress in the horizontal direction is set to 0.67 f_c' according to numerical results [Petrold, 2000 a, b]. This stress is less than 0.85 f_c' to account for the orientation of the principal stresses not being horizontal.

The round column was replaced with an equivalent square column and b_{eff} was calculated.

$$b_{eff} = \sqrt{\pi}\frac{D}{2} \quad \text{Eq. 2-42}$$

Where

D = Column diameter

Pertold et al., (2000) showed that the embedment length H will fall in the range of two boundaries:

$$b_{eff} \le H \le 2b_{eff} \quad \text{Eq. 2-43}$$

Based on Fig. 2-67, horizontal forces at the top, F_t, and at the bottom, F_b, transmitted from the column to the concrete can be calculated as

$$\begin{aligned} F_t &= 0.8 \times 0.67 f_c' b_{eff} \\ F_b &= 0.8(H-x)0.67 f_c' b_{eff} \end{aligned} \quad \text{Eq. 2-44}$$

Using horizontal equilibrium the position of the neutral axis can be derived as

$$x = \frac{0.93V_{Sd} + 0.5b_{eff} f_c' H}{b_{eff} f_c'} \quad \text{Eq. 2-45}$$

Taking the moments about the bottom of the column, the following equation can be obtained:

$$M_{Sd} + V_{Sd}H + F_b 0.4(H-x) - F_t(H-0.4x) = 0 \quad \text{Eq. 2-46}$$

Combining Eqs. (2-44) to (2-46), the embedded length H of the column can be calculated as:

$$H = \frac{1.56V_{Sd} + \sqrt{4.74V_{sd}^2 + 6.22M_{Sd} f_c' b_{eff}}}{b_{eff} f_c'} \quad \text{Eq. 2-47}$$

Where

V_{sd} = Maximum shear force acting at bottom of the column

M_{sd} = Maximum moment acting at bottom of the column

f_c' = Concrete compressive strength

To design the embedded length, the maximum plastic moment of the section was calculated. Maximum shear force was calculated by dividing the moment by the column height. The concrete compressive strength was assumed to be 5 ksi.

2.4.4. Construction and Assembling

Construction of PEFB included building the steel cages, casting of concrete in the footing and columns, and finally, assembling the bent. The steel cages were built for footing and two columns. Steel pipes were ordered and shipped to the construction site. The steel pipes were filled with concrete and were instrumented with strain gauges (Fig. 2-68). Strain gauges were installed on the longitudinal and transverse bars of RC-ECC column and on longitudinal bars of FRP column where the maximum strain was expected. The FRP tube was also instrumented with strain gauges after bent assembly.

The cap beam was reused from a previous study and, it was cleaned and repaired before using in the specimen. The concrete hinge throat around the steel can was ground from the cap beam and a new throat was cast on top of each column.

Since fitting the new columns and old cap beam was critical, it was decided to cast the concrete in the columns upside down on the top of the cap beam. For this purpose the steel pipes were placed in the steel cans first and were fixed in place. To make sure that the gap between the pipe and the can was even all around, four wooden spacers with a thickness of 0.15 in (3.8 mm) were placed between the can and the pipe. The space around the can was sealed by silicon glue to ensure concrete does not leak into the gap (Fig. 2-68 (b)). The hinge spirals were placed around the steel pipe and fixed (Fig. 2-69). The column cages were placed on the top of the cap beam and were centered and stabilized (Fig. 2-70).

Two hexagonal wooden forms were placed in the footing to shape the openings. Two 0.5 in. (13 mm) diameter PVC pipe were installed between the holes and the side of the footing to bleed the air after casting the grout. Figures 2-71 and 2-72 show the footing before and after concrete casting.

The footing and the upper part of RC-ECC column were filled with concrete at the first cast. The part of RC-ECC column made of ECC was cast second. A local contractor provided the ECC. The dried components of ECC including small aggregate, fly ash, and polyvinyl alcohol fibers were combined before transferring to the construction site. Water was added to the batch and mixed by an electric mortar mixer. The FRP tube and rest of RC-ECC column were cast with concrete as the last step. Casting of concrete in RC-ECC column and FRP tube is shown in Fig. 2-73.

Assembling the bent included inserting the columns in to the footing holes, placing the cap beam, and filling the gap with grout. The columns were detached from cap beam and turned upside down (Fig 2-74). Two wooden pieces, 2 in. (51 mm) thick each, were put under the column in the footing holes to provide the specified gaps. The columns were placed at the center of opening and fixed with four wooden wedges (Fig. 2-75). The cap beam was then placed on the top of the columns, and the gap between the pipe and the can was adjusted. The pipe-pin, before inserting the cap beam, is shown in Fig. 2-76. Figure 2-77 shows the installation of cap beam on the bent.

Finally high strength-fast setting grout was cast and filled the space between the column and the opening of the footing (Fig. 2-78). PEFB after assembling is shown in Fig. 2-79.

2.4.5. Material Properties

2.4.5.1. Concrete

The concrete was ordered with a specified 28-day compressive strength of 5.0 ksi (34.5 MPa). The concrete had a 3/8 in (9.5 mm) maximum aggregate size. The small aggregate size was required because of relatively small pipe size and small cover due to scaling. Table 2-10 lists the test data for the concrete from each cast. It took two cast for PEFB. The footing and a part of RC-ECC column were placed during the first casting of concrete. The second casting of concrete included filling the FRP tube and the rest of the RC-ECC column. Standard 6 x 12 in (150 x 300 mm) cylinders were taken to measure concrete compressive strength at 7 days, 28 days, and at the end of the shake table tests.

The measured compressive strength of concrete is listed in Table 2-10. The measured compressive strength of the concrete for the footing and part of the RC-ECC column at the end of shake table testing was 5.25 ksi (36.2 MPa). The concrete compressive strength for FRP column and RC-ECC column on the test day was measured 5.68 ksi (39.2 MPa).

2.4.5.2. ECC

The plastic hinge of RC-ECC column was made of ECC. ECC was ordered with a specified 28-day compressive strength of 5.0 ksi (34.5 MPa). The ECC mix design was similar to the batch used in SE-2. The mix design properties are explained in section 2.3.6.2. To determine the ECC compressive strength, standard 4 x 8 in (100 x 200 mm) cylinders were taken. Three cylinders were tested at 28 days and the test day for each cast on a SATEC MKIII-C testing machine. The ECC curing process is longer than standard concrete; therefore, the strength was not measures at 7 days. The compressive strength results are listed in Table 2-11. The ECC strength on the test day was 5.61 ksi (38.7 MPa).

2.4.5.3. Steel

Tensile testing was conducted for #3 and #5 bars reinforcement. Bar size #3 was used as longitudinal reinforcement in FRP tube and as transverse reinforcement in RC-ECC column. Three sample bars were tested for each size and subjected to a tensile stress test on a Tinius Olson testing machine. The specimen was designed for a specified yield stress of 60 ksi (414 MPa). The actual average yield stresses of 67 ksi (466 MPa) and 80 (551 MPa) were measured for #3 and # 5 bars, respectively. The measured elastic modulus was approximately 29000 ksi (2e5 MPa). The measured stress-strain curves for # 5 bars are shown in Fig. 2-80. The curves displayed a clear plateau at the yield point and yield stress was determined from this point. The ultimate stress was taken as the maximum stress before bar rupture, and it was 105 ksi (724 MPa) for both bar sizes. The measured stress-strain curves for # 3 bars are shown in Figs. 2-81. The yield and ultimate stresses were 67.7 ksi (466 MPa) and 105.7 ksi (728 MPa), respectively.

2.4.5.4. High Strength-Fast Setting Grout

A high strength, fast-setting grout was used to fill the gap and fix the column base at the opening. The SPEED-E-ROC grout produced by W.R. Meadows was used for this purpose. SPEED-E-ROC is a fluid, rapid setting and hardening, high strength, non-shrink hydraulic cement compound designed for anchoring and grouting. SPEED-E-ROC has an initial set time of 10-20 minutes at 77° F (25° C), and its specified one hour compressive strength is 5 ksi (34.4 MPa). To determine the mortar compressive strength, standard 3 x 6 in (75 x 150 mm) cylinders were taken. Three cylinders were tested each at 7 days, 28 days, and at the end of the shake table tests on a SATEC MKIII-C testing machine. The specified compressive strength based on the technical data sheet was 11.5 ksi (79 MPa) after 28 days. The compressive strength of 6.41 ksi (44.2 MPa) was measured for the grout after 28 days which was still satisfactory for the purpose of project. The test results are listed in Table 2-12.

2.4.5.5. GFRP Tube

The material properties for FRP tube were based on the supplier technical information. The mechanical properties of the FRP tube are provided for temperatures of 75° F (24° C) and 210 ° F (99° C) by the supplier. Table 2-13 summarizes the mechanical properties of the FRP tube, but only the lower temperature is of concerned in structural engineering. Two important values from Table 2-13 are the hoop strength and beam bending strength that are 23 ksi (158.6 MPa) and 34 ksi (234 MPa), respectively. Using the ultimate stress and modulus of elasticity in bending results in a rupture strain of 26500 microstrains.

2.4.6. Instrumentation

To monitor various aspects of the behavior, 171 channels of data were collected during the experiment. A large number of strain gauges, Novotechnik displacement transducers, strain potentiometers, load cells, and accelerometers were installed on the specimen. Details of the strain gauges are presented in Figs. 2-82 and 2-83. Strain gauges were installed at the lower part of the columns on the longitudinal and transverse reinforcement where the maximum strain was expected. The strain was monitored at five levels to help determine the length of plastic hinging and the extent of yielding in the longitudinal bars. A pair of strain gauge was installed on the steel pipes on top of the both columns. Eight strain gauges were placed on the diagonal bars in the footing top mat (Fig. 2-83). To determine the distribution of flexural, hoop, and shear stresses on the FRP tube, it was instrumented with 16 strain gauges. In a previous similar test on GFRP tubes, horizontal and vertical strain gauges failed during early runs due to the fine cracks in the epoxy in FRP tube. To prevent the failure of gauges in the present study, they were installed parallel to the fibers (+/- 55°). The shear strains were measured at two levels on the FRP tube using four rosette strain gauges.

To measure curvatures and bond-slip rotations, eight Novotechnik sensors were attached to the bottom of each column at four levels (Fig. 2-84). Four Novotechniks transducers were also installed at the top of each column, two to measure the relative slip between the bent cap and the column, and two to measure relative rotations. Two strain potentiometers were installed between the cap beam and a reference frame to measure the absolute in-plane displacements the bent cap. Two more were installed between the bent cap and the western wall of the lab to measure any out-of-plane movement. In addition, two displacement sensors were installed between the cap beam and the footing to measure vertical movements of the cap beam. An accelerometer was installed on the cap beam to measure the acceleration histories. The lateral forces were measured using two load cells. One was part of the link assembly and measured the total lateral force including the P-Delta effects generated by the mass rig. The second was a six-DOF load cell that was placed between the two cap beam segments. All the components of the load were recorded in this load cell but only the axial force was of concern. Four load cells were installed on top of the steel vertical load beams to measure the axial loads in the columns. A total of eight high strength rods were used to apply the axial load on the column (four on each column). The load cells were placed on every other axial load rods in a zigzag pattern.

2.4.7. Test Setup

After the bent was assembled the specimen was moved inside of the lab and was centered on the shake table and placed on top of several 1.5 in. (38 mm) thick wooden spacers. Formwork was placed around the footing and grout was placed to a thickness of approximately 2 in. (51 mm). Threaded rods extended through the footing holes and were anchored on the top of the footing to securely attach the footing to the shake table. The threaded rods were stressed to provide 30 kips (133 kN) clamping force between the footing and the shake table. The mass rig system was connected to the head of the specimen via one rigid link. To create an inertial mass of 100 kips (445 kN), four inertial concrete blocks weighing approximately 20 kips (89 kN) each were placed on the top of the mass rig system. The mass rig frame weight was 20 kips (89 kN); therefore, the total inertial mass of the system was approximately 100 kips (356 kN). To provide the specimen with the proper axial load, four steel spreader beams were bolted to the top of the cap beam. In addition, eight hydraulic jacks connected to an accumulator were placed on the top of the spreader beams. Four jacks were used to apply 12.5 kips (55.6 kN) on the bent resulting in 50 kips (222.4 kN) axial load on each column. Finally, a steel link was used to connect the cap beam and the mass rig. The shake table setup is shown in Figs. 2-85 and 2-86.

2.4.8. Input Ground Motion and Loading Protocol

The selected input motions for the specimen were similar to those used in the previous study on the behavior of pipe-pin hinges in a two column bent (Zaghi and Saiidi, 2010).

The earthquake record used in the experiment was the modified version of the motions measured at the Sylmar Converter station during the 1994 Northridge, California earthquake. The Sylmar Converter station is located at 34.3110 Latitude, -118.490 Longitude on a soil layer with V_{s30} of 824.14 ft/s (251.2 m/s) with 13.11 km (8.1 miles) epicenter distance. More information regarding the earthquake and the station is presented in Fig. 2-87. The 142-degree lateral component of the acceleration history was used in the test. The acceleration history of the motion is presented in Fig. 2-88.

The time axis of the acceleration was compressed by a factor of $\sqrt{0.3} = 0.547$ to take the effect of scaling into account.

The bent was subjected to a series of six excitations, from low amplitude to high amplitude (Table 2-14). The scaling factors were 0.1, 0.4, 0.7, 1.0, 1.3, and 1.65 with the corresponding PGA values of 0.091 g, 0.364 g, 0.637 g, 0.91 g, 1.183 g, 1.44 g, and 1.729 g, respectively. To determine the dynamic characteristics of the bent as the level of motions increased, a white noise motion was applied to the specimens after each earthquake motion.

3. EXPERIMENTAL RESULTS AND OBSERVATIONS

3.1. Introduction

This chapter presents the test results for five segmental columns and a two- column bent. The test variable among the segmental columns was the type of construction in the base segment and the segment immediately above the base segment. The PEFB bent consisted of one CFFT (concrete filled FRP tube) column and one conventional concrete column incorporating ECC (engineered cementitious composite) material in the plastic hinge zone. The results include force-displacement hysteresis curves, envelopes of the hysteresis curves, measured strains, strain rates, moment-curvatures graphs, PT (post-tensioning) force in segmental columns, residual displacements, energy dissipation, and other measured data. The measured strain data in segmental columns and the two-column bent are presented in Appendix A.

3.2. Segmental Columns

3.2.1. Presentation of Test Results

The segmental columns had nearly the same geometry, loading protocol, and instrumentation. The approach to process the measured data for the segmental column was similar; therefore, the discussion is presented here for all the columns to prevent repetition.

3.2.1.1. Load-Displacement Response

The accumulated lateral force-displacement hysteresis curves for segmental columns followed by the hysteretic curves for each run are presented in this section. Displacement on the hysteretic curve refers to the top specimen displacement relative to the shake table. Absolute displacement was measured using a transducer attached to a fixed steel frame to the center of the column head. Shake table displacement was recorded using an internal shake table transducer. A positive displacement on the hysteretic curves denotes southward displacement.

The force refers to the lateral force that a specimen resisted at the top of the column, at the center of the loading head. The lateral force was calculated by adding the link load and inertial force of the column. A load cell was placed on the link assembly to record the link load. The inertial force was calculated by multiplying the acceleration at the top of the specimen by mass. One half of the column mass was included in the calculation of the mass. The acceleration was recorded by accelerometer located on the link load assembly.

The average load-deflection envelope for positive and negative direction of displacement was calculated for each column. To determine the effective yield point, each envelope was simplified by an elasto-plastic idealization. This was accomplished by equating the area under the force displacement envelope with that of the idealized model. The elastic slope was computed as the slope of a line passing through the point equal to 50% of ultimate lateral load capacity. The ultimate displacements were the same in the envelope and the idealized model for each column. The idealized force displacement relationships were utilized in determining the displacement ductility capacities.

3.2.1.2. Measured Strains

Strains at various locations in each specimen were recorded using strain gauges. The maximum and the minimum strains in the longitudinal and transverse reinforcement for each run are presented in this section. Positive strains denote tension and negative strains indicate compression. Extra strain gauges were installed on the innovative materials in different specimens. For example there were strain gauges on the elastomeric pad in SBR-1 to measure the deformation of rubber. In SF-2 and SC-2R, strain gauges were installed on the FRP jacket to evaluate the jacket behavior. Strain-displacement hysteresis curves for longitudinal and transverse bars also are provided in this section. The figure on each plot illustrates the location of the strain gauge. The shaded region is where the strain gauge was attached on the cross section and the value in the middle signifies how high the gauge was located with respect to the top of the footing. In all figures, the right side of the column is the north.

The profile of the strain in the longitudinal reinforcement is drawn for each segmental column and bent columns. The average strain at each level was calculated and is shown in the profile. Based on this figure the location of the maximum strain could be identified.

To calculate the force in the PT rod, four strain gauges were placed on the rod in SC-2, SF-2, SE-2 and SC-2R. Strains on the post-tensioning rod were multiplied by E (the modulus of elasticity of the rod) and area of the rod to obtain the force. Strain-displacement hysteresis curves for these strain gauges are presented in this section for each column. Strain gauges were not installed on the PT rod in SBR-1 and the force in the rod was measured only by a load cell.

3.2.1.3. Moment-Curvature Relationships

The curvatures, bond-slip rotations and separation between the segments were measured by ten Novotechnik transducers that were installed on the columns as described in Chapter 2. The rotation was calculated by dividing the difference between the readings of the two opposite transducers at each level by their distance. Each Novotechnik transducer measured changes in length over a gauge length. The gauge length was 7.5 in. (190 mm) for the first pair of transducers from the top of the footing. Other Novotechnik transducers had the gauge length of 7 in. (178 mm).

The curvature peaked at the interface between the base and second segments due to the large segment separation. The average curvature over the length of each segment can be calculated from Eq. 3-1.

$$\phi_i = \frac{\frac{\Delta_{i,1}}{l_{i,1}} - \frac{\Delta_{i,2}}{l_{i,2}}}{x_{i,1} + D + x_{i,2}} \qquad \text{Eq. 3-1}$$

ϕ_i = Average curvature at location i

Δ_{i1}, Δ_{i2} = Measured transducer displacements of location i

l_{i1}, l_{i2} = Gauge lengths of transducers at location i

x_{i1}, x_{i2} = Distances from edge of the column to the transducers at location i

D = Diameter of the column

Moment was computed as the measured lateral force at the centroid of the loading head multiplied by the distance to the midpoint of the relevant gauge length.

The profile of the maximum curvatures between each two levels of Novotechnik transducers was calculated and presented for each column.

3.2.1.4. Energy Dissipation

The dissipated energy was measured by integrating the area enclosed by the force-displacement hysteretic curves. The dissipated energy for each run and total cumulative dissipated energy were calculated and the results are presented in separate tables. It should be noted that the main source of energy dissipation in the segmental columns was the yielding of longitudinal reinforcement connecting the base segment to the footing.

3.2.1.5. Residual Displacement

The residual displacement was taken as the last recorded specimen displacement for each run after all ground motion forces had dissipated. Plots of residual drift ratios versus the target peak ground acceleration (PGA) are presented for each column. Residual drift ratio is defined as residual displacement divided by the height of the column. PGA was the maximum acceleration applied by the shake table. Also the ratio of residual displacement to the maximum displacement for each run was calculated and drawn versus PGA. Residual displacements are particularly important when the column experiences large displacements. Therefore, the ratio of residual displacement to the maximum displacement can show the ability of column to recover large drifts.

In general residual displacements were minimal in all segmental columns due to unbonded post tensioning system. The post-tensioning rod was designed such that the maximum estimated force in the rod would not exceed 70% of the yield strength.

Therefore, the force in the rod was always in elastic region, and after unloading the elongation was fully recovered.

Displacement histories for each column during the test was plotted to show the column response and the residual displacement at the end of each run schematically. These graphs demonstrate that the residual displacement was minimal in all runs except for the last run in some cases where the extensive damage was observed in the columns.

3.2.1.6. Unbonded Post-Tensioning Rod Force

A 1-5/8 in. (40 mm) diameter post-tensioning (PT) rod was used in all segmental columns. The minimum ultimate strength and yield strength for the 1-5/8 in. (40 mm) were 297 kips (1321 kN) and 268 kips (1192 kN), respectively, according to the rod manufacture data sheet. The PT force was recorded by a load cell that was installed under the post-tensioning plate at the top of the column. The post tensioning force was measured as the PT rod was tensioned. The cumulative force-displacement responses of post-tensioning rods were plotted.

To verify the load cell data, the rod strains were also recorded by strain gauges at two locations on each rod. The strains in the rod were multiplied by its modulus of elasticity and its area to convert to the force. The modulus of elasticity for PT rod was 27000 ksi (186160 MPa). The initial post-tensioning force was added to this calculated force. The load cell data and strain gauge data were plotted and compared for each segmental column.

3.2.1.7. Separation between Column Segments

In all of the segmental columns, a gap was formed at the interface between the base and the second segments during high amplitude earthquake runs. The interface between other segments stayed closed during the tests.

Separation between segments was measured by a pair of Novotechnik transducers installed on two opposite faces of the column at level of the interfaces. The magnitude of this opening on the column face was calculated based on similar triangle relationships.

No separation of segments occurred during the earlier runs. During the high amplitude runs, gap formation was the main source of column lateral displacement. The interface between the base and second segments failed due to rocking movement of second segment over the base segment.

The histories of opening between the base and second segments are presented for each column. This opening was due to the rigid body rotation of the second segment about its compression toe and it led to additional top column displacement. To verify the contribution of opening to the total top column displacement, rotation was calculated from transducers data and multiplied by the effective height. A table including the total top column displacement, openings and contribution of opening to the top column displacement was provided for each specimen for each run.

3.2.1.8. Strain Rate

Past research on dynamic load effects on stress-strain relationship in steel reinforcement indicates that the yield stress and the ultimate stress increase at high strain rates; however, the steel modulus of elasticity is not significantly influenced by strain rate (Kulkarni and Shah 1998, Zadeh and Saiidi 2007). Only Zadeh and Saiidi (2007) studied the mechanical properties of reinforcing steel under variable strain rates. Based on Zadeh-Saiidi method, the strain rate of concern was the average rate for strains between one half of yield strain and the yield strain (Zadeh and Saiidi 2007). The strain-rate effect in this method is calculated as follows:

$$\frac{f_y'}{f_y} = \left(\frac{SRI}{10^{-4}}\right)^{\alpha} \qquad \text{Eq. 3-2}$$

$$SRI = K\dot{\varepsilon}_{avg} \qquad \text{Eq. 3-3}$$

$$K = \left(\frac{\dot{\varepsilon}_y}{\dot{\varepsilon}_{0.5y}}\right)^{0.5} \qquad \text{Eq. 3-4}$$

$$\alpha = 0.022\left(\frac{\phi}{\phi_8}\right)^{0.15} - 0.006\left(\frac{f_y}{60}\right) \qquad \text{Eq. 3-5}$$

Where

$f_y,\ f_y'$ = Static and Dynamic Yield Stress, Respectively

$\dot{\varepsilon}_{0.5y}, \dot{\varepsilon}_y \text{ and } \dot{\varepsilon}_{avg}$ = Strain rate at half yield, at yield, and the average strain rate between half yield and yield

$\phi,\ \phi_8$ = Bar diameter and diameter of #8 bar

To calculate the dynamic yield stress, the strain history of the gauge that recorded the first yield strain, and the run corresponded to the first yield were used.

The strain rate factor was also calculated for a range that affects concrete strength. For the concrete, the average strain rate was considered when the strain in the longitudinal bar was approximately 6000 μs (the crushing strain of concrete). The concrete compressive strain rate was determined using the compressive steel bar strain data. This is because it was assumed that perfect bond existed between the bars and the concrete before yielding [Kulkarni et al., 1998]. Equation 3-6 was used based on a study done by Kulkarni et al., (1998).

$$SRF = 0.0222\ln(\dot{\varepsilon}) + 0.9973 \qquad \text{Eq. 3-6}$$

SRF (the strain rate factor) was multiplied by concrete strength and the result was used to determine the properties of the concrete core in the post-test analysis model.

3.2.1.9. Achieved Shake Table Motions

Since the shake tables and the specimens are two separate systems that interact with each other, the achieved shake tables are generally different from the target motions depending on the mass and stiffness of the specimens. The software that drives the shake table, adjusts the motions during testing to compensate for the response of the payload on the tables. However, because of the nonlinearity of the test models, the compensation does not always lead to close match between the target and achieved shake table motions. The input ground acceleration was factored by 0.1 to 1.5 in 0.25 increments, which led to total number of seven runs. In SF-2 and SE-2 the last run was repeated, and a total of eight runs were applied. The time coordinate of the input acceleration was compressed by a factor of $\sqrt{0.33} = 0.577$ to account for the scale of the test model that was 0.33.

The pseudo acceleration spectra were compared for the target and achieved motion to determine the effect of deviation between this two. The measured natural period of the structure after each run was indicated by a dashed line to identify the periods that were of concern. The period was calculated using the Fourier spectra for the applied white noise after each run. The maximum Fourier amplitude corresponds to the period of column. SeismoSignal version 3.3.0 software was used for Fourier analysis. In general, there was an acceptable match between the target and achieved table motions at fundamental periods.

Damping ratio was also calculated based on half-power bandwidth method for all segmental columns using the response of columns to the white noise motions applied before the first subsequent run and after each run [Chopra, 2006].

The pseudo acceleration spectra, periods, and damping ratios are presented for each segmental column in subsequent sections.

3.2.2. SC-2

3.2.2.1. General Observations

The photographs showing the damage progression in the column from Run 1 to 7 are shown in Figs. 3-1 through 3-4, respectively. No damage was observed during Runs 1 and 2 (Fig. 3-1). Minor cracks were visible at the border of the base and second segments during Run 3 (Fig. 3-2 (a)) with the maximum drift ratio of 2%. The first yielding of the bar occurred in the extreme longitudinal bar at 5 in. (127 mm) above the footing during this run. The cover concrete flaked off on the north side of the column during Run 4 (Fig. 3-2 (c)) that corresponded to drift ratio of 2.8%. During Run 5, cover concrete spalled and spirals were visible on the south and north faces of the base segment (Fig. 3-3 (a) and (b)). Concrete spalling extended to the second segment after Run 6 (drift of 6.3%) due to rigid body rotation of the second segment about its compression toe (Fig. 3-3 (c) and (d)). During the last run extensive damage in the core and cover was observed on both sides of the base and second segments (Fig. 3-4 (a) and (b)). Run 7 was considered to be the failure run because of significant drop in the column lateral load capacity. Virtually no damage was seen on the upper two-thirds of the column during the entire testing. As expected for a cantilever member, extensive damage was localized in the plastic hinge region. The apparent core damage in the plastic hinge was minimal.

3.2.2.2. Load-Displacement Response

Lateral force-displacement hysteresis curves for SC-2 are shown in Fig. 3-5. The force-displacement results for each run are shown in Figs. 3-6 through 3-12.

SC-2 showed elastic behavior during Runs 1 and 2. Yielding occurred in the extreme bars at north face of column, 5 in. (127 mm) above the footing during Run 3. During the post-yielding phase, the column showed asymmetric behavior since the input motion (the Sylmar ground motion) was not symmetric. The peak forces and displacements for each run in SC-2 are listed in Table 3-1.

The maximum force of 23.3 kips (103.6kN) occurred during Run 5 that was corresponded to drift ratio of 4.9%. The maximum displacement of 8.42 in. (214 mm) (11.7% Drift) was recorded during Run 7. The maximum lateral load was dropped by approximately 15 percent during this run and it was 19.8 kips (88kN).

The average load-deflection envelope for the positive and negative direction of displacement is shown in Fig. 3-13. The lateral load capacity dropped by 7% after displacement of 3 in. (76 mm) corresponding to drift ratio of 4.2 %. There was not a sudden drop in the lateral load capacity and the capacity gradually decreases until ultimate displacement.

3.2.2.3. Measured Strains

The accumulated strain-displacement response for longitudinal bars, transverse bars, and PT rod are displayed in Appendix A (Fig. A-1 through A-15). The strains were larger in the longitudinal bars located at the bottom of the base segment. The strains in transverse bars were small and well below yielding. Strains in the PT rod were converted to the force and the results are presented in section 3.2.2.7. The longitudinal bars strains in other segments were small due to the short length of the bars.

Figure 3-14 presents the maximum strain profile along the column height. This figure demonstrates that the maximum strain occurred at the height of 14 in. (356 mm) from top of the footing.

The maximum and the minimum strains for each run at different locations are presented in Table A-1. Some strain gauges damaged or slipped during the test, therefore their data was not shown. Strain gauges that did not function at the beginning of the test are listed in Table A-1, but their data are not included. The yield strain in longitudinal bars was

2207 μs based on the material test report, and it occurred in strain gauge 18 during Run 3 for the first time (Fig. A-5 a). The maximum strain of 16000 μs was recorded during Run 7 in strain gauge 32 (Fig. A-8 b).

3.2.2.4. Moment-Curvature Relationships

The moment-curvature relationships for specimen SC-2 are presented in Figs. 3-15 through 3-19. The maximum curvature occurred 20 in. (508mm) above the footing at the interface between the base and second segments (Fig. 3-16). Separation between the base and second segments was followed by rotation of the second segment about its compression toe and it produced this large curvature. The curvatures were negligible at other levels of column. This demonstrates that the interface between other segments stayed close.

The profile of the maximum curvature that occurred between each two levels of Novotechniks is presented in Fig. 3-20 for all runs. The maximum curvature in this graph shows that the opening was at 20 in. (508 mm) above the footing where the first gap was formed between the base and second segments.

3.2.2.5. Energy Dissipation

The dissipated energy in SC-2 was determined by integrating the area enclosed by the force displacement hysteretic curves. Energy dissipation in SC-2 was 539 kip-in. (60895 kN-mm). Table 3-2 lists the dissipated energy for each run and the total cumulative dissipated energy. The main source of energy dissipation in column SC-2 was yielding of the bars placed at the base segment and plastic straining of concrete near the top of the segment.

3.2.2.6. Residual Displacement

Minimal residual displacements were observed after each run in column SC-2 due to incorporation of unbonded post-tensioning system. Figure 3-21 displays the residual drift ratio versus PGA (peak ground acceleration) for all runs in SC-2. The maximum residual drift ratio was observed in the last run (1.5 × Sylmar) corresponding to a residual drift ratio of 0.38% and was negligible. Minimizing residual displacements is essential when the structural element is under high ground motion amplitudes causing large displacements. To study the recentering ability of the column, the ratio of residual displacement to the maximum displacement at each run was plotted against the PGA in Fig. 3-22. The ratio of residual displacement to the maximum displacement was small in all runs and demonstrated the successful performance of unbonded post-tensioning system in minimizing the permanent displacement of the column.

Displacement history for SC-2 is shown in Fig. 3-23. This figure shows the minimal residual displacement of the column at the end of each run.

3.2.2.7. Post-Tensioning Rod Forces and Gravity Loads

Figure 3-24 displays accumulated PT rod force versus column displacement. This force was recorded by the load cell located on the top of the column head. The force in the rod increased by 116% of the initial force due to column displacement, but it remained under the yielding force. The initial post-tensioning force was 95 kips (422.5 kN). The force in the rod reached the maximum value of 206 kips (916.3 kN) at displacement of 8.4 in. (214 mm) during Run 7. This force was approximately 77% of the ultimate strength of the PT rod. Table 3-3 lists the maximum PT force and the corresponding displacement for each run. The force in the PT rod dropped to 70.8 kips (315 kN) at the end of last run (1.5 × Sylmar). The drop in the force is attributed to the loss of column cross section caused by spalling of concrete.

It was explained in section 3.2.1.3 that the strain in the rod was measured by four gauges during the test. Three out of four strain gauges remained operational and showed nearly the same data. Strain gauge 62 was used to calculate the PT force (Fig, A-15 b). The strains were converted to force and the data were compared with the measured data by the load cell. This comparison is presented in Fig. 3-25. It can be seen that the correlation between this two data sets was very good.

The history of gravity load in SC-2 is showed in Fig. 3-26. The target axial load on SC-2 was 80 kips (355.8 kN). The gravity load was fluctuated between the maximum value of 85 kips (378 kN) and the minimum value of 78 kips (345 kN) due to column displacement. The gravity load was adjusted during the test by two hydraulic jacks to prevent the load fluctuations.

3.2.2.8. Separation between Column Segments

The opening histories at the interface between the base and second segments on the south and north sides of the column are presented in Figs. 3-27 and 3-28, respectively. The first separation between the segments was measured during Run 3. Negative values that reflect concrete spalling at the interface were observed during Run 5 and reached the maximum values at last run where the damage was extensive on both sides of the interface. The maximum opening at the south and north sides of the column were approximately 1 in. (25 mm) and 1.6 in. (40 mm), respectively.

The maximum displacement of the column and contribution of the opening to the total displacement are listed in Table 3-4. The calculation method for contribution of opening to the total displacement is described in section 3.2.1.7. The average contribution of opening to total column displacement for all runs was 45% and the rest was due to the base segment plastic hinge deformation.

3.2.2.9. Strain Rate

The measured strains in gauge 18 during Run 3 and gauge 31 during Run 4 were used to calculate strain rate effect in steel and concrete, respectively. Figure 3-29 shows the strain rate versus the strain for these strain gauges. The strain rate corresponding to yield strain of 2207 μs and half of yield strain were considered in calculation of strain rate effect on steel properties. The ratio of 1.07 was calculated for dynamic yield stress to static yield stress. The strain rate corresponding to strain of 6000 μs (crushing strain of concrete) was used to calculate the strain rate effect in concrete. The strain rate factor was 1.2 for concrete in SC-2.

3.2.2.10. Achieved Shake Table Motions

The comparison of the target and achieved pseudo acceleration spectra for the target motions is presented in Figs. 3-30 through 3-36 for Runs 1 to 7, respectively. The measured natural period of the structure after each run is indicated by the dashed line to identify the period that were of concern.

The period of the column was calculated based on the measured data under white noise motion after each run. As expected the period of the column increased at higher amplitude runs due to a reduction in stiffness of the column caused by damage. The achieved motions were larger than target motions during the last three runs at periods less than 0.7 second.

The column damping ratios was calculated based on half-power bandwidth method and are listed in Table 3-5 for each run. The measured data from the white noise motions after each run were used to calculate the damping ratios. The maximum damping ratio was measured after Run 6 and it was 6.9%.

3.2.3. SBR-1

3.2.3.1. General Observations

Damage progression photographs for column SBR-1 are shown in Figs. 3-37 through 3-40 during Runs 1 to 7. The first horizontal cracks were observed during Run 3 on the south face of the column at the interface of the base and second segments (Fig. 3-38 (b)). The cracks were extended during Run 4 (Fig 3-38 (c)). The spalling of cover concrete started during Run 5 near the top of the base segment corresponding to drift ratio of 4.8% (Fig. 3-39 (a)). Concrete failure was attributed to the separation and rocking action of the second segment over the base segment. During Run 6 (drift ratio 6.9%), both side of the first concrete segment lost their cover (Fig. 3-39 (c) and (d)). The bottom part of the second segment on the south face lost the cover due to the large impact from opening-closing action at the interface. During Run 7 (1.5 × Sylmar), the cover concrete spalled in the second segment, and concrete damage extended to the core in the base segment. The maximum drift ratio was 14% during this run. Figures 3-40 (a) and (b) show the extension of damage after this run.

Concrete spalling at the interface between the first and the second segments was the main failure in SBR-1. The plastic hinge zone made out of elastomeric pad was free from damage (Fig. 3-40). Steel bars passing through elastomeric bearing pad yielded but not buckled. The first yielding of the longitudinal bars occurred in compression during Run 1, at 3 in. (76 mm) below the footing surface. The stresses in the bars in other segments were low; therefore, no yielding or buckling occurred. By the end of Run 6 the residual displacement was minimal, indicating that the unbonded post-tensioning rod performed well in recovering of the column drift.

Virtually no damage was seen on the upper two-thirds of the column during the entire test. The elastomeric bearing pad in SBR-1 was free from damage, and the damage was localized to the interface between the first and the second segments.

3.2.3.2. Load-Displacement Response

Accumulated force-displacement hysteresis curves for specimen SBR-1 is displayed in Fig. 3-41. The force-displacement results are shown in Figs. 3-42 through 3-48. The behavior of SBR-1 was elastic during the first two runs. Yielding occurred in the extreme bars at the north face of column, 10 in. (254 mm) above the footing during Run 2. SBR-1 force-displacement response was not symmetric due to asymmetric input motion. Table 3-6 lists peak forces and displacements for each run in SBR-1.

Figure 3-49 shows the average force-displacement envelope for the negative and positive directions of displacement in SBR-1. The maximum lateral force and displacement were recorded during Run 7. The maximum lateral force was 26.5 kips (117.8kN), and the maximum displacement was 10.12 in. (257-mm) corresponding to drift ratio of 14%. As shown in Fig. 3-49, the lateral load capacity did not drop in SBR-1.

3.2.3.3. Measured Strains

The accumulated strain-displacement response for longitudinal, transverse bars, rubber pad, and central steel pipe of bearing are displayed in Appendix A, Figs. A-16 through A-29. The strains were larger in longitudinal bars located at the bottom of base segment. Negligible strain was measured in transverse bars. The maximum strain of 2500 µs was measured just at one location in transverse bars, and the strains in other transverse reinforcements were well below the yielding.

Figure 3-50 presents the strain profile along the column height. This figure demonstrates that the maximum strain occurred at the height of 10 in. (254 mm) above the footing. This location was immediately above the elastomeric pad where the steel bars were bonded with concrete; therefore, the local strain was larger.

The maximum and the minimum strains for each run at different locations are presented in Table A-6. Strain gauges that did not function are listed in Table A-6 but their data are not presented. The measured yield strain was 2630 µs for #5 bars. During run 1 strain gauge 12 recorded a strain that exceeded the yield value. (Fig. A-18 d). The maximum strain of 9700 µs was measured during Run 7, at 10 in. (254 mm) above the footing, and it was approximately 4 times the yielding.

3.2.3.4. Moment-Curvature Relationships

Accumulated moment curvature results for column SBR-1 are presented in Figs. 3-51 through 3-57. The transducers plan is shown in Fig. 2-32.

The maximum curvature occurred 20 in. (508mm) above the footing at interface between the base and second segments (Fig. 3-52). Rigid body rotation of the second segment over the base segment produced this large curvature. The curvatures were negligible at other levels of column, indicating that the segment separation did not occur between other segments and the column segments above the first gap showed a rigid behavior.

The profile of the maximum curvature between each two levels of Novotechnik transducers is presented in Fig. 3-58 for all the runs. This figure showed that the maximum curvature was measured at 20 in. (508 mm) above the footing at the top of the base segment.

3.2.3.5. Energy Dissipation

Energy in SBR-1 dissipated mostly through the rotation of elastomeric bearing and yielding of the longitudinal bars in the base segment. The total dissipated energy in SBR-1 was 616 kip-in. (69638 kN-mm), 56% of which was due to rotation of elastomeric bearing and the rest was through the yielding of the bars. Energy dissipation due to the rotation of bearing was calculated by integrating the area enclosed by moment-rotation hysteresis graph. The rotation of elastomeric bearing was measured by Novotechnik transducers installed at the top of elastomeric bearing. Figure 3-59 shows the accumulated moment rotation relationship at the elastomeric bearing. Equation 3-7 was used to calculate rotation from the transducers data.

$$\theta = \frac{(x_2 - x_1)}{(D + a_1 + a_2)} \qquad \text{Eq. 3-7}$$

$x_1, x_2 =$ Transducers data at two opposite faces of the column

$a_1, a_2 =$ Distances between transducers and column faces on opposite sides

$D =$ Column diameter

Table 3-7 lists the dissipated energy for each run and total cumulative dissipated energy.

3.2.3.6. Residual Displacement

The residual displacements of SBR-1 were minimal in all runs except Run 7 during which the column was severely damaged near the top of the base segment. Figure 3-60 displays residual drift ratios versus PGA during the test. It can be seen in the figure that the residual drift ratios were negligible during Run 1 through Run 6. The maximum residual displacement of 2.1 in. (53 mm) was observed after Run 7 because of severe damage at the interface between the base and the adjacent segments.

The ratios of residual over the maximum displacements versus the PGA are plotted in Fig. 3-61. It can be seen that the ratios were relatively small and indicate that the

SBR-1 could recover most of the drift. Using the unbonded PT system in the column was the main source for minimizing the displacement.

The displacement history for all the runs is displayed in Fig. 3-62. This figure shows that the maximum displacements gradually increased in subsequent runs and that the residual displacement was very small until the last run.

3.2.3.7. Unbonded Post-Tensioning Rod Force and Gravity Loads

The initial PT force in SBR-1 was 97 kips (431.4 kN), and it reached the maximum axial load of 199 kips (885.1 kN) during Run 7, which was corresponded to a 105% increase in initial force. The maximum force was 67% of the ultimate strength of the rod, and it was under yield load. The accumulated tendon axial force versus displacement for all runs is displayed in Fig. 3-63. Table 3-8 presents the maximum axial load in the PT rod and its corresponding drift during each run. The ultimate PT force dropped to 48 kips (213 kN) after the last run that was attributed to the loss of column cross section caused by spalling of concrete.

The history of gravity load in SBR-1 is showed in Fig. 3-64. The target axial load on SBR-1 was 80 kips (355.8 kN). The gravity load was fluctuated between the maximum value of 80.5 kips (358 kN) and the minimum value of 77.5 kips (344.7 kN) due to column displacement. The gravity load was adjusted during the test by two hydraulic jacks to prevent the load fluctuations.

3.2.3.8. Separation between Column Segments

The opening histories at the interface between the base and second segments on the north and south sides of SBR-1 are displayed in Figs. 3-65 and 3-66, respectively. The first separation between the first two segments was measured during Run 3 on the south side of the column. The negative values in the graph indicating concrete spalling occurred during Runs 5 and 6 on the north and south sides of column, respectively. The maximum opening of 1 in. (25 mm) occurred during the last run on the north face of the column. The contribution of opening to the total column displacement was calculated and presented in Table 3-9. This table shows that approximately 50% of the total displacement at the last three runs was due to the segments separation, and the rest was because of plastic hinge rotation.

3.2.3.9. Strain Rate

The measured strains in gauge 12 during Run 3 and Run 4 were used to calculate strain rate effect in steel and concrete, respectively. Figure 3-67 shows the strain rate versus the strain for these strain gauges. The strain rate corresponding to yield strain of 2630 μs and half of yield strain were considered in calculation of strain rate effect on steel properties. The ratio of 1.06 was calculated for dynamic yield stress to static yield stress. The strain rate corresponding to strain of 6000 μs (crushing strain of concrete) was used to calculate the strain rate effect in concrete. The strain rate factor was 1.3 for concrete in SBR-1.

3.2.3.10. Achieved Shake Table Motions

The comparison of the target and achieved pseudo acceleration spectra of the target motions are presented in Figs. 3-68 through 3-74 for Runs 1 to 7, respectively. The measured natural period of the structure after each run is indicated by the dashed line to identify the periods that were of concern.

The period of the column was calculated based on the applied white noise after each run. As expected the period of the column increased at higher amplitude runs due to a reduction in stiffness of the column caused by damage. Achieved peak acceleration was larger than target in all runs especially during Run 3 where the achieved acceleration was 32% larger than target.

The column damping ratios was calculated based on half-power bandwidth method and are listed in Table 3-10 for each run. The measured data from the white noise motions after each run were used to calculate the damping ratios. The maximum damping ratio was measured after Run 4, and it was 7%.

3.2.4. SF-2

3.2.4.1. General Observations

The photographs showing the damage progression in SF-2 are presented in Figs. 3-75 through 3-78 for all runs. SF-2 showed the least damage amongst segmental columns. No damage was observed up to Run 7 (1.5 × Sylmar). The gray area seen between the base segment and the second segment is due to extra epoxy adhesive that came out from interfaces after the post-tensioning. The first separation between the base and second segments was observed during Run 6 corresponding to drift ratio of 5.9%. Rupture of FRP was observed on the south side of the column during Run 7 near the top of the base segment (Fig. 3-78 (a) and (b)). Core spalling and extensive FRP rupture around the column were observed during Run 8 (Fig. 3-78 (c) and (d)). Steel reinforcement at the base segment yielded during Run 2, at 5 in. (127 mm) above footing. No rupture or buckling of the bars was observed during the test. Figure 3-78 displays the extent of the damage after the last two runs. The lateral load capacity of the column did not drop until Run 7; therefore it was decided to repeat the last run to reach the failure of the column. The residual displacement was minimal by the end of the test that indicated good drift recovery of the column due to the incorporation of unbonded post-tensioning system.

3.2.4.2. Load-Displacement Response

The accumulated force-displacement hysteresis curves for SF-2 are shown in Fig. 3-79. The force-displacement results for each run are shown in Figs. 3-80 through 3-87. Force-displacement response of SF-2 was elastic during Runs 1 and 2. The specimen showed a nearly symmetric force displacement response up to Run 7. The peak forces and displacements for each run are listed in Table 3-11. The maximum force of 30.3 kips

(134.6 kN) was recorded in SF-2 during Run 6 corresponding to drift ratio of 5.9%. The maximum displacement of 14.94 in. (379-mm) (15% Drift) was observed during Run 8. The maximum lateral load capacity dropped by 12% during Run 8 to 26.6 kips (118.3 kN). SF-2 displayed the largest lateral load capacity among the segmental columns due to its minimal damage.

The average load deflection envelope for the positive and negative displacements is shown in Fig. 3-88. No sudden drop in the lateral load capacity was observed in SF-2. The drop in the lateral load capacity occurred at displacement of 5.2 in. (132 mm) corresponding to a drift ratio of 7.2 % during Run 8.

3.2.4.3. Measured Strains

The accumulated strain-displacement response for longitudinal bars, transverse bars, PT rod, and FRP jacket are displayed in Appendix A (Figs. A-30 through A-47). The strains were larger in the longitudinal bars located at the bottom of base segment. Negligible strains were measured in transverse bars and typical upper segments longitudinal bars. The maximum strain in the transverse bars was 124 µs which was well below yielding. Strains in the PT rod were converted to a force, and the results are discussed in section 3.2.4.7.

Figure 3-89 presents the strain profile along the column height. In this graph, the tensile strains are positive and compressive strains are negative. This figure demonstrates that the maximum strain occurred near the top of the footing (level 0 (Fig. 2-42)).

Residual tensile strains were measured in the strain gauges at 14 in. (355 mm) above the footing (Figs. A-36 d and A-37). The maximum and minimum strains for each run at different locations are presented in Table A-4. Strain gauges that did not function at the beginning of the test are listed in Table A-4, but their data are not included. The measured yield strain in longitudinal bars was 2207 µs, and it was reached during Run 2 in strain gauge 21 (Fig. A-35 (a)). The maximum compressive strain of 20000 µs was recorded during Run 8 in strain gauge 33 (Fig. A- 37 (d)).

3.2.4.4. Moment-Curvature Relationships

The moment-curvature results for specimen SF-2 are presented in Figs. 3-90 through 3-94. The maximum curvature occurred 20 in. (508mm) above the footing at interface between the base and the second segments (Fig. 3-91). Rigid body rotation of second segment about its compression toe produced this large curvature. The profile of the maximum measured curvature is presented in Fig. 3-95 for all runs. The maximum curvature was at 20 in. (508 mm) above the footing where the opening occurred between the base and second segment. The minimal curvatures in upper levels indicate that no separation occurred between other segments, and column segments deformed rigidly.

3.2.4.5. Energy Dissipation

The dissipated energy in SF-2 was determined by integrating the area enclosed by the force displacement hysteretic curves. Energy dissipation in SF-2 was the largest among segmental columns with advanced materials. Energy dissipation in SF-2 was 788.4 kip-in. (89072 kN-mm). The main source of energy dissipation in SF-2 was yielding of the bars in the base segment and plastic straining of concrete near the top of the segment. Concrete spalling due to segment separation was minor in SF-2 compared to other segmental columns. The minimal spalling of concrete allowed for more extensive yielding of the longitudinal bars and higher energy dissipation. Table 3-12 lists the dissipated energy for each run, and the total cumulative dissipated energy for SF-2.

3.2.4.6. Residual Displacement

Minimal residual displacements were recorded after each run in column SF-2 due to incorporation of unbonded post-tensioning system. Figure 3-96 displays the residual drift ratio versus PGA for all runs in SF-2. The maximum residual drift ratio was observed after Run 8 (1.5 × Sylmar) corresponding to a residual drift ratio of 0.6% and was negligible. To study the recentering ability of the column, the ratio of residual displacement over the maximum displacement for each run was plotted against the PGA in Fig.3-97. This ratio was small in all runs, and it demonstrated the successful performance of unbonded post-tensioning system in minimizing permanent displacement of the column.

The displacement history for SF-2 is shown in Fig. 3-98. This figure shows increasing maximum displacements in successive runs and minimal residual displacement of the column at the end of each run.

3.2.4.7. Unbonded Post-Tensioning Rod Force and Gravity Loads

Figure 3-99 displays cumulative axial PT rod force versus column displacement. The maximum axial force of 258.8 kips (1151.1 kN) was measured in the PT rod at displacement of 10.7 in (273 mm) during Run 8. This force was measured by the load cell on the top of the column. The peak force was less than the yield force and was 87% of ultimate strength of the rod. The initial force in the rod dropped from 100 kips (444.8kN) before Run 1 to 50.3 kips (223.7kN) after Run 8. The drop in the force is attributed to the loss of column cross section caused by spalling of concrete. The maximum PT rod forces and the maximum displacements for each run are presented in Table 3-13.

It was explained in section 3.2.1.3 that the strain in the rod was measured by four gauges during the test. The strains were converted to force, and the data were compared with the measured data by the load cell. Figure 3-100 compares the recorded axial load by the load cell with the load calculated from strain gauges data. It can be seen that the correlation between this two data sets was very good.

The history of gravity load in SF-2 is showed in Fig. 3-101. The target axial load on SF-2 was 80 kips (355.8 kN). The gravity load was fluctuated between the maximum value of 84 kips (373.6 kN) and the minimum value of 77 kips (342.5 kN) due to column displacement. The gravity load was adjusted during the test by two hydraulic jacks to prevent the load fluctuations.

3.2.4.8. Separation between Column Segments

Figure 3-102 and Figure 3-103 show the history of separation between the base and second segments on the north and south sides of the column, respectively. Opening between the segments are indicated with positive values in the graphs. The first segment separation was measured during Run 3. The negative values in the graph indicate the concrete spalling, and they were recorded starting in Run 3 although they were not visible until Run 7. Rupture of FRP fibers was observed during Runs 7 and 8 near the top of the base segment due to the large impact from the opening-closing action. The maximum opening of 1.7 in (42 mm) was measured on the south side of the column during Run 8.

The maximum displacement of the column and contribution of the opening to the total displacement are listed in Table 3-14. The method for calculating the contribution of opening to the total displacement is described in section 3.2.1.7. The contribution of opening in total displacement was relatively small in early runs and increased during the high amplitude motions. The average contribution of opening to the total column displacement for all the runs was 50%, and the rest was due to the base segment plastic hinge deformation.

3.2.4.9. Strain Rate

The measured strains in gauge 21 during Run 3 and gauge 33 during Run 4 were used to calculate strain rate effect in steel and concrete, respectively. Figure 3-104 shows the strain rate versus the strain for these strain gauges. The strain rate corresponding to yield strain of 2207 μs and half of yield strain were considered in calculation of strain rate effect on steel properties. The ratio of 1.07 was calculated for dynamic yield stress to static yield stress. The strain rate corresponding to strain of 6000 μs (crushing strain of concrete) was used to calculate the strain rate effect in concrete. The strain rate factor was 1.22 for concrete in SF-2.

3.2.4.10. Achieved Shake Table Motions

The comparison of the target and achieved pseudo acceleration spectra of the target motions is presented in Figs. 3-105 through 3-112 for Runs 1 to 8, respectively. The measured natural period of the structure after each run is indicated by the dashed line.

The period of the column was calculated based on the white noise test after each run. As expected the period of the column increased at higher amplitude runs due to a reduction in stiffness of the column caused by damage. The achieved peak accelerations were larger than the target accelerations but in general the correlation between the target and achieved motions was acceptable.

The column damping ratios were calculated based on half-power bandwidth method and are listed in Table 3-15 for each run. The measured data from the white noise motions after each run were used to calculate the damping ratios. The maximum damping ratio was measured after Run 6, and it was 4.2%.

3.2.5. SE-2

3.2.5.1. General Observations

The photographs showing the damage progression in the column from Run 1 to Run 8 are shown in Figs. 3-113 through 3-116. The first separation between the base and second segments was observed during Run 3. The first yielding occurred in the extreme longitudinal bar near the top of the footing during this run. A piece of ECC cover flaked off on the north side of the second segment during Run 4 (Fig. 3-114 (c)). Figure 3-115 (c) and (d) show the column after Run 6 where the cover spalling extended to near the top of the base segment and the lower of the second segment. During Run 8 some headed bars were exposed in the base segment but no buckling or rupture of bars were observed (Fig. 3-115). The lateral load capacity did not drop up to Run 8. The test was stopped since the load cell measuring the PT rod force reached its maximum capacity. Virtually no damage was seen in the upper two-thirds of the column during the entire test sequence and most of the damage was localized to the interface of base and second segments. The SE-2 failure scenario was similar to that of SC-2 (reference column), but the extension of damage was significantly less.

3.2.5.2. Load-Displacement Response

The accumulated force-displacement hysteresis curves for SE-2 are displayed in Fig. 3-117. The force-displacement results for each run are shown in Figs. 3-118 through 3-125. SE-2 showed elastic behavior during Runs 1 and 2. Asymmetric response of SE-2 was biased in the positive direction from Run 3 to Run 6. Due to softness of column during Run 7 and Run 8, the maximum displacements occurred in the negative direction (Figs. 3-124 and 3-125). The peak forces and displacements for each run in SE-2 are listed in Table 3-16.

The average load-deflection envelope for the positive and negative directions of displacement is shown in Fig. 3-126. No drop in the lateral load capacity was observed in SE-2. The maximum force of 22-kips (97.8-kN) was recorded during Run 6. A displacement of 3.6 in. (91.7mm), corresponding to 5% drift ratio, was recorded during this run. The maximum displacement occurred during Run 7 and it was 7.7 in. (195 mm) corresponding to a drift ratio of 10.7%.

SE-2 and SC-2 (reference column) had approximately the same lateral load capacity, but the SE-2 was able to maintain its capacity because ECC experienced substantially less damage than conventional concrete.

3.2.5.3. Measured Strains

The accumulated strain-displacement response for the longitudinal bars, transverse bars, and PT rod are displayed in Appendix A (Figs. A-48 through A-62). The strains were larger in the longitudinal bars located at the bottom of base segment. Negligible strain was observed in the transverse bars. The maximum strain in the transverse reinforcement was 190 μs, which was well below the yield strain.

Figure 3-127 presents the strain profile along the column height. This figure demonstrates that the maximum strain occurred near the top of the footing (Level 0) (Fig. 2-49).

The maximum and the minimum strains for each run at different locations are presented in Table A-5. Strain gauges that did not function at the beginning of the test are listed in Table A-5, but their data are not included. The yield strain in the longitudinal bars was 2207 μs based on the material test report, and it was reached during Run 3 in strain gauge 13 (Fig. A- 51 a). The maximum compressive strain of 4440 μs was recorded during Run 8 in strain gauge 38 (Fig. A-57 (a)).

3.2.5.4. Moments-Curvature Relationships

The moment-curvature relationships for SE-2 are presented in Figs. 3-128 through 3-132. Figure 3-128 shows the curvature due to the yielding of the longitudinal bars in the base segment. The moment–curvature curve was linear at this level, and it demonstrates that longitudinal bars did not yield extensively.

The maximum curvature occurred 20 in. (508mm) above the footing at interface between the base and second segments (Fig. 3-129). The separation between the base and the second segments and rotation of second segment about its compression toe produced this large curvature. The curvatures were negligible at other levels of the column, which indicates that there was no separation at other interfaces.

The profile of the maximum curvatures is presented in Fig. 3-133 for all runs. The maximum curvature in this graph shows that the opening was at 20 in. (508 mm) above the footing where the first gap was formed between the base and second segments.

3.2.5.5. Energy Dissipation

The dissipated energy in SE-2 was determined by integrating the area enclosed by the force displacement hysteretic curves. Energy Dissipation in SE-2 was 637.4 kip-in. (72013 kN-mm). Although the lateral load capacity was about the same in SE-2 and SC-2 (reference column), the dissipated energy was 18% larger in SE-2. The ductile behavior of ECC and minor damage in SE-2 are believed to have increased the energy dissipation in SE-2. Table 3-17 lists the dissipated energy for each run and the total cumulative dissipated energy for column SE-2. The main source of energy dissipation in SE-2 was yielding of the bars placed at the base segment and the deformation of ECC near the top of the segment.

3.2.5.6. Residual Displacement

Minimal residual displacements were observed after each run in column SE-2 due to incorporation of unbonded post-tensioning rod. Figure 3-134 displays the residual drift ratio versus PGA (peak ground acceleration) for all the runs in SE-2. The maximum residual drift ratio of 1% was observed after Run 7 (1.5 × Sylmar) and was negligible. To study the recentering ability of the column, the ratio of residual displacement to the maximum displacement after each run was plotted against the PGA in Fig. 3-135. The ratio of residual displacement to the maximum displacement was small in all runs and demonstrated the successful performance of unbonded post-tensioning system in minimizing the permanent displacement of the column.

The displacement history of SE-2 is shown in Fig. 3-136. This figure demonstrates that the minimal residual displacement of the column at the end of runs. An average residual displacement of 0.6 in. (15 mm) was observed at the end of Runs 6 to 8, which was small compared to that of the conventional concrete column.

3.2.5.7. Unbonded Post-Tensioning Rod Force and Gravity Loads

Figure 3-137 displays accumulated PT rod force versus column displacement. This force was recorded by the load cell located on the top of the column head. The maximum axial force of 205.4 kips (913.6kN) was recorded during Run 8 at displacement of 7.7 in. (195 mm). The PT rod was elastic and did not yield. The maximum force in the rod was 69% of ultimate strength capacity. Table 3-18 displays the maximum PT force and the corresponding displacement for each run. The force in the PT rod dropped to 53 kips (2355 kN) at the end of the last run (1.5 × Sylmar). The drop in the force is attributed to the loss of column cross section caused by spalling of ECC.

It was explained in section 3.2.1.3 that the strain in the rod was measured by four gauges during the test. The strains were converted to force and the data were compared with the measured data by the load cell. This comparison is presented in Fig. 3-138. It can be seen that the correlation between this two data sets was very good.

The history of gravity load in SE-2 is showed in Fig. 3-139. The target axial load on SE-2 was 80 kips (355.8 kN). The gravity load was fluctuated between the maximum value of 86 kips (382 kN) and the minimum value of 78 kips (345 kN) due to column displacement. The gravity load was adjusted during the test by two hydraulic jacks to prevent the load fluctuations.

3.2.5.8. Separation between Column Segments

History of opening at interface between the base and second segments on the north and south sides of the column are presented in Figs. 3-140 and 3-141, respectively. The first segment separation occurred during Run 3. Negative values on the graph reflect gap closing and indicate concrete spalling at the interface of the first two segments and they were observed during Run 4 and reached the maximum values during the last run when the damage was extensive. The maximum opening at the south and north sides of the column were approximately 1.5 in. (38 mm) and 1.3 in. (33 mm), respectively.

The maximum displacement of the column and contribution of the opening to the total displacement are listed in Table 3-19. The calculation method for contribution of opening to the total displacement is described in section 3.2.1.7. The contribution of opening to the total displacement was lower in early runs and increased during the amplitude motions. The average contribution of opening to the total column displacement for all runs was 64%, and the rest was due to the base segment plastic hinge deformation.

3.2.5.9. Strain Rate

The measured strains in gauge 13 during Run 4 were used to calculate strain rate effect in steel. Figure 3-142 shows the strain rate versus the strain in this gauge. The strain rate corresponding to yield strain of 2207 μs and half of yield strain were considered in calculation of strain rate effect on steel properties. The ratio of 1.06 was calculated for dynamic yield stress to static yield stress. The strain rate corresponding to strain of 5000 μs (crushing strain of ECC) was used to calculate the strain rate effect in ECC, but none of the strain gauges reached to this value; therefore, the strain rate factor was not calculated for concrete in SE-2.

3.2.5.10. Achieved Shake Table Motions

The comparison of the target and achieved pseudo acceleration spectra of the target motions is presented in Figs. 3-143 through 3-150 for Runs 1 to 8, respectively. The measured natural period of the structure after each run is indicated by the dashed line to identify the period that were of concern.

The period of the column was calculated based on the white noise after each run. As expected the period of the column increased at higher amplitude runs due to a reduction in stiffness of the column caused by damage. Achieved peak accelerations were larger than target accelerations in the last four runs, but in general the correlation between the target accelerations and achieved accelerations was acceptable.

The column damping ratios was calculated based on half-power bandwidth method and are listed in Table 3-20 for each run. The measured data from the white noise motions after each run were used to calculate the damping ratios. The maximum damping ratio was measured after Run 5, and it was 8.7%.

3.2.6. SC-2R

3.2.6.1. General Observations

The photographs showing the damage progression in SC-2R are presented in Figs. 3-151 through 3-153 for all runs. Failure in SC-2R was similar to SF-2, since the first two segments were wrapped with FRP. No damage such as rupture of FRP or concrete spalling was observed up to Run 4. One layer of FRP ruptured on the north and east sides of the column during Run 4 (Fig. 3-152 (c)). The failure of the column including extensive FRP rupture and concrete spalling occurred during Run 5 (1.75 × Sylmar) corresponding to drift ratio of 14.8% (Fig. 3-153). Residual displacement was minimal before the last run that indicated good drift recovery of the column due to the incorporation of unbonded post-tensioning system.

3.2.6.2. Load-Displacement Response

The accumulated force-displacement hysteresis curves of SC-2R are displayed in Fig. 3-154. The force-displacement results for all the run are shown in Figs. 3-155 through 3-159. The maximum lateral force of 32 kips (142.3kN) occurred during Run 5 (Sylmar × 1.75). The maximum displacement during this run was 10.6 in. (269 mm) corresponding to drift ratio of 14.8%. The peak forces and displacements for each run for SC-2R are listed in Table 3-21.

The average load-deflection envelope for the positive and negative direction of displacement is shown in Fig. 3-160. No drop in the lateral load capacity was observed until column failure. The test was stopped after Run 5 since the post-tensioning force reached its limit and also FRP ruptures occurred during this run. SC-2R had a softer initial stiffness compared to SC-2 (original column) due to the presence of damage in the column. The maximum force in SC-2R was 37% larger than SC-2, and it demonstrated that the repair was successful in restoring the capacity of the column.

3.2.6.3. Measured Strains

The accumulated strain displacement response for the longitudinal bars, transverse bars, PT rod, and FRP jacket are displayed in Appendix A (Figs. A-63 through A-79). The strains were larger in the longitudinal bars located at the bottom of base segment. Strains in the PT rod were converted to the force and the results are presented in section 3.2.6.7. Relatively small strains were observed in the transverse bars. The maximum strain in the transverse bars was 1180 μs, which was below the yield strain of 2207 μs.

Figure 3-161 presents the average strain profile along the column height. Positive values indicate tensile strains and negative values show the compressive strains. This figure shows that the maximum strain occurred at the height of 14 in. (355 mm) from top of the footing, and it was in tension. There was a permanent residual tensile strain at this level in this column.

The maximum and the minimum strains for each run at different locations are presented in Table A-6. The damaged or slipped strain gauges were listed in Table A-6, but their data were not shown. The maximum compressive strain of 15100 μs, which was approximately seven times the yield strain, was recorded during Run 5 in strain gauge 32 (Fig. A-70 b).

3.2.6.4. Moments-Curvatures Relationships

The moment-curvature relationships for specimen SC-2R are presented in Figs. 3-162 through 3-166. The maximum curvature occurred 20 in. (508mm) above the footing at the interface between the base and second segments (Fig. 3-163). Rigid body rotation of second segment about its compression toe produced this large curvature. The curvatures were negligible at upper levels of column. These small curvatures indicated that the separation did not occur in those levels.

The profile of the maximum curvatures is presented in Fig. 3-167 for all runs. The maximum curvature was at 20 in. (508 mm) above the footing where the opening occurred between the base and second segments.

3.2.6.5. Energy Dissipation

The dissipated energy in SC-2R was determined by integrating the area enclosed by the force-displacement hysteretic curves. The total energy dissipation in SC-2R was 673 kip-in. (76035 kN-mm). The main source of energy dissipation in SC-2R was yielding of the bars in the base segment and plastic straining of concrete near the top of the segment. Concrete spalling due to segment separation was minor in SC-2R compared to that of the other segmental columns, and it led to more extensive yielding of the longitudinal bars and higher energy dissipation. It should be noted that the loading protocol for SC-2R included fewer earthquake runs compared to other segmental columns. Therefore, it is necessary that the difference in the input motion to be considered when energy dissipation is compared among the columns.

Table 3-22 lists the dissipated energy for each run and the total cumulative dissipated energy for column SC-2R.

3.2.6.6. Residual Displacement

Minimal residual displacements were observed in column SC-2R due to incorporation of unbonded post-tensioning rod. Figure 3-168 displays the residual drift ratio versus PGA (Peak Ground Acceleration) for all runs in SC-2R. Residual displacements were negligible in all runs except for the last run (1.75 × Sylmar) during which FRP rupture occurred. The maximum residual displacement after the last run was 1.3 in. (33mm) corresponding to residual drift ratio of 1.8%. To study the recentering ability of the column, the ratio of the residual displacement to the maximum displacement at each run was plotted against the PGA in Fig. 3-169. The ratio of residual displacement to the maximum displacement was small in Runs 1 to 4, and it demonstrated the successful performance of unbonded PT rod in minimizing the permanent displacement of the column.

The displacement history of SC-2R is shown in Fig. 3-170. This figure demonstrates increasing peak displacements in successive runs and the minimal residual displacement of the column at the end of runs.

3.2.6.7. Unbonded Post-Tensioning rod Force and Gravity Loads

Figure 3-171 displays accumulated PT rod force versus column displacement. This force was recorded by the load cell located on the top of the column head. The maximum force of 254.7 kips (1132.8 kN) was measured during the last run in SC-2R. This force was

85% of the ultimate strength of the PT rod. Table 3-23 lists the maximum PT force and the corresponding displacement for each run. The force in the rod increased by 258% due to column displacement, but it remained under the yielding force. The force in the PT rod dropped to 55 kips (245 kN) after the last run (1.75 × Sylmar). The drop in the force is attributed to the loss of column cross section caused by spalling of concrete.

It was explained in section 3.2.1.3 that the strain in the rod was measured by four gauges during the test. The strains were converted to force and the data were compared with the measured data by the load cell. This comparison is presented in Fig. 3-172. It can be seen that the correlation between the two data sets was very good.

The history of gravity load in SC-2R is showed in Fig. 3-173. The target axial load on SC-2R was 80 kips (355.8 kN). The gravity load was fluctuated between the maximum value of 85 kips (378 kN) and the minimum value of 77 kips (342.5 kN) due to column displacement. The gravity load was adjusted during the test by two hydraulic jacks to prevent the load fluctuations.

3.2.6.8. Separation between Column Segments

History of opening between the base and second segments on the south and north sides of the SC-2R are presented in Figs. 3-174 and 3-175 respectively. Segment separation occurred during Run 2 (Sylmar × 0.5) for the first time between the base and second segments. Negative values in the graph indicate the concrete spalling, and they were observed during Run 3. There was a large permanent displacement at the location of the opening in SC-2R. The transducer on the south and north side of the column malfunctioned during the last run and its data were not included. The maximum openings at the south and north sides of the column were approximately 1.5 in. (38 mm) and 1.4 in. (35 mm), respectively.

The maximum displacement of the column and contribution of the opening to the total displacement are listed in Table 3-24. The calculation method for contribution of opening to the total displacement is described in section 3.2.1.7. The contribution of opening to the total displacement was lower in early runs and increased during the amplitude motions. Approximately 36% of the total top column displacement was due to separation between the first two segments, and the rest was due to plastic hinge deformation.

3.2.6.9. Strain Rate

The measured strains in gauge 15 during Run 2 and gauge 12 during Run 4 were used to calculate strain rate effect in steel and concrete, respectively. Figure 3-176 shows the strain rate versus the strain for these strain gauges. The strain rate corresponding to yield strain of 2207 μs and half of yield strain were considered in calculation of strain rate effect on steel properties. The ratio of 1.07 was calculated for dynamic yield stress to static yield stress. The strain rate corresponding to strain of 6000 μs (crushing strain of concrete) was used to calculate the strain rate effect in concrete. The strain rate factor was 1.22 for concrete in SC-2R.

3.2.6.10. Achieved Shake Table Motions

The comparison of the target and achieved pseudo acceleration spectra of the target motions is presented in Figs. 3-177 through 3-181 for Runs 1 to 5, respectively. The measured natural period of the structure after each run is indicated by the dashed line to identify the period that was of concern.

The period of the column was calculated based on the white noise data after each run. As expected the period of the column increased at higher amplitude runs due to reduction in stiffness of the column caused by damage. The achieved peak accelerations were larger than the target accelerations in the last three runs, but in general the correlation between the target accelerations and achieved accelerations was acceptable.

The column damping ratios was calculated based on half-power bandwidth method and are listed in Table 3-25 for each run. The measured data from the white noise motions after each run were used to calculate the damping ratios. The maximum damping ratio was measured after Run 5, and it was 6.1%.

3.3. Two Column Bent

3.3.1. General Observations

3.3.1.1. RC-ECC Column

Figures 3-182 through 3-184 show the damage progression in RC-ECC column during all runs. Initial flexural cracking in the RC-ECC column began during Run 2 (Fig. 3.182 (c) and (d)). A deep flexural crack following by minor ECC spalling was observed on the south face of the column during Run 4 (Fig. 3-183 (d)). Additional ECC spalling on the south side of the column and some radial cracks at the junction of column and footing surface were observed after Run 5. Two longitudinal bars on the south and one longitudinal bar at the north side of the column ruptured during the last run (Fig. 3-185). Observable damage in RC-ECC column was so minor due to application of ECC material in the plastic hinge zone. ECC spalling was limited to the small zone at the bottom of the column (Fig. 3-184)

The hinge area at the top of the column was also carefully monitored during the test. This area was free from damage and it demonstrated successful performance of pipe-pin hinges in the construction. Figure 3-186 shows the condition of the top of the column after Run 6.

3.3.1.2. FRP Column

The damage progression photographs for the bottom of the FRP column are presented in Figs. 3-187 through 3-189.

No sign of damage was detected on the FRP column until Run 6 during which the FRP tube ruptured. The tensile rupture of the FRP tube occurred at the south side of the column. Figure 3-190 (a) shows the close-up view of the ruptured tube. On the north side, the FRP tube buckled at the bottom of the column in an elephant foot shape as indicated with an arrow in Fig. 3-190 (b). To investigate the condition of longitudinal bars in FRP column, the FRP tube was removed and the concrete was chipped off after test. Some horizontal cracks with no spalling were observed on the south side of the column near the top of the footing before removing the concrete cover (Fig. 3-190 (c)). The longitudinal bars on the north side of the column were undamaged, but two buckled bars were observed on the south side of the FRP column (Fig. 3-190 (d)). No damage was detected at the top of the FRP column and the hinge area remained intact. The top of the FRP column condition after the last run is shown in Fig. 3-191.

3.3.2. Measured Load and Displacements

3.3.2.1. Column Displacements and Hinge Slippage

The displacement was measured by two potentiometers that were attached to the mid height of the cap beam on the east and the west side. The readings from these two instruments were averaged and the shake table displacements were subtracted from the average displacements to calculate the deformations of the bent.

The bent deformation was the summation of the column deformation and the sliding that occurred in pipe-pin hinges between the column and the bent cap beam. Two Novotechnik displacement transducers were installed on the north and south sides of each column along with two on the sides to measure the sliding. Comparing the readings of these two transducers revealed the presence of very sharp jumps, when the friction was released and the column moved towards the transducer. This was due the large velocity of the column applying an impulsive displacement to the middle rod of the transducer and moving it backward. The axial rod then was returned to the initial position by the spring inside the instrument. As a sample, these spikes are shown in Run 6 as Fig. 3-192. Figures 3-193 and 3-194 show the history of the hinge slip after correcting the data. These graphs show that the first sliding occurred in the fourth and third runs in the RC-ECC column and FRP column, respectively. The maximum hinge slip reached approximately 0.6 in. (15 mm) and 0.5 in. (13 mm) in the FRP and RC-ECC columns, respectively. Figures 3-195 and 3-196 show the column displacement histories. The maximum displacement reached 6.97 in. (177 mm) and 6.75 in (172 mm) for the RC-ECC column and FRP column, respectively, which corresponds to approximately 11% drift. The slight difference between the two is because of slight variation of the gap at the pipe-pin connections.

3.3.2.2. Column Shear Forces

It was explained in Chapter 2 that a load cell was placed in the middle of the bent cap beam to enable the determination of the column shears. The middle load cell reading was the shear in the FRP column. The base shear in the RC-ECC column was obtained by subtracting the readings of the middle load cell from the readings of the link load cell.

There was a significant noise that entered the data because of the impact between the pipe-pin and the exterior can after each friction release. This impact energy was propagated through the length of the bent cap beam as axial compressive waves and added a very high frequency noise to the load cell readings. Figure 3-197 zooms on a small portion of data from Run 6. Four impacts are detectable in this graph.

To smooth the data, the moving average method was used (Zaghi and Saiidi, 2010). This method is a time domain filtering technique that could remove the noise from data, without distorting it. In this method the smoothed i_{th} value is obtained from Eq. 3-8:

$$x_n = \frac{\sum_{n-a}^{n+a} x_i}{2a+1} \qquad \text{Eq. 3-8}$$

$2a$ data points will be lost in this method from the beginning and end of the data series. a was assumed to be equal to 5 to obtain the best answer. In other words, value of each point in the smoothed curve is the average of 11 points, including the original data point in addition to five date points before and five date points after the current data.

Figures 3-199 through 3-204 present the accumulated force-displacement response of the bent and force-displacement hysteresis curves for each run. The maximum lateral load capacity of the bent was 55 kips (244.6 kN) and was recorded during Run 5 ($1.3\times$Sylmar). It can be seen that the maximum displacements in the positive and negative directions were comparable. The average envelope of the hysteresis curves for the positive and negative direction of displacement is displayed in Fig. 3-205.

The accumulated force-displacement response of RC-ECC column and force-displacement hysteresis curves for all the runs is shown in Figs. 3-206 through 3-212. The average envelope of the hysteresis curves for the positive and negative directions of displacement is displayed in Fig. 3-213. The maximum lateral load capacity of the column was 24.7 kips (109.8 kN) and it was recorded during Run 4 ($1.0\times$Sylmar). The lateral load capacity dropped to 13.3 kips (59.1 kN) during the last run, which was equal to 46% drop in column capacity.

The accumulated force-displacement response of FRP column is displayed in Fig. 3-214. The force-displacement hysteresis curves for Runs 1 to 6 are shown in Figs. 3-215 through 3-220. The maximum lateral load capacity of 33.7 kips (149.9 kN) was recorded in the negative region at the last run in the FRP column. At this run there was a large drop in the lateral load capacity that was due to the rupture of FRP tube. The positive lateral load capacity was 31.7 kips (141 kN) during Run 5 (Fig. 3-219), and it dropped to 15.4 kips (68.5 kN) during Run 6 (Fig. 3-220) which was equal to 51 % loss in the lateral load capacity. The average envelope of the hysteresis curves for the positive and negative directions of displacement is shown in Fig. 3-221. The hardening after the yielding was larger in FRP column, because the FRP tube remained elastic, while the steel reinforcing bars in RC-ECC column yielded.

3.3.3. Measured Strains

As discussed in Chapter 2, and shown in the instrumentation plan of Figs. 2-83 and 2-84 , strains were measured during the test on the longitudinal bars of RC-ECC and FRP columns, the transverse bars of the RC-ECC column, the longitudinal and transverse direction on the FRP tube, longitudinal direction on the pipe, and footing bars around the columns. The yield strain in the longitudinal bars was approximately 3500 μs based on the material test report. Strain gauges could be reliable for strains up to approximately 200000 μs (20 percent).

While strain gauges are accurate instruments, cracks and interaction of aggregates and ribs on the bars with the cement paste can cause highly localized strains. Therefore, erratic measurements may be recorded during some tests. Some of the strain gauges or their wires broke during the test. For these gauges only the meaningful part of data is shown in the graphs. All strain gauges data are presented in Appendix A.

3.3.3.1. RC-ECC Column

The displacement-strain plots of the longitudinal bars and spirals in the plastic hinge area of the RC-ECC column are shown in Appendix A (Figs. A-80 through A-87). Figures A-99 d and A-100 also show the strain in the top footing bars located around the column. Almost all of the strain gauges that were installed on the longitudinal bars recorded reliable data through the end of the experiment except strain gauges 16 and 22. Table A-7 shows the maximum and the minimum measured strains in the longitudinal bars for each run. The maximum axial strain of the longitudinal reinforcing bars reached 82500 μs , which is approximately 41 times the yielding strain. Table A-8 also summarizes the maximum measured strains. The maximum strain on the transverse reinforcement was 3960 μs , which slightly larger than the measured yield strain of the bars.

Figure 3-222 shows the maximum and the minimum strain profiles of the outermost northern longitudinal bars. The figure reveals that most of the yielding occurred at the bottom of the column (level E-2) (Fig. 2-82).

The longitudinal strain hysteresis curves that were measured on two sides of the steel pipe in RC-ECC column are presented in Fig. A-98. Table A-9 is the summary of the largest recorded longitudinal strains on the steel pipe. The yield force in the steel pipe was 52.2 ksi (360 MPa) corresponding to strain of 1800 μs . The largest strains occurred during Run 5 and it was 4600 μs in compression that was approximately 2.5 times of yield strain.

3.3.3.2. FRP Column

The displacement-strain plots of the longitudinal bars and spirals in the plastic hinge area of the FRP column are presented in Appendix A (Figs. A-88 through A-97). Table A-10 shows the maximum and the minimum measured strains on the longitudinal bars for each run. The maximum axial strain of the longitudinal reinforcing bars was 41150 μs, which is approximately 20 times the measured yield strain.

Comparing the strains of the longitudinal bars of the RC-ECC column and FRP column indicates that the compressive strains were smaller in reinforcing bars of the FRP column. This observation can be explained by the fact that the depth of natural axis was smaller in FRP column because the encased concrete had a larger compressive strength comparing to the core concrete strength of the RC-ECC column.

Figure 3-223 shows the maximum and the minimum strain profiles of the longitudinal bars. The strain profiles are quite similar for tension and compression during the low amplitude shake table motions. The figure shows that the maximum strain occurred at 10 in. (254 mm) above the footing and it indicates the spread of plastic hinge zone.

Many of the strain gauges glued on the FRP tube malfunctioned during early runs, because the flexural cracks that occurred in the resin broke the gauges. Table A-11 also summarizes the maximum and the minimum recorded strains on the FRP pipe.

As described in Chapter 2, two groups of strain gauges were installed on the FRP tube surface. One group of strain gauges measured the strains along the FRP fiber that were $+/-55^\circ$,and the strains were transferred to the x and y axis to calculate the hoop and longitudinal strains, respectively. Appendix A shows the strain hysteresis curves along the fibers. The maximum hoop strain reached 18220 μs, 1 in (25 mm) above the footing level.

The shear strains recorded by the rosette gauges that were installed on the sides of the column are presented in Figs. A-95, A-96 and, A-97. Longitudinal strain on the south and north sides of the steel pipe in FRP tube column are presented in Fig. A-98. Figures A-99 (d) and A-100 also show the strains in the top footing bars located around the column. Table A-12 lists the maximum recorded longitudinal strains on the steel pipe.

3.3.4. Moment-Curvature Relationships

3.3.4.1. RC-ECC Column

The curvatures and bond-slip rotation were measured by eight displacement transducers that were installed on the columns. The rotation was calculated by dividing the difference of the readings of the two transducers at each level by the distance of Novotechniks from each other.

Figure 3-224 shows the moment-rotation relationships at the lower most level, which is a measure of the bond slip rotation due to yield penetration of the longitudinal bars inside the footing. Figures 3-225 to 3-228 present the moment-curvature relationships at the first, second, third, and fourth levels of instrumentations in RC-ECC column.

The profile of the curvature between each two levels of displacement transducers is presented in Fig. 3-229 for all the runs. The maximum curvature was recorded at the bottom of column (level E-2 in Fig. 2-82).

3.3.4.2. FRP Column

Figure 3-229 shows the moment-rotation relationships at the lower most level, which is a measure of the rotation of the embedded part of the FRP tube in the footing. The rotation at the base of the FRP column was smaller than the bond-slip rotation in the RC-ECC column. Weaker bond between the FRP tube and grout around the column can explain this small rotation.

Figures 3-231 to 3-234 present the moment-curvature relationships at the first, second, third, and fourth levels of instrumentations on the FRP tube column. The threaded rods at the bottom of the FRP tube that were used to attach the displacement transducers broke during Run 6, and it was not possible to record the curvatures in subsequent motions. The part of the Figs. 3-230 and 3-231 with a large shift in curvature indicates the point at which threaded rod breakage.

The profile of the curvature between each two levels of displacement transducers is presented in Fig. 3-235 for the all runs. The maximum curvature was recorded at the bottom of the FRP column (level F-3 in Fig. 2-82).

3.3.5. Energy Dissipation

The dissipated energy was determined by integrating the area enclosed by the force displacement hysteresis curves. Energy dissipation was calculated for FRP column and RC-ECC column, and the results are presented in Tables 3-26 and 3-27. These tables list the energy dissipation during each run and also the cumulative energy dissipation. The total energy dissipation was 852 kip-inch (96311 kN.mm) in RC-ECC column, and it was mainly due to the yielding of the bar in the plastic hinge zone. The FRP column dissipated energy of 744.2 kip-inch (84078 kN.mm). Although the lateral load capacity of FRP column was 28% larger than RC-ECC column, its energy dissipation was 12% smaller. The lower energy dissipation in FRP column was attributed to its lower steel ratio compared to that of RC-ECC column.

3.3.6. Residual Displacements

The residual displacement was minimal in both columns in PEFB. Figure 3-236 displays the residual drift ratio versus PGA (peak ground acceleration) for all runs in the FRP column. It can be seen that the residual displacements were negligible in all runs. The residual displacement in FRP column reached its peak value during Run 5, and it was 0.22 in. (5 mm). The ratio of the residual to the maximum displacement at each run was plotted against the PGA in Fig. 3-237 for the FRP column. The small ratios of residual displacement to the maximum displacement indicate that the FRP column could fully recover the large drifts.

The residual drift ratio versus PGA for RC-ECC column is plotted in Fig. 3-238. Negligible values were recorded for the residual displacement in this column. Figure 3-

239 is also displaying the ratio of residual to the maximum displacement versus PGA. This graph shows that the RC-ECC column could recover the drift even after large displacement.

3.3.7. Strain Rates

The effect of strain rate on steel and concrete strength and the methods to calculate the strain rate factors are presented in section 3.2.1.8. The measured strains in gauge 45 during Run 3 in FRP column was used to calculate strain rate effect in steel and concrete. Figure 3-240 shows the strain rate versus the strain for this strain gauge. The measured strains in gauge 6 during Run 3 in RC-ECC column was used to calculate strain rate effect in steel and concrete. The strain rate versus the strain for this strain gauge is shown in Fig. 3-241. The strain rate corresponding to yield strain of 3500 μs and half of yield strain were considered in calculation of strain rate effect on steel properties. The ratios of 1.09 and 1.07 were calculated for dynamic yield stress to static yield stress for FRP column and RC-ECC column, respectively. The strain rate corresponding to strain of 6000 μs (crushing strain of concrete) was considered to calculate the strain rate effect in concrete. The strain rate factors were 1.24 and 1.28 for concrete in FRP column and RC-ECC column, respectively.

3.3.8. Axial Load Variation and Vertical Displacements

Because the vertical loads were applied through post-tensioning rods, as the pier moved in the transverse direction the axial loads tended to increase. The axial load rams were attached to accumulator to compensate for the variations during the motion. Fluctuation in axial load was observed because of small diameter of the connecting hoses that did not allow for the surcharge hydraulic oil flow to the accumulator.

The history of axial load in FRP and RC-ECC columns are showed in Figs. 3-242 and 3-243, respectively. The axial load on the FRP column was approximately 51 kips (226 kN) at the beginning of the test. Some of the axial load was lost due to the plastic deformation of the FRP column, and the final axial load on the FRP column was 34 kips (151 kN).

The initial axial load in RC-ECC column was approximately 47 kips (209 kN) and it dropped to 31 kips (138 kN) at the end of the test. This axial load lost was due to the plastic deformation of column.

3.3.9. Target and Achieved Shake Table Motions

Since the shake tables and the bent model are two separate systems that interact, the achieved motions of the shake tables depend on the mass and stiffness of the bent. The software that drives the shake tables modifies the target motions during testing as an attempt to compensate for the response of the payload on the tables. However, the bent model in this experiment was highly nonlinear and relatively stiff and strong with respect to the tables, which makes compensation of the motions very difficult. As a result, there were differences between the achieved and target shake table motions.

The input ground acceleration was factored by 0.1 to 1.6 in 0.3 increments, which lead to total number of 6 Runs. Figures 3-244 through 3-249 show the comparison of the target pseudo acceleration spectra of the target motions versus the achieved motions. The natural period of the structure before each run is marked by the dashed line. The period of the bent increased from 0.278 second at the first run to the period of 0.626 second during Run 6. The rupture of the FRP tube and longitudinal bars in RC-ECC column made the bent softer and led to these increased periods.

In general, there was an acceptable match between the target and achieved table motions in a range of natural period plus/minus tenth of a second except for the second run that the motion was overshot.

The bent damping ratios were calculated based on half-power bandwidth method and are listed in Table 3-28 for each run. The measured data from the white noise motions after each run were used to calculate the damping ratios. The damping ratio was in range of 1.6% to 2.7% in early runs and it increased in high amplitude motions. The maximum damping ratio was measured after Run 6 and it was 9.3%. A damping ratio in range of 3% to 5% is recommended for a reinforced concrete structure by most of the building codes [Chopra, 2006]. Contribution of FRP tube and ECC material in PEFB are believed to have caused this higher damping.

4. EVALUATION OF TEST MODELS

4.1. Introduction

Evaluation and comparison of test results for precast segmental columns with different plastic hinge details and two innovative columns of the PEFB bent are presented in this chapter. Apparent damage, the maximum lateral load capacity, column ductility, dissipated energy, and recentering capability were studied and compared for different columns.

4.2. Precast Segmental Columns

4.2.1. Apparent Damage

The major failure mode in segmental columns was concrete spalling at interface between the base and second segments. Failure of concrete was attributed to the large cyclic compressive strains from opening and closing action at the interface. The extension of damage was different in different segmental columns depending on the material at the first two segments.

Table 4-1 lists the apparent damage for each segmental column at drift ratios of 2%, 5% and 10%. Based on this table, the most extensive concrete spalling occurred in SC-2. SF-2 and SC-2R experienced the least damage, among the segmental columns. The longitudinal bars located at the base segments of all columns yielded but did not rupture.

Figures 4-1 through 4-3 show the columns after drift ratios of 2%, 5%, and 10%, respectively. As described in Chapter 2, SC-2 was the benchmark column, and the performance of specimens consisting of innovative materials was judged based on comparison with the SC-2 performance.

Figure 4-1 compares the extension of cracks in segmental columns at 2% drift that corresponded to input motion of $0.5\times$Sylmar. Some minor cracks were observed in columns SC-2, SE-2 and SBR-1 at the interface of the base and second segments. No sign of concrete failure was seen in SC-2R and SF-2 that were wrapped with FRP in the lower segments.

Apparent damage at 5% drift in segmental columns is shown in Fig. 4-2. The pictures show the columns after they were subjected to $1.0\times$Sylmar. The most extensive spalling was seen in SC-2 and SBR-1, in which the conventional concrete was used in their base segments (Figs. 4-2 (a) and (b)). SF-2 and SC-2R did not show any rupture of FRP or concrete spalling. The cover spalling in SE-2 was minimal due to application of ECC material.

Segmental columns after experiencing 10% drift are shown in Fig. 4-3. The pictures show the columns after they were subjected to $1.5\times$Sylmar. The most extensive cover spalling was observed in SC-2. The spalling extended over the entire height of the base segment, and spirals and longitudinal bars were exposed (Fig. 4-3 (a)). SBR-1 also experienced concrete spalling at the interface between the base and second segments, but the damage was not as extensive as that in SC-2. The lower part of the base segment in SBR-1 was free from damage due to the incorporation of the elastomeric bearing pad. The rubber pad was intact after the last run (Fig. 4-3 (b)). The FRP jacket ruptured in SF-2 and SC-2R but the concrete spalling was minor compared to that of SC-2 (Figs. 4-3 (c) and (e)). The minimal damage observed in SF-2 and SC-2R revealed that using FRP jacket can reduce the concrete spalling substantially. FRP rupture in SC-2R was more severe than the rupture in SF-2. The weak bond between the repair grout and concrete in SC-2R is believed to have caused the damage.

The cover spalling in SE-2 was minimal and limited to two sides of the interface (Fig. 4-3 (d)). Minimal ECC spalling was observed due to the ductile behavior of ECC material.

4.2.2. Lateral Load Capacity and Ultimate Drift Ratio

The lateral load capacities in segmental columns with innovative detail are compared with that of the reference column (SC-2). The average response envelope in the positive and negative directions was used to compare the lateral load response of the columns. Segmental columns showed various lateral load capacities under the dynamic motion. This difference in the capacity was because of different details and various extension of damage in columns. Table 4-2 lists the maximum lateral load capacity and ultimate displacement for each column.

Figure 4-4 shows the normalized lateral load response in SBR-1 and SC-2. Since the longitudinal steel ratios were different in SC-2 and SBR-1, the normalized load-deflection envelopes were used to compare their performances. Normalizing was conducted by dividing the loads by the lateral load capacity at 5% drift ratio. The force at 5% drift was chosen for normalizing, since 5% drift is considered to be a large drift ratio that might be expected under strong earthquakes. It can be seen that the initial stiffness of SBR-1 was smaller than the SC-2 stiffness. This is because of the lower compressive modulus of elasticity of the rubber compared to that of concrete. The normalized peak lateral force in SC-2 was reached at a drift ratio of 4.2%, and the strength deteriorated after this displacement. In contrast, SBR-1 was able to maintain its capacity even at a drift ratio of 14%. Defining the failure point where the capacity drops by 15%, the measured drift capacity of SC-2 was 11%, which was 28% lower than the maximum measured drift of SBR-1. Also, because the capacity of SBR-1 did not deteriorate, the column was able to reach a lateral load that was 15% larger than the SC-2 capacity.

Comparison between the lateral load capacities in SF-2 and SC-2 is made in Fig. 4-5. Both columns showed the same initial stiffness. The lateral load capacity of SF-2 was 32% larger than SC-2 capacity. The larger capacity of SF-2 was attributed to the confinement provided by the CFRP jacket, which delayed failure of concrete at the interface of its bottom two segments. The maximum measured drift capacity of SF-2 was 15%, which was 36% larger than the SC-2 drift capacity.

Figure 4-6 displays the lateral load versus displacement relationships for SC-2 and SE-2. Unlike SC-2, SE-2 showed no degradation of strength. The maximum lateral load capacity and ultimate drift ratio of SC-2 were slightly larger than that of SE-2. Defining the failure point, where the capacity drops by 15%, the measured drift capacity of SC-2 was approximately 2% larger than the maximum measured drift in SE-2. The maximum lateral load capacity of SC-2 was larger than that of SE-2 by 6%. No degradation in the capacity of SE-2 was observed due to the ductile behavior of ECC, which resulted in minimal spalling and minor section loss at the interface of two lower segments.

The lateral load displacement relationships for SC-2 and SC-2R are plotted in Fig. 4-7. The lateral load capacity in SC-2R was 45% larger than that of SC-2, and it did not deteriorate. However, the initial stiffness of SC-2 was not restored by the repair due to material degradation during the original column tests. The larger capacity of SC-2R was attributed to the confinement provided by the CFRP jacket, which delayed failure of concrete at the interface of its bottom two segments. The ultimate drift in SC-2 R was 14.8% which was 35% larger than drift in SC-2. Successful performance of SC-2R demonstrated that the repair of column SC-2 was effective in restoring its strength and drift capacity.

4.2.3. Energy Dissipation

The dissipated energy was calculated by integrating the area enclosed by the force displacement hysteretic curves. It should be noted that the main source of energy dissipation in the segmental columns was the yielding of longitudinal reinforcement connecting the base segment to the footing. The dissipated energy in different column models is listed in Table 4-3.

It was described in chapter 2 that all columns were tested under the simulated Sylmar motions with increasing amplitudes until failure. The last motion (1.5 × Sylmar) was repeated in SF-2 and SE-2 since no failure signs were observed in them after Run 7. Some motions were also skipped in testing SC-2R since that column was repaired and applying numerous motions was not desirable for this column. Since the scale and number of motions were not the same in the columns, comparing the dissipated energy listed in Table 4-3 may not be appropriate to judge the performance of the columns.

To study and compare the ability of each column in dissipating the energy of earthquake, the dissipated energy was plotted against the maximum displacement for each run in Fig. 4-8. There was no significant difference in the dissipated energy in the test models until a displacement of 3.5 in. (89 mm) (4.8 % drift). It can be seen in Fig. 4-8 that the amount of energy dissipation was the highest in SF-2, followed by SC-2R, and SBR-1, between displacement of 3.5 in. (89 mm) to 5.5 in. (140 mm) (7.6 % drift). At the ultimate displacement of 10.5 in. (267 mm) (14.5 % drift), SC-2R, SBR-1 and SF-2 dissipated higher energy than other columns. SE-2 and SC-2 dissipated the least amount of energy.

A conventional precast concrete segmental column with no dowels connecting the base segment to the footing was analyzed using OpenSees [OpenSees Manual, 2005] to investigate if segmental columns with the base segment connected to the footing dissipated more energy of earthquake over a conventional precast segmental column.

The conventional segmental column had similar dimensions and reinforcement details as those of the test specimens. The dissipated energy was calculated when the column was analyzed under a generally similar motion (Sylmar scaled by 0.1, 0.25, 0.5, 0.75, 1, 1.25, and 1.5) as that of the test specimens. The results are included in Fig. 4-8. Comparison of graphs at drift ratios of 4 % and 8% showed that the dissipated energy in segmental columns with the base segment connected to the footing was 2 to 4 times larger than that of a column with no connection between the base segment and the footing.

Using FRP jacket in SF-2 and SC-2R delayed concrete failure and increased the energy dissipation due to increased yielding of the bars. Flexural deformation of elastomeric pad in the plastic hinge of SBR-1 increased dissipated energy and eliminated the damage in that area. Comparison between the test specimen responses with that of a conventional precast segmental column revealed that connecting the base segment to the footing and incorporating materials such as concrete, rubber pad, ECC, and FRP are attractive alternatives for accelerated bridge construction in high seismic zones because of higher energy dissipation and the resulting lower damage.

4.2.4. Residual Displacements

It was explained in chapter 2 that an unbonded post-tensioning rod was used to connect the column segments to each other and to the footing and to minimize residual displacements. The residual drift ratio is defined as the ratio of ultimate column displacement to the column height. Figure 4-9 displays the residual drift ratio in different segmental columns during each run.

An examination of residual displacement of bridge columns was included in the Japanese seismic design specification for highway bridges when the specifications were revised after the Hyogo-ken Nanbu in earthquake 1996 [Kawashima, et al., 1998]. In the specifications, the calculated residual drift ratio at the center of gravity of superstructure of important bridges after an earthquake should be less than 1%. This limit is arbitrary. Reinforced concrete columns with a drift larger than 1.75% had to be demolished and rebuilt after the Hyogo-ken Nanbu earthquake [Kawashima, et al., 1998]. It can be seen in the Fig. 4-9 that the residual drift ratios are much lower than 1 % in all columns except in SBR-1 and SC-2R after the columns had failed. The maximum displacement in these two columns during the last run was relatively large and was approximately 10 in (254 mm) corresponding to drift ratio of 14%.

Minimal residual drifts in segmental columns demonstrated the successful performance of unbonded post-tensioning system in minimizing permanent displacements of the column.

4.3. Precast Two-Column Bent

4.3.1. Apparent Damage

Bent condition at drift ratios of 2%, 5%, and 10% are displayed in Figs. 4-10 through 4-12. In these figures the north and south faces of the FRP and RC-ECC columns are shown. Table 4-4 lists the levels of damage including minor cracks, cover spalling, the number of exposed spirals and longitudinal bars, and the number of ruptured or buckled longitudinal bars.

Drift ratio of 2% occurred during Run 3 (0.70 × Sylmar). The north and south faces of FRP column was intact (Fig.4-9 (b) and (d)). No sign of ECC spalling was observed in RC-ECC column and only minor horizontal cracks were observed (Fig. 4-10 (a) and (c)). Top of the columns and the cap beam were free from damage after this drift.

The maximum drift ratio was 5% during Run 4 (1.0 × Sylmar). FRP column was still undamaged, but a wide flexural crack was observed at the bottom of RC-ECC column. Figure 4-10 shows the north and south faces of both columns after 5% drift. The crack in RC-ECC column is marked with an arrow in the close up view in Fig. 4-11 (c).

The maximum drift ratio of 10% was measured during the last run when the bent was under 1.65 × Sylmar. Three steel longitudinal bars ruptured in the RC-ECC column. Two of the bars were in the south side, and one was in the north side of the column. Due to ductile behavior of ECC, spalling was minor, and it was limited to 5 in. (127 mm) height of RC-ECC column from top of the footing. Extensive FRP rupture occurred on the south face of FRP column at failure. Longitudinal bars were not exposed in FRP column during the test. To investigate the condition of longitudinal bars in the FRP column, the FRP tube was removed, and the loose concrete was removed after the test. Some horizontal cracks with no spalling were observed on the south side of the column near the top of the footing (Fig. 4-13 (a)). The longitudinal bars on the north side of the column were undamaged but two buckled bars were observed on the south side of the FRP column (Fig. 4-13 (b)).

Both columns were nearly damage-free until very high amplitude motions were applied. The test results demonstrated that ECC and FRP tube are promising materials in accelerated column construction in seismic zone and could remain intact until very large drifts.

4.3.2. Lateral Load Capacity and Ultimate Drift Ratio

The force-displacement envelopes of the hysteresis curves for FRP and RC-ECC columns are plotted in Fig. 4-14. The envelopes were calculated from the average response of columns in the positive and negative displacement directions. Table 4-5 lists the maximum lateral load capacity, the maximum displacement, and displacement ductility for RC-ECC and FRP columns. Ductility was calculated from bilinear elasto-plastic curve presented in Chapter 3. The lateral load capacity of FRP column was 30% larger than RC-ECC column.

The initial stiffness in the columns was the same, but the hardening after yielding was substantially more significant in FRP column because the FRP tube remained elastic, while the steel reinforcing bars in RC-ECC column yielded.

The ductility capacity of RC-ECC column was 7.77 compared to the FRP column ductility capacity, which was 5.77. Larger ductility of RC-ECC column was attributed to usage of ECC material in the plastic hinge area. It was explained in Chapter 1 that ECC displays higher tensile ductility, tensile strain hardening behavior, and energy dissipation than conventional concrete.

4.3.3. Energy Dissipation

Total cumulative dissipated energy in columns was determined by integrating the area enclosed by the force-displacement hysteretic curves. Table 4-6 lists the energy dissipation and the maximum lateral load capacity for each column. The dissipated energy in RC-ECC column was 13% larger than that of the FRP column, although its lateral load capacity was 30% less than that of the FRP column.

The dissipated energy versus the maximum displacement during each run is plotted in Fig. 4-15. The energy dissipation was larger in RC-ECC column in all the runs except the last run when the bars ruptured during Run 6.

The steel ratio in RC-ECC column was 1.6 % compared to the steel ratio of 0.46% that was used in FRP column. The larger energy dissipation in RC-ECC column was attributed to larger steel ratio and usage of ECC in its plastic hinge.

4.3.4. Comparison of Response of Precast and Cast-in-Place Bents

A scaled two-column bridge pier was tested at UNR and labeled PPTC (pipe-pin, two-circular-column) to study the seismic behavior of pipe-pin hinges [Zaghi and Saiidi, 2010]. PPTC consisted of one CFFT (concrete filled FRP tube) column and one conventional reinforced concrete column.

Similar to PEFB, the diameter of the columns in PPTC was 14 in. (356 mm), but unlike the PEFB, PPTC was cast-in-place (CIP). The FRP tubes with similar properties were used in both bents. Unlike the RC column in PPTC, that was made up of conventional concrete, the RC-ECC column in PEFB incorporated ECC material in its plastic hinge zone. The longitudinal steel ratios of the columns were not the same in the two bents. The steel ratio in the FRP tube column in PEFB (the precast bent) was 0.46%, as opposed to 1.04% in PPTC. The steel ratio in RC-ECC column in PEFB was 1.6%, while this ratio in the RC column in PPTC was 2.6%. Both bents were subjected to the same vertical load and were tested under similar motions until failure. The results of PEFB and PPTC including apparent damage and normalized force-displacement responses are compared in subsequent sections.

4.3.4.1. Apparent Damage after Failure

The failure in PEFB occurred during 1.65 × Sylmar. The maximum drift ratio during this run was 11.5%. PPTC failed during 1.9 × Sylmar with the maximum drift ratio of approximately 8.5 %.

Figures 4-16 and 4-17 display the north and south faces of the FRP columns after the last runs. In both bents, at the base of the FRP tube columns, one side was buckled in an elephant foot shape; while on the other side the FRP tube ruptured in tension. The FRP rupture was more extensive in PEFB. The lower amount of steel reinforcement in the FRP tube in PEFB is attributed to the severe rupture of FRP tube in this bent. Because of the relatively low steel ratio in PEFB, the tensile and compressive strain demands on the FRP shell were higher and resulted in more severe damage.

The comparisons of the RC and RC-ECC columns in the two bents are displayed in Figs. 4-18 and 4-19. The concrete cover extensively spalled in the RC column in PPTC. In contrast, spalling in ECC material was minor in PEFB. This indicates that the use of the ECC material in plastic hinge of RC-ECC helped minimizing damage. The damage was also more localized over a shorter height of the RC-ECC column.

4.3.4.2. Lateral Load Capacity and Ultimate Drift Ratio

Since the longitudinal steel ratios and lateral load capacities were different in the two bents, direct comparison of response is not appropriate; therefore, the normalized load-deflection envelopes were used to compare PEFB and PPTC performances. Figures 4-20 through 4-22 compare the normalized load-deflection response of the bents, FRP columns, and RC columns, respectively. Normalizing was conducted by dividing the loads by the lateral load capacity at 5% drift. The force at 5% drift was chosen for normalizing, since there was significant hardening in the response due the presence of the FRP tube and 5% drift is considered to be a large drift ratio that might be expected under strong earthquakes.

It can be seen in Figs. 4-20 through 4-22 that the normalized load-deflection responses of precast bent are closely correlated with those of cast-in-place specimen. This demonstrates that precast construction can provide strengths and ductilities similar to those of comparable cast-in-place construction. The column embedment length in the precast bent was sufficient to develop the full plastic moment in each column in the plastic hinge area and provide complete moment connection.

The load-deflection responses were simplified by an elasto-plastic idealization to determine the displacement ductility capacities. The elasto-plastic responses were calculated based on the method described in section 3.2.1.1. Figures 4-23 through 4-25 display the elasto-plastic curves for the bent, FRP columns, and RC columns, respectively. The displacement ductility was defined as the ratio of ultimate displacement to the displacement at the effective yield displacement. The ductility capacities of PEFB and PPTC were 7.46 and 4.6, respectively. The higher ductility of PEFB can be attributed to its lower longitudinal steel ratios. The ductility in FRP column in PEFB bent was 5.77, while the ductility in the FRP column in PPTC was 4.97. The displacement ductilities in the RC and RC-ECC columns were 7.77 and 6.9, respectively.

5. STRESS- STRAIN MODEL FOR CONFINED ECC

5.1. Introduction

Transverse reinforcement provides confinement for cementitious materials and improves their strength and ductility. Many researchers have studied the effect of confinement on concrete and developed different confinement models, but there is no available model for confined ECC.

Two specimens including one segmental column, SE-2, and RC-ECC column in PEFB bent incorporated ECC in combination of transverse reinforcement in the plastic hinge zone. In the course of the analytical studies of the specimens it was found necessary to develop a model for confined properties of ECC based on the unconfined ECC strength and transverse reinforcement.

To study the effect of confinement on ECC, four groups of samples were built and tested under compression. The test details including samples geometry, material characteristics, instrumentations, and test setup, and development of equations are described in this chapter.

5.2. Past Research on ECC

ECC is a fiber-reinforced cement-based composite engineered for high tensile ductility. ECC contains water, cement, fine sand, fiber, and common chemical additives. Coarse aggregates are not used in the mix, because they adversely affect the unique ductile behavior of the composite. The fibers are typically made with poly vinyl alcohol (PVA) or high modulus polyethylene (PE). It has been mentioned in previous studies that ECC provides its own confinement and maintains its integrity without the need for additional transverse reinforcement (Billington, et al., 2004).

Tension behavior of ECC has been investigated by many researchers, but there are few studies about ECC compressive behavior. A uniaxial compression was performed on ECC by Li, (1998). He showed that ECC has a lower compressive elastic modulus compared with concrete, and it reaches its compressive strength at a larger strain due to the lack of large aggregates. He demonstrated that the compressive strength of ECC is usually on the order of 4.3 ksi (30 MPa) to 11.6 ksi (80 MPa), depending on its composition (Fig. 5-1 (a)). After reaching the maximum compressive strength, the compressive strength drops to approximately 0.5 f_c' (f_c' is the maximum ECC stress); and subsequently the strength decreases gradually with increasing deformation. The compressive strain capacity is approximately 50%-100% larger than compressive strain capacity of normal concrete. The modulus of elasticity of ECC, as in ordinary concrete, depends on the amount of aggregates (Fig. 5-1 (b)). The compressive modulus of ECC is approximately 3000 ksi (20300 MPa) [Li, 1998].

A comprehensive experimental study including uniaxial compression, tension and cyclic loading experiment on ECC with 1% fiber content was performed in Japan [Zafra, et al., 2010]. The samples were dog bone shaped and had an average compressive modulus of elasticity of 1262 ksi (8700 MPa). The compressive strength was 6.2 ksi (43 MPa), and strain at peak compressive stress was 0.0063. The test results are shown in Fig. 5-2.

Kesner,et al., (2003) performed cyclic testing included monotonic uniaxial compression, cyclic uniaxial compression, and reversed cyclic uniaxial tension/compression experiments. The compressive strength of 9.1 ksi (63 MPa) and compressive modulus of elasticity of 2000 ksi (13800 MPa) were measured. The average measured strain at peak stress was 0.5% in this study (Fig. 5-3) [Kesner,et al., 2003]

The confined behavior of ECC was not studied in any of the tests described above. A series of ECC cylinders with different amount of transverse reinforcements were built and tested at UNR to develop a confinement model for ECC.

5.3. Material

5.3.1. ECC

The mix proportions of the ECC are listed in Table 5-1. The volume fraction of the fiber was 2%. ASTM Type I/II Portland cement and FT Bridger fly ash were used in the batch. Types of materials used in ECC batch are listed in Table 5-2. Large aggregates were excluded in ECC mix design, and only fine sand was incorporated. The size of sand was # 60 medium. The Kurary PVA KII 8X15 fibers used in the mix. The average strength of 5.6 ksi (38.6 MPa) was measured for the unconfined ECC.

5.3.2. Steel Wire

Steel wire spirals were wrapped around the sample cylinders. Tensile testing was conducted on the wires, which had a diameter of 0.135 in. (3.4 mm). The measured stress-strain curves of steel wire are shown in Fig. 5-4. Three samples were tested on a Tinius Olson machine (Fig. 5-5). For each test, the yield stress was taken as the intersection of the stress-strain curve and a 2% offset line. The stress-strain curve for sample 2 did not agree with the curve for other bars; therefore, the steel properties were determined based on samples 1 and 3 (Fig. 5-4). The yield stresses of 60 ksi (413.7 MPa) and 80 (551.6 MPa) were measured for samples 1 and 3.

5.4. Test Specimens

To investigate the confinement effect of transverse reinforcement on ECC, an experiment was designed and performed at UNR structural laboratory. Four groups of specimens each with different confinement levels were designed and studied here. Each group included four 4×8 in. (100×200 mm) cylindrical samples. All the cylinders were tested under compressive load. Table 5-3 lists properties for each group of samples including the transverse reinforcement spacing and f_l (confinement stress).

$$f_l = \frac{2A_s f_y}{d_s s} ksi\ (MPa) \qquad \text{Eq. 5-1}$$

The steel wire was rolled around a pipe to form the spirals (Fig. 5-6 (a)). No longitudinal bars and no cover were provided for the samples. One group of samples were unconfined and spiral spacing in other groups were 2 in. (51 mm), 1.5 in. (38 mm) , and 1 in. (25 mm). The steel wire spirals were anchored to the molding wall with a thin wire (Fig. 5-6 (b)).

ECC dried materials were combined before transferring to the construction site. Water was added to the mix and combined with a hand held mixer. Cylinders were filled with ECC (Fig. 5-6 (c)) and cured for 77 days. Before testing, cylinders were capped with sulfur-mortar to eliminate surface roughness (Fig. 5-6 (d)).

5.5. Instrumentations

A compressometer with digital indicator, 4 × 8 in. (101 × 203mm) H-2916D was used to measure the vertical deformation of cylinders during the compressive loading. A load cell was placed underneath the samples during the test and was connected to a data acquisition system to record the compressive load. Four strain gauges of type YFLA-2-3L were installed on the spirals at mid height of the ECC samples. Figure 5-6 (d) shows the ECC cylinders with strain gauges connected.

Measuring the vertical deformation by compressometer required reading the data from the gauge causing some error. Therefore, two cylinders were tested with the vertical deformation recorded by a pair of Novotechnik transducers. The transducers and the load cell were connected to the data acquisition systems during the test to record forces and deformations simultaneously.

5.6. Test Set up and Loading

Fourteen of the sixteen cylinders were tested using the compressometer for recording deformations (Fig. 5-7). The load was recorded by a data acquisition system connected to the computer and deformation was read from the digital gauge. The loading was initially force controlled, but after the maximum loading, it was changed to displacement controlled. In the first step, the deformation was read from the gauge at specified incremental loading. The load increment was 5 kips (22.2 kN). The displacement controlled loading started when the samples reached the maximum capacity. After the peak load, the deformation of cylinders was unstable, and reading from the digital gauge was not possible; therefore, the cylinders were unloaded. The samples were loaded until reaching the maximum displacement recorded from the last step, and then the force was read at a specified displacement until reaching the failure.

Because of the difficulties in using the compressometer, the two remaining cylinders were tested with the vertical deformation recorded by a pair of Novotechnik transducers (Fig. 5-8).

5.7. Observations and Test Results

As the load increased, fine vertical cracks were formed along the height of the cylinders followed by spiral rupture (Fig. 5-9). The failure of ECC cylinders was gradual, and the samples could maintain their integrity until very high load amplitude. The cylinders capacity dropped by 40-70% after passing the maximum strength, but this residual capacity was maintained until very large deformations.

Stresses and strains were derived from raw data. The stress was calculated by dividing the force by the loading area (12.5 in^2 (8107 mm^2)). The measured deformations were divided by gauge length (5.5 in (139 mm)) to convert to the strains.

Figures 5-10 through 5-13 display the stress-strain results for four groups of samples. The average curves also are shown in the graphs with a bold line. The average stress-strain curves for all categories are plotted in Fig. 5-14. This graph shows that samples with larger confinement had a higher compressive strength.

The average measured strains in spirals were calculated from the four strain gauges on each sample, and they are plotted in Figs. 5-15 through 5-17 for different spiral spacing. The vertical axis in the graph is the compressive stress for each sample. The maximum strain in spirals was approximately 9000 μs which was 4.3 times the yield strain (2068 μs).

5.8. Development of Confinement Model

A confinement model was developed to calculate the parameters of stress-strain curve for confined ECC based on spiral yield stress, area, spacing and the unconfined ECC strength.

The model for calculating the confined concrete stress-strain properties by Mander, et al., (1988) was studied, and the parameters were adjusted for confined ECC. In addition, the Popovics‟ model for stress-strain relation of mortar was used to model the stress-strain curve of confined ECC.

5.8.1. Applicability of Mander's Model for ECC

To investigate the validity of Mander‟s equations for ECC, the test results and calculated stress-strain curves using Mander‟s equations were superimposed and compared. Figures 5-18 through 5-21 compare the results. These graphs demonstrate that Mander‟s model predicts slightly larger maximum strengths (f'_{cc}). The initial stiffness calculated by Mander' model was larger than the measured stiffnesses. In the cases with medium to large confinements (f'_l =0.3 and 0.44 ksi (2 and 3 MPa)), the strength capacity in Mander‟s model decreased more gradually than that of ECC samples.

5.8.1.1. Maximum Confined Strength f'_{ce}

The Mander‟s equation for estimating the maximum strength of confined concrete is:

$$f'_{cc} = f'_{co}(-1.254 + 2.254\sqrt{1 + \frac{7.94 f'_l}{f'_{co}}} - 2\frac{f'_l}{f'_{co}}) \qquad \text{Eq. 5-2}$$

Where:

$$f'_l = \frac{2A_{sp} f_y}{d_s s} \qquad \text{Eq. 5-3}$$

f'_l = Confinement stress

f'_{cc} = Confined strength

f'_{co} = Unconfined strength

A_{sp} = Transverse steel area

f_y =Yield stress of transverse steel

d_s =Core diameter (center of spirals to center)

s =Spacing of transverse steel

Equation 5-2 can be simplified to Eq. 5-4.

$$\frac{f'_{cc}}{f'_{co}} = a + b\sqrt{1 + c\frac{f'_l}{f'_{co}}} - \frac{2 f'_l}{f'_{co}} \qquad \text{Eq. 5-4}$$

Where:

$a = -1.254, \quad b = 2.254, \quad c = 7.94$

Equation 5-4 was plotted in Fig. 5-22 (a) with the abscissa and ordinate were (f'_{cc} / f'_{co}) and (f'_l / f'_{co}), respectively. The ratios of (f'_{cc} / f'_{co}) and (f'_l / f'_{co}) were calculated from confined ECC test results and plotted in Fig. 5-22 (a). Table 5-4 lists the average (f'_{ce} / f'_{co}) and (f'_l / f'_{co}) for confined ECC samples.

The coefficients a, b and c in Eq. 5-4 were adjusted until two graphs matched (Fig. 5-22(b)). The new coefficient of $a = -1.25, \quad b = 2, \quad c = 10.5$ were selected for Fig. 5-22(b). It can be seen in Fig. 5-22 (b) that the graph between $0 < \frac{f_l'}{f_{co}'} \le 0.035$ is flat, which means that confinement does not increase the compressive strength.

Equations 5-5 and 5-6 are proposed to estimate the maximum compressive strength of confined ECC.

For $\frac{f_l'}{f_{co}'} \le 0.035$ $\qquad f_{ce}' = f_{co}'$ Eq. 5-5

For $\frac{f_l'}{f_{co}'} > 0.035$ $\qquad f_{ce}' = f_{co}'(-1.25 + 2\sqrt{1 + \frac{10.5 f_l'}{f_{co}'}} - 2\frac{f_l'}{f_{co}'})$ Eq. 5-6

5.8.1.2. Strain at Maximum Strength ε_{ce}

Mander recommended Eq. 5-4 to calculate the strain at the peak strength.

$$\varepsilon_{cc} = 0.002\left[1 + 5(\frac{f'cc}{f'co} - 1)\right] \qquad \text{Eq. 5-7}$$

The coefficient 0.002 in Eq. 5-7 is ε_{co}, which is the strain at peak strength for unconfined concrete.

Therefore:

$$\varepsilon_{co} = 0.002 \qquad \text{Eq. 5-8}$$

Substituting Eq. 5-8 in Eq. 5-7 gives Eq. 5-9.

$$\frac{\varepsilon cc}{\varepsilon co} = \frac{5f'cc}{f'co} - 4 \qquad \text{Eq. 5-9}$$

Or

$$\frac{\varepsilon_{cc}}{\varepsilon_{co}} = \frac{a\, f_{cc}'}{f_{co}'} - b \qquad \text{Eq. 5-10}$$

Where $a = 5 \quad and \quad b = 4$

Equation 5-9 was plotted in Fig. 5-23(a) with the abscissa and ordinate were

$\frac{\varepsilon_{cc}}{\varepsilon_{co}}$ and $\frac{f_{cc}}{f_c}$, respectively. The test results for confined ECC were also calculated in the same format and plotted in the same graph. Coefficients a and b in Eq. 5-10 were adjusted until the two graphs matched (Fig. 5-23 (b)). The new coefficient of a =2.7 and b =1.7 were used for the Fig. 5-23 (b). Because the test results for the unconfined ECC demonstrated that ε_{co} was 0.0025, the strain at peak stress was revised:

$$\varepsilon_{co(ECC)} = 0.0025 \qquad \text{Eq. 5-11}$$

Equation 5-11, a =2.7 and b =1.7 were replaced in Eq. 5-10 to derive Eq. 5-12 to estimate the strain at peak stress for confined ECC:

$$\varepsilon_{ce} = 0.0025\left[1 + 2.7\left(\frac{f'_{ce}}{f'_{co}} - 1\right)\right] \qquad \text{Eq. 5-12}$$

5.8.2. Popovics' Model

Popovics proposed equations to calculate stress-strain relationships for cementitious materials [Popovics, 1973]. Mander also used these equations for confined concrete stress-strain curves. To estimate the general stress-strain curve for confined ECC and to calculate the stress for a given strain, the Popovics" equations were used in the present study. Figure 5-24 shows the Popovics" general stress-strain relationship, which is represented by Eq. 5-13.

$$f = f_0 \frac{\varepsilon}{\varepsilon_0} \frac{n}{n - 1 + \left(\frac{\varepsilon}{\varepsilon_0}\right)^n} \qquad \text{Eq. 5-13}$$

Where

f_0 = Maximum strength

ε_0 = Strain at maximum strength

And n is defined depend on the material

$$n_{Concrete} = 0.4 \times 10^{-3} f_0 + 1.0 \qquad \text{Eq. 5-14}$$

$$n_{Mortar} = 0.2 \times 10^{-3} f_0 + 2 \qquad \text{Eq. 5-15}$$

$$n_{Paste} = 0.12 \qquad \text{Eq. 5-16}$$

The best correlation between the test results and Popovics" equation was achieved when n_{Mortar} (Eq. 5-15) was used in Eq. 5-13. Large aggregate are excluded from ECC mix design; therefore, ECC can be categorized as a mortar.

The test results are superimposed and compared with the calculated curves from Popovics" equation in Figs. 5-25 through 5-27. Note that to draw Popovics" curve (Eq. 5-13) f_0 and ε_0 should be known. For ECC f_0 and ε_0 correspond to f'_{ce} and ε_{ce}, respectively, which can be calculated from Eq. 5-5 or 5-6 and Eq. 5-12.

In Figs. 5-25 through 5-27 it can be noted that the strength in confined ECC curves drops after reaching peak strength and then is stabilized to a residual strength until very large strains. To duplicate this behavior, the ratio of the maximum strength of confined ECC to the residual strength for all samples was calculated and listed in Table 5-5. The average ratio and average minus the standard deviation were approximately 0.6 and 0.4, respectively. It was also necessary to determine the strain in the beginning of stabilized part of the curve. It was assumed that this strain (ε_f) corresponds to a stress of $0.4 f_0$ on the stress strain curve determined using Popovics" equation (Eq. 5-13). To calculate ε_f substitute $0.4 f_0$ in equation 5-13:

$$0.4 f_0 = f_0 \frac{\varepsilon_f}{\varepsilon_0} \frac{n}{n-1+\left(\frac{\varepsilon_f}{\varepsilon_0}\right)^n} \qquad \text{Eq. 5-17}$$

To calculate ε_f from Eq. 5-17, it was assumed that

$$\frac{\varepsilon_f}{\varepsilon_0} = y \qquad \text{Eq. 5-18}$$

Substituting Eq. 5-15 and 5-18 in Eq. 5-17 leads to an equation from which y can be determined.

$$0.4 = \frac{(0.2\times10^{-3}\ f_0+2)\ y}{0.2\times10^{-3}\ f_0+1+y^{(0.2\times10^{-3}\ f_0+2)}} \qquad \text{Eq. 5-19}$$

The y value was calculated for different f_0 in Eq. 5-19, and it was plotted in Fig. 5-28.

A regression analysis was performed and Eq. 5-20 was obtained.

$$\frac{\varepsilon_f}{\varepsilon_0} = -0.8Ln(f_0)+9.5 \qquad \text{Eq. 5-20}$$

$\varepsilon_f = \varepsilon_0 \times (-0.8Ln(f_0) + 9.5)$ Eq. 5-21

$\varepsilon_0 = \varepsilon_{ce}$ = Strain at peak strength from Eq. 5-12

$f_0 = f'_{ce}$ = Confined ECC strength from Eqs. 5-5 or 5-6

To draw the complete stress-strain curve for confined ECC, Eqs. 5-22 and 5-23 are recommended.

For $0 \le \varepsilon \le \varepsilon_f$ $$f = f'_{ce} \frac{\varepsilon}{\varepsilon_{ce}} \frac{n}{n - 1 + \left(\frac{\varepsilon}{\varepsilon_{ce}}\right)^n}$$ Eq. 5-22

For $\varepsilon_f \le \varepsilon \le \varepsilon_{ue}$ $f = 0.4 f'_{ce}$ Eq. 5-23

Where

$\varepsilon_f = \varepsilon_{ce} \times (-0.8Ln(f'_{ce}) + 9.5)$

5.8.3. Ultimate Strain ε_{ue}

The ultimate compressive strain of confined concrete in the Mander"s model is based on energy method. The ultimate strain was defined as the strain at which first hoop fractures. The area under stress-strain curves represents the total strain energy per unit volume required to "fail" the concrete. The increase in strain energy at failure resulting from confinement is provided by the strain energy capacity of the confining reinforcement as it yields in tension. By equating the ultimate strain energy capacity of the confining reinforcement per unit volume of concrete core (U_{sh}) to the difference in area between the confined (U_{cc}) and the unconfined (U_{co}) concrete stress-strain curves, plus additional energy required to maintain yielding in the longitudinal steel in compression, the longitudinal concrete compressive strain corresponding to hoop fracture can be calculated.

$U_{sh} = U_{cc} + U_{sc} - U_{co}$ Eq. 5-24

Equation 5-24 can be displayed as follow

$$\rho_s A_{cc} \cdot \int_0^{\varepsilon_{sf}} f_s d\varepsilon_s = A_{cc} \cdot \int_0^{\varepsilon_{cu}} f_c d\varepsilon_c + \rho_{cc} A_{cc} \cdot \int_0^{\varepsilon_{cu}} f_{sl} d\varepsilon_c - A_{cc} \cdot \int_0^{\varepsilon_{sp}} f_c d\varepsilon_c$$ Eq. 5-25

where ρ_s = volumetric transverse reinforcement ratio, A_{cc} = area of concrete core, f_s and ε_s =stress and strain in transverse reinforcement, ε_{sf} = fracture strain of transverse reinforcement, f_c and ε_c = longitudinal compressive stress and strain in concrete, ε_{cu} = ultimate longitudinal concrete compressive strain, ρ_{cc} = ratio of volume of longitudinal reinforcement to volume of concrete core, f_{sl} = stress in longitudinal reinforcement; ε_{sp} = spalling strain of unconfined concrete

Mander showed that the term of $\int_0^{\varepsilon_{sf}} f_s d\varepsilon_s = U_{sf}$ in Eq. 5-25 is effectively independent of bar size or yield strength, and may be taken (within ±10%) as

$$U_{sf} = 110 \quad MJ/m^3 \qquad \text{Eq. 5-26}$$

For the term $\int_0^{\varepsilon_{sp}} f_c d\varepsilon_c$ in Eq. 5-25, the area under the stress-strain curve for unconfined concrete is required. Mander showed that the area under the stress-strain curve for unconfined concrete may be approximated as

$$\int_0^{\varepsilon_{sp}} f_c d\varepsilon_c = 0.017\sqrt{f'_{co}} \quad MJ/m^3 \qquad \text{Eq. 5-27}$$

Substituting Eqs. 5-26 and 5-27 in Eq. 5-25 gives Eq. 5-28

$$110\rho_s = \int_0^{\varepsilon_{cu}} f_c d\varepsilon_c + \int_0^{\varepsilon_{cu}} f_{sl} d\varepsilon_c - 0.017\sqrt{f'_{co}} \quad MJ/m^3 \qquad \text{Eq. 5-28}$$

With a knowledge of f_c and f_{sl} as a function of longitudinal strain, the longitudinal concrete compressive strain, ε_{cu} at the fracture of the transverse reinforcement can be solved using Eq. 5-28.

In the current study there were no longitudinal bars in the samples and f_{sl} is unknown; therefore, Mander"s methods could not be applied directly. In the absence of sufficient data, however, it was decided to use Mander"s method to estimate the ultimate strain in ECC.

$$\varepsilon_{ue} = 0.004 + 1.4\rho_s f_y \frac{\varepsilon_{sm}}{f'_{ce}} \qquad \text{Eq. 5-29}$$

Where

$$\rho_s = \frac{4A_{sp}}{d_s s} \qquad \text{Eq. 5-30}$$

ρ_s =Volumetric transverse steel ratio

A_{sp} = Transverse steel area

d_s =Core diameter (center of spirals to center)

s_h =Spacing of transverse steel

f_y =Yield stress of transverse steel

ε_{sm} =Steel strain at maximum tensile stress

Figure 5-29 shows the complete stress-strain diagram for confined ECC and the corresponding equations. An illustrative example is presented in Appendix B to demonstrate the application of the proposed model.

5.8.3.1. Ultimate ECC Strain in Columns

Advantages of using ECC in column plastic hinges have been studied in several specimens at the University of Nevada, Reno. The specimens incorporating ECC included RNE [O'Brien and Saiidi, 2007], SMAC-2 [Wang and Saiidi, 2005], ECC bent in a four span bridge model [Cruz and Saiidi, 2010] PEFB bent, and SE-2. The observations and recorded data were utilized to estimate the ultimate strain at the column cores of these specimens.

Using similar triangle relationships, the deformation at the column core was calculated from vertical deformations on the face of column recorded by displacement transducers. The deformation at the core was divided by the gauge length to calculate the strain.

The column photos for SE-2, PEFB bent, and the ECC bent in the four spans bridge model clearly showed the core spalling during a particular runs; therefore, the ECC strain was calculated based on that run. The core failure was not observed in RNE and SMAC-2 and just minor cover spalling occurred. The ECC strain was calculated when ECC cover spalled in these two columns.

The measured strains are not necessary the ultimate values. The measured ECC strain in the specimens was called effective strain and it was shown with ε_e.

Table 5-6 lists the properties of columns including diameter, transverse reinforcement properties, unconfined and confined ECC strength, measured effective strain, and calculated ultimate strain from Eq. 5-29.

The measured ultimate strain was larger than that of calculated from Eq. 5-29 in all columns. This demonstrates that Mander‟s equation estimates the ultimate strain conservatively for ECC, and that material is able to undergo large deformation.

6. ANALYTICAL STUDIES

6.1. Introduction

Details of the analytical studies of the test models are explained in this chapter. The objective of the analytical studies was to determine the validity of the modeling assumptions based on the correlation between the analytical and experimental results.

OpenSees software was utilized to model the specimens. OpenSees is an open-source software for nonlinear seismic analysis of structures. This program includes several material models, element types, and analysis methods. Modeling the specimens using this program served three purposes. First, the pre-test analysis results were used to design the shake table model and to select the ground motion such that the specimens could be tested to failure without exceeding the physical limitations of the shake table facilities. The second reason for modeling the specimens in OpenSees was to develop and verify macro models for precast elements that can be used in real bridge models. The third reason was to develop a reliable analytical model to be used for parametric studies.

Material models, sections, elements, and an OpenSees model for each specimen are described. Comparison of the analytical and experimental results including force-displacement envelopes, force-displacement hysteresis curves, displacement histories, and the maximum drift ratios for all specimens are presented and discussed. For segmental columns, additional comparison of the analytical and experimental results was made including residual displacements, opening between lower segments, and the post-tensioning forces.

6.2. OpenSees Model for Segmental Columns

6.2.1. Introduction

A detailed OpenSees model for each column was developed. Various uniaxial materials, different sections, and elements were utilized to model different components of the segmental columns.

The columns were modeled by assigning the elements with appropriate cross sections between nodes. The column sections were defined with a fiber model using the measured material properties of the test columns. This model was capable of simulating force, displacement, post-tensioning force, segment separation, and material strain.

6.2.2. Material Models

6.2.2.1. Concrete

The “uniaxialMaterial Concrete01” was used to model the unconfined and confined concrete fibers. This is a uniaxial concrete model based on model developed by Kent and

Park, (1971) with degrading linear unloading/reloading stiffness according to the study by Karsan and Jirsa [OpenSees Manual, 2005]. The tensile strength of concrete was neglected to account for the possible existing thermal and shrinkage cracks. The concrete01 parameters and its typical hysteretic stress-strain relation are shown in Fig. 6-1.

Unconfined concreted strength used in the pre-test analysis was 5 ksi (34.5 MPa). The strain at the maximum strength and failure strain for unconfined concrete were assumed to be 0.002 and 0.004, respectively. The ultimate strength was taken as 85% of the maximum strength and was equal to 4.25 ksi (29.3 MPa). The Mander"s model [Mander, et al., 1988] was used to determine the properties of the confined core in the concrete segments. In the pre-test analysis, the maximum strength of 7.67 ksi (52.8 MPa) and ultimate strength of 6.6 ksi (45.5 MPa) were used for the confined concrete. The strain at the maximum strength and failure strain were 0.0073 and 0.021, respectively.

The concrete strength used in the post-test analysis was based on the measured cylindrical samples strength on the test day. The compressive strength test results for different segmental columns are listed in Table 2-2. The strain rate effects were included in the post-test analysis of the columns. The strain rate modification factors were discussed in Chapter 3 for all segmental columns. Modeling parameters of the concrete material for the post-test analytical models and the strain rate factors are listed in Table 6-1. This table includes the unconfined and confined properties of concrete segments in different segmental columns before applying the strain rate factors. The base and second segments of SE-2 were made out of ECC. Since there was no model available to account for strain rate effect on ECC, the effect of strain rate factor was neglected on the ECC strengths. In addition, none of the strain gauges in SE-2 reached the failure strain of concrete (6000 μs); therefore, the strain rate factor was not calculated for concrete used in segments third and fourth. The concrete material model in OpenSees requires a residual strength value. The residual strength was assumed to be 40% of the maximum strength. Defining the residual strength and ultimate strain using Mander"s equations could not reflect the concrete failure following by degrading capacities of the column in the OpenSees; therefore, the residual strength was defined as 40% of the maximum strength. To define the ultimate strain, the descending branch of Mander"s stress-strain curve was extended until reaching 40% of the maximum strength, and the corresponding strain was considered as ultimate strain.

6.2.2.2. Steel Reinforcement

The "uniaxialMaterial Steel02" was used to model the steel in the pre-test analysis with yield strength of 60 ksi (413.7 MPa), strain hardening ratio of 0.02, and modulus of elasticity of 29000 ksi (199948 MPa). Strain hardening ratio was defined as the slope ratio of the post-yield tangent to the initial elastic tangent in stress-strain curve of steel material [OpenSees Manual, 2005]. In addition, Steel02 includes parameters of R0, cR1, and cR2 that control the transition from elastic to plastic branch. The recommended values of R0=18, cR1=0.925, and cR2=0.15 were used in the models. The Steel02 material parameters and typical hysteretic stress-strain relations are shown in Fig. 6-2.

The steel strength and strain hardening ratio were modified after measuring the bar properties. Table 6-2 lists the steel strength, strain rate factor, and strain hardening ratio in different models in the post-test analysis.

6.2.2.3. Rubber

Rubber in SBR-1 was modeled with "uniaxialMaterial Elastic". The material stress-strain relationship is shown in Fig. 6-3. The modulus of elasticity (E) was calculated based on compression stiffness of the bearing (Eq. 6-1).

$$E_c = 5.6 G S^2 \qquad \text{Eq. 6-1}$$

Where

G = Shear modulus (obtained from material test)

$$S = \text{Shape factor} = \frac{Area\ of\ pad}{Area\ of\ the\ pad\ circumference} \qquad \text{Eq. 6-2}$$

With the shape factor of 14 and rubber shear modulus (G) of 115 psi (1 MPa), the compression stiffness of rubber was equal to 126 ksi (868 MPa).

6.2.2.4. FRP

The FRP jacket was not directly modeled in OpenSees model; rather the effect of FRP on concrete confinement was included in the parameter of the "uniaxialMaterial Concrete01". The Saiidi"s confinement model [Saiidi, et al., 2005] was used for the FRP wrapped concrete in SF-2 and SC-2R. This model defines a bilinear stress-strain relationship for FRP-confined concrete (Fig. 2-35). Details of this model are presented in section 2.3.5.2.

In the pre-test analysis E_j (the modulus of elasticity of FRP laminate) of 13500 ksi (93080 MPa) was used to calculate the confined concrete strength. After the tests, based on the measured FRP material properties, an E_j of 11000 ksi (75842 MPa) was used to calculate the properties of confined concrete.

There was no available model for the repaired concrete using FRP jacket; therefore, the Saiidi"s confinement model [Saiidi, et al., 2005] was modified to calculate the concrete properties in the lower segments of SC-2R by assuming that the concrete strength was 50% of its original compressive strength. The strain at the break point (ε_{cy}) for confined damaged concrete was assumed to be 0.004, which was twice original model (ε_{cy} = 0.002). By defining a larger strain at the break point, a lower initial stiffness was defined for repaired concrete material model. Table 6-3 lists the modeling parameters of the FRP confined concrete material in the post-test analysis. The strain rate effects were included in the post-test analysis of the columns. The confinement effect of spirals was neglected; therefore, unconfined and confined concrete properties were similar. Figure 6-4 shows the stress-strain model for the original and damaged concrete wrapped with FRP.

6.2.2.5. ECC

The "uniaxialMaterial Concrete02" was used to model the unconfined and confined ECC in the pre-test analysis of SE-2. This is a uniaxial concrete material model with tensile strength and linear tension softening. The maximum strength of 5 ksi (34.5 MPa) was assumed for the compressive strength in the pre-test analysis. The tensile strength and tensile modulus of elasticity were assumed to be 10% of compressive strength and compressive modulus of elasticity based on the previous studies on ECC stress-strain behavior [Keith, et al., 2003]. The stress-strain relation for concrete02 is shown in Fig. 6-5.

The confined ECC properties were calculated using Mander‟s model [Mander, et al., 1988] in the pre test analysis. The new equations for stress-strain model of confined ECC presented in Chapter 5 were utilized to calculate confined ECC properties in the post-test analysis. Modeling parameters of the ECC for the post-test analytical models are listed in Table 6-4.

The "uniaxialMaterial Concrete01" was used to model the ECC in post-test analysis and the tensile strength of ECC was neglected. The main failure mode of SE-2 was failure of ECC due to the joint separation at the interface between the base and second segments. The tensile capacity of ECC was not used at the joint during the test; therefore, it was neglected in the analysis. Since there was no model available to account for strain rate effect on ECC, the effect of strain rate factor was neglected on the ECC strengths.

6.2.2.6. Post-Tensioning Rods

The "uniaxialMaterial ElasticPP" was used to model the post-tensioning rod constitutive relationship. The general stress-strain behavior of elastio-plastic is shown in Fig. 6-6. A modulus of elasticity of 27000 ksi (186158 MPa) was used. An initial strain corresponding to the initial force in the rod was specified. The initial force in the rod was divided by the area and modulus of elasticity to calculate the initial strain. The strain at which the material reached the plastic state was defined with a large value (1E15) in both tension and compression.

6.2.2.7. Material for Modeling Separation between Segments

As explained in Chapters 3, the base and second segments separated during some of the earthquake runs. Joint separation was simulated in the OpenSees model.

A material tolerating only compression, the "uniaxialMaterial ENT" (elastic no tension) was assigned to to zero length elements, one on each side of the joint in the loading plane. A large modulus of elasticity equal to 10000 ksi (69000MPa) was assigned to the material to prevent penetration of the segments into each other. No stiffness or strength was provided in tension to simulate the lack of force transfer during opening.

6.2.3. Analytical Model

The analytical model for the segmental columns used in the OpenSees analyses is shown in Fig. 6-7. The model includes 20 nodes and 20 elements. The lowermost node represents the connection between the column and the footing. The materials were defined as discussed in section 6.2.2. The column sections were defined using a fiber model with the measured material properties of the test columns. In the fiber element model, equilibrium between the external forces and the fibers forces and deformation compatibility among the fibers are satisfied. The fibers shorten or elongate so that plane sections remain plane after deformation. The steel longitudinal bars were modeled in the base segment because they were anchored in the footing and the yielding was expected. Due to the discontinuity between segments 2 and higher, the longitudinal reinforcement was not expected to yield. The "nonlinearBeamColumn" element was used to model the segments in the columns. Variable sections consisting of different materials were assigned to the elements in different segmental columns. The P-Delta effect was included in the model. Each of the base and second segments were defined with two elements. One element was defined for the third and fourth segments since no segment separation was expected between them. The number of integration points was selected such that the sub-element length was the same along the length of the member. The number of integration points for the base and second segment elements was 2 and for the third and fourth segments element was 5.

To model the bond-slip rotation, an additional node was defined at the base of the column. This node was connected to the footing node with a "zeroLength element". The zeroLength element included a tri-linear "uniaxialMaterial Hysteretic" material with bond-slip rotation parameters. The bond-slip model and method of calculation are discussed in section 6.2.4.2.

The most severe concrete spalling in segmental columns was observed at the interface between the base and second segments. This was because the top of the base segment and bottom of the second segment were not confined. To simulate this assumption, unconfined sections were defined for the elements with the length of 3.5 in. (89 mm) above and below the interface.

Using the "elasticBeamColumn element" and "zeroLength element" the interface between the base and second segments was modeled in the OpenSees. The elastic beam-column element was used to model the two surfaces of the base and second segments. In the test specimens, the displacement transducers that measured the opening during the tests were attached between two pairs of horizontal rods located 3.5 in. (89 mm) above and below the interface. Therefore, four elasticBeamColumn elements at the same locations were defined in the OpenSees model. A large value equivalent to 1000000 ksi (6894760 MPa) was assigned to the modulus of elasticity of elastic elements to ensure rigid behavior. Two vertical zero length elements including ENT (elastic no tension) material defined in section 6.2.2.7 connected the interface surfaces at two extreme ends. The calculation of opening from the analytical results is discussed in section 6.2.5.8.

The unbonded PT rod was modeled by multiple "CorotTruss element". A co-rotational formulation adopts a set of co-rotational axes that rotate with the element, thus taking into account an exact geometric transformation between local and global frames of [OpenSees Manual, 2005]. The area of the rod was 1.95 in^2 (1258 mm^2) based on the manufacturer data. The uniaxialMaterial ElasticPP defined in section 6.2.2.6 was assigned to this element. Post-tensioning rod elements were defined at the same height of those of the column. Using equalDOF command in OpenSees, horizontal deformation and rotation of PT nodes became similar to that of the column nodes. The first node in the PT element was defined at 40 in. (1016 mm) under the top surface of footing to simulate the exact length of PT rod in the specimens. The mass and the axial load of 80 kips (355 kN) were assigned to the top column node.

Several recorders were defined in the model to capture the column forces and displacements, the force in the PT rod, joint opening, and stress-strain in the sections during pushover analyses and nonlinear dynamic analyses. The input OpenSees files for dynamic analysis of SC-2, SBR-1, SF-2, SE-2 and SC-2R are presented in Appendix C.

6.2.4. Post-Test Analyses

6.2.4.1. Strain Rate Effect

Material strength increases by increasing the rate of loading. The strain rate factors were calculated for concrete and steel and the results were presented for each column in Chapter 3. The strain rate factors were applied to the concrete and steel strengths in post-test analyses.

6.2.4.2. Bond-Slip Model

The bond slip effects were not included in the pre-test analytical models. Bond-slip rotation is the result of yield penetration of the longitudinal bars into the footing. The bond-slip effect can be modeled with a lumped nonlinear rotational spring at the bottom of the columns.

Wehbe et al. (1999) developed a method to calculate the bond-slip rotations associated with cracking, yielding, and the ultimate capacity of the RC columns. This method was utilized to find the properties of the rotational spring at the base of the segmental columns in post-test analyses. Wehbe‟s method was developed based on a tri-linear stress-strain relationship for steel. For # 11 [Φ 35 mm] or smaller deformed bars, the basic bond strength of tension bars can be found using the following equations:

$$u = \frac{20\sqrt{f'_c}}{d_b} \leq 5.5 \qquad \text{(MPa)} \qquad \text{Eq. 6-3}$$

$$u = \frac{9.5\sqrt{f'_c}}{d_b} \leq 800 \qquad \text{(ksi)} \qquad \text{Eq. 6-4}$$

Where u is the bond strength and d_b is the bar diameter.

Assuming a constant bond stress distribution along the embedded bar length, the development length can be calculated from equilibrium as follows:

$$l_d = \frac{f_s d_b}{4u} \qquad \text{Eq. 6-5}$$

Where l_d is the development length, f_s is the bar stress at the interface, d_b is the bar diameter, and u is the bond strength. The bar slippage can be calculated by integrating the strain profile along the development length as follows:

$$\delta l = \int_0^{l_d} \varepsilon_s dz \qquad \text{Eq. 6-6}$$

Where δl is the additional bar extension at the interface, ε_s is the bar strain at the depth of z from the interface, and l_d is the development length. The bond-slip rotation is assumed to occur about the neutral axis of the column cross section at the connection interface as follows:

$$\theta_b = \frac{\delta l}{d - c} \qquad \text{Eq. 6-7}$$

Where θ_b is the bond-slip rotation, d is the effective depth of the column section, c is the compression region depth of the column section at the interface. δl was calculated at yield and ultimate moment as follows:

$$\delta l = \frac{d_b f_s^2}{8E_s u} \qquad \text{if } f_s \le f_y \qquad \text{Eq. 6-8}$$

$$\delta l = \frac{d_b}{8u}(\varepsilon_s f_s - \varepsilon_s f_y + \varepsilon_y f_s) \qquad \text{if } f_s > f_y \qquad \text{Eq. 6-9}$$

Where E_s is steel modulus of elasticity, ε_y and f_y are yield strain and stress, respectively.

Moment-curvature analyses were conducted to calculate strains required for bond slip calculations. Xtract software was used for the analyses [Chadwell, 2007]. The measured material properties were used in the analyses.

The bond-slip spring was modeled by a tri-linear “uniaxialMaterial Hysteretic” material composed of the bilinear idealized curve followed by an extension branch with zero stiffness. It should be noted that the spring properties are identical in the positive and negative directions because the column sections are symmetric. In this material, the stiffness of unloading branch is a function of initial stiffness, ductility, and the factor of β. β is degrading factor of unloading stiffness and it needs to be defined by the user. The unloading branch was defined between the positive M_u and negative M_y (Fig. 6-8). The slope of unloading branch was defined as:

Slope of unloading branch= $K_1 \times {\mu_\theta}^{\beta}$ Eq. 6-10

Where

K_1 = Initial slope of the moment-rotation curve (Fig. 6-8)

$$\mu_\theta = \frac{\theta_u}{\theta_y} \qquad \text{Eq. 6-11}$$

Therefore, β can be calculated as follows:

$$\beta = -\frac{\log \alpha}{\log \mu_\theta} \qquad \text{Eq. 6-12}$$

$$\alpha = \frac{\textit{Slope of unloading branch}}{K_1} = \frac{M_y + M_u}{M_y(\mu_\theta + 1)} \qquad \text{Eq. 6-13}$$

Where M_y and M_u are effective yield and ultimate moments, and θ_y and θ_u are corresponding bond-slip rotations, respectively. The coordinates of yield and ultimate points of the bond-slip rotation springs are listed in Table 6-5.

6.2.5. Analytical Results

6.2.5.1. Force-Displacements Envelopes and Pushover Curves

Pushover analyses of the test columns were conducted with drift increment of 0.05%. The force-displacement response of columns under earthquake motions was calculated in OpenSees and the envelopes of response in the positive and negative direction of displacement were averaged. The calculated pushover analysis results and force-displacement envelopes were compared with the measured load-deflection envelope curves of columns. It can be seen in Fig. 6-9 that the pushover analysis result for SC-2 and the envelope of dynamic analysis were in close agreement. It will be seen subsequently that the same trend existed for other columns.

The initial stiffness of SC-2 was well estimated by the analytical model. Generally, the strength of the column was overestimated by OpenSees. The calculated maximum lateral load capacity was 23.5 kips (104.5 kN), which was 6.3% larger than the maximum measured capacity. The calculated ultimate lateral load capacity of SC-2 was 18.8 kips (83.6 kN) and was 7% larger than the measured ultimate capacity.

The measured initial stiffness of SBR-1 was well calculated by the analytical model. Figure 6-10 shows that the lateral load capacity of SBR-1 was slightly overestimated in model. The calculated maximum lateral load capacity was 26.3 kips (116.9 kN), which was 0.7% lower than the maximum measured capacity.

Close agreement was seen between the measured and calculated initial stiffness of SF-2 (Fig. 6-11). The calculated maximum lateral load capacity was 30.7 kips (136.5 kN), which was 5% larger than the maximum measured capacity. The measured and calculated ultimate lateral load capacities were 26.1 kips (116.1 kN) and 30.7 kips (136.5 kN), respectively, which means that the analytical model overestimated the lateral load capacity by 17%. The difference between the measured and calculated capacity can be attributed to the FRP confined concrete model, which does not include the degrading branch after concrete failure (Fig. 6-4). The drop in column capacity was due to the concrete failure at lower segments interface, which was not reflected in the FRP confined concrete model.

The initial stiffness of SE-2 was well estimated by the analytical model (Fig. 6-12). Generally, the analytical model overestimated the response of SE-2. The calculated maximum lateral load capacity was 24.4 kips (108.4 kN), which was 17% larger than the maximum measured capacity. The calculated ultimate lateral load capacity in SE-2 was 23.9 kips (106.3 kN), which was 19.2 % larger than the measured ultimate capacity. The overestimation in capacity of SE-2 can be attributed to the ECC material model that did not reflect the ECC failure at the interface of base and second segments.

Figure 6-13 shows that the measured and calculated initial stiffness of SC-2R were well correlated. Generally, very close agreement was seen between the measured and calculated response of SC-2R. The maximum measured lateral load capacity of SC-2R was 32 kips (142.33 kN). The OpenSees model calculated the maximum lateral load capacity of 32.3 kips (143.7 kN), which was only 0.9 % larger than the maximum measured capacity.

6.2.5.2. Dynamic Analysis

Nonlinear dynamic analyses were conducted for all segmental columns. Achieved shake table motions for different runs were spliced and used in dynamic analyses. A damping ratio of 5% was used in the analyses. The measured and calculated cumulative force-displacement hysteresis curves, displacement histories, the maximum drift ratio and residual displacements, PT forces, and the history of opening between the base and second segments were superimposed to evaluate the accuracy of the applied techniques in calculating the nonlinear response of the test columns.

6.2.5.3. Cumulative Force-Displacement Curves

The measured and calculated cumulative force-displacement hysteresis curves for SC-2, SBR-1, SF-2, SE-2, and SC-2R are plotted in Figs. 6-14 through 6-18, respectively.

Good correlation was observed between the measured and calculated force-displacement response of SC-2 (Fig. 6-14). The maximum calculated lateral load capacity of the column in the positive direction of displacement was equal to that of measured capacity. The maximum lateral load capacity was overestimated in the negative direction of motion by 12%. The ultimate displacement was slightly underestimated in the positive direction of motion.

Very close agreement was observed between the measured and calculated force-displacement response of SBR-1 in the positive direction of displacement (Fig. 6-15). The force was overestimated in the negative direction of displacement in SBR-1. The maximum calculated lateral load capacity in the negative direction was 21% larger than the maximum measured capacity during the last run. The ultimate displacement was overestimated in the negative direction of displacement by 30% during the last run.

The calculated force-displacement response of SF-2 was well correlated with the experimental results for Runs 1 through 7. However, the measured drop in the lateral load capacity of SF-2 during the last run was not seen in the analytical results (Fig. 6-16). The maximum force was overestimated in the positive and negative directions of displacement by approximately 15% and 27%, respectively during Run 8. The maximum displacement in the positive direction of motion was underestimated by 22% during Run 8 but the maximum displacement in the negative direction of motion was overestimated by 28%.

Generally, close agreement was seen between the calculated and measured force-displacement response of SE-2 in the positive direction of displacement (Fig. 6-17). The calculated maximum lateral load capacity and displacement in the negative direction of motion were respectively 30% and 21% larger than those of measured responses during Run 8.

The calculated cumulative force-displacement response of SC-2R was in very close agreement with that of measured response (Fig. 6-18). The maximum displacements in the positive and negative direction of displacements were underestimated by 8% and 16%, respectively.

6.2.5.4. Dissipated Energy

The dissipated energy was calculated by integrating the area enclosed by the force displacement hysteretic curves. The measured and calculated dissipated energy and the percentage of their difference are listed in Table 6-6. The best correlations between the measured and calculated data were achieved in SF-2 and SE-2. The dissipated energy was underestimated in SC-2, SC-2R and SBR-1 by 28%, 21%, and 19%, respectively. Considering the large number of cyclic response, these differences are satisfactory.

6.2.5.5. Displacement Histories

The measured and calculated displacement histories for each run in SC-2, SBR-1, SF-2, SE-2, and SC-2R are plotted in Figs. 6-19 through 6-28.

The analytical model in SC-2 overestimated the displacements during the low-amplitude Runs 1 through 3 (Fig. 6-19 (a), (b), (c)), but led to good correlation during stronger motions. The large difference between the measured and calculated displacements during the initial runs was due to the relatively large damping that the test model experienced in early runs. Analytical models typically treat the system as a linear model during smaller amplitude runs and underestimate the hysteretic damping. The calculated and measured residual displacements were in close agreement.

Generally, the displacement history of SBR-1 was well estimated by the analytical model for all runs (Figs. 6-21 and 6-22). The maximum calculated displacements were in close agreement with that of measured response in the positive direction. The displacements in negative direction were slightly overestimated during Runs 5 through 7. Good correlation was seen between the calculated and measured residual displacements.

Reasonable correlation was seen between the measured and calculated displacement histories of SF-2 during Runs 3 through 8 in SF-2 (Figs. 6-23 and 6-24). The calculated peak displacements were slightly larger than the measured peak displacements during Runs 5 through 7. The residual displacements were well estimated by the analytical model.

The displacement histories of SE-2 were overestimated by the analytical model during Runs 1 and 2 due to the relatively large damping that the model experienced in early runs (Fig. 6-25 (a) and (b)). Reasonable match was observed between the calculated and measured displacements during Runs 3 through 8 (Figs. 6-25(c), (d), and 6-26). The negative peak displacements were slightly overestimated during all runs. The calculated residual displacements correlated closely with that of measured until Run 6. The calculated residual displacements were lower than the measured residual displacements during Runs 7 and 8.

Very good correlation was seen between the measured and calculated displacement histories of SC-2R during Runs 2 through 5 (Figs. 6-27(b), (c), (d), and 6-28). The calculated displacements were overestimated during Run 1 because of relatively large damping that the model experienced during that run. The positive peak displacements were slightly underestimated during Runs 4 and 5. The calculated and measured residual displacements were in close agreement.

6.2.5.6. Maximum Drift Ratios and Residual Displacements

The maximum drift ratios versus PGA and the residual drift ratios versus PGA were calculated for each column from the analytical model results and were compared with those of measured responses during the experiment. The maximum drift ratio was defined as the maximum displacement during each run over the height of column (72 in.

(1829 mm). The residual drift ratio was defined as the ratio of residual displacement over the height of the column. Differences between the measured and calculated residual drift ratios were observed during the high amplitude motions. The calculated hysteretic behavior of column was slightly different from the measured ones due to the discrepancy between the pinching model of material used in OpenSees and the actual response of the material. It is believed that approximations in material modeling led to the differences between the measured and calculated residual displacements during high amplitude motions.

Very good correlation was observed between the measured and calculated maximum drift ratios for column SC-2 during all runs (Fig. 6-29). The calculated residual drift ratios are compared with that of measured data in Fig. 6-30. The correlation between the measured and calculated results was very good during Runs 1 through 6. The calculated residual drift ratio was larger than the measured residual drift ratio by 130% during Run 7. .

Figure 6-31 displays the measured and calculated maximum drift ratios versus PGA for SBR-1. The measured and calculated maximum drift ratios were well correlated in all runs. The calculated and measured residual drift ratios are compared in Fig. 6-32. Reasonable agreement was seen between the measured and calculated data during Runs 1 through 6. The calculated residual drift ratio was smaller than the measured residual drift ratio by 35% during Run 7.

The measured and calculated maximum drift ratios for SF-2 are compared in Fig. 6-33. Close agreement was seen between the measured and calculated data during all runs except Run 7 and 8. The analytical model overestimated the maximum drift ratio during Run 7 and underestimated it during Run 8. The FRP jacket ruptured and concrete failed in SF-2 during the last run. Differences between the material model of OpenSees and the realistic response of the material could be a reason for inaccurate estimation of maximum drift ratio during high amplitude motions. Figure 6-34 shows the measured and calculated residual drift ratios for SF-2. Close agreement was seen between the measured and calculated data during Runs 1 through 7. The calculated residual drift ratio was 30% lower than the measured residual drift ratio during the last run.

Figure 6-35 displays the measured and calculated maximum drift ratios versus PGA for SE-2. The measured and calculated drift ratios were well correlated in all runs except Runs 7 and 8. The measured maximum drift ratios were underestimated by 15% and 20% during Runs 7 and 8, respectively. The calculated and measured residual drift ratios are compared in Fig. 6-36. The residual drift ratio during Run 7 was underestimated by 96% but was overestimated by 44% during Run 8.

Very good correlation was seen between the measured and calculated maximum drift ratios in SC-2R (Fig. 6-37). The calculated and measured residual drift ratios versus PGA are shown in Fig. 6-38. The measured and calculated data were good correlated during Run 1 through 4. The measured residual drift ratio was 30% larger than the measured residual drift ratio during the last run.

6.2.5.7. Post-Tensioning Rod Force

The cumulative calculated PT force versus displacement was compared with that of the measured data for each column. The maximum PT force was overestimated by approximately 50% in segmental columns during the last run. The force in the rod linearly increased with increase of displacement in the analytical model; therefore, a large increment was seen in the PT force under high amplitude motions when the column underwent large displacements. An overestimation of PT force up to 50% was also seen in previous researches by Hews, et al., (2001). They explained this difference due to the underestimation of neutral axis depth by the Mander model. Mander model predicts higher confined concrete compressive strengths than what may be appropriate for high strength concrete. This would result in overestimation of the tendon strain increase.

Figure 6-39 compares the measured and calculated PT forces in SC-2. The maximum calculated PT force exceeded the measured force by 47%. The overestimation in SBR-1 was 126% (Fig. 6-40) but was 47% in SF-2 (Fig. 6-41).

The analytical model overestimated the PT force under large motions in SE-2 and SC-2R by 43% and 38%, respectively (Fig. 6-42 and Fig. 6-43).

6.2.5.8. Separation between Segments

Separation between the base and second segments was calculated from displacement history of elements that were defined above and below the interface (Fig. 6-44). The vertical distance between the elements was 7 in. (178 mm). Equation 6-14 was used to calculate the opening from the displacement histories.

$$\text{Segment separation} = 7-\sqrt{(X_1-X_2)^2+(7-Y_1+Y_2)^2}\ \text{(in.)} \qquad \text{Eq. 6-14}$$

Where,

X_1 and Y_1 = horizontal and vertical displacement of upper elements end

X_2 and Y_2 = horizontal and vertical displacement of lower elements end

Figures 6-45 through 6-64 display the comparison between the measured and calculated opening histories on the north and south sides of columns SC-2, SBR-1, SF-2, SE-2, and SC-2R, respectively. The positive values indicate the opening between the base and second segments. The negative values reflect the penetration of the second segment into the base segment because of concrete spalling at the interface between the lower segments. The negative values were minor in early runs since concrete at interface between the base and second segments was undamaged.

The calculated opening was larger than the measured opening during Run 2 on the north and south sides of SC-2 (Fig. 6-45 (b) and 6-47 (b)). Good correlation was seen between the measured and calculated opening on the north side of SC-2 during Runs 3 through 7

(Figs. 6-45(c), (d), and 6-46). The negative peak openings on the north side of the column were slightly overestimated during Runs 5 and 6. The calculated positive openings were underestimated on the south side of SC-2 during Run 3 through 5 (Figs. 6-47 (c), (d), and 6-48 (a)). The negative opening on the south side of SC-2 was overestimated during Runs 6 and 7 by 75% and 140%, respectively (Fig. 6-48 (b) and (c)). As discussed earlier the negative values of opening indicated penetration of the second segment into the base segment and it was modeled with an element incorporating high compressive modulus of elasticity. The over prediction in negative values during the high amplitude motions can be attributed to the insufficient compressive modulus of elasticity assigned to the elements representing the opening-closing at the joint.

Generally, good correlation was seen between the measured and calculated opening on the north and south sides of SBR-1 during Runs 1 through 6 (Figs. 6-49 through 6-52). The maximum calculated openings on the south and north side of SBR-1 were approximately twice of the measured opening during Run 7 (Figs. 6-50 (c) and 6-52 (c)).

Close agreement was seen between the measured and calculated opening during Runs 5 through 8 on the north and south sides of SF-2 (Figs. 6-53 through 6-56). The opening was slightly overestimated during Run 2 on both sides of column (Figs. 6-53 (b) and 6-55 (b)). The analytical model underestimated the opening on the north and south sides of SF-2 during Runs 3 and 4.

The calculated openings were larger than the measured openings on the north side of SE-2 during Runs 2 and 3 (Figs. 6-57 (b) and (c)). Good correlation was seen between the measured and calculated openings on the north side of SE-2 during Runs 4 through 8. The opening on the south side of SE-2 was overestimated during Run 2 (Fig. 6-59 (b)), but good estimation was made during Runs 3 through 8. A negative shift in the calculated opening was seen during Runs 7 and 8 on the south side of SE-2 (Figs. 6-60 (c) and (d)). The negative shift in the opening data was consistent with the poor correlation between the measured and calculated residual displacement in the previous run. The underestimation of residual displacement was attributed to discrepancy between the pinching model of material used in OpenSees and the realistic response of the material.

The openings were overestimated on the north side of SC-2R during Runs 1 and 2 (Figs. 6-61 (a) and (b)). The measured and calculated openings were not closely correlated during Runs 3 to 5 on the north side of SC-2R (Figs. 6-61 (c), (d), and 6-62). A large jump was observed in the measured opening due to malfunction of displacement transducers. The openings on the south side of SC-2R were underestimated by the analytical model during Runs 2 through 5 (Figs. 6-63 (b), (c), (d), and 6-64). As discussed in section 3.2.6.8, the transducer on the south and north side of SC-2R malfunctioned during the high amplitude motions and the difference between the measured and calculated openings was attributed to the error in the measured data caused by malfunction of transducers as explained in Sec. 3.2.6.8.

6.3. OpenSees Model for Two-Column Bent

6.3.1. Introduction

A detailed OpenSees model was developed for the two-column bent. Various uniaxial materials, different sections, and elements were utilized in the analytical model.

The columns were modeled by assigning elements with appropriate cross sections between nodes. The column sections were defined with a fiber model using the measured material properties. The analytical model was capable of simulating force, displacement, and material strains.

6.3.2. Material Models

6.3.2.1. Concrete

The "uniaxialMaterial Concrete01" was used to model the unconfined and confined concrete fibers in upper part of RC-ECC column. The description of concrete01 in OpenSees was provided in section 6.2.2.1 and its parameters and typical hysteretic stress-strain relation were shown in Fig. 6-1.

The unconfined concreted strength used in the pre-test analysis was 5.0 ksi (34.5 MPa). The strain at the maximum strength and failure strain for unconfined concrete were assumed to be 0.002 and 0.004, respectively. The ultimate unconfined strength was taken 0.85 of the maximum strength and was equal to 4.25 ksi (29.3 MPa). The Mander‟s model [Mander, et al., 1988] was used to determine the properties of the confined core. Modeling parameters of the concrete material for the post-test analytical model were based on the measured strength. The strain rate factor was applied. Table 6-7 lists the unconfined and confined properties of concrete in upper part of RC-ECC column before applying the strain rate factors.

6.3.2.2. ECC

The "uniaxialMaterial Concrete02" was used to model the unconfined and confined ECC in pre-test analysis. This is a uniaxial concrete material model with tensile strength and linear tension softening. The stress-strain relation for concrete02 is shown in Fig. 6-5. A maximum strength of 5.0 ksi (34.5 MPa) was assumed for compressive strength in the pre-test analysis. The tensile strength and tensile modulus of elasticity were assumed to be 10% of the compressive strength and the compressive modulus of elasticity based on the previous studies on ECC stress-strain behavior [Keith, et al., 2003].

The confined ECC properties were calculated from Mander‟s model [Mander, et al., 1988] in the pre-test analysis because no confined models were available for ECC. The new equations for stress-strain model of confined ECC presented in Chapter 5 were utilized to calculate confined ECC properties in the post-test analysis. Since there was no model available to account for strain rate effect on ECC, the effect of strain rate factor was neglected on the ECC strengths. Modeling parameters of the ECC for the post-test analytical models are presented in Table 6-8.

6.3.2.3. FRP Encased Concrete

The “uniaxialMaterial Concrete01” was used to model the FRP encased concrete in the FRP Column. Saiidi‟s confinement model [Saiidi, et al., 2005] was used to determine the confined concrete parameters. The Saiidi‟s model defines a bilinear stress-strain relationship for FRP-confined concrete (Fig. 2-35). A detailed explanation of this model is presented in section 2.3.5.2. In this model the module of elasticity of the FRP tube in the hoop direction was assumed to be 1850 ksi (12755 MPa) and the rupture stress of the fiber assumed to be 34 ksi (234 MPa) based on the manufacturer data. Modeling parameters of the FRP encased concrete for the post-test analytical models are presented in Table 6-9.

6.3.2.4. Steel

The “uniaxialMaterial Steel02” was used to model the steel in the pre-test analysis with yield strength of 60 ksi (413.7 MPa) and modulus of elasticity of 29000 ksi (199948 MPa). Strain hardening ratio was defined as the slope ratio of the post-yield tangent to the initial elastic tangent in stress-strain curve of steel material [OpenSees Manual, 2005]. Strain hardening ratio of 0.02 was assumed in pre-test analysis. In addition, Steel02 includes parameters of R0, cR1, and cR2 that control the transition from elastic to plastic branch. The recommended values of R0=18, cR1=0.925, and cR2=0.15 were used in the models. The Steel02 material parameters and typical hysteretic stress-strain relations are shown in Fig. 6-2. The steel strength and strain hardening ratio were modified after measuring the bar properties. The strain rate factor was applied to the yield strength. Table 6-10 lists the steel strength in RC-ECC and FRP column in the post-test analysis.

6.3.2.5. FRP Tube

Glass fibers in the FRP tube were aligned at ±55° to provide strength in hoop as well as longitudinal directions. In the pre-test analysis longitudinal behavior of the FRP tube was defined using a model that was proposed by Zhu, (2004). This model assumes a tri-linear “uniaxialMaterial Hysteretic” material to define the longitudinal behavior of the FRP tube. Figure 6-65 shows the stress-strain hysteresis curve associated with this material. The points that define the model are shown on the graph. Pinching factor for strain, pinching factor for stress, damage due to ductility, damage due to energy, and degrading factor of unloading stiffness were taken as 1, 1, 0, 0, and 0.3, respectively [Zhu, 2004].

It was determined from post-test analysis that using the material model proposed by Zhu et al. (2004) substantially underestimates the FRP column lateral load capacity. Therefore a parametric study was conducted and a modified FRP material model was proposed. The initial modulus of elasticity in Zhu‟s model was 1460 ksi (10066 MPa), but it was increased to 3600 ksi (24820 MPa) in the modified FRP model. The modified FRP material was defined with “uniaxialMaterial Hysteretic” in OpenSees. Figure 6-66 shows the modified FRP material stress-strain graph.

6.3.3. Analytical Model

The OpenSees model for the two-column bent is shown in Fig. 6-67. The model includes 11 nodes and 10 elements. The materials were defined as discussed in section 6.3.2. The column sections were defined with a fiber model using the measured material properties of the test columns. In the fiber element model, equilibrium between external forces and fiber forces and compatibility among fiber deformations need to be satisfied. The fibers shorten or elongate so that plane sections remain plane after deformation. Two different sections were defined for RC-ECC column including the ECC and concrete. The FRP column section included the FRP tube material in the cover and confined concrete in the core.

The columns were modeled by assigning the "nonlinearBeamColumn"elements with appropriate cross sections between nodes. The P-Delta effect was included in the model. The RC-ECC column was defined with two elements. The first element including ECC was defined from elevation 0 in. (0 mm) to elevation 21 in. (533 mm). The second element including concrete was defined from elevation 21 in. (533 mm) to 63 in. (1600 mm). The FRP column was defined with one element along the column height. A fixed support was defined for each column.

To model the bond-slip rotation, an additional node was defined at the base of each column. This node was connected to the footing node with a "zeroLength element". The zeroLength element included a tri-linear "uniaxialMaterial Hysteretic" material with bond-slip rotation parameters. The bond-slip model and method of calculation are discussed in section 6.3.4.2.

Since the pipe-pin detail was originally designed for larger demands and their capacity was larger than what was required in PEFB, it was assumed that the pipe-pins remained elastic during the test. The pipe-pins were modeled with two truss elements on top of the columns with modulus of elasticity of 1000 ksi (6894 MPa). The pipe-pin elements were defined between the top column nodes and cap beam nodes. It was assumed that the cap beam was rigid; therefore, the "elasticBeamColumn" elements with a large modulus of elasticity were used to model the beam.

The mass was assigned to the nodes in the middle of the beam. The measured axial load history was applied to the bent model during nonlinear dynamic analysis.

Column forces, displacements, and stress-strain variation in the sections were measured with several recorders during pushover analyses and nonlinear dynamic analyses. The input OpenSees file for dynamic analysis of two-column bent is presented in Appendix C.

6.3.4. Post-Test Analysis

6.3.4.1. Strain Rate Effect

The strain rate factors were calculated for concrete and steel and the results were presented for each column in Chapter 3. The strain rate factors were applied to the concrete and steel strengths in post-test analysis.

6.3.4.2. Bond-Slip Model

The bond slip effects were not included in the pre-test analytical model. A comprehensive definition of the bond-slip calculation and the modeling method in OpenSees is presented in section 6.1.5.2. The yield and ultimate points of the bond-slip springs are listed in Table 6-11.

For the FRP tube column, there is no established method that addresses the bond-slip properties of the embedded tubes. Due to lack of a theoretical method, the experimental data were used to model the bond-slip spring at the base of the FRP tube column. Moment-rotation relationships at the lower most level, which is a measure of the bond-slip rotation due to yield penetration of the longitudinal bars inside the footing was used to model the bond-slip spring. The calculation method for moment-rotation is discussed in section 3.3.4.1.

6.3.5. Analytical Results

6.3.5.1. Pushover Curve and Force-Displacements Envelopes

The pushover analysis of PEFB was conducted for two models; one including the FRP material model developed by Zhu, (2004) and the other including the modified FRP material model. The drift ratio increment in the pushover analysis was 0.05%. The force-displacement response of each column to the shake table motions was calculated in OpenSees and the envelopes of response in the positive and negative direction of displacement were averaged. The pushover analysis results and calculated force-displacement envelopes were compared with the measured load-deflection envelopes of the bent.

6.3.5.1.1. Pushover Analysis Using Zhu"s FRP Material Model

The pushover results and the measured and calculated force-displacement envelopes of FRP column are shown in Fig. 6-68. The initial stiffness of the force-displacement curves was lower than the measured stiffness. The envelope of measured force-displacement response of FRP column showed that the maximum lateral load capacity was 32.7 kips (145 kN) at displacement of 4.9 in. (124 mm). The calculated lateral load at the same displacement was 25.3 kips (112 kN), which was 22% lower than the measured lateral load. Also, the strength degradation seen in the measured results was not captured by the OpenSees model. The difference can be attributed to the OpenSees material model that did not simulate the rupture of FRP during the high amplitude motion.

Figure 6-69 shows the pushover analysis result and the measured and calculated backbone curves of RC-ECC column. Good correlation was seen between the measured and calculated data in terms of initial column stiffness and the lateral load capacity. The degrading measured strength of RC-ECC column was not calculated by OpenSees model.

The difference can be attributed to the material models in OpenSees that did not simulate the ECC spalling and bars rupture during the last run.

The lateral load capacity of the two-column bent was calculated by summation of lateral forces of RC-ECC and FRP columns. Figure 6-70 shows that the calculated initial stiffness of the bent was lower than the calculated stiffness. Generally, the calculated lateral load capacity of the bent was lower than the measured lateral load capacity. The calculated lateral load capacity of the bent at the displacement of 3 in. (76 mm) was 44.6 kips (198 kN) that was 13% lower than the measured force at the same displacement. The underestimation in initial stiffness and lateral load capacity of the bent was due to the underestimated response of the FRP column.

6.3.5.1.2. Pushover Analysis Using Modified FRP Material Model

A modified FRP material model with a larger initial stiffness (Fig. 6-51) was replaced in the analytical model to improve the calculated response.

Figure 6-71 shows the comparison between the pushover analysis result and the measured and calculated envelopes of force-displacement responses of FRP column. Reasonable agreement was seen between the calculated and measured initial stiffness of the column. The maximum calculated lateral load capacity of the FRP column was 30.1 kips (133 kN) at displacement of 4.9 in. (124 mm) that was 8% smaller than the measured force. The difference between the measured and calculated maximum lateral load capacity of FRP column reduced from 22% in the model using Zhu‟s FRP material model to 8% in the model using the modified FRP material.

Good correlation was observed between the calculated and measured force-displacement response of RC-ECC column in terms of initial stiffness and the lateral load capacity (Fig. 6-72).

The comparison between the measured and calculated response of the bent is shown in Fig. 6-73. Good correlation was seen between the measured and calculated data in terms of initial stiffness and lateral load capacity.

The degrading measured strength in the columns and the bent during the last run was not calculated by OpenSees model. The difference can be attributed to the OpenSees material models that did not simulate the rupture of FRP, ECC spalling, and rupture of bars during high amplitude motions.

6.3.5.2. Dynamic Analysis

Nonlinear dynamic analyses were conducted for the two-column bent. Achieved shake table motions for different runs were spliced and used in dynamic analyses. A damping ratio of 5% was used in the pre-test analyses. It was determined in the post-test analysis that the damping ratio of 15% leads to a better match between the measured and calculated data. The sources of large damping in PEFB were friction between concrete and the FRP tube and the ECC in plastic hinge of RC-ECC column. The measured and calculated cumulative force-displacement hysteresis curves, displacement histories, and the maximum drift ratios were superimposed to evaluate the accuracy of the applied techniques in calculating the nonlinear response of the test columns.

The dynamic analysis of the PEFB was conducted for two models; one using the FRP material model developed by Zhu, (2004) and the other using the modified FRP material model.

6.3.5.2.1. Cumulative Force-Displacement Using Zhu"s FRP Material Model

Figure 6-74 shows the comparison between the measured and calculated cumulative force-displacement response of FRP column. The maximum lateral load capacity was underestimated in the negative and positive direction of displacement by 12% and 30%, respectively. The maximum displacement was well estimated in the positive direction but it was underestimated in the negative direction.

The comparison between the measured and calculated force-displacement response of RC-ECC column is shown in Fig. 6-75. Good correlation was seen between the measured and calculated lateral load capacity of the column before the last run. The analytical model did not calculate the measured drop in the lateral load capacity. The maximum displacement of column was well correlated with the measured response in the positive direction of motion. The maximum displacement in the negative direction of displacement was underestimated.

The comparison between the measured and calculated force-displacement response of the bent is shown in Fig. 6-76. The lateral load capacity of the bent was calculated by summation of lateral forces of RC-ECC and FRP columns. The maximum lateral load capacity of the bent was 8% lower than the maximum measured capacity during the test and it was due to the underestimated response of FRP column. The bent displacement was similar to the calculated displacement for RC-ECC and FRP columns. The positive displacements of bent were well estimated by the analytical model but the negative displacements were underestimated.

6.3.5.2.2. Cumulative Force- Displacement Using Modified FRP Material Model

Figure 6-77 shows the measured and calculated response of FRP column. The lateral load capacity of FRP column and the displacement were well estimated in the positive direction of motion before the last run. The maximum calculated lateral load capacity of FRP column in positive direction of motion was 35.2 kips (156.5 kN) that was 11% larger than the maximum measured capacity. The maximum lateral load capacity of the FRP column in the negative direction of motion was only 8% lower than the maximum measured capacity. The measured drop in the lateral load capacity of the column due to the FRP rupture was not captured by the analytical model during the last run. The lateral load capacity and displacement in the negative direction of motion were underestimated. Using higher initial stiffness in the modified FRP material resulted in a better estimation for initial stiffness of FRP column. Also using the modified FRP material model rather than the Zhu‟s FRP material model reduced the difference between the measured and calculated maximum lateral load capacity of FRP column from 30% to 8% in negative direction of motion. The maximum lateral load capacity of FRP column in positive direction of motion was overestimated by 11% using the modified FRP material model compared to 12% underestimation in lateral load capacity in the model using Zhu‟s FRP material model.

The lateral load capacity of RC-ECC column was well estimated by the analytical model before the last run (Fig. 6-78). There was a large drop in the lateral load capacity due to the rupture of bars that was not captured by the analytical model. Good correlation was seen between the measured and calculated displacements in the positive direction of motion. The displacements in the negative direction of motion were underestimated.

Good match was achieved between the measured and calculated force-displacement of bent before the last run (Fig. 6-79). The maximum calculated lateral load capacity of the bent was only 0.4% larger than the maximum measured capacity. The large drop in lateral load capacity was not calculated by the analytical model. The maximum displacement was well correlated with that of measured in the positive direction but not in the negative direction.

6.3.5.3. Displacement History

The displacement histories of the bent are presented in Figs. 6-80 and 6-81. The bent and the columns had similar displacement histories because the beam was rigid; therefore, the comparison between the calculated and measured data is made only for the bent. The displacement histories calculated from the two models including two different FRP martial models were similar; thus only one set of results using Zhu‟s FRP material are presented here.

The analytical model in the bent overestimated the displacement during the low-amplitude Runs 1 through 3 (Figs. 6-80 (a), (b), (c)), but led to good correlation during stronger motions. The large difference between the measured and calculated displacements during the initial runs was due to the very large damping that the test model experienced during early runs. This damping was not captured by the analytical model during early runs. The maximum displacements were well estimated during Runs 4 and 5 (Figs. 6-80 (d) and 6-81). The calculated and measured positive peak displacements were in close agreement during Run 6.

6.3.5.4. Maximum Drift Ratios

The maximum calculated and measured drift ratios versus PGA for the two-column bent were compared. The maximum drift ratio was defined as the maximum displacement during each run divided by the clear height of the bent (63 in. (1600 mm). Figure 6-82 shows that the calculated maximum drift ratios were larger than the measured drift ratios during Runs 1 through 3 but were in close agreement during Runs 4 through 6.

6.3.5.5. Dissipated Energy

The dissipated energy was calculated by integrating the area enclosed by the force displacement hysteretic curves. The dissipated energy was calculated for two analytical models, one including the Zhu‟s FRP material model and the other including the modified FRP material model.

Table 6-12 lists the measured and calculated cumulative dissipated energy for Runs 1 through 5 and for all runs. The difference between calculated and measured energy dissipation is calculated for RC-ECC and FRP columns and is listed in Table 6-12.

The dissipated energy for all runs in RC-ECC column was overestimated by approximately 42% in both analytical models. In contrast the difference between calculated and measured dissipated energy when the last run was excluded was only 13% and 3% for the models using Zhu‟s FRP material model and modified FRP material model, respectively. The degrading response of RC-ECC column during Run 6 was not calculated by OpenSees model; therefore, it resulted in overestimation of energy dissipation for all runs.

The calculated energy dissipation in FRP column for Runs 1 through 5 was 13% larger than measured energy dissipation when Zhu‟s FRP material was used. This percentage was 42% when the modified FRP material was used. The differences between the measured and calculated energy dissipation for all runs in the FRP column were 3% and 25% for the models including Zhu‟s FRP material and modified FRP material, respectively. The reason for overestimation of energy dissipation in both models was non-degraded stress-strain behavior of FRP material model that resulted in non-degraded response of the FRP column. The underestimated lateral load capacity of the FRP column in the model incorporating Zhu‟s FRP material compensates for the overestimated dissipated energy that was mentioned above. Therefore a better correlation was seen between the measured and calculated energy dissipation when Zhu‟s FRP material was used in the model.

7. PARAMETRIC STUDIES

7.1. Introduction

To develop a general design method for precast columns, the impact of different parameters on the capacity and performance need to be known. Due to time and cost limitations, analytical studies are necessary because it is not possible to study parameter experimentally. To understand and quantify the importance of each parameter, an extensive study was performed using nonlinear cyclic analysis in OpenSees.

The parametric studies were conducted for SC-2, SBR-1, and the FRP column (one of the columns in PEFP). SF-2, SE-2 and SC-2R were not studied in this section, since it was expected that the results from SC-2 would be applicable to the other columns. No parametric studies were conducted for RC-ECC (one of the columns in PEFP), since RC-ECC column performed similarly to a conventional reinforced concrete column with limited material failure in the plastic hinge zone. Four column parameters were selected for a pseudo-static loading analysis in SC-2: base segment height, base segment longitudinal steel reinforcement ratio, concrete strength, and post-tensioning force level. The performance of SC-2 was also compared with a conventional segmental column with no dowels connecting the base segment to the footing. The effects of rubber pad height and rubber pad shape factor were studied in SBR-1. In the FRP column, the influence of FRP tube thickness, fiber orientation, and longitudinal steel reinforcement ratio on the column lateral load capacity was investigated.

In Chapter 7, the basic prototype model that was used in the study is first described. Then the parameters and their range are explained and justified. The analytical results are presented subsequently and the sensitivity of the results is discussed. The analytical models were calibrated and checked against the experimental data that was generated as part of this project as explained in Chapter 6.

7.2. Precast Segmental Columns

A parametric study was conducted for SC-2 and SBR-1. Columns SC-2, SF-2, SE-2 and SC-2R had generally similar configurations. Therefore, the results from SC-2 would be applicable to the other columns. The parameters that were studied for SC-2 were base segment height, longitudinal steel reinforcement ratio, concrete strength, and initial post-tensioning force. In SBR-1, the rubber pad height and shape factor were selected as the parameters.

To scope the size of the parametric studies manageable, only one parameter at a time was changed. For each parameter, several values were selected within a practical range, with one value identified as the base value, which was kept constant for studying other parameters. Table 7-1 shows the parameters and their selected values for SC-2. Table 7-2 lists the parameters for SBR-1. The shaded areas in Tables 7-1 and 7-2 represent the basic models of SC-2, SBR-1, which were the test specimens.

The basic model in the SC-2 and SBR-1 studies was a segmental column with the base segment monolithically connected to the footing. The diameter of the column was 16 in. (406 mm) and the height was 72 in. (1829 mm). The total axial load on the columns was comprised of 80 kips (355.8 kN) gravity load and 100 kips (444.8 kN) post-tensioning force. The total base segment depth was 20 in. (508 mm). The base segment height in the SBR-1 basic model included 8 in. (203 mm) rubber pad and 12 in. (305 mm) reinforced concrete. The reinforcing yield strength of 68 ksi (468.8 MPa) and an unconfined concrete strength of 5 ksi (34.5 MPa) were assumed. The confined concrete properties were calculated based on the Mander"s model [Mander, et al., 1988] as discussed in section 6.2.2.1, the ultimate strength and strain were defined where the concrete strength dropped by 40%. Unconfined concrete strength dropped by 40% at strain of 0.015. In addition to variations of SC-2 model, a conventional segmental column (a column in which the base segment is not monolithically connected to the footing) was modeled in the OpenSees and the results were compared with those of SC-2. The conventional segmental column model had similar geometry, details, and post-tensioning force as those of SC-2.

Each column was analyzed under two half cycle loadings with maximum drift ratios of 5% and 10%. The results include force-displacement curve, separation between the base and second segments, and post-tensioning force versus displacement for each case. The lateral load capacity of each column was compared with that of the basic model. The dissipated energy was calculated for all cases by integrating the area enclosed by the force displacement curves and it was compared with that of the basic model.

7.2.1. Parameters and Results of SC-2

7.2.1.1. Effect of Base Segment Height

7.1.2.1.1. Force-Displacement Relationship

Figure 7-1 (a) and (b) show the force-displacement response of column SC-2 incorporating 1% longitudinal steel ratio at the base segment for 5% and 10% drift ratios, respectively. For the cases with the base segment height less than 32 in. (813 mm) ($0.44 \times$column height), the maximum lateral load capacity of column dropped by approximately10% and 20% for loading to 5% and 10% drift ratios, respectively. The drop in the lateral load capacity was due to concrete failure at the interface between the base and second segments. No drop in the lateral load capacity was observed in the columns with base segment heights of 32 in. (813 mm) and 40 in. (1016 mm) (0.44 and $0.55\times$column height, respectively); the full moment capacity was developed and the behavior was similar to that of monolithic concrete columns. The opening between the end and adjacent segments occurs when the section at the interface elevation undergoes a large enough tensile stress to crack the concrete. The tensile stress at extreme fiber occurs when the moment is equivalent to the "cracking moment". When the base segment height is sufficiently tall, the cracking moment occurs somewhere along the base segment and joint opening does not occur. The residual displacements were approximately the same in all cases for loading to 5 % drift ratio. The columns with the base segment heights of 32 in. (813 mm) and 40 in. (1016 mm) (0.44 and 0.55 × column height, respectively) showed slightly larger residual displacement than other columns at 5% drift ratio (DR). Table 7-3 lists the maximum lateral load capacity of the columns for different base segment heights. Lower lateral load capacity was obtained for the columns with shorter base segments. Approximately an increase of 48% was observed in lateral load capacity of the columns with the base segment heights of 32 in. (813 mm) and taller compared to that of the basic model for loading to 10% drift ratio.

The force-displacement response of column SC-2 with 0.5% longitudinal steel ratio at the base segment for loading to 5% and 10% drift ratios are shown in Fig. 7-2 (a) and (b), respectively. The minimum base segment height to develop the full moment capacity was 20 in. (508 mm) (0.27 × column height). The maximum lateral load capacity of column with the base segment height less than 20 in. (508 mm) dropped by approximately10% and 20% for loading to 5% and 10% drift ratios, respectively. The drop in lateral load capacity was attributed to concrete failure at the interface between the base and second segments. The initial tensile stress at extreme fiber occurs when the moment is equivalent to the "cracking moment". The cracking moment causes the joint separation. When small amount of longitudinal steel ratio is placed in the base segment, the difference between the cracking moment and the full moment capacity of the section is small; therefore, the cracking moment occurs at a short distance from the column base along the base segment height and the full moment capacity can be developed at the base without opening between the base segment and the adjacent segment. The residual displacements in all cases were nearly the same. The maximum lateral load capacities of columns are listed in Table 7-4. The maximum lateral load capacity of the basic model was 31% larger than that of the column with 8 in. (203 mm) (0.11 × column height) tall base segment.

7.1.2.1.2. Dissipated Energy

Table 7-5 lists the dissipated energies in column SC-2 with different base segment height and 1% longitudinal steel ratio in the base segment. The dissipated energy at 10% drift ratio for the columns with the base segment height of 32 in. (813 mm) (0.44 × column height) and taller was approximately 55% larger than that of basic model. The increase in dissipated energy is attributed to the development of full moment capacity and extensive yielding of the bars.

The dissipated energy for the columns with different base segment heights and 0.5% longitudinal steel ratio in the base segment are listed in Table 7-6. The column with shorter base segment dissipated less energy than the basic model. The dissipated energy in the column with 8 in. (203 mm) (0.11 × column height) base segment height was 34% lower than that of the basic model for loading to 10% drift ratio.

7.1.2.1.3. Separation between Segments

Figure 7-3 (a) and (b) show the separation between the base and second segments versus top column displacement for the columns with different base segment heights for the longitudinal steel ratio of 1%. The joint openings in the columns with the base segment shorter than 32 in. (813 mm) (0.44 × column height) were comparable. No joint separation occurred in the columns with the base segment heights of 32 in. (813 mm) and 40 in. (1016 mm) (0.44 and 0.55 × column height, respectively).

The joint separation for the columns with different base segment height and 0.5% longitudinal steel ratio is shown in Fig. 7-4 for 5% and 10% drift ratios. No opening between the base segment and second segment was recorded for the columns with the base segment heights of 20 in. (508 mm) (0.27 × column height) and taller. These columns performed similar to conventional cast-in-place reinforced concrete column.

7.1.2.1.4. PT Force vs. Displacement

The post-tensioning force versus top column displacement for the columns with different base segment heights and 1% longitudinal steel ratio is plotted in Fig. 7-5.

Figure 7-6 shows the PT force versus displacement for the columns with different base segment heights and 0.5% longitudinal steel ratio in the base segment. The maximum PT force for loading to 5% drift ratio was nearly the same in all columns and was approximately 174 kips (775 kN). The initial PT force was 100 kips (445 kN) and the area of the rod was 1.95 in^2 (1258 mm^2). The maximum PT force for 10% drift ratio loading in the columns with base segment height of 20 in. (508 mm) (0.27 × column height) and taller was approximately 16% larger than that of the columns with the base segment shorter than that of the basic model. The maximum PT force in the basic model was 278 kips (1238 kN).

7.2.1.2. Effect of Longitudinal Steel Ratio

The parametric study on SC-2 was conducted for different longitudinal steel reinforcement ratios in the base segment including 0.5%, 0.8%, 1%, 1.2%, and 1.5%. It should be noted that the segmental column performance is different than a monolithic conventional concrete column and lower amount of steel reinforcement may be placed in them to eliminate separation between the segments. The longitudinal steel ratio in the basic model was 1%.

7.1.2.2.1. Force-Displacement Relationship

The force-displacement responses of SC-2 incorporating different longitudinal steel ratios at 5% and 10% drift ratios are shown in Figs. 7-7 (a) and (b), respectively. The maximum lateral load capacity in all columns containing longitudinal steel ratios larger than 0.5% was 21 kips (93.4 kN) and it dropped by 14% when loaded to 10% drift ratio. The full moment capacity in the column incorporating 0.5% longitudinal steel ratio was developed and the maximum lateral load capacity was 25.2 kips (112 kN). When small amount of longitudinal steel ratio is placed in the base segment, the difference between the cracking moment and the full moment capacity of the section is small; therefore, the cracking moment occurs within the base segment height and the full moment capacity can be developed. The residual displacements were essentially the same in all cases. Table 7-7 lists the maximum lateral load capacity of the columns containing different longitudinal steel ratios at 5% and 10% drift ratios. The maximum lateral load capacity of the column with 0.5% steel ratio was 18% larger than that of the basic model.

7.1.2.2.2. Dissipated Energy

The dissipated energies for SC-2 incorporating different longitudinal steel ratios are listed in Table 7-8. The energy dissipations in all columns were relatively the same for loading to 5% drift ratio. The energy dissipation in the column containing 0.5% longitudinal steel ratio was 18% larger than that of the basic model. The dissipated energy in columns containing longitudinal steel ratio larger than 0.5% was approximately similar at 10% drift ratio.

7.1.2.2.3. Separation between Segments

The opening between the base and adjacent segments at 5% and 10% drift ratios for the columns incorporating different longitudinal steel ratios is shown in Fig. 7-8. Comparable opening between the base and second segments occurred in all columns with longitudinal steel ratios larger than 0.5%.

7.1.2.2.4. PT Force vs. Displacement

Figure 7-9 shows the PT force versus displacement for SC-2 incorporating different longitudinal steel ratios in the base segment. The maximum PT force in all cases for loading to 5% and 10% drift ratios was approximately 180 kips (800 kN) and 266 kips (1185 kN), respectively. The initial PT force was 100 kips (444 kN) in all columns. The influence of the longitudinal steel ratio in the base segment on the PT force was not significant.

7.2.1.3. Effect of Concrete Strength

The effect of concrete strength on performance of SC-2 was investigated by modeling the column with different concrete strengths. An unconfined concrete strength of 5 ksi (34.5 MPa), 8 ksi (55.1 MPa), and 10 ksi (68.9 MPa) was assumed for the model. The confined concrete properties were calculated based on the Mander"s model [Mander, et al., 1988]. As discussed in Chapter 6, the ultimate strength and strain were defined where the maximum concrete strength dropped by 40%. The column with 5 ksi (34.5 MPa) concrete strength was considered as the basic model.

7.1.2.3.1. Force-Displacement Relationship

Figure 7-10 (a) and (b) shows the force-displacement response of SC-2 with different concrete strengths for loading to 5% and 10% drift ratios, respectively. Using high strength concrete increased the maximum lateral load capacity and decreased the residual displacement. This improvement in response of the column incorporating high strength concrete was attributed to delay in the failure of concrete at the joint interface. Table 7-9 lists the maximum lateral load capacities of SC-2 for different cases. The maximum lateral load capacity of column incorporating concrete with strength of 10 ksi (68.9 MPa) was 41% larger than that of basic model for loading to 10% drift ratio. Table 7-10 lists the residual displacements of the column with different concrete strengths. The residual displacement was decreased when the high strength concrete was placed in the model. The residual displacement for loading to 10% drift ratio in the basic model was 1.4 in. (37 mm) and it dropped to 0.2 in. (5 mm) in the model incorporating concrete strength of 10 ksi (68.9 MPa). The lower residual displacement in the columns with higher concrete strength was attributed to the less plastic deformation of concrete (concrete failure) at interface between the base and second segments.

7.1.2.3.2. Dissipated Energy

The dissipated energy in column SC-2 with different concrete strengths is listed in Table 7-11. The dissipated energy increased by 8% in the column incorporating concrete with strength of 10 ksi (68.9 MPa) compared to that of the basic model.

7.1.2.3.3. Separation between Segments

The segment separation for SC-2 with different concrete strengths is shown in Fig. 7-11. The opening between the base and second segments occurred in all cases, but the column with higher concrete strength showed slightly larger opening.

7.1.2.3.4. PT Force vs. Displacement

The PT force versus displacement in SC-2 with different concrete strengths at 5% and 10% drift ratios are shown in Fig. 7-12. The maximum PT force in columns with higher concrete strength was larger than that of the basic model. This is because concrete damage at the interface between the base and second segments was less severe and the section loss was less extensive in the columns with higher concrete strength. The elongation of PT rod for a constant joint rotation was larger in the columns with shorter compressive toe and it resulted in larger PT force (Fig. 7-13). The maximum PT force in the column incorporating concrete with strength of 10 ksi (68.9 MPa) reached 352 kips (1566 kN) for loading to 10% drift ratio that was 33% larger than that of the basic model.

7.2.1.4. Effect of Post-Tensioning Force Level

The parametric study on SC-2 was conducted for different initial post-tensioning levels under the maximum 5% and 10% drift ratios. The initial post-tensioning force was chosen as 0.15, 0.33, and 0.6 of the ultimate PT force strength corresponding to 45 kips (200 kN), 100 kips (444 kN), and 180 kips (800 kN), respectively. The ultimate strength of a 1-5/8 in. (40 mm) diameter PT rod is 297 kips (1321 kN). The initial PT force in the basic model was 100 kips (444 kN).

7.1.2.4.1. Force-Displacement Relationship

The force-displacement response of SC-2 with different initial PT force is shown in Fig. 7-14. Using larger initial PT force led to an increase in lateral load capacity of the column, but the capacity dropped after approximately 2% drift ratio. Table 7-12 lists the maximum lateral load capacities of SC-2 with different initial PT forces. The maximum lateral load capacity of column with initial PT force of 180 kips (800 kN) was 22 % larger than that of the basic model. The drop in the lateral load capacity was greater in the columns with larger initial PT force level. Approximately the same ultimate lateral load capacities were obtained in all columns. The separation between the segments was delayed in the columns with larger initial PT force; therefore, a larger moment capacity was developed at the base segment that led to a larger lateral load capacity. After separation between the lower segments, all columns with different initial PT force showed similar capacities. The moment capacity of the column after joint opening was determined based on the section area, concrete material strength, and PT force at the interface between the base and second segments. As it will be shown later in section 7.1.2.4.4, the columns with lower initial PT force showed larger increase in the PT force; hence, the maximum PT forces in all columns were nearly the same. At ultimate stage, the moment capacities of the columns with different initial PT forces were similar due to the similarity between the sections and ultimate applied total axial load.

The residual displacement increased in the columns with larger initial PT force level. Plastic deformation of concrete (concrete failure) at the interface between the base and second segments in the columns with higher initial PT force was more extensive than that of the other columns; therefore, larger permanent displacement was seen in the column after unloading. Prior to concrete failure, higher PT forces lead to lower residual displacements. Table 7-13 lists the residual displacements of columns for loading to 5% and 10% drift ratios. The residual displacement in column with initial PT force of 180 kips (800 kN) and 100 kips (444 kN) were 2.08 in. (53 mm) and 1.44 in. (36 mm), respectively. This means that the residual displacement increased by 44 % in the column with larger PT force compared to that of the basic model.

7.1.2.4.2. Dissipated Energy

The dissipated energies in SC-2 with different initial PT force are listed in Table 7-14. The column with initial PT force of 45 kips (200 kN) dissipated 18% less energy compared to that of basic model. The increase in energy dissipation was 40% in the model with the PT force of 180 kips (800 kN) compared to that of the basic model.

7.1.2.4.3. Separation between Segments

Figure 7-15 shows the separation between segments for different cases. The opening in the column with larger initial PT force level was slightly smaller than that of the basic model.

7.1.2.4.4. PT Force vs. Displacement

The PT force versus displacement at 5% and 10% drift ratios for SC-2 with different initial PT forces is shown in Fig. 7-16. The increase in the PT force compared to the initial force is listed in Table 7-15. The columns with lower initial PT force showed larger increase in the PT force. The maximum PT force in the column with initial PT force of 45 kips (200 kN) reached 233 kips (1036 kN) at 10% drift ratio, which corresponds to a 417% increase in the PT force. The increase in the PT force in the column with initial PT force of 180 kips (800 kN) was 62% at 10% drift ratio. Concrete failure at the interface between the base and second segments was less in the columns with lower initial PT force; therefore, the compressive toe (failed zone) was shorter than that of the columns with higher initial PT force. The elongation of PT rod for a constant joint rotation was larger in the columns with shorter compressive toe and it resulted in larger increment in PT force (Fig. 7-13).

7.2.2. Parameters and Results of SBR-1

7.2.2.1. Effect of Height of Rubber Pad in SBR-1

The height of rubber pad in the lower part of SBR-1 was chosen as a different with three different heights. The height of rubber pad was selected as the ratio of column diameter: 0.25, 0.5, and 1. Versions of SBR-1 incorporating rubber pad with heights of 4 in. (101 mm), 8 in. (203 mm), and 16 in. (406 mm) were analyzed at 5% and 10% drift ratios. The rubber pad height of 8 in. (203 mm) was selected for the basic model. The column rotational demand was compared with each rubber pad rotational capacity. All rubber pad heights satisfied the rotational demand.

7.2.2.1.1. Force-Displacement Relationship

The force-displacement response of SBR-1 incorporating different rubber pad heights at 5% and 10% drift ratios is shown in Fig. 7-17. The initial stiffness of the column with taller elastomeric bearing was lower than that of the column incorporating a shorter bearing pad. The maximum lateral load capacities of the columns were approximately the same. Table 7-16 lists the maximum lateral load capacity for SBR-1 with different rubber pad heights.

7.2.2.1.2. Dissipated Energy

The dissipated energy in SBR-1 with different rubber pad heights is listed in Table 7-17. The column with bearing height of 16 in. (406 mm) dissipated 8% more energy compared to that of the basic model under loading to 5% drift ratio. The difference in energy dissipation between the columns was negligible when the columns were analyzed at 10% drift ratio because the differences in the initial stiffness did not affect the total energy significantly.

7.2.2.1.3. Separation between Segments

Separation between the base segment and the second segment in SBR-1 with different rubber pad heights at 5% and 10% drift ratio is shown in Fig. 7-18. The gap opening in the column with taller elastomeric pad was less than that of the basic model. This is because the higher flexibility of the taller pad placed smaller rotational demand at the junction between the base segment and the second segment. The opening in the column with rubber pad height of 4 in. (101 mm) was slightly larger than that of the basic model.

7.2.2.1.4. PT Force vs. Displacement

Figure 7-19 shows the PT force versus displacement in variations of SBR-1 with different rubber pad heights. The maximum PT force was larger in the column with shorter elastomeric bearing for the case with 5% drift ratio. The maximum PT forces were approximately the same when the column was analyzed at 10% drift ratio. The PT force was generally lower in the column with the elastomeric bearing height of 16 in. (406 mm).

7.2.2.2. Effect of Shape Factor of Rubber Pad in SBR-1

The shape factor is defined as the ratio of the pad cross-sectional area to the area of the pad circumference. Considering a constant diameter of bearing, different rubber thickness led to different shape factors. Three rubber thicknesses of 1/16 in. (2 mm), 3/16 in. (5 mm), and 8/16 (13 mm) were selected and the shape factors of 42, 14, and 5 were obtained, respectively. The shape factor of 14 was used in the basic model.

7.2.2.2.1. Force-Displacement Relationship

The force-displacement response of SBR-1 with different shape factors is shown in Fig. 7-20. The columns with lower shape factors showed lower initial stiffness. Table 7-18 lists the maximum lateral load capacities for different cases. The maximum lateral load capacity of SBR-1 with shape factor of 5 was 10% lower than that of the basic model for loading to 5 % drift ratio. The lateral load capacity in the column with low shape factor rubber pad of 5 was 5% larger than that of the basic model when the column was loaded to 10% drift ratio due to more extensive yielding and strain hardening of the longitudinal steel.

The residual displacement in column with a shape factor of 5 was 40% larger than those of other columns for loading to 5% drift ratio due to more extensive yielding of the longitudinal bars and the resulting permanent strains.

7.2.2.2.2. Dissipated Energy

Table 7-19 lists the dissipated energies in SBR-1 incorporating different rubber pad shape factors. The column containing the rubber pad with low shape factor of 5 showed larger energy dissipation by 11% and 5% than that of the basic model for loading to 5% and 10% drift ratios, respectively. The dissipated energy in the column including rubber pad with shape factor of 42 was slightly different (1%) than that of the basic mode.

7.2.2.2.3. Separation between Segments

The opening between the base and second segments in SBR-1 for different shape factors is shown in Fig. 7-21. The joint opening in the case with shape factor of 5 was negligible at 5% drift ratio compared to the opening in two other columns. Since the low shape factor bearing pad provides higher rotational capacity, the rotation of column occurred through the elastomeric bearing rather than through the joint separation. Therefore, less joint opening was recorded for the column with shape factor of 5 than that of other columns. The joint separation in the column with shape factor of 42 was slightly larger than that of the basic model. This is because pads with higher shape factors have higher rotational stiffness and shift the rotational demand elsewhere in the column.

7.2.2.2.4. PT Force vs. Displacement

Figure 7-22 shows the PT force versus displacement in SBR-1 with different shape factors at 5% and 10% drift ratios. The maximum PT force in cases with shape factors of 14 and 42 were comparable, but the PT force in the case with low shape factor of 5 was much lower at 5% drift ratio. The maximum PT force was 17% lower than that of the basic model at 10% drift ratio. This is because the higher rotational capacity of the low shape factor pad placed smaller rotational demand at the junction between the base segment and the second segment. Less elongation of PT rod occurred due to less joint opening in the column with low shape factor pad and it resulted in less increase in the PT force.

7.2.3. Conventional Precast Segmental Column

To compare the effect of using a base segment that is fixed to the footing, a conventional segmental column was analyzed using OpenSees. In a conventional segmental column the base segment is not connected to the footing by dowels and the only connection is through the post-tensioning rod. The column geometry, material properties, PT force, and reinforcing details were similar to those of SC-2. Note that no conventional segmental column was tested as part of this study. Since the base segment and footing were discontinued in the conventional segmental column, yielding of the bars was not expected; therefore, nominal longitudinal reinforcement was assumed for the base segment.

7.2.3.1.1. Force-Displacement Relationship

The force-displacement response of SC-2 and conventional segmental column at 5% and 10% drift ratio is shown in Fig. 7-23. The initial stiffnesses in both columns were similar. The lateral load capacity of SC-2 was 26% larger than that of conventional segmental column because of the moment connection at the base. Table 7-20 lists the maximum lateral load capacity of the columns for loading to 5% and 10% drift ratios. The maximum lateral load capacity of SC-2 and conventional segmental column were 21.1 kips (94 kN) and 15.5 kips (69 kN), respectively.

7.2.3.1.2. Dissipated Energy

Table 7-21 lists the dissipated energy in SC-2 and the conventional segmental. The dissipated energy in conventional segmental column was 35% and 29% lower than that of SC-2 at 5% and 10% drift ratios, respectively.

7.2.3.1.3. PT Force vs. Displacement

The PT force versus displacement for SC-2 and the conventional segmental column is plotted in Fig. 7-24. The PT force variations were similar in both columns. The conventional segmental column showed slightly lower PT force compared to that of SC-2.

7.3. FRP Column

The parametric studies of FRP column that had been used as a part of PEFB were conducted in this section. The effects of FRP tube thickness, FRP tube fiber orientation, and longitudinal steel reinforcement ratio were studied in the FRP column. The RC-ECC column performed similarly to a conventional reinforced concrete column with limited material failure in the plastic hinge zone; therefore, no parametric studies were conducted for RC-ECC.

To limit the size of the case study matrix, only one parameter at a time was varied. For each parameter, several values were selected in their practical range, with one value identified as the base value and was kept constant for studying the effects of other parameters. Table 7-22 shows the parameters and their selected values. The shaded areas in the table indicate the data for the basic column.

The basic model for the parametric study was a single cantilever FRP column. The diameter of the column was 14 in. (356 mm) and the height was 63 in. (1600 mm). An axial load of 50 kips (222.4 kN) was applied on the column as the gravity load. The column section was defined with a fiber model that included the FRP tube material in the cover, longitudinal steel reinforcement, and confined concrete in the core. The Saiidi‟s confinement model [Saiidi, et al., 2005] was used to determine the confined concrete properties. The longitudinal behavior of the FRP tube was defined using a model that was proposed by Zhu et al. [2004]. Seven #3 bars leading to 0.5% longitudinal steel ratio were used in the basic model. The FRP tube thickness and FRP fiber orientation were assumed to be 0.269 in. (6.8 mm) and 55 degrees, respectively, in the basic model. The reinforcing yield strength of 68 ksi (468.8 MPa) and an unconfined concrete strength of 5 ksi (34.5 MPa) were assumed.

The column was analyzed under two half cycle loadings with maximum drift ratios of 5% and 10%. The results including the force-displacement curve was plotted for each case. The change in the lateral load capacity of columns was compared with that of the basic model. The dissipated energy was calculated and compared for all cases by integrating the area enclosed by the force displacement curves.

7.3.1. Parameters and Results

7.3.1.1. Effect of FRP Tube Thickness

The FRP tube thicknesses were chosen in a practical range based on the manufacturer product catalog. The tube thicknesses of 0.187 in. (4.7 mm), 0.216 in. (5.5 mm), 0.269

in. (6.8 mm), 0.303 in. (7.5 mm), and 0.32 in. (8.1 mm) were used in the parametric studies. The FRP tube thickness mainly affects the encased concrete confinement. The thicker tubes provide more confinement to the concrete and increased its strength and ductility.

7.3.1.1.1. Force-Displacement Relationship

Figure 7-25 shows the force-displacement response of FRP columns with different FRP tube thicknesses. The initial stiffness in all cases was similar, but the maximum lateral load capacities increased for thicker tubes. Table 7-23 lists the maximum lateral load capacities of the column for different cases. The lateral load capacity of the column with FRP tube thickness of 0.187 in. (4.7 mm) was less than that of the basic model by 16% at 10% drift ratio. The column with a tube thickness of 0.32 in. (8.1 mm) showed larger maximum lateral load capacity than that of the basic model by 9% at 10% drift ratio.

7.3.1.1.2. Dissipated Energy

The energy dissipation in FRP column with different FRP tube thicknesses is listed in Table 7-24. The dissipated energies varied slightly in different columns. The columns with thicker tube dissipated slightly more energy.

7.3.1.2. Effect of FRP Tube Fiber Orientation

The parametric study on FRP column was conducted for three fiber orientations including $\pm 35^\circ$, $\pm 45^\circ$, and $\pm 55^\circ$. The fiber orientation was selected in the range of $\pm 35^\circ$ to $\pm 55^\circ$ because the available FRP formulations from previous studies were available for this range [Zhu, 2004]. The fiber angle is measured between the fiber and the column axes. The fiber angle affects both the longitudinal and hoop properties of FRP tube. The fiber orientation affects the confined concrete properties. Different longitudinal stress-strain behavior of FRP was assigned to the fiber sections in the OpenSees model for different fiber orientations. Table 7-25 lists the FRP material properties in hoop direction, for different fiber architectures using the laminate analysis [Zhu, 2004]. The stress-strain behavior of FRP tube in longitudinal direction with different fiber orientations was calculated by Eq. 7-1.

$$\sigma = \left(\varepsilon / ABS(\varepsilon) \right) \times \frac{\left(-b + \sqrt{b^2 + 4a \times ABS(\varepsilon)} \right)}{2a} \qquad ABS(\varepsilon) \le 0.05 \qquad \text{Eq. 7-1}$$

Where a and b can be determined from Table 7-26. Symmetric performance of the FRP tube was assumed in the parametric study. The stress-strain behaviors of FRP tube in longitudinal direction with different fiber orientations are plotted in Fig. 7-26.

7.3.1.2.1. Force-Displacement Relationship

Figure 7-27 shows the force-displacement response of FRP column with different fiber orientations for different cases. The lateral load capacity was the highest when the fiber orientation of $\pm 35^\circ$ was used. The maximum lateral load capacities of the FRP column with different fiber orientation are listed in Table 7-27. The maximum lateral load capacities of column with fiber angles of $\pm 45^\circ$ and $\pm 35^\circ$ were larger than that of the basic model by 12% and 24%, respectively at 10% drift ratio. Higher lateral load capacity in the cases with smaller fiber angles was attributed to their larger longitudinal component of fiber stress. Figure 7-26 displays that the longitudinal strength of FRP tube material with $\pm 35^\circ$ angle was the largest among all fiber orientations.

7.3.1.2.2. Dissipated Energy

The dissipated energy in FRP column with different fiber angles is listed in Table 7-28. The dissipated energy was not sensitive to changes in fiber angle. Energy dissipation in the column with fiber orientation of $\pm 35^\circ$ was 7% larger than that of the basic model at 10% drift ratio.

7.3.1.3. Effect of Longitudinal Steel Ratio in FRP Column

The parametric study on FRP column was conducted for different longitudinal steel ratios of 0.5%, 0.8%, 1%, 1.3%, and 1.5%. The longitudinal steel ratio in the basic model was 0.5%.

7.3.1.3.1. Force-Displacement Relationship

The force displacement relationship response of FRP column with different longitudinal steel reinforcement ratios is plotted in Fig. 7-28. Larger amount of longitudinal steel reinforcement in FRP column increased the lateral load capacities, as expected. Table 7-29 lists the maximum lateral load capacities of the FRP column with different longitudinal steel ratios. The maximum lateral load capacity of the column incorporating 1.5% longitudinal steel ratio was 33% larger than that of the basic model for loading to 10% drift ratio.

Table 7-30 lists the residual displacements of columns for loading to 5% and 10% drift ratios. The residual displacement was larger in columns containing higher longitudinal steel ratio. The residual displacement in FRP column containing 1.5% steel ratio was 122% larger than that of the basic model at 10% drift ratio. The large permanent deformation of the columns with higher steel is attributed to the more dominant effect of the residual strains in steel reinforcements.

7.3.1.3.2. Dissipated Energy

The dissipated energy of FRP column containing different longitudinal steel reinforcement is listed in Table 7-31. The column with larger amount of steel reinforcement dissipated more energy. The column with 1.5% longitudinal steel ratio dissipated 97% larger energy than that of the basic model at 10% drift ratio.

8. DESIGN RECOMMENDATIONS

8.1. Introduction

This chapter presents seismic design recommendations for segmental columns and precast bents based on the test observations, measured data, and parametric studies. Design methods for end segment height, post-tensioning force, and elastomeric bearing pad are discussed for segmental columns. Design recommendations for embedded length and flexural design of precast FRP column are also presented.

8.2. Precast Segmental Columns

Design of end segment height, post-tensioning, and built-in elastomeric bearing pad is presented in this section. Design of PT includes selection of initial PT force and PT area for a specified drift level. Criteria for selection of bearing height, bearing shape factor, rubber thickness, steel shim thickness, and central shear key are recommended in this section.

8.2.1. Selection of End Segment Height

The parametric study on SC-2 with different base segment heights and steel ratios indicated that increasing the base segment height or decreasing the base segment steel ratio in the basic model are effective in developing the full moment capacity of the column and eliminating the opening at interface between the base and second segments. For columns that bend in double curvature the method applies to the base segment connecting to the footing and the top segment connecting to the bent cap.

The opening between the end and adjacent segments occurs when the section at the interface elevation undergoes the tensile stress. The tensile stress at extreme fiber occurs when the moment is equivalent to the “cracking moment”. To eliminate joint opening, the end segment height should be at least as tall as the distance between the point of ultimate moment and cracking moment (Fig. 8-1(a)). When small amount of longitudinal steel ratio is placed in the end segment, the difference between the cracking and the moment capacity of the section is relatively small; therefore, a short end segment is required to develop the full moment capacity of the section without opening between the end segment and adjacent segment (Fig. 8-1 (a)). In columns with relatively high longitudinal steel reinforcement in the end segment, the ultimate moment is relatively large and the difference between the ultimate and cracking moment is high and a taller end segment is required if opening between segments is to be avoided (Fig. 8-1 (b)).

The following steps are recommended to calculate the end segment height.

Step 1: Calculate the ultimate moment capacity of the section taking into account the gravity load and post-tensioning force. The expected increase in the PT force under lateral displacement should be included. The segmental columns test data showed that joint opening was initiated and the PT force increased by 30% under approximately 2% lateral drift ratio. Therefore, it is recommended to increase the PT force used in calculating the ultimate moment capacity 30%.

Step 2: Calculate the cracking moment of the section.

To calculate ACI (2005) recommends Eqs. 8-1 and 8-2 to calculate f_r.

$$f_r = 7.5\sqrt{f_c'}\ (psi) \qquad \text{Eq. 8-1}$$

$$f_r = 0.623\sqrt{f_c'}\ (MPa) \qquad \text{Eq. 8-2}$$

Where

f_c'=Concrete strength

AASHTO (2002) section 5.4.2.6 recommends Eq. 8-3 to calculate f_r.

$$f_r = 0.24\sqrt{f_c'}\ (ksi) \qquad \text{Eq. 8-3}$$

Smaller cracking moment was calculated using Eqs. 8-1 through 8-3 compared to the measured cracking moment. The value of f_r was calculated for all segmental columns by comparing the measured and calculated cracking moments. The cracking moment in segmental columns corresponded to the lateral load capacity when the first joint opening occurred. The average and average less one standard deviation of f_r were $20.3\sqrt{f_c'}$ and $17.5\sqrt{f_c'}$, respectively, in segmental columns. The larger f_r compared to those recommended by ACI and AASHTO can be attributed to the application of epoxy between the segments to keep the segments aligned during assembly. The following modified equation of f_r is recommended to calculate M_{crack} in segmental columns.

$$f_r = 17.5\sqrt{f_c'}\ (psi) \qquad \text{Eq. 8-4}$$

$$f_r = 1.45\sqrt{f_c'}\ (MPa) \qquad \text{Eq. 8-5}$$

Step 3: Calculate the end segment height based on similar triangle relationships.

8.2.2. Post-Tensioning Design

The parametric study on segmental column with different initial PT force level showed that a very low PT force results in a response with steep strain hardening segment in the pushover curve while using a relatively high initial PT force results in lower overall ductility and a negative post-elastic stiffness (Fig. 7-13). Clearly, the response obtained using a high initial axial load ratio is not desirable. Using a low initial axial load ratio may not be desirable either since relatively low column strengths would be achieved. Hews and Priestley, (2002) suggested:

$$\frac{F_{pt} + F_{gravity}}{f_c' A_g} < 0.3 \qquad \text{Eq.8-6}$$

Where:

F_{pt} =Post-tensioning force

$F_{gravity}$ =Gravity load

f_c' =Concrete strength

A_g =Area of column section

The F_{pt} in Eq. 8-6 is the ultimate PT force.

$$F_{pt} = F_{i(PT)} + \Delta P \qquad \text{Eq. 8-7}$$

Where:

$F_{i(PT)}$ =Initial PT force

ΔP =The increase in PT force at ultimate displacement

The studies on the unbonded post-tensioned segmental columns including the current study showed that the PT force increases by 100% to 150%.

$$\Delta P \approx [1 \;\; to \;\; 1.5] \times F_{i(PT)} \qquad \text{Eq. 8-8}$$

To minimize residual displacement, the tendons should be designed to remain elastic at ultimate lateral loads, thus retaining their recentering ability.

$$F_{i(PT)} + \Delta P < F_{y(PT)} \qquad \text{Eq. 8-9}$$

Where:

$F_{y(PT)}$ =Yield force of PT tendon(s)

Substituting Eq. 8-8 in Eq. 8-9 gives:

$$[2 \;\; to \;\; 2.5] \times F_{i(PT)} < F_{y(PT)} \qquad \text{Eq. 8-10}$$

Therefore, Eq. 8-11 is used to select the initial PT force level.

$$F_{i(PT)} \approx [0.4 \ \ to \ \ 0.5] \times F_{y(PT)} \qquad \text{Eq. 8-11}$$

Substituting Eq. 8-11 with a factor of 0.4 (corresponding to 150% increase in post-tensioning force) in Eq. 8-6 leads to Eq. 8-12a and simplified form of Eq. 8-12b to estimates the required post-tensioning area, A_{pt}.

$$\frac{0.4 A_{pt} f_{y(pt)} + F_{gravity}}{f_c' A_g} < 0.3 \qquad \text{Eq. 8-12a}$$

or

$$A_{pt} > \frac{0.3 \times f_c' A_g - F_{gravity}}{0.4 \times f_{y(pt)}} \qquad \text{Eq. 8-12b}$$

Where:

$f_{y(pt)}$ = Yield strength of PT rod

The aforementioned derivation is based on an estimated increase in the PT force of 150%. A more accurate estimate of the PT force increase (ΔP) can be determined for a design drift level (ΔU) and the ultimate PT force can be checked against the elastic limit. ΔP is calculated for two modes of segment interface behavior: (1) with opening and (2) without opening.

1) The end segment height is less than that calculated in section 8.2.1 and joint opening is expected.

Referring to Fig. 8-2, the PT rod is stretched once the end segment and adjacent segment separate. Knowing the length of unbonded PT rod, L_t, the PT rod area, A_{pt}, and modulus of elasticity of PT rod E_{pt}, the elongation of PT rod is given by Eq. 8-13.

$$\Delta L = \frac{\Delta P \times L_t}{A_{pt} \times E_{pt}} \qquad \text{Eq. 8-13}$$

Using similar triangle relationship in Fig. 8-2 and assuming a contact length of $\frac{D}{4}$:

$$\frac{\Delta L}{D/4} = \frac{\Delta U}{H_c - H_{base}} \qquad \text{Eq. 8-14}$$

Where:

D=Column diameter

H_{base}=End segment height

H_c=Column height to the inflection point

The contact length was based the average of measured data for all segmental columns under maximum opening.

Replacing Eq. 8-14 in Eq. 8-13 leads to:

$$\Delta P = \frac{D \times A_{pt} \times E_{pt} \times \Delta U}{4 \times L_t \times (H_c - H_{base})} \quad \text{Eq. 8-15}$$

2) The end segment height is larger than that calculated in section 8.2.1 and no opening occurs.

Referring to Fig. 8-3, the PT rod is stretched once the column undergoes lateral displacement. Knowing the length of unbonded PT rod, L_t, the PT rod area, A_{pt}, and modulus of elasticity of PT rod E_{pt}, the elongation of PT is calculated by Eq. 8-13.

Using the similar triangle relationships in Fig. 8-3 and considering the design drift of ΔU,

$$\frac{\Delta U}{H} = \frac{\Delta L}{\sqrt{\Delta U^2 - \Delta L^2}} \quad \text{Eq. 8-16a}$$

Or

$$\Delta L = \frac{\Delta U^2}{\sqrt{\Delta U^2 + H^2}} \quad \text{Eq. 8-16b}$$

Where

$$H = H_c - \frac{L_p}{2}$$

L_p= Plastic hinge length, calculated from Eqs. 8-17 and 8-18 [Paulay and Priestley, 1992]

$$L_p = 0.08 \times H_c + 0.15 \times d_b \times f_y \ (ksi) \quad \text{Eq. 8-17}$$

$$L_p = 0.08 \times H_c + 0.022 \times d_b \times f_y \,(MPa) \qquad \text{Eq. 8-18}$$

Replacing Eq. 8-16b in Eq. 8-13 leads to:

$$\Delta P = \frac{A_{pt} \times E_{pt} \times \Delta U^2}{L_t \times \sqrt{H^2 + \Delta U^2}} \qquad \text{Eq. 8-19}$$

The following steps are recommended to design the post-tensioning.

Step 1: Determine the initial PT force

$$F_{i(PT)} = 0.4 \times F_{y(PT)} \qquad \text{Eq. 8-20}$$

Step 2: Estimate the required PT area

$$A_{pt} = \frac{0.3 \times f_c' A_g - F_{gravity}}{0.4 \times f_{y(pt)}} \qquad \text{Eq. 8-21}$$

Step 3: Calculate the increase of PT force under design level drift (ΔU)

If

$$H_{base} < \frac{H_c \times (M_u - M_{crack})}{M_u} \qquad \Delta P = \frac{D \times A_{pt} \times E_{pt} \times \Delta U}{4 \times L_t \times (H_c - H_{base})} \qquad \text{Eq. 8-22}$$

$$H_{base} \geq \frac{H_c \times (M_u - M_{crack})}{M_u} \qquad \Delta P = \frac{A_{pt} \times E_{pt} \times \Delta U^2}{L_t \times \sqrt{H^2 + \Delta U^2}} \qquad \text{Eq. 8-23}$$

Step 4: Check

If $F_{i(PT)} + \Delta P < F_{y(PT)}$ OK Eq. 8-24a

If $F_{i(PT)} + \Delta P > F_{y(PT)}$ NG Eq. 8-24b

If Eq. 8-24a is satisfied, the designer might consider reducing the PT area. Otherwise, the PT area will need to be increased.

8.2.3. Elastomeric Bearing Pad Design

As discussed in Chapter 2, the elastomeric bearing pad was designed by controlling the failure of the rubber when it was subjected to axial compression and bending moment. The following steps are recommended to design the bearing pad.

Step 1: Select the bearing diameter as the column diameter, D.

Step 2: Assume a bearing thickness of $D/2$.

Step 3: Design the steel shear key. Shear deformation in the pad needs to be restrained using a central shear key. Design of central shear key area is based on the demand in the bearing.

$V_{capacity} > V_{demand}$

$V_{capacity}$ and V_{demand} are the shear capacity and shear demand, respectively.

The shear demand is given by Eq. 8-25.

$$V_{demand} = \frac{M_p}{H_c} \qquad \text{Eq. 8-25}$$

Where:

M_p=Column plastic moment

H_c=Column height

The shear capacity is given by Eq. 8-26 [AASHTO, 2002].

$$V_{capacity} = Smaller \;\; of \begin{cases} \dfrac{\sqrt{3}}{3} A_g f_y \\ \dfrac{2 \times M_y}{H_{bearing}} \end{cases} \qquad \text{Eq. 8-26}$$

Where:

A_g =Gross area of the shear key

f_y= Yield stress of steel pipe

M_y=Yield moment of the shear key

$$M_y = \frac{f_y \times I}{c} \qquad \text{Eq. 8-27}$$

Where I and c are moment of inertia and neutral axis depth of the shear key section. The required shear key section is calculated based on A_g or $\frac{I}{c}$ in Eq. 8-26.

Step 4: Select the rubber thickness. The rubber thickness is determined from the bearing shape factor. The parametric study showed that choosing low shape factor results in low initial stiffness of the column. Thus, it is recommended to choose a shape factor larger than 15. The shape factor is defined as the ratio of the pad area to the area of the pad circumference, which for a round elastomeric bearing is:

$$S = \frac{Area\ of\ pad}{Area\ of\ the\ pad\ circumference} = \frac{\frac{\pi D^2}{4}}{\pi D t} = \frac{D}{4t} \qquad \text{Eq. 8-28}$$

It should be noted that the area of the drilled holes for passage of the longitudinal bars and the area of central shear key should be accounted for in calculation of shape factor [Wassef, et al., 2003]. Equation 8-29 provides the shape factor after considering the effects of holes.

$$S = \frac{A_b - n \times A_s - A_{sk}}{t \times (P_b + n \times P_s + P_{sk})} \qquad \text{Eq. 8-29}$$

Where A_b, A_s, and A_{sk} are areas of the bearing, longitudinal bars, and the shear key, respectively. P_b, P_s, and P_{sk} are perimeters of the bearing, longitudinal bars, and the shear key, respectively. n is the number of longitudinal bars.

Step 5: Select steel shim thickness. The thickness of the shims is determined by controlling the shim stress against the yielding [Wassef, et al., 2003].

$$\sigma_{shim} \le f_y \qquad \text{Eq. 8-30}$$

$$\sigma_{shim} = 1.5 \left[\frac{t_1 + t_2}{t_s} \right] \sigma_c \qquad \text{Eq. 8-31}$$

Where

t_1 and t_2 =Thickness of two adjacent rubber layers

t_s =Steel shims thickness

f_y =Yield stress of steel

σ_c =Compressive stress on the bearing (Eq. 8-32)

$$\sigma_c = \frac{F_{axial}}{A_b} \qquad \text{Eq. 8-32}$$

F_{axial} is the total load on the bearing including the gravity load and the PT force, including the estimated increase due to lateral displacement of the column. A_b is the elastomeric bearing area.

Step 5: Check the rotational demand of column against the rotational capacity of the bearing.

$$\theta_c \geq \theta_d \qquad \text{Eq. 8-33}$$

θ_c and θ_d are rotational capacity and rotational demand, respectively.

The required rotational stiffness of the section is determined by Eq. 8-34.

$$K_\theta = \frac{M_u}{\theta_u} \qquad \text{Eq. 8-34}$$

M_u and θ_u are the ultimate moment and rotation of the bearing, respectively. A moment-curvature analysis of the rubber pad section including the steel bars and excluding the shear key area can be used to determine the ultimate moment and rotation. The total axial load including the gravity load and the expected PT force should be included in the analysis. In the moment-curvature analysis, the bearing is modeled with an elastic material with modulus of elasticity of E_c. Derham and Kelley (1982) suggested for S>3

$$E_c = 5.6GS^2 \qquad \text{Eq. 8-35}$$

Where S is the shape factor and G is the shear modulus of rubber.

Equation 8-36 shows the required height of the bearing to satisfy the rotational demand.

$$T_r = \frac{E_b I}{K_\theta} \qquad \text{Eq. 8-36}$$

Where E_b, I, and T_r are the bending stiffness, moment of inertia, and total thickness of bearing, respectively. E_b is calculated using Eq. 8-37.

$$E_b = E(1 + \frac{2}{3}S^2) \qquad \text{Eq. 8-37}$$

The selected height in step 2 should be checked against T_r.

If $H_{bearing} > T_r$ OK Eq. 8-38a

If $H_{bearing} < T_r$ NG Eq. 8-38b

The bearing height should be increased.

8.3. Precast Bent

8.3.1. Embedment Length Design

The column embedment length in the footing should be sufficient for the full moment capacity of the column to develop at the top of the footing. The column footing connection is subjected to axial load, shear, and bending moment (Fig. 8-4). The stress distribution can be simplified using the rigid plastic stress theory (Petrold et al. 2000) (Fig. 8-5). The concrete stress in the horizontal direction is set to 0.67 f_c'. This stress is less than 0.85 f_c' to account for the orientation of the principal stresses not being horizontal.

The round column may be replaced with an equivalent square column with b_{eff} :

$$b_{eff} = \sqrt{\pi}\frac{D}{2} \qquad \text{Eq. 8-39}$$

Where

D = Column diameter

Based on Fig. 8-5, horizontal forces at the top, F_t, and at the bottom, F_b, transmitted from the column to the concrete can be calculated as

$$\begin{aligned} F_t &= 0.8 \times 0.67 f_c' b_{eff} \\ F_b &= 0.8(H - x)0.67 f_c' b_{eff} \end{aligned} \qquad \text{Eq. 8-40}$$

Using horizontal equilibrium the position of the neutral axis can be derived as

$$x = \frac{0.93V_{Sd} + 0.5b_{eff} f_c' H}{b_{eff} f_c'} \qquad \text{Eq. 8-41}$$

Where:
V_{sd} = Maximum shear force acting at bottom of the column

f_c' = Concrete compressive strength

b_{eff} = Effective column width (Eq. 8-39)

H = Embedded length

Taking the moments about the bottom of the column and combining Eqs. 8-40 and 8-41, the embedded length H of the column is calculated as:

$$H = \frac{1.56V_{Sd} + \sqrt{4.74V_{sd}^{\ 2} + 6.22M_{Sd}\, f_c' b_{eff}}}{b_{eff}\, f_c'} \qquad \text{Eq. 8-42}$$

Where:

M_{sd} = Maximum moment acting at bottom of the column

To determine the required embedded length, the maximum plastic moment of the column section should be calculated. The plastic shear is calculated by dividing the moment by the column height. Concrete strength can be assumed between 3 ksi (20.7 MPa) to 4 ksi (27.5 MPa).

Pertold et al. (2000) showed that the required embedment length H is typically between the effective width and twice the effective width and recommended the latter length.

Sadeghian and Fam (2010) recommended a minimum embedded length of 0.7D, where the D is the column diameter.

The provided embedded length in the current study was calculated based on Eqs. 8-39 through 8-42 and was increased by 25% to 1.5 D, where D is the column diameter. The test results showed that this length was sufficient to develop the full plastic moment capacity of the column.

8.3.2. CFFT Flexural Design

The flexural capacity of a concrete filled FRP tube can be determined using moment-curvature analysis. The FRP tube material is a filament wound product with fibers providing confinement and shear strength in the hoop direction and longitudinal reinforcement parallel to the columns axis. The steel transverse reinforcement may be eliminated since the FRP tube provides significant confinement to the concrete material. The Saiidi"s confinement model [Saiidi, et al., 2005], as described in Chapter 2, can be used to determine the confined concrete parameters.

The stress-strain behavior of FRP tube material in the longitudinal direction can be determined by Eq. 8-43 [Zhu, 2004]. A symmetric tri-linear curve in tension and compression can be replaced with the stress-strain curve of FRP tube (Eq. 8-42) and be used in moment-curvature analysis.

$$\sigma = \left(\frac{\varepsilon}{ABS(\varepsilon)} \right) \times \frac{\left(-b + \sqrt{b^2 + 4a \times ABS(\varepsilon)} \right)}{2a} \qquad ABS(\varepsilon) \le 0.05 \qquad \text{Eq. 8-43}$$

Where σ and ε are stress and strain, respectively. Parameters a and b are listed in Table 7-25 for different fiber orientation based on the laminate analysis. The stress-strain behavior of filament wound FRP material in tension and compression needs to be more investigated using ASTM D-5449 and ASTM D-5450, respectively.

The parametric study on effect of longitudinal steel ratio on force-displacement response of column showed that larger amount of longitudinal steel reinforcement in FRP column increased the lateral load capacities, as expected. Shao and Mirmiran, (2003) recommended that a moderate amount of internal steel reinforcement in the range of 1%-2% may improve the cyclic response of CFFT members. The improvement is more significant for under-reinforced FRP tubes. Adding internal steel, especially for members with thick FRP tubes, can be ineffective and may result in premature failure.

9. SUMMARY AND CONCLUSIONS

9.1. Summary

The incorporation of precast concrete elements, which can be fabricated off-site, can reduce the negative impacts of construction on traffic flow by shortening the construction time. However, knowledge of the behavior and performance of precast bridge columns during earthquakes is lacking, and consequently their widespread use in seismic regions is yet to be realized. An attractive type of precast columns is the segmental column. In standard segmental columns, the segments are connected by post-tensioned rods or cables to the footing, the cap beam, or both. Studies have shown that, under seismic loading, standard segmental columns offer minimal energy dissipation because there are no yielding elements. This weakness limits the use of standard segmental columns in areas of moderate and high seismicity. An alternative to standard segmental columns is a system that uses single-segment precast columns. It is necessary to design proper connection details between the column and footing, or column and cap beam to develop full plastic hinge moment and dissipate the earthquake energy.

The purpose of the study presented in this document was to develop precast columns that are able to dissipate energy under seismic loads. Several innovative precast concrete columns were designed and studied experimentally on a shake table and analyzed. Two types of precast bridge column were studied including segmental columns and precast monolithic columns.

The segmental columns were one-third scale cantilever models with plastic hinges incorporating different advanced materials to resist earthquake damage. Longitudinal steel dowels connected the base segment to the footing. Energy dissipation took place mostly through the yielding of the longitudinal bars in the base segment. Unbonded post tensioning was used to connect the segments and to minimize the residual displacements. The columns were subjected to the Sylmar earthquake (Northridge 1994) record with increasing amplitudes until failure. The target acceleration amplitude at failure was generally 0.9g. In the benchmark column, SC-2 (segmental with concrete), a conventional reinforced concrete detail was used. The performance of other specimens consisting of advanced materials in the plastic hinge region was compared with SC-2. The second specimen, referred to as SBR-1 (segmental with built-in rubber pad), was a segmental concrete column incorporating an elastomeric bearing pad in the plastic hinge. The purpose of using the pad was to minimize damage while dissipating energy through yielding of the longitudinal bars and deformation of the pad. The third and forth columns were designated SE-2 (segmental with ECC, engineered cementitious composite) and SF-2 (segmental with FRP, fiber reinforce polymer). The purpose of using ECC in lower segments was to minimize damage while dissipating energy through yielding of the longitudinal bars. Unidirectional FRP fabrics were used in the lower two segments of SF-2 to confine the concrete and minimize damage at the interface between the base and second segments. SC-2 was repaired after failure with unidirectional FRP fabrics and was labeled SC-2R (SC-2 repaired) to study the feasibility and the effectiveness of the repair.

A precast two-column pier PFEB (precast FRP-ECC bent) was also tested and analyzed to investigate the feasibility and seismic performance of monolithic precast columns. Two innovative details were used in the columns of PFEB: one column was a conventional concrete column incorporating ECC in the plastic hinge area, and the other was a concrete-filled FRP tube. Pipe-pin hinges were used at column-cap beam connections. The footing of the specimen was built leaving two openings to allow for embedment of columns.

In the course of analytical modeling it was found that no confinement models are available for the ECC. Several groups of cylindrical specimens each with different confinement steel ratios were tested. Using the measured data, a model was developed to calculate the confined properties of the ECC based on the unconfined ECC strength and transverse reinforcement.

Extensive analytical modeling of the columns and the two-column pier were conducted using OpenSees. The analytical models were utilized to model the specimens for the design phase prior to the tests and to evaluate their adequacy in duplicating the measured response. Generally close correlation between the measured and calculated results were obtained and the analytical models were deemed to be reliable. Extensive parametric studies were performed to understand the influence of different factors on the capacity and performance of specimens.

Seismic design recommendations for segmental columns and precast bent based on the test observations, measured data, and parametric studies were developed. Design methods for base segment height, post-tensioning force, and elastomeric bearing pad were developed for segmental columns. In addition, design recommendations for the embedment length and flexural design of precast concrete-filled FRP columns were made.

9.2. Observations

The following observations present the highlights of what was learned from the experimental and analytical results:

9.2.1. Precast Segmental Columns

10. The segmental column model construction took only three hours.

11. The performance of all segmental columns incorporating advanced materials (rubber pad, FRP jacket, and ECC) was better than the performance of SC-2 (reference column) in terms of lateral load capacity and damage.

12. The largest lateral load capacity in segmental column was observed in SC-2R followed by SF-2 where the two lower segments were wrapped with FRP jacket.

The most extensive yielding of the longitudinal steel reinforcement was seen also in these columns.

13. Ductile behavior of ECC resulted in minimal spalling and minor section loss at the interface of two lower segments of SE-2. Therefore, no degradation in the capacity of SE-2 was observed.

14. The strength and ductility of the ECC increased by increasing the transverse steel ratio. Additional strength that was gained by confinement effect of transverse reinforcement was lower than that of similarly confined concrete.

15. SC-2R, SBR-1 and SF-2 dissipated higher energy than other columns. Using FRP jacket in SF-2 and SC-2R delayed concrete failure and increased the energy dissipation due to more extensive yielding of the bars. Concrete failure in SF-2 and SC-2R occurred at displacements that were, respectively, 157% and 177% larger than the corresponding displacement of SC-2. Flexural deformation of elastomeric pad in the plastic hinge of SBR-1 increased dissipated energy and eliminated damage in that area.

16. The residual drift ratios were minimal and lower than 1% in all columns prior to failure.

17. The comparison between the test results and analytical results of a standard segmental column (a column in which the base segment is not monolithically connected to the footing) showed that the dissipated energy in segmental columns with the base segment connected to the footing was 2 to 4 times larger than that of a standard segmental column.

18. The primary failure mode in segmental columns was concrete spalling at the interface between the base and second segments. Failure of concrete was attributed to the large cyclic compressive strains from opening and closing action at the interface.

19. The most extensive spalling was seen in SC-2 and SBR-1, in which conventional concrete was used in the base segments. The least amount of concrete spalling was seen in SF-2 and SC-2R. The FRP jacket ruptured in SF-2 and SC-2R during high amplitude motion. Spalling of the ECC was minimal in SE-2 due to the ductile behavior of ECC.

20. Reasonable agreement was seen between the measured data and calculated results using OpenSees for all segmental columns.

21. The parametric study on SC-2 with different base segment heights and steel ratios indicated that increasing the base segment height or decreasing the base segment steel ratio are effective in developing the full moment capacity of the column and eliminating the opening at the interface between the base and second segments.

9.2.2. Precast Bent

8. Minimal ECC spalling was observed after 10% drift ratio in the precast monolithic column incorporating ECC in the plastic hinge. Due to ductile behavior of ECC, spalling was minor and it was limited to a short height.

9. No apparent damage was detected in the plastic hinge zone of FRP column before tensile rupture of the FRP tube. Two buckled bars were observed on the south side of the FRP column after removing the FRP tube and loose concrete.

10. The response hardening after yielding was substantially more significant in the concrete-filled FRP column compared to RC-ECC column. The FRP tube remained elastic while the steel reinforcing bars in RC-ECC column yielded.

11. The displacement ductility capacity of the RC-ECC column was larger than that of the FRP column by 35%, but lateral drift capacity was the same in these columns.

12. The energy dissipation was larger in the RC-ECC column compared to that of the FRP column.

13. The embedment length of 1.5 times the column diameter in the footing was sufficient to provide full fixity at the base in both the RC-ECC and FRP columns.

14. Comparison of PEFB and PPTC (a similar cast in place bent) in terms of lateral load and ductility capacity demonstrated that precast construction can provide strengths and ductilities similar to those of comparable cast-in-place construction.

15. The post-test analytical results for PEFB reasonably matched the experimental results.

9.3. Conclusions

The following conclusions were reached based on the experimental and analytical results presented in this document:

11. Monolithic connection between the column base segment and the footing provides energy dissipation capacity under seismic loading through yielding of the bars. Energy dissipation in this type of segmental column is 2 to 4 times larger than that of a column with no monolithic connection between the base segment and the footing.

12. Incorporating a rubber pad in the plastic hinge area is effective in improving energy dissipation while substantially reducing damage.

13. Application of ECC (engineered cementitious composite) in the plastic hinge area

improves ductility capacity and significantly reduces damage.

14. Using transverse reinforcement in combination with the ECC can improve strength and ductility of the ECC. The proposed confinement model for the ECC may be utilized in analytical studies of columns incorporating ECC.
15. FRP (fiber reinforced polymer) jacketing around column segments is effective in reducing damage at junctions of column segments and improving the strength and ductility capacity of the column.
16. Using an unbonded post-tensioning is an effective approach to provide continuity among the column segments and to reduce residual lateral displacements under earthquake loading.
17. Using the proposed method to calculate the end segment height can eliminate the joint opening and allows for development of full moment capacity of the column section.
18. The satisfactory agreement between the measured and calculated data using OpenSees suggest that existing analytical tools may be used to model the seismic performance of bridges with advanced details of the type used in this study.
19. Pier systems with precast monolithic columns, footings, and cap beams with connections of the type included in this study may be used in accelerated bridge construction in areas of moderate and high seismicity.
20. Concrete-filled FRP tube columns incorporating a minimum amount of longitudinal steel are ductile and appropriate for use in earthquake-resistant bridges.
21. Pipe-pin hinges can be effectively used in accelerated bridge construction because of their ease of construction.

REFERENCES

AASHTO [2002]. “Standard Specifications for Highway Bridges, Division I – Design,” 17th Edition, American Association of State Highway and Transportation Officials, Washington, D.C.

Aiken, I., Kelly, J., Tajirian F. [1989]. “Mechanics of low shape factor elastomeric seismic isolation bearings,” University of California, Berkeley, Report No. UCB.EERC-89/13.

American Concrete Institute ACI. [2008]. “Building code requirements for structural concrete,” *ACI 318-08,* ACI, Detroit, MI.

American Association of State Highway and Transportation Officials (AASHTO) [1999]. “Guide Specification for Design and Construction of Segmental Concrete Bridges,” Second Edition.

ASTM [2006a] “Standard Test Method for Transverse Compressive Properties of Hoop Wound Polymer Matrix Composite Cylinders,” D5449/D5449M,, West Conshohocken, PA.

ASTM [2006b] “Standard Test Method for Transverse Tensile Properties of Hoop Wound Polymer Matrix Composite Cylinders,” D5450/D5450M,, West Conshohocken, PA.

Billington, S.L., Barnes, R.W. and Breen, J.E. [1999]. “A precast segmental substructure system for standard bridges,” PCI J, 44(4), 56–73.

Billington, S.L., Yoon, J.K. [2002]. “Cyclic Behavior of Precast Post-Tensioned Segmental Concrete Columns with ECC,” Proceedings of the JCI International Workshop on Ductile Fiber Reinforced Cementitious Composites,

Billington, S.L., Yoon, J.K. [2004]. “Cyclic Response of Unbonded Post-tensioned Precast Columns with Ductile Fiber-Reinforced Concrete,” Journal of Bridge Engineering, © ASCE, 353-363.

California Department of Transportation [2006]. “Seismic Design Criteria (SDC),” Division of engineering services, Sacramento, California.

California Department of Transportation [2008]. “Memos To Designers (MTD),” Division of engineering services, Sacramento, California.

Chadwell, C. [2007]. <http://www.imbsen.com/xtract.htm>, Xtract, Ver. 3.0.8, Single User, Educational.

Chopra, A.K. [2006]. “Dynamics of Structures (3rd Edition),” Prentice Hall, New Jersey.

Chou, C. and Chen, Y. [2005]. “Cyclic tests of post-tensioned precast CFT segmental bridge columns with unbonded strands,” Earthquake Eng Struct Dyn, 35, 159 – 175.

Cruz-Noguez, C., Saiidi, M. [2010]. “Experimental and Analytical Seismic Studies of a Four-Span Bridge System with Innovative Materials,” Center for Civil Engineering Earthquake Research, Department of Civil and Environmental Engineering, University of Nevada, Reno, Nevada, Report No. CCEER-10-04.

Derham, C.J. [1982]. “THE Design of Laminated Bearings, II,” in: Proceeding of the International Conference on Natural Rubber for Earthquakle Protection of Building and Vibration Isolation, Kuala Lumpur, Malaysia, 247-256.

Gent, A.N., Lindley, P.B. [1959]. “The Compression of Bonded Rubber Block,” Proceeding of Institution of mechanical Engineers, 173(3), 111-122.

Hewes, J.T. and Priestley, M.J.N. [2002]. “Seismic design and performance of precast concrete segmental bridge columns,” University of California at San Diego, Report No. SSRP-2001/25.

Hieber, D.G., Wacker, J.M., Eberhard, M., Stanton, J.F. [2005]. “Precast Concrete Pier Systems for Rapid Construction of Bridges in Seismic Regions,” Final Technical Report, Washington State Transportation Center (TRAC), University of Washington and Washington State Department of Transportation.

Johnson, N., Saiidi M., Itani, A. and Ladkany, S. [2005]. “Seismic Retrofit of Octagonal Columns with Pedestal and One-Way Hinge at the Base,” American Concrete Institute, ACI Structural Journal, Vol. 102, No. 5, 699-708.

Karbhari, V.M., Seible, F., Burgueno, R., Davol, A., Wernli, M., and Zhao, L. [2000]. „„Structural characterization of fiber-reinforced composite short and medium-span bridge systems,‘‘‘‘Appl. Compos. Mater., 7(2), 151–182.

Kawashima, K., MacRae, G.A., Hoshikuma, J., and Nagaya, K. [1998]. “Residual displacement response spectrum,” Journal of Structural Engineering, 124(5): 523-530.

Kawashima, K. and Watanabe, G. [2006]. “Seismic Performance of Unbonded Columns and Isolator Built-in Columns based on Cyclic Loading Tests,” Proceedings, IABMAS, Porto, Portugal.

Kawashima, K. and Nagai, M. [2002]. “Development of a reinforced concrete pier with a rubber layer in the plastic hinge region,” Structural and Earthquake Engineering, Proc. JSCE, 703/I-59, 113-128.

Kent, D.C., Park, R. [1971]. “Flexural Members with Confined Concrete,” Journal of the Structural Division, Vol. 97, No. 7, 1969-1990.

Kesner, K.E., Billington, S.L., Douglas, K.S. [2003]. “Cyclic Response of Highly Ductile

Fiber-Reinforced Cement-Based Composites," ACI Materials Journal, V. 100, No. 5, 381-390.

Keys, W.C. [1937]. "Rubber springs," Mechanical Engineering, 59, New York, 345-349.

Khaleghi, B. [2005]. "Use of Precast Concrete Members for Accelerated Bridge Construction in Washington State," Transportation Research Record: Journal of the Transportation Research Board, CD 11-S, Transportation Research Board of the National Academies, Washington, D.C., 187–196.

Kulkarni, S. and Shah, S. [1998]. "Response of Reinforced Concrete Beams at High Strain Rates," ACI Structural Journal, V. 95, No. 6, 705-715.

Kwan, W.P., and Billington, S.L. [2003a]. "Unbonded Posttensioned Concrete Bridge Piers. I: Monotonic and Cyclic Analyses," J. Bridge. Eng., 8 (2), 92–101.

Kwan, W.P., and Billington, S. L. [2003b]. "Unbonded Posttensioned Concrete Bridge Piers. II: Seismic Analyses," J. Bridge. Eng., 8 (2), 102–111.

Lepech, M., and Li, V.C. [2005]. "Durability and Long Term Performance of Engineered Cementitious Composites," International Workshop on HPFRCC Structural Applications, Hawaii.

Li, V.C. [1998]. "Engineered Cementitious Composites – Tailored Composites Through Micromechanical Modeling," in Fiber Reinforced Concrete: Present and the Future, N. Banthia, A. Bentur, and A. Mufti (eds), Canadian Soc. for Civ. Engrg., Montreal, 64-97.

Lindley, P.B. [1974]. "Engineering Design with Natural Rubber," NR Technical Bulletin, 4th Edition. Malaysian Rubber Producers‟‟ Research Association (MRPRA), 1974. ISSN 09560-3856.

Mander, J., Priestley, M.J.N. and Park, R. [1988]. "Theoretical Stress-Strain Model for Confined Concrete," Journal of Structural Engineering, ASCE, V.114, No.8, 1804-1826.

Mander, J.B. and Chen, C.T. [1997]. "Seismic design of bridge piers based on damage avoidance design," National Center for Earthquake Engineering Research, Report No. NCEER-97-0014.

Mazzoni, S., McKenna, F., Scott, M.H., Fenves, G.L. [2007]. "OpenSees Command Language Manual," Berkeley, CA.

Mirmiran, A., Naguib, W., and Shahawy, M. [2000]. „„„Principles and analysis of concrete-filled composite tubes,‟‟‟‟J. Adv. Mater., 32(4), 16–23.

O'Brien, M., Saiidi, M. and Sadrossadat-Zadeh, M. [2007]. "A Study of Concrete Bridge Columns Using Innovative Materials Subjected to Cyclic Loading," Center for Civil Engineering Earthquake Research, Department of Civil Engineering, University of Nevada, Reno, Nevada, Report No. CCEER-07-01.

Ou, Y., Chiewanichakorn, M., Aref, A., Lee, G. [2007]. "Seismic Performance of Segmental Precast Unbonded Posttensioned Concrete Bridge Columns," Journal of Structural Engineering, ASCE, V.133, No.11, 1636-1647.

Park, R., and Paulay, T. [1979]. Reinforced Concrete Structures, John Wiley & Sons, Inc., New York.

Paulay, T., Priestley, M. J.N. [1992]. "Seismic Design of Reinforced Concrete and Masonry Buildings," Wiley Interscinece.

Pertold, J., Xiao, R.Y, Wald, F. [2000a]. "Embedded steel column bases I. Experiments and numerical simulation," Journal of Constructional Steel Research 56 (2000), 253–270.

Pertold, J., Xiao, R.Y, Wald, F. [2000b]. "Embedded steel column bases II. Design Model Proposal," Journal of Constructional Steel Research 56 (2000), 271–286.

Phan, V., Saiidi, S. and Anderson, J. [2005]. "Near Fault (Near Field) Ground Motion Effects on Reinforced Concrete Bridge Columns," Center for Civil Engineering Earthquake Research, Department of Civil Engineering, University of Nevada, Reno, Nevada, Report No. CCEER-05-7.

Popovics, S. [1973]. "A numerical approach to the complete stress-strain curve of concrete," Cement and Concrete Research, 3(5), 583–599.

Priestley, M.J.N. and MacRae, G.A. [1996]. "Seismic tests of precast beam-to column joint subassemblages with unbonded tendons," PCI J, 41(1), 64 – 80.

Rouse, J.M., and Billington, S.L. [2007]. "Creep and Shrinkage of High-Performance Fiber-Reinforced Cementitious Composites", ACI Materials Journal, 129-136.

Sadeghian, P., Fam, A. [2010]. "Bond-Slip Analytical Formulation toward Optimal Embedment of Concrete-Filled Circular FRP Tubes into Concrete Footings," Journal of Engineering Mechanics, ASCE, Vol. 136, No. 4, 524-533.

Saiidi, M., Sureshkumar, K., and Pulido, C. [2005]. "A Simple Model for CFRP Confined Concrete," Journal of Composites for Construction, ASCE, Vol. 9, No. 1, 101-104.

Sakai, J. and Mahin, S. [2004]. "Analytical Investigations of New Methods for Reducing Residual Displacements of Reinforced Concrete Bridge Columns," PEER Report 2004/02 Pacific Earthquake Engineering Research Center College of Engineering University of California, Berkeley.

SeismoSoft "SeismoSignal" [online], 2004. Available from URL: http://www.seismosoft.com/

Shao, Y. [2003]. "Seismic performance of FRP-concrete beam-column," Ph.D. dissertation, North Carolina State University, Raleigh, North Carolina.

Shao, Y., Zhu, Z., and Mirmiran, A. [2006]. “Cyclic Modeling of FRP-Confined Concrete with Improved Ductility,” Cement & Concrete Composites, 28(10), 959-968.

Teng, J.G., Chen, J.F., Smith, S.T., and Lam, L. [2002]. “FRP strengthened RC structures,” John Wiley & Sons Ltd., New York.

Teng, J.G, and Lam , L. [2004]. “Behavior and Modeling of Fiber Reinforced Polymer-Confined Concrete,” Journal of structural Engineering, ASCE, Vol. 130, No. 11, 1713-1723.

Vosooghi, A., Saiidi, M. [2010]. “Post-Earthquake Evaluation and Emergency Repair of Damaged RC Bridge Columns Using CFRP Materials,” Center for Civil Engineering Earthquake Research, Department of Civil and Environmental Engineering, University of Nevada, Reno, Nevada, Report No. CCEER-10-05.

Wang, H. and Saiidi, S. [2005]. “A Study of RC Columns with Shape Memory Alloy and Engineered Cementitious Composites,” Center for Civil Engineering Earthquake Research, Department of Civil Engineering, University of Nevada, Reno, Nevada Report No. CCEER-05-1.

Wassef, W. G., Smith, C., Clancy, C. M., Smith, M.J. [2003]. “Comprehensive Design Examople for Prestressed Concrete (PSC) Girder Superstructure Bridge with Commentary,” The Federal Highway Administration.

Wehbe, N., Saiidi, M., and Sanders, D. [1999]. “Seismic Performance of Rectangular Bridge Columns with Moderate Confinement,” American Concrete Institute, ACI Structural Journal, Vol. 96, No. 2, 248-259.

Yamashita, R. and Sanders, D. [2006]. “Seismic performance of unbonded prestressed concrete columns constructed with precast segments,” in Proceedings of the 8th National Conference on Earthquake Engineering, San Francisco, California, Paper no. 1434.

Yu, T.;Wong; Y.L., Teng, J.G.; Dong, S.L.; and Lam , E.S.S. [2006]. “Flexural Behavior of Hybrid FRP-Concrete-Steel Double-Skin Tubular Members,” Journal of Composites for Construction, ASCE, Vol. 10, No. 5, 443-452.

Zadeh, M. S., and Saiidi, M. S. [2007]. “Effect of Constant and Variable Strain Rates on Stress-Strain Properties and Yield Propagation in Steel Reinforcing Bars,” Report No. CCEER-07-02, Center for Civil Eng. Earthquake Research, Dept. of Civil Eng., Univ. of Nevada, Reno, NV.

Zafra, R., Kawashima, K., Nakayama, M., Kajiwara, K. [2010]. “Compression and Tension and Cyclic Loading Experiments on Polypropylene Fiber Reinforced Cement Composite,” E-Defense Report.

Zaghi, A., and Saiidi, M. [2008]. “Mechanism of shear force transfer in RC columns with pipe-pins,” Proceedings, 10th Pan Am. Cong. of Applied Mech., Cancun, Mexico, 243-246.

Zaghi, A. E., and Saiidi, M. [2010a]. "Seismic Design of Pipe-Pin Connections in Concrete Bridges," Center for Civil Engineering Earthquake Research, Department of Civil and Environmental Engineering, University of Nevada, Reno, Nevada, Report No. CCEER-10-01.

Zaghi, A.E., and Saiidi, M. [2010b]. "Bearing and Shear Failure of Pipe-Pin Hinges Subjected to Earthquakes," Journal of Bridge Engineering, ASCE, posted ahead of print, http://dx.doi.org/10.1061/(ASCE)BE.1943-5592.0000160.

Zaghi, A.E., Saiidi, M., and El-Azazi, S. [2010c]. "Shake Table Evaluation of a Two-Column Bridge Bent Model Incorporating Pipe-Pin Hinges," Journal of Bridge Engineering, ASCE, posted ahead of print, http://dx.doi.org/10.1061/(ASCE)BE.1943-5592.0000191.

Zaghi, A.E., and Saiidi, M., Mirmiran, A. [2010d]. "Shake Table Experiment on a Concrete Filled GFRP Pipe as a New Bridge Column System," Journal of Composite for Construction, ASCE, Under Review.

Zaghi, A.E., and Saiidi, M. [2010e]. "Seismic Performance of Pipe-Pin Two-Way Hinges in Concrete Bridge Columns," Journal of Earthquake Engineering, Taylor & Francis, UK, 14(8), 1253-1302.

Zhu, Z. [2004]. "Joint Construction and Seismic Performance of Concrete-Filled Fiber Reinforced Polymer Tubes," Ph.D. dissertation, North Carolina State University, Raleigh, North Carolina.

Zhu, Z., Mirmiran, A., and Shahawy, M. [2004]. "Stay-in-place fiber reinforced polymer forms for precast modular bridge pier system," J. Compos. Constr., 8 (6), 560–568.

Zhu, Z., Ahmad, I., Mirmiran, A. [2006]. "Seismic Performance of Concrete-Filled FRP Tube Columns for Bridge Substructure," Journal of Bridge Engineering © ASCE Vol. 11, No. 3, 359-370.

Zhu, Z., Mirmiran, A., and Saiidi, M.S. [2006]. "Seismic Performance of Fiber Composite Tubed Reinforced Concrete Bridge Substructure," Transportation Research Record No. 1976, Design of Structures, Part 7 – Structural Fiber Reinforced Plastics, Transportation Research Board, National Research Council, Washington, D.C., 197-206.

TABLES

Table 2-1. General Column Properties

Column Height [inch]		72
Column Diameter [inch]		16
Longitudinal Steel ratio in first segment [%]	SC-2, SF-2, SE-2	1
	SBR-1	1.2
Transverse Steel ratio in all segment [%]		1.41
Aspect Ratio [%]		4.5
Axial Load [kips]	Gravity Load [kips]	80
	Post-tensioning [kips]	103
Axial Load Index	Specified	21
Scale		0.33
Subjected ground Motion		Sylmar

Table 2-2. Measured Concrete Compressive Strength in Segmental Columns

		Concrete Strength ksi (MPa)		
		7 Days	28 Days	Test Day
SC-2	**Footing and Third Segment**	5.22 (36)	7.31 (50.4)	8.62 (59.4)
	Base Segment	3.13 (21.6)	5.45 (37.5)	6.73 (46.4)
	Second and Fourth Segments	3.81 (26.2)	5.21 (35.9)	5.96 (41.1)
SF-2	**Footing and Third Segment**	5.22 (36)	7.31 (50.4)	9.32 (64.2)
	Base Segment	3.13 (21.6)	5.45 (37.5)	6.87 (47.3)
	Second and Fourth segments	3.81 (26.2)	5.21 (35.9)	6.06 (41.7)
SE-2	**Footing**	3.13 (21.6)	5.45 (37.5)	6.87 (47.3)
	Third Segments	5.22 (36)	7.31 (50.4)	N/A
	Fourth Segments	3.81 (26.2)	5.21 (35.9)	6.34 (43.7)
SBR-1	**Footing, Base and Third Segments**	3.81 (26.2)	5.71 (39.4)	6.54 (45.1)
	Head block, Second and Fourth segments	3.53 (24.3)	6.02 (41.5)	7.23 (49.8)

Table 2-3. Measured ECC Compressive Strength in SE-2

		Strength ksi (MPa)	
		28 Days	Test Day
SE-2	**Base Segment**	5.76 (39.7)	7.11 (49)
	Second Segment	5.55 (38.2)	7.4 (51)

Table 2-4. Measured grout Compressive Strength in SC-2R

		Strength ksi (MPa)
		6Days
SC-2R	**Repair Grout**	7.04 (48.5)

Table 2-5. Loading Plan in SC-2segmental Columns

Run	**Input Ground Motion**	**SC-2**	**SBR-1**	**SF-2**	**SE-2**	**SC-2R**
A	Whitenoise	**X**	**X**	**X**	**X**	
1	0.1XSylmar	**X**	**X**	**X**	**X**	
B	Whitenoise	**X**	**X**	**X**	**X**	**X**
2	0.25XSylmar	**X**	**X**	**X**	**X**	**X**
C	Whitenoise	**X**	**X**	**X**	**X**	**X**
3	0.50XSylmar	**X**	**X**	**X**	**X**	**X**
D	Whitenoise	**X**	**X**	**X**	**X**	**X**
4	0.75XSylmar	**X**	**X**	**X**	**X**	
E	Whitenoise	**X**	**X**	**X**	**X**	
5	1.00XSylmar	**0**	**X**	**X**	**X**	**X**
F	Whitenoise	**X**	**X**	**X**	**X**	**X**
6	1.25XSylmar	**X**	**X**	**X**	**X**	
G	Whitenoise	**X**	**X**	**X**	**X**	
7	1.50XSylmar	**X**	**X**	**X**	**X**	**X**
H	Whitenoise	**X**	**X**	**X**	**X**	**X**
8	1.50XSylmar			**X**	**X**	
I	Whitenoise			**X**	**X**	
9	1.75XSylmar					**X**
J	Whitenoise					**X**

Table 2-6. Mix Proportion of ECC $kg/m^3 \left(lb/ft^3\right)$

Cement	**Fly Ash**	**Sand**	**Fiber**	**Super Plasticizer**	**Viscous Agent**	**Water**	**W/C+FA**	**S/C**	**FA/C**
380 (23.7)	790 (49.3)	470 (29.3)	26 (1.6)	18 (1.1)	1.2 (0.07)	305 (19)	0.26 (0.016)	1.24 (0.07)	2.08 (0.13)

Table 2-7. Material Type of ECC Mix

Material	Type
Cement	Type I/II
Fly Ash	FT Bridger
Sand	#60 Medium
VA	Dow Methocel
SP	Basf Melfox 2651
Fiber	Kurary PVA KII 8X15

Table 2-8. PEFB Bent Properties

	Concrete-ECC column	Concrete filled FRP tube
Column Height [inch]	63	63
Column Diameter [inch]	14	14.567
Longitudinal Steel ratio[%]	1.6	0.46
Transverse steel ratio	1.7	-
Aspect ratio	4.5	4.32
Scale	0.3	0.3
Spiral around the Pipe	Φ0.25@1”	Φ0.25@1”
FRP tube O.D.[in].	-	14.567
FRP tube thickness[in.]	-	0.269
Axial load [kips]	50	50
Axial load index [%]	7.58	6.26
Subjected ground motion	Sylmar	Sylmar

Table 2-9. Pipe-pin Detail in PEFB

	Column Diameter [in]	Steel pipe O.D. [in]	Steel pipe Thickness [in]	Vertical Gap [in]	Horizontal Gap [in]	Can thickness [in]	Pipe Protrusion [in]	Pipe embedment [in]
Model	14	2.88	0.276	0.25	0.15	0.125	3.5	13

Table 2-10. Measured Concrete Compressive Strength in PEFB

Columns		**Strength ksi (MPa)**		
		7 Days	**28 Days**	**Test Day**
RC-ECC	**Footing and Top part of Column**	3.45 (23.7)	4.28 (29.5)	5.25 (36.2)
FRP	**Inside the FRP Tube**	3.66 (25.2)	4.79 (33)	5.68 (39.2)

Table 2-11. Measured ECC Compressive Strength in PEFB

		Strength ksi (MPa)	
		28 Days	**Test Day**
RC-ECC	**ECC in Plastic Hinge**	5.22 (36)	5.61 (38.7)

Table 2-12. Measured Fast Setting Grout Compressive Strength in PEFB

	Strength ksi (MPa)		
	7 Days	**28 Days**	**Test Day**
High Strength Grout Used In Embedment Hole	5.59 (38.5)	6.41 (44.2)	7.05 (48.6)

Table 2-13. Mechanical Properties of FRP Tube

Property	75° F (24° C) ksi (MPa)	210° F (99° C) ksi (MPa)
Axial tensile ultimate stress	10.3 (71)	7.7 (53)
Axial tensile modules of elasticity	1820 (12548)	1180 (8136)
Axial compressive ultimate stress	33 (230)	19.4 (134)
Axial compressive modules of elasticity	1260 (8687)	600 (4137)
Beam bending ultimate stress	23 (158.6)	16 (110)
Beam bending modules of elasticity	1460 (10000)	960 (6630)
Ultimate hoop tensile stress	34 (234)	43.5 (300)

Table 2-14. Loading Plan in PEFB

Run	**Input Ground Motion**
A	Whitenoise
1	0.1XSylmar
B	Whitenoise
2	0.4XSylmar
C	Whitenoise
3	0.7XSylmar
D	Whitenoise
4	1.0XSylmar
E	Whitenoise
5	1.3XSylmar
F	Whitenoise
6	1.65XSylmar
G	Whitenoise

Table 3-1. Measured Maximum Force-Displacement Response in SC-2

Run	Achieved PGA at table (g)	Max. Disp. inch (mm)	Max. Lateral Force kips (kN)
1	0.06	0.10 (3)	6.79 (30.2)
2	0.15	0.33 (8)	13.65 (60.7)
3	0.30	1.42 (36)	20.68 (92.0)
4	0.55	2.02 (51)	21.64 (96.3)
5	0.75	3.55 (90)	23.31 (103.7)
6	0.93	4.57 (116)	21.04 (93.6)
7	1.08	8.42 (214)	19.83 (88.2)

Table 3-2. Energy Dissipation in SC-2

	Energy Dissipation kip.inch (kN.mm)	Cumulative Energy Dissipation kip.inch (kN.mm)
Run 1	1.4 (160)	1.4 (160)
Run 2	9.3 (1052)	10.7 (1212)
Run 3	30.1 (3400)	40.8 (4613)
Run 4	42.4 (4793)	83.2 (9405)
Run 5	115.3 (13031)	198.6 (22437)
Run 6	146.5 (16557)	345.1 (38993)
Run 7	193.9 (21901)	539 (60895)

Table 3-3. PT Force and Max. Displacement in SC-2

	Max. Displacement in. (mm)	Max. PT Force kips (kN)
Run 1	0.1 (3)	95.4 (424.3)
Run 2	0.3 (8)	96.8 (430.7)
Run 3	1.4 (36)	125.8 (559.4)
Run 4	2 (51)	142.1 (632)
Run 5	3.6 (90)	178.4 (793.5)
Run 6	4.6 (116)	188.7 (839.4)
Run 7	8.4 (214)	205.9 (913)

Table 3-4. Contribution of Segments Separation in Total Displacement in SC-2

	Maximum Displacement (in.)	Maximum Segments Separation (in.)	Contribution of Segment Separation in total displacement %
Run 1	0.10 (3)	0.002 (0.05)	8.15
Run 2	0.33 (8)	0.01 (0.025)	7.84
Run 3	1.42 (36)	0.25 (6.4)	47.78
Run 4	2.02 (51)	0.42 (10.7)	57.64
Run 5	3.55 (90)	0.85 (21.6)	70.38
Run 6	4.57 (116)	1.19 (30.2)	68.70
Run 7	8.42 (214)	1.60 (40.6)	54.76

Table 3-5. Damping Ratios in SC-2

Run	Damping Ratio ξ (%)
0	2.3
1	2.3
2	1.7
3	2.0
4	2.2
5	3.6
6	6.9
7	3.0

Table 3-6. Measured Maximum Force-Displacement Response in SBR-1

Run	Achieved PGA at table (g)	Max. Disp. inch (mm)	Max. Lateral Force kips (kN)
1	0.07	0.3 (7)	6.93 (30.8)
2	0.16	0.6 (14)	11.56 (51.4)
3	0.40	1.3 (32)	16.60 (73..9)
4	0.62	2.4 (62)	21.12 (93.9)
5	0.78	3.5 (89)	22.73 (101.1)
6	0.84	5 (126)	24.39 (108.5)
7	0.94	10.1 (257)	26.53 (118.0)

Table 3-7. Energy Dissipation in SBR-1

	Energy Dissipation kip.inch (kN.mm)	Cumulative Energy Dissipation kip.inch (kN.mm)
Run 1	1.6 (187)	1.6 (187)
Run 2	5.2 (584)	6.8 (771)
Run 3	16.2 (1827)	23 (2599)
Run 4	43.7 (4942)	66.7 (7541)
Run 5	113.3 (12801)	180 (20343)
Run 6	168.7 (19050)	348.7 (39393)
Run 7	267.7 (30244)	616.4 (69638)

Table 3-8. PT Force and Max. Displacement in SBR-1

	Max. Displacement in. (mm)	Max. PT Force kips (kN)
Run 1	0.3 (7)	97 (431)
Run 2	0.6 (14)	97 (431)
Run 3	1.3 (32)	97 (432)
Run 4	2.4 (62)	101 (448)
Run 5	3.5 (89)	120 (534)
Run 6	5 (126)	146 (647)
Run 7	10.1 (257)	199 (885)

Table 3-9. Contribution of Segments Separation in Total Displacement in SBR-1

	Maximum Displacement in. (mm)	Maximum Segments Separation in. (mm)	Contribution of Segment Separation in total displacement %
Run 1	0.3 (7)	0.0075 (0.2)	10.4
Run 2	0.6 (14)	0.0078 (0.2)	7.0
Run 3	1.3 (32)	0.0542 (1.4)	11.8
Run 4	2.4 (62)	0.2108 (5.4)	22.4
Run 5	3.5 (89)	0.4475 (11.4)	41.3
Run 6	5 (126)	0.7898 (20.1)	57.1
Run 7	10.1 (257)	0.9919 (25.2)	53.7

Table 3-10. Damping Ratios in SBR-1

Run	Damping Ratio ξ (%)
0	4.2
1	4.6
2	2.7
3	4.0
4	7.0
5	6.2
6	3.5
7	4.4

Table 3-11. Measured Maximum Force-Displacement Response in SF-2

Run	Achieved PGA at table (g)	Max. Disp. inch (mm)	Max. Lateral Force kips (kN)
1	0.05	0.1 (3)	7.23 (32.2)
2	0.13	0.3 (7)	14.21 (63.2)
3	0.31	1.4 (35)	22.85 (101.7)
4	0.54	1.8 (46)	24.77 (110.2)
5	0.76	2.7 70)	27.28 (121.3)
6	0.90	4.3 (109)	30.27 (134.6)
7	1.05	5.2 (132)9	29.72 (132.2)
8	1.01	10.8 (273)	26.61 (118.3)

Table 3-12. Energy Dissipation in SF-2

	Energy Dissipation kip.inch (kN.mm)	Cumulative Energy Dissipation kip.inch (kN.mm)
Run 1	1 (162)	1 (162)
Run 2	9 (961)	10 (1123)
Run 3	34 (3785)	43 (4908)
Run 4	38 (150)	82 (9209)
Run 5	69 (326)	150 (16960)
Run 6	176 (326)	326 (36798)
Run 7	221 (24962)	547 (61760)
Run 8	242 (27320)	788 (89080)

Table 3-13. PT Force and Max. Displacement in SF-2

	Max. Displacement in. (mm)	Max. PT Force kips (kN)
Run 1	0.1 (3)	98.9 (439.8)
Run 2	0.3 (7)	99.8 (443.8)
Run 3	1.4 (35)	143.3 (637.2)
Run 4	1.8 (46)	129.8 (577.2)
Run 5	2.7 70)	171.1 (760.9)
Run 6	4.3 (109)	210.3 (953.3)
Run 7	5.2 (132)	218.2 (970.6)
Run 8	10.8 (273)	258.8 (1151.2)

Table 3-14. Contribution of Segments Separation in Total Displacement in SF-2

	Maximum Displacement in. (mm)	Maximum Segments Separation in. (mm)	Contribution of Segment Separation %
Run 1	0.1 (3)	0.003 (0.09)	13.2
Run 2	0.3 (7)	0.01 (0.3)	14.8
Run 3	1.4 (35)	0.23 (6)	50.4
Run 4	1.8 (46)	0.34 (9)	55.6
Run 5	2.7 70)	0.58 (15)	63.9
Run 6	4.3 (109)	0.99 (25)	71.2
Run 7	5.2 (132)	1.27 (32)	72.6
Run 8	10.8 (273)	1.68 (43)	61.7

Table 3-15. Damping Ratios in SF-2

Run	Damping Ratio ξ (%)
0	1.4
1	1.4
2	1.9
3	3.0
4	2.3
5	2.1
6	4.2
7	1.6
8	2.6

Table 3-16. Measured Maximum Force-Displacement Response in SE-2

Run	Achieved PGA at table (g)	Max. Disp. inch (mm)	Max. Lateral Force kips (kN)
1	0.06	0.1 (3)	6.61 (29.4)
2	0.14	0.3 (7)	12.98 (57.8)
3	0.30	1.4 (35)	19.34 (86)
4	0.59	2.2 (55)	20.23 (90)
5	0.77	3.6 (92)	20.87 (92.8)
6	0.95	7.3 (184)	22.01 (97.9)
7	1.08	6.3 (161)	19.73 (87.8)
8	1.22	7.7 (197)	18.54 (82.5)

Table 3-17. Energy Dissipation in SE-2

	Energy Dissipation kip.inch (kN.mm)	Cumulative Energy Dissipation kip.inch (kN.mm)
Run 1	1 (144)	1 (144)
Run 2	9 (10121)	10 (1156)
Run 3	31 (3524)	41 (4680)
Run 4	43 (4888)	85 (9568)
Run 5	108 (12184)	193 (21753)
Run 6	165 (8585)	357 (40338)
Run 7	145 (16376)	502 (56714)
Run 8	136 (15315)	638 (72030)

Table 3-18. PT Force and Max. Displacement in SE-2

	Max. Displacement in. (mm)	Max. PT Force kips (kN)
Run 1	0.1 (3)	100.4 (446.7)
Run 2	0.3 (7)	101 (449.3)
Run 3	1.4 (35)	124.4 (553.3)
Run 4	2.2 (55)	141.1 (627.4)
Run 5	3.6 (92)	165.1 (734.5)
Run 6	7.3 (184)	204.6 (909.8)
Run 7	6.3 (161)	196.9 (857.9)
Run 8	7.7 (197)	205.4 (913.8)

Table 3-19. Contribution of Segments Separation in Total Displacement in SE-2

	Maximum Displacement (in.)	Maximum Segments Separation (in.)	Contribution of Segment Separation %
Run 1	0.1 (3)	0.004 (0.1)	18.7
Run 2	0.3 (7)	0.02 (0.5)	26.6
Run 3	1.4 (35)	0.27 (7)	62.1
Run 4	2.2 (55)	0.48 (12)	77.8
Run 5	3.6 (92)	0.86 (22)	87.1
Run 6	7.3 (184)	1.49 (38)	82.4
Run 7	6.3 (161)	1.40 (36)	84.5
Run 8	7.7 (197)	1.49 (38)	76.7

Table 3-20. Damping Ratios in SE-2

Run	Damping Ratio ξ (%)
0	2.8
1	1.9
2	2.0
3	3.2
4	3.1
5	8.7
6	7.6
7	2.8
8	3.0

Table 3-21. Measured Maximum Force-Displacement Response in SC-2R

Run	Achieved PGA at table (g)	Max. Disp. inch (mm)	Max. Lateral Force kips (kN)
1	0.16	0.5 (13)	13.64 (60.7)
2	0.33	1.3 (34)	19.00 (84.5)
3	0.76	3.3 (84)	23.08 (102.7)
4	1.14	5.6 (143)	26.69 (118.7)
5	1.33	10.7 (271)	32.06 (142.6)

Table 3-22. Energy Dissipation in SC-2R

	Energy Dissipation kip.inch (kN.mm)	**Cumulative Energy Dissipation kip.inch (kN.mm)**
Run 1	10.1 (1144)	10.1 (1144)
Run 2	24 (2709)	34.1 (3853)
Run 3	103.5 (11696)	137.6(15550)
Run 4	210.3 (23764)	348 (39314)
Run 5	324.6 (36678)	672.6(75992)

Table 3-23. PT Force and Max. Displacement in SC-2R

	Max. Displacement in. (mm)	**Max. PT Force kips (kN)**
Run 1	0.5 (13)	77.2 (343.4)
Run 2	1.3 (34)	97.3 (432.7)
Run 3	3.3 (84)	146.3 (650.6)
Run 4	5.6 (143)	186.7 (830.2)
Run 5	10.7 (271)	254.7 (1132.9)

Table 3-24. Contribution of Segments Separation in Total Displacement in SC-2R

	Maximum Displacement in. (mm)	**Maximum Segments Separation in. (mm)**	**Contribution of Segment Separation %**
Run 1	0.5 (13)	0.1 (1)	29.3
Run 2	1.3 (34)	0.2 (6)	39.6
Run 3	3.3 (84)	0.8 (20)	42.3
Run 4	5.6 (143)	1.5 (39)	46.5
Run 5	10.7 (271)	1.5 (39)	25.6

Table 3-25. Damping Ratios in SC-2R

Run	Damping Ratio ξ (%)
0	2.2
1	3.5
2	2.5
3	4.2
4	5.4
5	6.1

Table 3-26. Energy Dissipation in RC-ECC Column

	Energy dissipation kip.inch (kN.mm)	Comulative Energy dissipation kip.inch (kN.mm)
Run 1	0.3 (34)	0.3 (34)
Run 2	7.9 (890)	8.2 (924)
Run 3	43.7 (4938)	51.9 5862)
Run 4	248.7 (28102)	300.6 (33964)
Run 5	338.3 (38217)	638.9 (72180)
Run 6	213.6 (24131)	852.5 (96311)

Table 3-27. Energy Dissipation in FRP Column

	Energy dissipation kip.inch (kN.mm)	Comulative Energy dissipation kip.inch (kN.mm)
Run 1	0.3 (38)	0.3 (38)
Run 2	8.2 (924)	8.5 (963)
Run 3	55.4 (6254)	63.9 (7217)
Run 4	141 (15930)	204.9 (23147)
Run 5	232.1 (26221)	437 (49367)
Run 6	307.2 (34711)	744.2 (84078)

Table 3-28. Damping Ratios in PEFB

Run	**Damping Ratio ξ (%)**
0	2.6
1	2.4
2	1.6
3	2.7
4	4.6
5	5.8
6	9.3

Table 4-1. Apparent Damages in Precast Segmental Columns

Columns	Drift	Cracks at near the interface	Cover spalling	Number of exposed spirals	Core spalling	Number of exposed longitudinal bars
SC-2	2%	Yes	No	0	No	0
	5%	Yes	Yes	5	No	4
	10%	Yes	Yes	7	Yes	7
SBR-1	2%	Yes	No	0	No	0
	5%	Yes	Yes	1	No	0
	10%	Yes	Yes	6	Yes	1
SF-2	2%	No	No	0	No	0
	5%	No	No	0	No	0
	10%	Yes	Yes	1	No	3
SE-2	2%	Yes	No	0	No	0
	5%	Yes	Yes	1	No	0
	10%	Yes	Yes	2	Yes	3
SC-2R	2%	No	No	0	No	0
	5%	No	No	0	No	0
	10%	Yes	Yes	0	Yes	0

Table 4-2. Comparison of Lateral Loads and Ultimate Displacements

Specimen	Lateral load capacity kips (kN)	Increase/Decrease compare to SC-2 (%)	Ultimate displacement in. (mm)	Increase/Decrease compare to SC-2 (%)
SC-2	22.1 (98.5)	0	7.9 (201)	0
SBR-1	26.5 (118)	20	10.12 (257)	28
SF-2	29.1 (129.6)	32	10.76 (273)	36
SE-2	20.8 (92.4)	-6	7.75 (197)	-8
SC-2R	32 (142.4)	45	10.67 (271)	35

Table 4-3. Energy Dissipation in Segmental Columns

Specimen	Dissipated energy kip-inch (kN-mm)
SC-2	539 (60895)
SBR-1	616.3 (69629)
SF-2	788.4 (89072)
SE-2	637.4(72012)
SC-2R	672.6 (75990)
Conv. segmental	179 (20223)

Table 4-4. Apparent Damages in Bent Columns

Columns	**Drift**	**Cracks at plastic Hinge**	**Cover spalling**	**Number of exposed spirals**	**Core spalling**	**Number of exposed longitudinal bars**	**Number of fractured/buckled bars**
RC-ECC	2%	Yes	No	0	No	0	0
	5%	Yes	Yes	0	No	4	0
	10%	Yes	Yes	1	Yes	7	3/fractured
FRP	2%	NO	NO	0	No	0	0
	5%	NO	NO	0	No	0	0
	10%	Yes	Yes	0	No	0	2/buckled

Table 4-5. Comparison of Lateral Loads and Ultimate Displacements

Specimen	**Lateral load capacity kips (kN)**	**Ultimate displacement in. (mm)**	**Ductility (%)**
RC-ECC	23.5 (104.7)	5.3 (135)	7.77
FRP	32.7 (145.4)	5.5 (140)	5.77

Table 4-6. Comparison of Energy Dissipation in Bent Columns

Column	**Maximum lateral load capacity kips (kN)**	**Cumulative energy dissipation kips-in (kN-mm)**
RC-ECC	23.5 (104.7)	852.5 (96311)
FRP	32.7 (145.4)	744.2 (84078)

Table 5-1. Mix Proportion of ECC $kg/m^3\left(lb/ft^3\right)$

Cement	Fly Ash	Sand	Fiber	Super Plasticizer	Viscous Agent	Water	W/C+FA	S/C	FA/C
380 (23.7)	790 (49.3)	470 (29.3)	26 (1.6)	18 (1.1)	1.2 (0.07)	305 (19)	0.26 (0.016)	1.24 (0.07)	2.08 (0.13)

Table 5-2. Material Type of ECC Mix

Material	Cement	Fly Ash	Sand	Viscous Agent	Super Plasticizer	Fiber
Type	Type I/II	FT Bridger	#60 Medium	Dow Methocel	Basf Melfox 2651	Kurary PVA KII 8X15

Table 5-3. Samples Properties

Group	Spacing of the spirals in. (mm)	* f_l' (Confinement Pressure) ksi (MPa)
1	No spiral	0
2	2 (51)	0.222 (1.5)
3	1.5 (38)	0.296 (2)
4	1 (25)	0.444 (3)

$$* \quad f_l' = \frac{2A_s\, f_y}{d_s s}$$

Table 5-4. ECC Samples Maximum Strength and Confinement Stress

f_l' ksi (MPa)	f_{ce}' ksi (MPa)	(f_l'/f_{co}')	(f_{ce}'/f_{co}')
0 (0)	5.59 (38.5)	0.00	1.00
0.22 (1.5)	5.86 (40.4)	0.04	1.05
0.3 (2)	6.63 (45.7)	0.05	1.19
0.44 (3)	7.19 (49.5)	0.08	1.29

Table 5-5. Ratio of the Maximum Strength to Residual Strength in ECC

Confinement		Max. Strength (a) ksi (MPa)	Residual Strength (b) ksi (MPa)	Ratio (b/a)
0 (0)	Sample 1	5.97 (41)	-	
	Sample 2	6.74 (46)	3.98 (27)	0.59
	Sample 3	5.37 (37)	2.46 (17)	0.46
	Sample 4	6.07 (42)	0.66 (5)	0.11
0.22 (1.5)	Sample 1	4.80 (33)	3.21 (22)	0.67
	Sample 2	6.64 (46)	-	
	Sample 3	5.87 (40)	4.58 (32)	0.78
	Sample 4	4.80 (33)	2.88 (20)	0.60
0.3 (2)	Sample 1	6.26 (43)	3.22 (22)	0.52
	Sample 2	6.58 (45)	3.56 (25)	0.54
	Sample 3	6.68 (46)	3.69 (25)	0.55
	Sample 4	7.42 (51)	4.29 (30)	0.58
0.44 (3)	Sample 1	7.40 (51)	5.89 (41)	0.80
	Sample 2	7.29 (50)	5.89 (41)	0.81
	Sample 3	5.79 (40)	4.28 (30)	0.74
	Sample 4	8.75 (60)	5.13 (35)	0.59
			Average	**0.594**

Table 5-6. Measured and Calculated ε_e

Specimen	**Section Diameter in. (mm)**	f'_{co} **ksi (MPa)**	f'_{ce} **ksi (MPa)**	ρ_s	ε_{sm}	f_y **ksi (MPa)**	**Measured** ε_e	**Calculated** ε_e
RNE	10 (254)	5.2 (35.8)	5.65 (38.9)	0.008	0.16	61.6 (425)	0.192	0.023
SMAC-2	12.5 (317)	10.1 (69.4)	10.1 (69.4)	0.007	0.16	68 (469)	0.021	0.015
ECC Bent-4 Span	12 (305)	8.3 (57.2)	8.3 (57.2)	0.009	0.16	60 (414)	0.017	0.018
PEFB	14 (356)	5.61 (38.7)	8.1 (55.8)	0.017	0.13	67.7 (467)	0.039	0.031
SE-2	16 (406)	7.11 (49)	8.9 (61.3)	0.015	0.11	68 (469)	0.024	0.022

Table 6-1. Uniaxial Material Concrete01 Properties in the Segmental Columns

			Strain Rate Factor	*Compressive Strength ksi (MPa)	Strain at Maximum Strength	*Failure Strength ksi (MPa)	Failure Strain
SC-2	The Base Segment	unconfined	1.2	6.7 (46.4)	0.003	2.7 (18.6)	0.011
		Confined		9.6 (66.4)	0.012	3.8 (26.6)	0.0456
	Other Segments	unconfined		5.9 (41.1)	0.003	2.4(16.4)	0.0113
		Confined		8.8 (60.7)	0.013	3.5 (24.3)	0.052
SBR-1	The Base Segment	unconfined	1.29	6 (41.4)	0.003	2.4 (16.5)	0.019
		Confined		9.0 (62.5)	0.007	3.6 (25)	0.02
	Other Segments	unconfined		7.2 (49.8)	0.003	2.9 (19.9)	0.0084
		Confined		10.2 (70.8)	0.0062	4.1 (28.3)	0.0373
SF-2	The Third and Fourth Segments	unconfined	1.22	9.3 (64.3)	0.003	3.7 (25.7)	0.006
		Confined		12.3 (85)	0.0052	4.9 (34)	0.015
SE-2	The Third and Fourth Segments	unconfined	-	8.8 (60.7)	0.003	3.5 (24.3)	0.052
		Confined		5.9 (41.1)	0.006	2.4 (16.4)	0.0113
SC-2R	The Third and Fourth Segments	unconfined	1.23	8.6 (59.4)	0.003	3.4 (59.4)	0.0137
		Confined		11.6 (80)	0.0054	4.6 (80)	0.027

- The strength values were multiplied by strain rate to account for strain rate affect

Table 6-2. Uniaxial Material steel02 Properties in the Segmental Columns

	Measured Yielding Strength ksi (MPa)	Strain Rate Factor	Strain rate X Yielding Strength ksi (MPa)	Strain Hardening Ratio
SC-2	64 (441)	1.07	68.6 (473)	0.005
SBR-1	74 (510)	1.06	78.8 (543)	0.005
SF-2	64 (441)	1.07	68.5 (472)	0.005
SE-2	64 (441)	1.06	68.0 (469)	0.005
SC-2R	64 (441)	1.08	69 (476)	0.005

Table 6-3. Uniaxial Material Concrete01 Properties for FRP Wrapped Segments

			Strain Rate Factor	Compressive Strength-f_{co} ksi (MPa)	Strain at Peak Strength-ε_{cy}	*Failure Strength-f_{cu} ksi (MPa)	*Failure Strain-ε_{cu}
SF-2	The Base Segment	unconfined	1.22	6.87 (47.4)	0.002	9.14 (63)	0.013
		Confined		6.87 (47.4)	0.002	9.14 (63)	0.013
	The Second Segment	unconfined		6.06 (41.8)	0.002	8.33 (57.4)	0.014
		Confined		6.06 (41.8)	0.002	8.33 (57.4)	0.014
SC-2R	The Base Segment	unconfined	1.23	3.36 (23.2)	0.004	5.63 (38)	0.017
		Confined		3.36 (23.2)	0.004	5.63 (38)	0.017
	The Second Segment	unconfined		2.98 (20.5)	0.004	5.25 (36)	0.018
		Confined		2.98 (20.5)	0.004	5.25 (36)	0.018

*The strength values were multiplied by strain rate to account for strain rate affect

Table 6-4. Uniaxial Material Concrete01 Properties for ECC

	Compressive strength ksi (MPa)	Strain at Maximum Strength	Failure Strength ksi (MPa)	Failure Strain

SE-2	The Base Segment	unconfined	7.11 (49)	0.005	2.8 (19)	0.005
		Confined	8.9 (61)	0.0065	3.5 (24)	0.0207
	Other Segments	unconfined	7.4 (51)	0.005	3 (21)	0.005
		Confined	9.1 (62)	0.0065	3.6 (24)	0.0207

Table 6-5. Bond-Slip Rotation Parameters in OpenSees for Segmental Column

	θ_y	M_y kips.inch (kN.mm)	θ_u	M_u kips.inch (kN.mm)
SC-2	0.0023	1716 (193872)	0.0021	1655 (186980)
SBR-1	0.0031	1320 (149132)	0.0148	1944 (219631)
SF-2	0.0023	1883 (212739)	0.0029	2124 (239967)
SE-2	0.0023	1734 (195905)	0.0031	1659 (187432)
SC-2R	0.0023	1646 (185963)	0.0030	1889 (213417)

Table 6-6. The Measured and Calculated Dissipated Energy in Segmental Column

Specimen	Measured Dissipated Energy Kip-inch (kN-mm)	Calculated Dissipated Energy Kip-inch (kN-mm)	Difference Between Measured and Calculated (%)
SC-2	539 (60895)	325 (36718)	39
SBR-1	616.3 (69629)	498 (56263)	19
SF-2	788.4 (89072)	807 (91250)	-2
SE-2	637.4(72012)	590 (66720)	7
SC-2R	672.6 (75990)	531 (60005)	21

Table 6-7. Uniaxial Material Concrete01 Properties in RC-ECC Column

		*Compressive strength ksi (MPa)	Strain at Maximum Strength	*Failure Strength ksi (MPa)	Failure Strain
RC-ECC	unconfined	5.68 (39)	0.002	4.82 (15)	0.006

	Confined	8.99 (62)	0.00783	7.69 (53)	0.02237

* The strength values were multiplied by 1.2 to account for strain rate affect

Table 6-8. Uniaxial Material Concrete02 Properties in RC-ECC Column

		Compressive strength ksi (MPa)	Strain at Maximum Strength	Failure Strength ksi (MPa)	Failure Strain
RC-ECC	unconfined	5.6 (38)	0.0025	2.24 (15)	0.006
	Confined	8.087 (55)	0.0055	3.23 (22)	0.0207

Table 6-9. Uniaxial Material Concrete01 Properties in FRP Column

		*Compressive strength ksi (MPa)	Strain at Maximum Strength	*Failure Strength ksi (MPa)	Failure Strain
FRP	unconfined	5.68 (39)	0.002	8.27 (57)	0.014
	Confined	5.68 (39)	0.002	8.27 (57)	0.014

* The strength values were multiplied by 1.24 to account for strain rate affect

Table 6-10. Uniaxial Material steel02 Properties in PEFB Bent

	Measured Yielding Strength ksi (MPa)	Strain Rate Factor	Strain Rate X Yield Strength ksi (MPa)	Strain Hardening Ratio
RC-ECC	80 (551)	1.08	86.8 (598)	0.01
FRP	67.7 (466)	1.09	74 (510)	0.005

Table 6-11. Bond-Slip Rotation Parameters in OpenSees, PEFB

θ_y	M_y kips.inch (kN.mm)	θ_u	M_u kips.inch (kN.mm)

RC-ECC	0.004622	1187 (134106)	0.0114	1317 (148793)
FRP	0.0031	1695 (191499)	0.0039	1996 (225506)

Table 6-12. The Measured and Calculated Dissipated Energy in PEFB

	Column	Measured Dissipated Energy Kip-inch (kN-mm)	Calculated Dissipated Energy Kip-inch (kN-mm)		Difference Between Measured and Calculated (%)	
			Zhu's FRP Material	Modified FRP Material	Zhu's FRP Material	Modified FRP Material
Runs 1 through 5	RC-ECC	593 (67047)	671 (75844)	610 (68948)	13%	3%
	FRP	420 (47544)	478 (54078)	601 (67945)	13%	42%
All Runs	RC-ECC	852 (96258)	1150 (129943)	1142 (129074)	42%	41%
	FRP	744 (84056)	720 (81345)	934 (105522)	3%	25%

Table 7-1. Parameter Matrix in SC-2

		Case 1	Case 2	Case 3	Case 4	Case 5	Case 6	Case 7
Base Segment	Height in(mm)	8 (203)	12 (305)	16 (406)	20 (508)	24 (609)	32 (813)	40 (1016)
	Height/Diameter	0.5	0.75	1	1.25	1.5	2	2.5
	Height/Col. Height	0.11	0.16	0.22	0.27	0.33	0.44	0.55
Base Segment Long. Reinforcement	Steel Bars	5 #4	8 #4	10 #4	12 #4	15 #4	-	-
	Steel Ratio	0.50%	0.80%	1%	1.20%	1.50%	-	-
Post-Tensioning	Force kips (kN)	45 (200)	100 (445)	180 (801)	-	-	-	-
	Force/F_u	0.15 F_u	0.33 F_u	0.60 F_u	-	-	-	-
Concrete Strength ksi (MPa)		5 (34.5)	8 (55.01)	10 (68.9)	-	-	-	-

Table 7-2. Parameter Matrix in SBR-1

		Case 1	Case 2	Case 3
Rubber pad	Height in(mm)	4 (101)	8 (203)	(16 (406)
	Height/Diameter	0.25	0.5	1
	Height/Col. Height	0.05	0.11	0.22
Rubber pad	Layer Thickness in. (mm)	1/16 (2)	3/16 (5)	8/16 (13)
	Shape Factor	50	14	6.25

Table 7-3. Maximum Lateral Load Capacity in SC-2 with Different Base Segment Heights (Steel Ratio 1%)

Base Segment Height in.	Max. Lateral	Increase/Decrease

(mm)	Load Capacity kips (kN)		Compared to Reference Column (%)	
	5% DR	10% DR	5% DR	10% DR
8 (203)	17.4 (77)	17.4 (77)	-18	-18
12 (305)	18.4 (82)	18.4 (82)	-13	-13
16 (406)	19.6 (87)	19.6 (87)	-7	-7
20 (508)	21.1 (94)	21.1 (94)	0	0
24 (609)	23 (102)	23 (102)	9	9
32 (812)	27.8 (123)	31.5 (140)	32	48
40 (1016)	27.8 (123)	31.3 (139)	32	44

Table 7-4. Maximum Lateral Load Capacity in SC-2 with Different Base Segment Heights (Steel Ratio 0.5%)

Base Segment Height in. (mm)	Max. Lateral Load Capacity kips (kN)		Increase/Decrease Compared to Reference Column (%)	
	5% DR	10% DR	5% DR	10% DR
8 (203)	17.4 (77)	17.4 (77)	-25	-31
12 (305)	18.5 (82)	18.5 (82)	-21	-26
16 (406)	20.0 (89)	20.0 (89)	-15	-21
20 (508)	23.4 (104)	25.3 (112)	0	0
24 (609)	23.3 (104)	25.7 (114)	0.4	2
32 (812)	23.3 (104)	26.3 (117)	0.6	4

Table 7-5. Dissipated Energy in SC-2 with Different Base Segment Heights (Steel Ratio 1%)

Base Segment Height in. (mm)	Dissipated Energy kips.in (kN.mm)	Increase/Decrease Compared to Reference

			Column (%)	
	5% DR	10% DR	5% DR	10% DR
8 (203)	27 (3066)	67 (7565)	-20	-17
12 (305)	29 (3320)	70 (7998)	-14	-12
16 (406)	31 (3542)	75 (8505)	-8	-6
20 (508)	34 (3869)	80 (9096)	0	0
24 (609)	38 (4327)	87 9859)	12	8
32 (812)	47 (5302)	127 (14406)	37	58
40 (1016)	44 (5055)	122 13785)	30	51

Table 7-6. Dissipated Energy in SC-2 with Different Base Segment Heights (Steel Ratio 0.5%)

Base Segment Height in. (mm)	Dissipated Energy kips.in (kN.mm)		Increase/Decrease Compared to Reference Column (%)	
	5% DR	10% DR	5% DR	10% DR
8 (203)	27 (3061)	67 (7568)	-18	-34
12 (305)	29 (16633)	71 (8018)	-12	-30
16 (406)	33 (3295)	91 (10280)	-1	-10
20 (508)	33 (3704)	102 (11468)	0	0
24 (609)	33 (3675)	97 (10947)	2	4
32 (812)	31 (3508)	91 (10300)	6	10

Table 7-7. Maximum Lateral Load Capacity in SC-2 with Different Steel Ratios

Steel Ratio in the	Max. Lateral	Increase/Decrease

Base Segment	Load Capacity kips (kN)		Compared to Reference Column (%)	
	5% DR	10% DR	5% DR	10% DR
0.50%	25 (111)	25 (111)	18	18
0.80%	21.3 (95)	21.3 (95)	0.8	0.8
1.00%	21.1 (94)	21.1 (94)	0	0
1.20%	21.1 (94)	21.1 (94)	0.06	0.06
1.50%	21 (93)	21 (93)	0.5	0.5
2.00%	21 (93)	21 (93)	0.6	0.6

Table 7-8. Dissipated Energy in SC-2 with Different Steel Ratios

Steel Ratio in the Base Segment	Dissipated Energy kips.in (kN.mm)		Increase/Decrease Compared to Reference Column (%)	
	5% DR	10% DR	5% DR	10% DR
0.50%	33(3748)	102 (11468)	-3	26
0.80%	34(3892)	81 (9166)	0.5	0.8
1.00%	34 (3869)	81(9096)	0	0
1.20%	35 (3913)	80 (9085)	1	0.1
1.50%	35 (3938)	80 (9091)	2	0.05
2.00%	34 (3894)	81 (9095)	0.6	0.01

Table 7-9. Maximum Lateral Load Capacity in SC-2 with Different Concrete Strengths

Concrete Strength ksi (MPA)	Max. Lateral Load Capacity kips (kN)		Increase/Decrease Compared to Reference Column (%)	
	5% DR	10% DR	5% DR	10% DR
5 (34)	21.1 (94)	21.1 (94)	0	0
8 (55)	24.1 (107)	24.9 (111)	14	17
10 (69)	27.4 (122)	29.8 (132)	30	41

Table 7-10. Residual Displacement in SC-2 with Different Concrete Strengths

Concrete Strength ksi (MPA)	Residual Displacement in. (mm)		Increase/Decrease compared to Refrence Column (%)	
	5% DR	10% DR	5% DR	10% DR
5 (34)	0.44 (4)	1.4 (37)	0	0
8 (55)	0.072 (23)	0.50 (13)	-83	-64
10 (69)	0 (0)	0.2 (5)	-100	-85

Table 7-11. Dissipated Energy in SC-2 with Different Concrete Strengths

Concrete Strength ksi (MPA)	Dissipated Energy kips.in (kN.mm)		Increase/Decrease Compared to Reference Column (%)	
	5% DR	10% DR	5% DR	10% DR
5 (34)	34 (3869)	80 (9096)	0	0
8 (55)	30 (3442)	84(9577)	11	4
10 (69)	28 (3178)	87 (9878)	18	8

Table 7-12. Maximum Lateral Load Capacity in SC-2 with Different Initial PT Force Levels

PT Force Level kips (kN)	Max. Lateral Load Capacity kips (kN)		Increase/Decrease Compared to Reference Column (%)	
	5% DR	10% DR	5% DR	10% DR
45 (200)	18.9 (84)	18.9 (84)	-10	-10
100 (444)	21.1 (94)	21.1 (94)	0	0
180 (800)	25.8 (115)	25.8 (115)	22	22

Table 7-13. Residual displacements in SC-2 with Different Initial PT Force Levels

PT Force Level kips (kN)	Residual Displacement in. (mm)		Increase/Decrease compared to Reference Column (%)	
	5% DR	10% DR	5% DR	10% DR
45 (200)	0.07 (2)	1.15 (29)	-50	-20
100 (444)	0.14 (3)	1.44 (36)	0	0
180 (800)	0.64 (16)	2.08 (53)	357	44

Table 7-14. Dissipated Energy in SC-2 with Different Initial PT Force Levels

PT Force Level kips (kN)	Dissipated Energy kips.in (kN.mm)		Increase/Decrease Compared to Reference Column (%)	
	5% DR	10% DR	5% DR	10% DR
45 (200)	28 (3143)	71 (8118)	-18	-18
100 (444)	34 (3869)	80 (9096)	0	0
180 (800)	48 (5394)	94 (10648)	40	40

Table 7-15. Max. PT Force in SC-2 with Different Initial PT Force Levels

Initial PT Force Level kips (kN)	Maximum PT Force Level kips (kN)		Increase Compared to initial force (%)	
	5% DR	10% DR	5% DR	10% DR
45 (200)	146 (650)	233 (1036)	224	417
100 (444)	180 (801)	263 (1170)	80	163
180 (800)	224 (998)	291 (1297)	24	62

Table 7-16. Maximum Lateral Load Capacity in SBR-1 with Different Rubber Pad Heights

Rubber Pad Height in. (mm)	Max. Lateral Load Capacity kips (kN)		Increase/Decrease Compared to Reference Column (%)	
	5% DR	10% DR	5% DR	10% DR
4 (101)	20.8 (93)	20.8 (93)	0.05	0.05
8 (203)	20.7 (92)	20.7 (92)	0	0
16 (406)	20.6 (92)	20.6 (92)	-0.05	-0.05

Table 7-17. Dissipated Energy in SBR-1 with Different Rubber Pad Heights

Rubber Pad Height in. (mm)	Dissipated Energy kips.in (kN.mm)		Increase/Decrease Compared to Reference Column (%)	
	5% DR	10% DR	5% DR	10% DR
4 (101)	33 (3725)	80 (9047)	-5	-0.4
8 (203)	31 (3523)	79 (9010)	0	0
16 (406)	28 (3215)	79 (8961)	8	0.5

Table 7-18. Maximum Lateral Load Capacity in SBR-1 with Different Rubber Pad Shape Factors

Rubber Pad Shape Factor	Max. Lateral Load Capacity kips (kN)		Increase/Decrease Compared to Reference Column (%)	
	5% DR	10% DR	5% DR	10% DR
42	20.9 (93)	20.9 (93)	0.7	0.7
14	20.7 (92)	20.7 (92)	0	0
5	18.5 (82)	21.8 (97)	-10	5

Table 7-19. Dissipated Energy in SBR-1 with Different Rubber Pad Shape Factors

Rubber Pad Shape Factor	Dissipated Energy kips.in (kN.mm)		Increase/Decrease Compared to Reference Column (%)	
	5% DR	10% DR	5% DR	10% DR
42	34 (3917)	80 (9102)	-7	-1
14	32 (3651)	79 (9010)	0	0
5	36 (4083)	84 (9509)	11	5

Table 7-20. Maximum Lateral Load Capacity in SC-2 and Conventional Precast Column

	Max. Lateral Load Capacity kips (kN)		Increase/Decrease Compared to Reference Column (%)	
	5% DR	10% DR	5% DR	10% DR
SC-2	21.1 (94)	21.1 (94)	0	0
No Base Segment Connected	15.5 (69)	15.5 (69)	-26	-26

Table 7-21. Dissipated Energy in SC-2 and Conventional Precast Column

	Dissipated Energy kips.in (kN.mm)		Increase/Decrease Compared to Reference Column (%)	
	5% DR	10% DR	5% DR	10% DR
SC-2	34 (3869)	80 (9096)	0	0
No Base Segment Connected	22 (2481)	57 (6457)	-35	-29

Table 7-22. Parameter Matrix in FRP Column

		Case 1	Case 2	Case 3	Case 4	Case 5
FRP Column Long. Reinforcement	Steel Bars	7 #3	11 #3	14 #3	18 #3	21 #4
	Steel Ratio	0.50%	0.80%	1%	1.30%	1.50%
FRP Column Tube Thickness in. (mm)		0.187 (4.7)	0.216 (5.5)	0.269 (6.8)	0.303 (7.7)	0.32 (8.1)
FRP Column Tube Fiber Orientation (Degree)		35	45	55	-	-

Table 7-23. Maximum Lateral Load Capacity in FRP Column with Different Tube Thickness

Tube Thickness in. (mm)	Max. Lateral Load Capacity kips (kN)		Increase/Decrease Compared to Reference Column (%)	
	5% DR	10% DR	5% DR	10% DR
0.187 (4.7)	22.4 (100)	28.9 (129)	-14	-16
0.216 (5.5)	23.7 (106)	30.9 (138)	-9	-10
0.269 (6.8)	26.1 (116)	34.5 (154)	0	0
0.303 (7.7)	27.5 (122)	36.7 (163)	5	6
0.32 (8.1)	28.1 (125)	37.8 (168)	8	9

Table 7-24. Dissipated Energy in FRP Column with Different Tube Thickness

Tube Thickness in. (mm)	Dissipated Energy kips.in (kN.mm)		Increase/Decrease Compared to Reference Column (%)	
	5% DR	10% DR	5% DR	10% DR
0.187 (4.7)	26.6 (3000)	74.7 (8438)	-7	-10
0.216 (5.5)	27.3 (30870)	77.7 (8775)	-4	-6
0.269 (6.8)	28.6 (3228)	82.8 (9358)	0	0
0.303 (7.7)	29.4 (3321)	86 (9715)	3	4
0.32 (8.1)	29.8 (3367)	87.5 (9887)	4	5

Table 7-25. FRP Tube Properties in Hoop Direction for Different Fiber Orientations

Fiber Orientation	Hoop Elastic Modulus ksi (MPa)	Hoop Ultimate Strength ksi (MPa)
$\pm 55^\circ$	1850 (12760)	34
$\pm 45^\circ$	1850 (12760)	28.5
$\pm 35^\circ$	1850 (12760)	23

Table 7-26. FRP Tube Stress-Strain Model Parameters in Longitudinal Direction

Fiber Orientation	a	b
$\pm 55^\circ$	2.97E-05	4.59 E-04
$\pm 45^\circ$	4.55E-05	4.59 E-04
$\pm 35^\circ$	7.46E-05	4.59 E-04

Table 7-27. Maximum Lateral Load Capacity in FRP Column with Different Fiber Orientations

Fiber Orientation (Degree)	Max. Lateral Load Capacity kips (kN)		Increase/Decrease Compared to Reference Column (%)	
	5% DR	10% DR	5% DR	10% DR
±55°	26 (115)	34.5 (153)	0	0
±45°	28.6 (127)	38.8 (172)	10	12
±35°	31 (138)	42.8 (190)	19	24

Table 7-28. Dissipated Energy in FRP Column with Different Fiber Orientations

Fiber Orientation (Degree)	Dissipated Energy kips.in (kN.mm)		Increase/Decrease Compared to Reference Column (%)	
	5% DR	10% DR	5% DR	10% DR
±55°	29 (3228)	83 (9358)	0	0
±45°	28 (3132)	80 (9092)	3	3
±35°	27 (3050)	77 (8686)	5	7

Table 7-29. Maximum Lateral Load Capacity in FRP Column with Different Steel Ratios

Steel Ratio (%)	Max. Lateral Load Capacity kips (kN)		Increase/Decrease compared to Reference Column (%)	
	5% DR	10% DR	5% DR	10% DR
0.5	34.3 (153)	34.5 (154)	0	0
0.8	37.6 (167)	37.8 (168)	9	9
1	40.1 (178)	40.2 (179)	16	16
1.3	43.2 (192)	43.4 (193)	26	26
1.5	45.6 (203)	45.8 (204)	33	33

Table 7-30. Residual Displacement in FRP Column with Different Steel Ratio

Steel Ratio (%)	Residual Displacement in. (mm)		Increase/Decrease compared to Reference Column (%)	
	5% DR	10% DR	5% DR	10% DR
0.5	0.44 (11)	1.13 (29)	0	0
0.8	0.69 (18)	1.64 (42)	57	44
1	0.88 (22)	1.95 (50)	100	72
1.3	1.07 (27)	2.33 (59)	143	106
1.5	1.2 (30)	2.52 (64)	171	122

Table 7-31. Dissipated Energy in FRP Column with Different Steel Ratios

Steel Ratio (%)	Dissipated Energy kips.in (kN.mm)		Increase/Decrease compared to Reference Column (%)	
	5% DR	10% DR	5% DR	10% DR
0.5	202.2 (22847)	82.8 (9358)	0	0
0.8	254.9 (29927)	106.9 (12073)	31	29
1	311.5 (35188)	124.2 (14032)	54	50
1.3	371.4 (41956)	147 (16612)	83	77
1.5	414.8 (46867)	163.5 (18470)	105	97

FIGURES

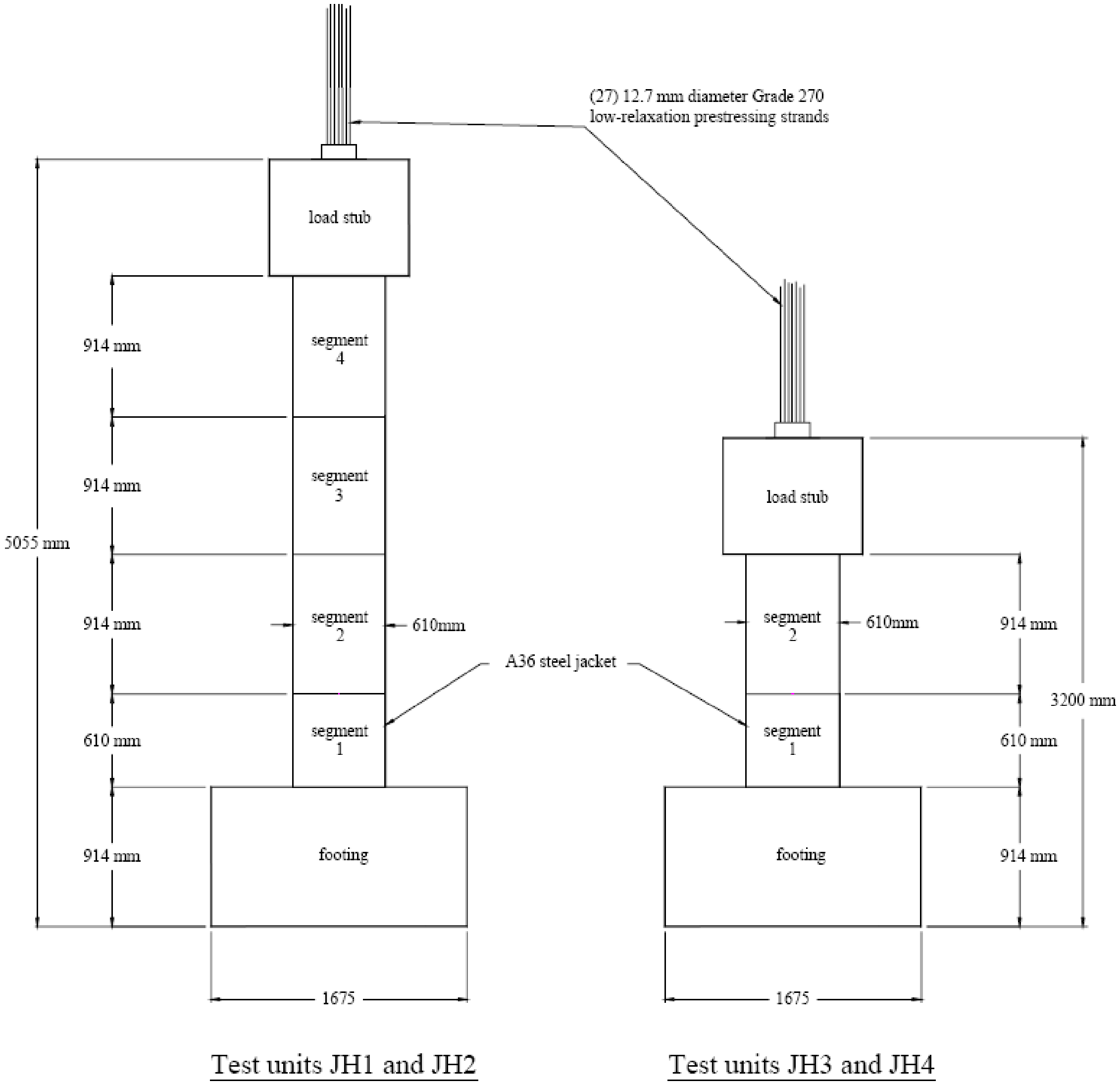

Fig. 1-1. Precast Segmental Columns Tested by Hews and Priestley (2002)

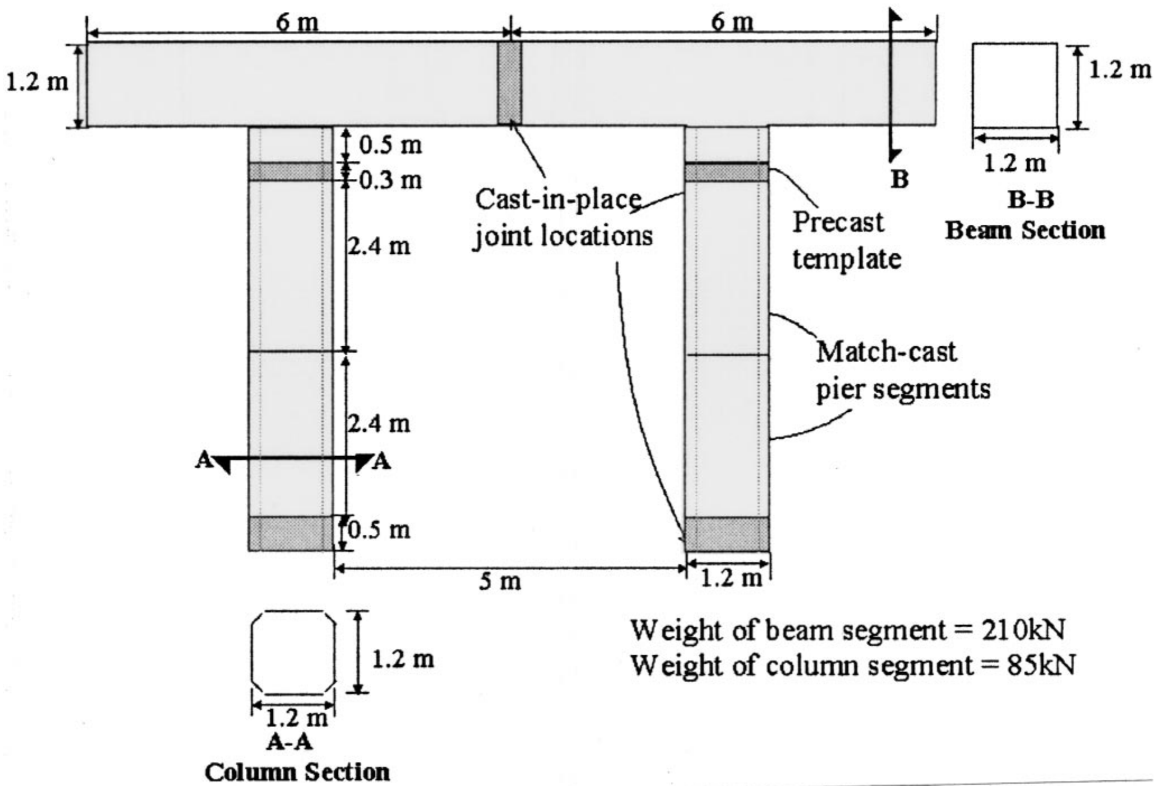

Fig. 1-2. Segmentally Precast, Post-Tensioned Bridge Pier System [Kwan and Billington, 2003]